Carbon Materials: Chemistry and Physics 11
Series Editors: Franco Cataldo · Paolo Milani

Francesca Borghi
Francesca Soavi
Paolo Milani *Editors*

Nanoporous Carbons for Soft and Flexible Energy Devices

Springer

Carbon Materials: Chemistry and Physics

Volume 11

Series Editors
Franco Cataldo
Actinium Chemical Research Institute
Roma
Italy

Paolo Milani
Dipartimento di Fisica and CIMAINA
University of Milan
Milano
Italy

Carbon Materials: Chemistry and Physics aims to be a comprehensive book series with complete coverage of carbon materials and carbon-rich molecules. From elemental carbon dust in the interstellar medium, to the most specialized industrial applications of the elemental carbon and derivatives. With great emphasis on the most advanced and promising applications ranging from electronics to medicinal chemistry.

The aim is to offer the reader a book series which not only should be made of self-sufficient reference works, but should stimulate further research and enthusiasm.

For further volumes:
http://www.springer.com/series/7825

Francesca Borghi • Francesca Soavi • Paolo Milani
Editors

Nanoporous Carbons for Soft and Flexible Energy Devices

Springer

Editors
Francesca Borghi
Department of Physics
University of Milan
Milan, Italy

Paolo Milani
Department of Physics
University of Milan
Milano, Italy

Francesca Soavi
Department of Chemistry "Giacomo Ciamician"
Alma Mater Studiorum University of Bologna
Bologna, Italy

ISSN 1875-0745 ISSN 1875-0737 (electronic)
Carbon Materials: Chemistry and Physics
ISBN 978-3-030-81826-5 ISBN 978-3-030-81827-2 (eBook)
https://doi.org/10.1007/978-3-030-81827-2

This Springer imprint is published by the registered company Springer Nature Switzerland AG
The registered company address is: Gewerbestrasse 11, 6330 Cham, Switzerland

Preface

The rapidly increasing demand for flexible electronics, portable energy harvesting/storage systems, autonomous sensors, soft robotics, and wearable and biomedical devices has stimulated the need of electrode materials to be integrated on nonconventional substrates such as flexible and soft polymers, textiles, fabrics, and biomaterials.

The low cost, abundance, and facile processing routes make nanoporous carbon electrodes ideal candidate for these applications. In fact, the structural properties of carbon-based nanomaterials in terms of porosity, specific surface area, and phase, combined with their mechanical, conductive, and catalytic properties, show promising results for a wide range of applications where soft, autonomous, and sustainable systems are necessary.

This book provides a timely and in-depth review of some of the main topics and trends about the use of carbonaceous materials as high performing and cost-effective ingredients for large scale technological implementation of devices. In order to serve as a reference source for a multidisciplinary community working at the development of sensors, energy harvesting and storage devices, actuators, etc., in this book, we focus our attention to the electrical and structural properties of porous carbonaceous materials, and how production and characterization approaches can lead to systems with tailored properties. In particular, we concentrated on enhanced interfacial interactions between fluids and the solid walls of the materials promoted by the high surface area available in the porous matrix.

This book addresses systems relevant for autonomous devices requiring efficient energy production and managing such as carbon-based flexible electronics with reduced power consumption. Carbon fiber electrodes are promising materials to be integrated into flexible batteries and carbon nanotubes-based flexible dual-material gate (DMG) technology. Carbon-based ion-gated transistors (IGTs) are also presented as enabling ingredient for the fabrication of energy harvester/storage microsystems due to their low-voltage operational characteristics, in view of the development of autonomous sensors with multiple functionalities on a single chip, that is, Systems on a Chip (SoC).

A very important issue is the sustainable production of energy: the case of carbonaceous materials integrated into microbial fuel cells is presented and discussed in view of scale-up of this technology. The focus will be on the most recent findings and incorporation of lightweight, robust, and biocompatible carbon fiber electrodes in the form of carbon veil both as the anode and cathode counterparts and their suitability in larger-scale designs.

Fabrication methods allowing to control the internal and external structure of the functional properties carbon-based systems will be discussed with particular attention to carbon-based filler and matrices integrated into sensor architectures. Solutions enabled by smart production approaches such as laser-induced graphene (LIG) for stretchable applications in soft piezoresistive, electrophysiological, and electrochemical sensors are also presented.

Finally, the last two chapters discuss and summarize the characterization of porous carbon films' growth mechanisms highlighting the achievement of the fine control of the morphological properties that regulate mass transfer rates in catalytic devices, electron diffusion pathway in dye-sensitize solar cells, double-layer organization of the electrolyte in electrochemical devices, and performance of gas sensors.

Milan, Italy Francesca Borghi

Bologna, Italy Francesca Soavi

Milan, Italy Paolo Milani

Contents

Acronym and Symbols

3D	Three dimensional
AC	Activated carbon
Al	Aluminium
ATP	Adenosine triphosphate
Au	Gold
BET	Brunauer–Emmett–Teller
CNT	Carbon nanotube
CV	Carbon veil
DIBL	Drain-induced barrier lowering
DMG	Dual-material gate
FET	Field effect transistor
GAC	Granular activated carbon
GDL	Gas diffusion layer
IC	Integrated circuit
$I_{diode\text{-}on}$	On-current of diode
I_{off}	Off-state current
I_{on}	On-state current
I-V curve	Current-voltage characteristic curves
L	Length of the device channel
MFC	Microbial fuel cell
MOSFET	Metal-oxide-semiconductor field effect transistor
NASA	National Aeronautics and Space Administration, USA
NG	Normal-gated
OCV	Open circuit voltage
ORR	Oxygen reduction reaction
PANI	Polyaniline
Pd	Palladium
PTFE	Polytetrafluoroethylene
PVA	Polyvinyl alcohol
PVDF	Polyvinylidene difluoride
SEM	Scanning electron microscopy

SS	Subthreshold swing
Ti	Titanium
V_{ctrl}	Controlling signal
$V_{d\text{-}in}$	Input signal applied on drain electrode
V_{ds}	Drain-to-source voltage
$V_{g\text{-}in}$	Input signal applied on gate electrode
V_{gs}	Gate-to-source voltage
V_{out}	Output signal
V_{th}	Threshold voltage
W	Width of the device channel
Y	Yttrium

Chapter 1
Carbon Nanotubes for Flexible Fiber Batteries

Ye Zhang, Tingting Ye, Luhe Li, and Huisheng Peng

Abstract The development of various wearable flexible electronic devices has become an important trend of modern electronics. Fiber batteries are seen as one of the most promising power supplies for powering these wearable electronics due to their flexible, lightweight, breathable, and weavable features. The key to achieving flexible fiber batteries lies in constructing flexible electrodes. Among many promising materials, carbon nanotubes, which have the merits of lightweight, flexible, conductive as well as large specific surface area, are widely used to produce fiber electrodes for flexible fiber batteries. In this chapter, the preparation and the properties of carbon nanotube fibers are firstly described. Subsequently, the application of carbon nanotube fiber for flexible fiber lithium-ion batteries, lithium-metal batteries, aqueous-metal batteries, and other batteries are summarized from the aspects of working principle, fabrication process, and electrochemical properties. Finally, the issues of flexible fiber battery need to be conquered also have been discussed for future development.

Keywords Carbon nanotubes · Flexible · Fiber electrodes · Fiber batteries · Lithium-ion batteries · Lithium-metal batteries · Aqueous-metal batteries

Y. Zhang (✉) · T. Ye · L. Li
National Laboratory of Solid State Microstructures, Jiangsu Key Laboratory of Artificial Functional Materials, College of Engineering and Applied Sciences, Nanjing University, Nanjing, China
e-mail: yezhang@nju.edu.cn

H. Peng
State Key Laboratory of Molecular Engineering of Polymers, Department of Macromolecular Science and Laboratory of Advanced Materials, Fudan University, Shanghai, China

F. Borghi et al. (eds.), *Nanoporous Carbons for Soft and Flexible Energy Devices*,
Carbon Materials: Chemistry and Physics 11,
https://doi.org/10.1007/978-3-030-81827-2_1

1.1 Brief Introduction

Flexible devices such as wearable electronics and smart clothes have emerged as an important branch of modern electronics and represented a promising direction for the future lifestyles. These devices would be directly worn on the human body and work stably under complex deformations. As a result, the corresponding power systems that match flexible devices should be miniaturized, flexible, and adaptable. To meet these requirements, the configuration of batteries has recently evolved from rigid three-dimensional bulks to flexible two-dimensional films, and finally to super-flexible one-dimensional fibers. Compared to three-dimensional bulks and two-dimensional films, these new fiber batteries can more effectively adapt to complex deformations such as bending, folding, twisting and stretching during use, and they may be also woven into breathable power textiles if necessary.

The key to realizing fiber batteries is the development of effective fiber electrodes. Carbon nanotube (CNT) fibers have been widely studied to simultaneously demonstrate high electrical conductivity, Young's modulus and tensile strength with large specific surface area as CNTs are aligned along the axial direction to extend their remarkable properties to macroscopic scale. In the development of flexible fiber batteries, the CNT fibers are usually used as supporting frameworks for active materials and current collectors to transport charges. This chapter summarizes the use of CNT fibers for fiber lithium-ion batteries, lithium-metal batteries and aqueous metal-air batteries.

1.2 Carbon Nanotubes

Since discovered in 1991, one-dimensional CNTs have captured enormous attention from researchers worldwide [1]. Depending on the wall numbers, CNTs are classified as single-walled CNTs (SWCNTs) and multi-walled CNTs (MWCNTs). SWCNTs can be idealized as a hollow cylinder rolled up with a 2D hexagonal lattice of C atoms along with one of the Bravais vectors. MWCNTs consist of concentric cylinders with an interlayer spacing of 0.32–0.35 nm [2]. Attributed to the superb electrical conductivity, Young's modulus, tensile strength, thermal conductivity, and large specific areas, CNTs have been broadly adopted as electrode materials, conductive additives, and flexible current collectors in various energy storage devices [3–6]. For flexible fiber batteries, aligned CNT fibers are commonly used to act as skeletons to support active materials and current collectors for charge transport.

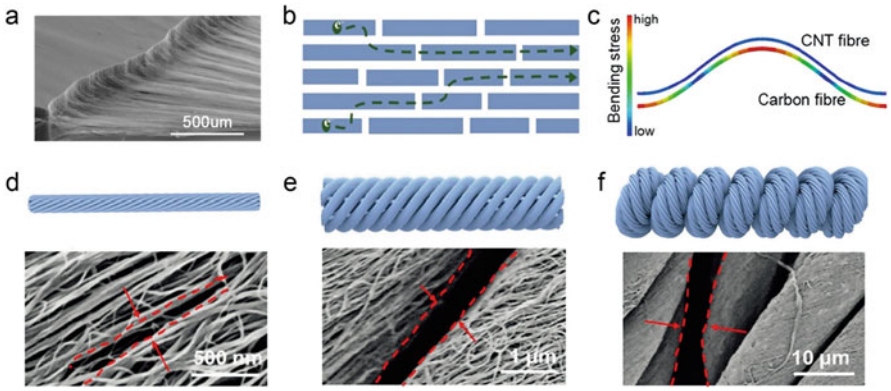

Fig. 1.1 (**a**) Scanning electron microscopy image of dry-drawing CNT bundles from a super-aligned CNT array. (**a**) From [30]. Reprinted with permission from Elsevier. (**b**) The three-dimensional electron hopping model in CNT fibers. (**c**) The simulated stress distribution of CNT fibers and carbon fibers under the same bending condition. (**d**) Single CNT fiber and scanning electron microscopy image of nanometer-sized gaps formed among CNTs. (**e**) Multiply fiber and scanning electron microscopy image of micrometer-sized gaps among building CNT fibers. (**f**) A spring-like fiber and scanning electron microscopy image of micrometer-sized gaps among screw threads. (**b-f**) From [21]. Reprinted with permission from Wiley-VCH Verlag GmbH & Co. KGaA, Weinheim

1.2.1 Preparation of Carbon Nanotube Fibers

CNT fibers were produced through various methods, including dry-spinning from aligned CNT array, direct spinning from CNT aerogel, wet spinning and filtering from suspension [7–10]. Compared to the others, CNT fibers dry-spun from the CNT array possess the merits of superior mechanical and electrical properties, which will be emphasized in the following section.

Dry-spinning of CNT fibers involves distinctive CNT precursors, spinnable CNT arrays, also named super-aligned CNT forests. In 2002, Jiang et al. reported a self-assembled CNT fiber produced by simply drawing out from a super-aligned CNT array and demonstrated its application as the filament and polarizer [7]. Great efforts have since been devoted to this specific field for its broad applications in various electronics and energy storage devices.

Figure 1.1a displays a scanning electron microscopy image of a spinnable CNT array. The CNT array was vertically aligned to the substrate, and the CNT bundle was directly drawn out from the side of the array. Generally, the spinnable CNT array was synthesized *via* chemical vapor deposition (CVD). A buffer layer (Al_2O_3, ZnO, MgO, *etc.*) was firstly deposited on a silicon wafer to prevent the penetration of catalyst into the substrate and limit the mobility and Ostwald ripening of catalyst particles, which were critical for controlling the diameter and wall number of the CNTs [11–13]. Subsequently, the catalytic iron layer of several nanometers in thickness was deposited by electron-beam/thermal evaporator at a low evaporation rate. Afterward, the CVD process was carried out in a furnace with

carbon source and carrier gas. Typically, the synthesis of the spinnable CNT array included two stages: the pretreatment of catalyst, in which the thin catalyst layer formed dense nanoparticles of small and uniform diameters; the growing stage, during which the carbon source was pyrolyzed and formed carbon clusters at high temperature. Carbon caps first appeared when these carbon clusters diffused into catalyst particles and reached a saturated state, and then they formed CNTs when more carbon clusters diffused into the catalyst. Meanwhile, amorphous carbon was also formed on the catalyst surface, which inhibited the diffusion of carbon clusters. Consequently, the catalyst lost its activity when fully covered by amorphous carbon, leading to growth termination. Properly extending the growth time before catalyst deactivation by introducing a small number of weak oxidants, such as water and ethanol, helps to produce higher CNT arrays [14–16]. After the final cooling stage, a spinnable CNT array can be taken out from the furnace to fabricate CNT fibers.

Studies have confirmed that a spinnable CNT array should have a clean surface, oriented arrangement, suitable density and proper length, which crucially depend on the catalyst. An appropriate thickness of the catalyst layer ensures catalyst particles of the right size, which impacts the diameter, orientation and length of the CNTs. Besides, the temperature, gas content/flow rate, pretreatment and growth time are all required to be optimized to synthesize the spinnable CNT array [17].

Under the optimized condition, suitable interaction and entanglement will emerge among neighboring CNT bundles, which are pivotal to dry-drawing the CNT sheet from the array [18]. CNTs in the CNT array tend to aggregate into bundles due to van der Waals forces among CNTs. The bundles are disrupted and redistributed by the flowing gas in the dynamic CVD process, leading to a unique structure where CNT bundles interpenetrate between two neighboring bundles. When a CNT bundle was pulled out by the external force, the CNT bundles that penetrated between adjacent bundles would be divorced and gathered at the ends of the bundles, which sufficed for peeling off the proximate CNT bundles. Therefore, CNT sheets can be produced by continuously drawing out CNT bundles. By further twisting the CNT sheet, a flexible and conductive CNT fiber was available.

1.2.2 Properties of CNT Fibers

Aligned CNT fibers show conductivities of ~10^4 S·cm^{-1}, which are higher than those of conductive polymer fibers (<10^2 S·cm^{-1}) and close to those of metal wires (10^5 S·cm^{-1}). The high conductivities of CNT fibers are attributed to the special hierarchical structure, i.e., individual nanometer-sized CNTs, CNT bundles, and macroscopically continuous CNT fibers. This hierarchical structure allows the electrons to conduct in a three-dimensional hopping model (Fig. 1.1b) in CNT fibers instead of being confined in a one-dimensional channel as normal linear nanotubes [19].

The excellent mechanical properties of CNT fibers include high strength and low bending stiffness. The tensile strength of an individual CNT is ~100 GPa. In the

hierarchically aligned structure, the CNT bundles inherited the ultrahigh strength of individual CNTs, and the effective interactions among CNT bundles kept the strength of the CNT fibers at the GPa order. Bending stiffness can be used to measure the flexibility of the fiber through the equation $D = (\pi \times d^3 \times E)/64$, where d is the diameter of fiber and E is Young's modulus. The Young's modulus is decreased from 1.8 TPa of individual CNTs to 400 MPa of CNT fibers in the hierarchical structure. The bending stiffnesses of CNT fibers rang from 1.76×10^{-7} to 1.23 $nN{\cdot}m^2$, even matching with the bending stiffnesses of tissues (from neuron, 1.57×10^{-5} $nN{\cdot}m^2$ to muscle, 3.77×10^{-3} $nN{\cdot}m^2$) [20]. Furthermore, different from the severe stress concentration in carbon fiber, the stresses are uniformly distributed in CNT fibers during bending (Fig. 1.1c) [21].

Compared with metal wires and conductive polymer fibers, the CNT fibers exhibit larger specific surface areas due to the abundant nanometer-sized gaps formed among the CNTs (Fig. 1.1d) [22]. The active materials can be loaded onto the CNT fibers by electrodeposition, electron beam evaporation, or co-spinning [23, 24]. High loading of 90% was achieved by directly impregnating the suspensions of active nanoparticles into the aligned CNT sheets, followed by twisting the sheets into a CNT fiber [25–27]. Furthermore, twisting several CNT fibers into a multiply fiber can form micrometer-sized gaps among single CNT fibers (Fig. 1.1e). And larger micrometer-sized gaps were formed by over-twisting multiply fiber into a spring-like fiber (Fig. 1.1f) [22]. This unique structure of CNT fibers enabled a high loading of active materials and rapid transport of electrolytes when used as a flexible skeleton and current collector for the fiber electrode.

Besides, the catalytic activity of CNTs for both oxygen reduction reaction (ORR) and oxygen evolution reaction (OER) makes them suitable for air electrodes in fiber metal-air batteries. The high specific surface area and porous framework of aligned CNT sheets afford abundant reaction sites and effectively gas diffusion channels. High-efficiency catalysts, such as Ag, MnO_2 and RuO_2 nanoparticles were deposited to further improve their catalytic performances [28, 29].

Benefiting from superior mechanical and electrical properties and large specific surface areas, CNT fibers made by dry-spinning demonstrated their immense merits in producing flexible fiber energy storage devices, which significantly promoted the development of flexible and wearable electronic devices in recent years.

1.3 Flexible Fiber Batteries

1.3.1 Lithium-Ion Batteries

The lithium-ion battery is a kind of secondary lithium battery, which uses intercalated electrode material instead of lithium metal to realize the movement of lithium ions between the cathode and anode during the charge-discharge process. Generally, lithium-ion batteries use lithium-alloy metal oxide ($LiCoO_2$, $LiMn_2O_4$, $LiNiO_2$

and $LiFePO_4$) as cathode, graphite or $Li_4Ti_5O_{12}$ as the anode, and non-aqueous electrolyte consisting of lithium salts (e.g., $LiPF_6$ and LiTFSI) and organic solvents (e.g., ethylene carbonate, propylene carbonate, dimethyl carbonate, ethyl methyl carbonate and diethyl carbonate). During the discharge process, lithium ions move from the anode, migrate through the electrolyte, and insert into the cathode. At the same time, electrons move from the anode to the cathode along the external circuit. While in the charging process, lithium ions return to the anode from the cathode. The energy delivery and storage of the lithium-ion battery are realized *via* this reversible process. Lithium-ion batteries have become one of the most ubiquitous power supplies for most electronic devices due to their superiority of high energy density, no memory effect, long life cycle, high working voltage, and environmental benignity.

1.3.1.1 Fiber Electrodes

The key to constructing fiber lithium-ion batteries is to prepare effective fiber electrodes. The fiber electrode requires the active materials to be stably anchored on the electrically conductive substrate. The substrate should also exhibit high flexibility and stability. The CNT fiber can effectively act as a skeleton to support active materials and a current collector for charge transport. Here, we discuss the process of obtaining fiber electrodes from aligned CNT fiber through several examples and analyze their structures and electrochemical performances.

The first fiber electrode based on CNT fiber was obtained by electrochemical deposition of MnO_2 nanoparticles on the CNT fiber in an aqueous solution [23]. The flower-shaped MnO_2 nanoparticles were uniformly strewn over the surface of CNT fiber, and the content of MnO_2 varied from 0.5 wt% to 8.6 wt% by adjusting the number of electrochemical deposition cycles. The CNT/MnO_2 hybrid fiber exhibited structural stability and electrical conductivity during the deformation process. The electrochemical performance of the hybrid fiber was investigated with a lithium wire as the anode in 1 $mol{\cdot}L^{-1}$ of $LiPF_6$. The CNT/MnO_2/Li battery had a discharge platform of 1.5 V *vs.* Li/Li^+, and the specific capacity reached 218 $mAh{\cdot}g^{-1}$ based on the whole mass of the CNT/MnO_2 electrode. However, the limited flexibility and security issue of lithium wire anode considerably restricts the practical application.

Silicon is a promising anode material due to the high theoretical capacity of 4200 $mAh{\cdot}g^{-1}$ and low lithiation potential within 0.2–0.4 V *vs.* Li/Li^+. As shown in Fig. 1.2a, silicon was deposited onto the outer surfaces of CNT sheets to form a core-sheath structure through electron beam evaporation, and then the hybrid sheets were twisted into a CNT/Si hybrid fiber [24]. The amount of silicon was controlled by the sputtering time. The decent flexibility of hybrid fiber enabled it to withstand repeated deformation without apparent damage, which also remarkably removed the shackle of lithium metal wire on the development of flexible fiber batteries. The CNT/Si hybrid fiber with silicon (38.1 wt%) displayed a voltage plateau around 0.4 V *vs.* Li/Li^+ and a specific capacity of 1670 $mAh{\cdot}g^{-1}$ at 1.0

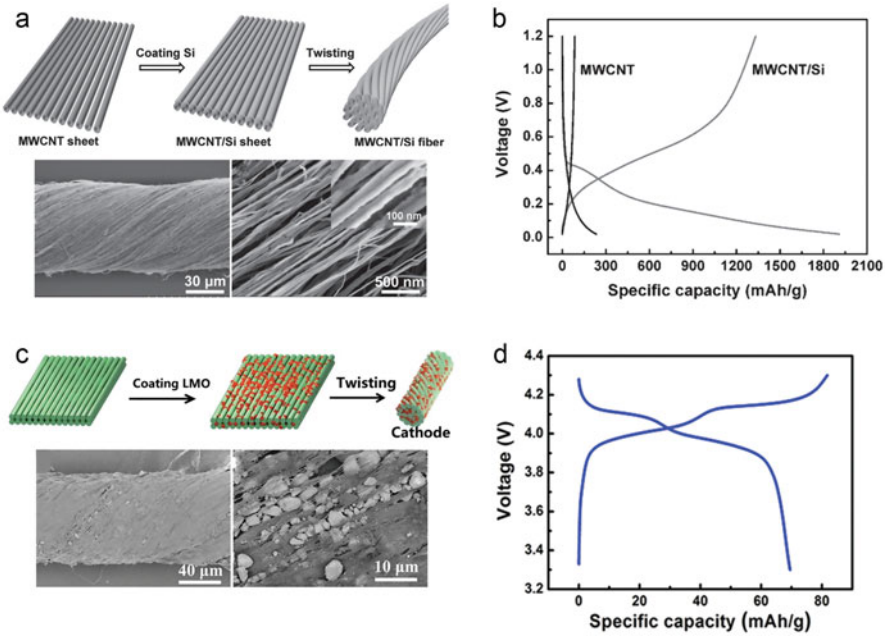

Fig. 1.2 (**a**) Preparation of the CNT/Si hybrid fiber and its scanning electron microscopy images at low and high magnifications. (**b**) Voltage profiles of CNT/Si fiber electrode *vs.* Li/Li^+. (**a, b**) From [24]. Reprinted with permission from Wiley-VCH Verlag GmbH & Co. KGaA, Weinheim. (**c**) Preparation of the CNT/$LiMn_2O_4$ hybrid fiber and its scanning electron microscopy images at low and high magnifications. (**c**) From [27]. Reprinted with permission from the Royal Society of Chemistry. (**d**) Voltage profiles of CNT/$LiMn_2O_4$ fiber electrode *vs.* Li/Li^+. (**d**) From [32]. Reprinted with permission from Wiley-VCH Verlag GmbH & Co. KGaA, Weinheim

$A \cdot g^{-1}$ (Fig. 1.2b). However, due to the volume change of silicon, the capacity decayed rapidly, which merely maintained 32% after 100 cycles. To solve this problem, the silicon-deposited CNT sheet was sandwiched between two bare CNT sheets and further scrolled into a hybrid fiber in a layered structure [31]. The bare CNT sheets performed as a buffer against volume expansion and immobilized the silicon layer. The CNT/Si/CNT hybrid fiber delivered a high delithiation capacity of 1523 $mAh \cdot g^{-1}$ at 2 C and more than 85% of the capacity was retained after 400 cycles.

Another method to construct hybrid fibers was directly impregnating the suspensions of active nanoparticles such as $LiMn_2O_4$ into the aligned CNT sheets, followed by twisting the sheets into a CNT/$LiMn_2O_4$ hybrid fiber [25, 27, 32]. As shown in Fig. 1.2c, a large amount of $LiMn_2O_4$ nanoparticles (e.g., 90% for $LiMn_2O_4$ in weight) were uniformly dispersed in the aligned CNTs. The electrochemical performance of the hybrid electrode is displayed in Fig. 1.2d. The CNT/$LiMn_2O_4$ electrode exhibited a high discharge voltage plateaus of 4.0 V *vs.* Li/Li^+. The specific capacity of the CNT/$LiMn_2O_4$ electrode was 72 $mAh \cdot g^{-1}$ and

remained 86.8% after 100 cycles at 0.1 $mA \cdot cm^{-1}$ due to the improved structural stability during the lithiation/delithiation processes.

1.3.1.2 Fiber Lithium-Ion Batteries

Benefitted from the fiber electrodes, a large number of flexible fiber lithium-ion batteries have been assembled. Here, we mainly introduce the assembling method of fiber lithium-ion batteries and demonstrate their application prospect in wearable electronic devices *via* their electrochemical performance, flexibility, stretchability, and weavability.

A coaxial fiber lithium-ion battery was assembled based on the CNT/Si/CNT hybrid anode and CNT/$LiMn_2O_4$ hybrid cathode [31]. The fiber electrodes were sequentially wound onto a cotton fiber separated with a gel electrolyte layer and covered with a shrinkable tube as the protective layer. The fiber lithium-ion battery featured a working voltage of 3.4 V, and the initial specific capacity reached 106 $mAh \cdot g^{-1}$. The capacity retention was also improved due to the stable CNT/Si/CNT anode. Besides, the fiber lithium-ion batteries could be woven into textile subjected to bending.

A more viable fiber lithium-ion battery was assembled in a parallel structure [25]. The CNT/$Li_4Ti_5O_{12}$ and CNT/$LiMn_2O_4$ hybrid electrodes, acting as anode and cathode respectively, were assembled with a poly(vinylidene fluoride) separator then encapsulated by a heat-shrinkable tube. The spinel $Li_4Ti_5O_{12}$ and $LiMn_2O_4$ featured small volume changes during the lithiation and delithiation processes, demonstrating high cyclic stability. The high lithiation potential of 1.5 V *vs*. Li/Li^+ for $Li_4Ti_5O_{12}$ could effectively avoid the dendrite formation on the anode surface. Therefore, this lithium-ion battery exhibited spectacular electrochemical performance and no safety issues were caused by lithium dendrites. The discharge voltage plateau of the battery was 2.5 V, and the specific capacity was 138 $mAh \cdot g^{-1}$, which retained 85% after 100 cycles. The fiber battery was also flexible and able to remain 97% capacity after bending for 1000 cycles. However, the lack of stretchability makes it difficult for practical application in various wearable electronic devices. Therefore, the parallel CNT/$Li_4Ti_5O_{12}$ and CNT/$LiMn_2O_4$ electrodes were further winded around an elastic poly(dimethylsiloxane) fiber substrate and coated gel electrolyte to assemble a stretchable fiber lithium-ion battery [27]. The stretching process was essential for the stretched elastic substrate to increase the two fiber electrodes' pitch distance. The winding structure remained unchanged, attributed to the effective anchoring of the gel electrolyte. The specific capacity of this stretchable fiber lithium-ion battery was 91 $mAh \cdot g^{-1}$ and could be maintained by up to 88% after stretching by 600%. However, an elastic substrate's introduction increased the battery's total weight and volume and resulted in poor electrochemical properties and narrow operating temperature.

Intrinsically stretchable fiber electrodes are the key to making stretchable fiber batteries without using an elastic substrate. To this end, new hybrid fiber electrodes

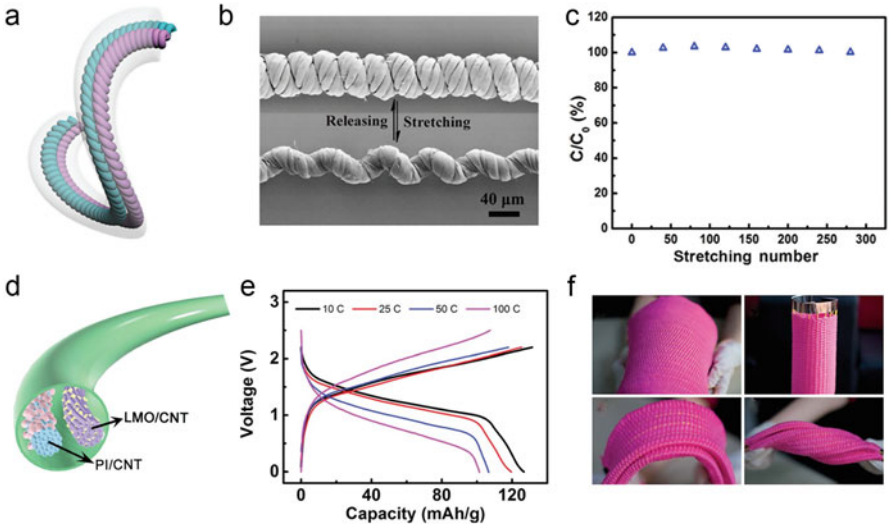

Fig. 1.3 (**a**) Schematic illustration of a stretchable fiber lithium-ion battery based on CNT hybrid fiber springs. (**b**) Scanning electron microscopy images of the CNT fiber springs before and after stretching for 100%. (**c**) Dependence of specific capacitance on stretching number. (**a-c**) From [32]. Reprinted with permission from Wiley-VCH Verlag GmbH & Co. KGaA, Weinheim. (**d**) Schematic illustration of the structure of a fiber aqueous lithium-ion battery. (**e**) Charge and discharge curves of the fiber aqueous lithium-ion battery under increasing current rates (1C = 183 $mA{\cdot}g^{-1}$). (**f**) Energy textile woven with fiber aqueous lithium-ion batteries under bending, folding and twisting. (**d-f**) From [33]. Reprinted with permission from the Royal Society of Chemistry

with springs structure were used to achieve stretchable fiber lithium-ion batteries [32]. As shown in Fig. 1.3a, two spring-like fibers were prepared by over-twisting CNT/$LiMn_2O_4$ and CNT/$Li_4Ti_5O_{12}$ fibers together, which were separated and filled by gel electrolyte. The spring-like fibers with uniform coiled loops could be elongated over 300% (Fig. 1.3b). The battery exhibited a discharge voltage plateau of 2.5 V and a specific capacity of 92 $mAh{\cdot}g^{-1}$, which could be maintained by 92.1% after 100 cycles. The specific capacity was maintained 85% after a 100% strain and varied by less than 1% after stretching for 300 cycles (Fig. 1.3c). Compared with stretchable fiber batteries based on a polymer substrate, the volume and weight of this lithium-ion battery were decreased by appropriately 400% and 300%, respectively, making it more suitable for portable and wearable electronic applications.

Lithium-ion batteries using flammable and toxic organic electrolytes suffer from risks of combustions and explosions caused by short-circuiting during deformation, which is a huge challenge that has hindered their potential applications. Although gel electrolytes can solve this problem, the ionic conductivity is much lower than the liquid electrolyte. A fiber aqueous lithium-ion battery assembled with CNT/polyimide (PI) hybrid fiber anode, CNT/$LiMn_2O_4$ hybrid fiber cathode, and

lithium sulfate solution electrolyte (Fig. 1.3d) avoided the safety issue and delivered an ultrafast charge and discharge compared with the previous fiber organic lithium-ion batteries [33]. PI determined capacitor-like properties of this fiber aqueous lithium-ion battery, and the rapid reaction of CNT/PI hybrid fiber resulted in excellent electrochemical performance. The battery exhibited a discharge voltage platform of 1.4 V at 10 C, and the specific discharge capacity reached 123 $mAh{\cdot}g^{-1}$ based on the mass of PI (Fig. 1.3e). The ultra-high power density of 10,218 $W{\cdot}kg^{-1}$ exceeded those of most supercapacitors, and the energy density of 49 $Wh{\cdot}kg^{-1}$ was also comparable to those of thin-film batteries. As shown in Fig. 1.3f, this fiber aqueous lithium-ion battery could be woven into various flexible structures, such as textiles, and be bent, folded and twisted.

Fiber lithium-ion batteries based on CNT fibers have made significant progress in electrochemical performance. Their excellent flexibility, stretchability and weavability have attracted increasing attention in wearable electronics. However, many efforts should be made to meet the needs of practical applications. On the one hand, active materials with higher theoretical specific capacities can be incorporated to improve batteries' capacity and energy density. The capacity compatibility of the cathode and anode also requires attention to maximize their superiority. On the other hand, high-performance gel electrolytes should be developed to replace liquid electrolytes.

1.3.2 Lithium-Metal Batteries

Lithium-metal batteries are batteries that use lithium metal as the anode. Due to the extremely reactive property of lithium metal, the processing, storage and use of lithium-metal batteries have very strict requirements on the environment. Here we mainly introduce flexible fiber lithium-sulfur batteries and lithium-air batteries.

1.3.2.1 Lithium-Sulfur Batteries

Lithium-sulfur batteries using sulfur cathode have attracted significant attention due to their high theoretical energy density (2600 $Wh{\cdot}kg^{-1}$) and capacity (1675 $mAh{\cdot}g^{-1}$). In the discharge process, lithium ions migrate toward the cathode and react with sulfur to produce lithiated polysulfide compounds (Li_2S_x). Due to the intrinsically non-conducting nature of sulfur and the soluble polysulfides (Li_2S_x), the cathodes usually introduce the second component (e. g., TiO_2, metal-organic frameworks, polyethylene dioxythiophene, polyaniline, carbon nanomaterials, *etc.*) as the conducting substrate and sulfur host [34].

A fiber lithium-sulfur battery was assembled with a fiber CNT/S (GO/CMK-3@S) hybrid electrode [35]. The preparation of hybrid cathode was similar to that of CNT/$LiMn_2O_4$, and the sulfur content reached 68 wt% due to the lightweight of CNT fiber and CMK-3 particles, which was favorable for maintaining high energy

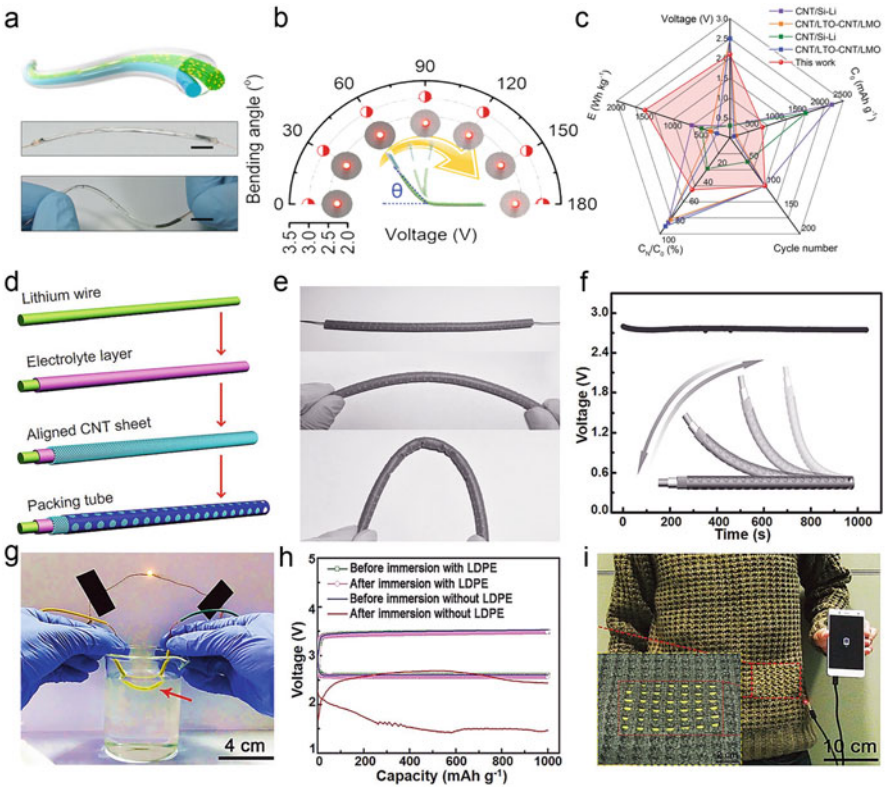

Fig. 1.4 (**a**) Schematic illustration of a fiber lithium-sulfur battery's structure and its photographs in bending and twisting states. (**b**) Open-circuit voltages of a fiber lithium-sulfur battery being bent from 0° to 180°. The inserted photographs display a red LED lit up by the battery bent at different angles. (**c**) Electrochemical performance comparison of this battery with previous fiber lithium-ion batteries. C_0, initial capacity specified to the total weight of cathode; E, energy density specified to the total weight of cathode, which is obtained by multiplying C_0 and V; C_N/C_0, the capacity retention after cycling. (**a-c**) From [35]. Reprinted with permission from Wiley-VCH Verlag GmbH & Co. KGaA, Weinheim. (**d**) Schematic illustration of the fabrication of a fiber Li-air battery. (**e**) Photographs of the flexible battery under bending. (**f**) Output voltage of the Li-air battery during the dynamic bending process. (**d-f**) From [37]. Reprinted with permission from Wiley-VCH Verlag GmbH & Co. KGaA, Weinheim. (**g**) Photograph of a fiber Li-air battery powering an LED after immersing into water. (**h**) Discharge/charge curves of a fiber Li-air battery before and after immersing in water with and without polyethylene film. (**i**) Six fiber Li-air battery was woven into cloth to charge a smartphone. (**g-i**) From [36]. Reprinted with permission from WILEY-VCH Verlag GmbH & Co. KGaA, Weinheim

density. The sulfur hybrid cathode had a voltage plateau of 2.0–2.1 V and excellent cyclic stability. After being paired with lithium wire (Fig. 1.4a), the fiber lithium-sulfur battery exhibited no apparent difference of open-circuit voltages during bending and could light up a red LED at different bend angles (Fig. 1.4b). The battery outputted a discharge voltage platform of 2.1 V, and the specific discharge

capacity reached 714 $mAh{\cdot}g^{-1}$ based on the total weight of the cathode. The high energy density of 1500 $Wh{\cdot}kg^{-1}$ was 2–6 times higher than reported fiber lithium-ion batteries (Fig. 1.4c).

1.3.2.2 Lithium-Air Batteries

The lithium-air battery is one of the most commonly studied metal-air batteries due to its unique high theoretical specific energy density of 3500 $Wh{\cdot}kg^{-1}$, which is 5–10 times higher than conventional lithium-ion battery batteries. Commonly, a flexible fiber lithium-air battery is composed of a lithium metal anode, gel electrolyte, and air cathode. CNT sheet is widely utilized as the air electrode due to its superior conductivity, tolerable catalytic activity and gas permeability. The lithium-air battery's primary reaction mechanism is ascribed to the reversible formation and decomposition of Li_2O_2 ($2Li^+ + O_2 + 2e^- \rightleftharpoons Li_2O_2, 2.96$ V *vs.* Li/Li^+) [36].

In a typical fabrication process of the flexible fiber Li-air battery, a gel electrolyte, which consists of lithium salts and organic polymers, was firstly coated on a lithium wire in an argon-filled glove box as the separator to prevent the oxidation and corrosion of active lithium wire [37]. Subsequently, the dry-drawn CNT sheet from the aligned CNT array was wrapped on the electrolyte, functioning as the air electrode. A punched heat-shrinkable tuber was lastly packed exterior to the whole fiber device to prevent damages (Fig. 1.4d). The thickness of the wrapped CNT sheet needs to be well controlled to optimize the battery's performance, as a thin CNT sheet will result in a high electrical resistance air electrode and a thick CNT sheet will lead to low O_2 diffusion efficiency. A Li-air battery with an optimized CNT sheet air electrode performed with a high specific capacity of 12,470 $mAh{\cdot}g^{-1}$ at a current density of 1400 $mA{\cdot}g^{-1}$. The discharge voltage remained almost unchanged with a cutoff capacity of 500 $mAh{\cdot}g^{-1}$ over 100 cycles. Due to the existence of lithium wire, the battery showed limited flexibility, and was able to be bent from 0° to 90° (Fig. 1.4e). The output voltage can be stably operated under a dynamic bending and releasing process at a speed of 10 degrees every second (Fig. 1.4f).

Generally, the Li-air battery's poor cyclability mainly resulted from the side reaction of the Li_2O_2 with moisture and carbon dioxide in ambient air, which produced chemically stable Li_2CO_3 that gradually accumulated to accelerate the failure of the Li-air battery. Besides, the organic components in the electrolyte are also easy to react with the moisture, leading to reduced service life. To tackle these challenges, a low-density polyethylene film was wrapped on the CNT surface to prevent water erosion before the packaging of the heat-shrink tube, and a gel electrolyte with LiI as a redox mediator was used to facilitate the electrochemical decomposition of Li_2O_2 during discharge [36]. The polyethylene film's nonpolar molecular structure delivered a high permeability for the nonpolar O_2/CO_2 molecules while preventing polar moisture molecules. As a result, the side reaction of transforming Li_2O_2 to Li_2CO_3 was suppressed as it relied on

the moisture, leading to an enhanced cycle life of 610 cycles. Furthermore, the produced battery was partly immersed in water to power an LED (Fig. 1.4g) and the discharge/charge curves were well maintained after immersion (Fig. 1.4h). Several fiber Li-air batteries were integrated into clothes to effectively charge a smartphone, which proved their enormous potential for wearable applications (Fig. 1.4i).

1.3.3 Aqueous Metal-Air Batteries

1.3.3.1 Aluminum-Air Batteries

Al-air battery attracts many researchers' attention because of its relatively high theoretical energy density of 2796 $Wh{\cdot}kg^{-1}$, abundant resources and lightweight features [28]. Similar to the fiber Li-air battery, typical Al-air batteries are in an open configuration with the CNT sheet air electrode wrapped on an Al anode coated with gel electrolyte. However, the discharge mechanism of the Al-air battery is quite different from the Li-air battery, which is as follows: [38].

$$\text{Metal anode}: \mathrm{Al} + 3\mathrm{OH}^- \rightarrow \mathrm{Al(OH)_3} + 3\mathrm{e}^-$$

$$\text{Air cathode}: \mathrm{O_2} + 2\mathrm{H_2O} + 4\mathrm{e}^- \rightarrow 4\mathrm{OH}^-$$

The metal ions are released from the metal anode and they need to react with the OH^- to form $Al(OH)_3$, which requires the electrolyte to be alkaline. Meanwhile, the oxygen from the ambient air is reduced to OH^- at the air cathode known as the ORR. Ordinarily, the low oxygen diffusion and sluggish ORR in the air electrode are the main limitations for the Al-air battery.

To produce a flexible and stretchable high-performance Al-air battery, alkaline hydrogel electrolyte that contains KOH/ZnO/Na_2SO_3 and Ag nanoparticle decorated dry-drawn CNT sheets were coated and wrapped on an Al spring anode sequentially (Fig. 1.5a) [28]. ZnO served as a corrosion inhibitor of the Al anode in the alkaline solution and Na_2SO_3 was used to decrease the open-circuit potential of Al, which promoted the dissolution of Al in KOH solution. Meanwhile, the hybrid CNT/Ag nanoparticle air electrode performed much higher ORR catalytic activity and conductivity than the bare CNT sheet. As a result, the produced battery showed a high energy density of 1168 Wh kg^{-1}. Besides, the battery also performed superior mechanical properties. It can be bent to 135° with almost unchanged output voltage at a discharge current of 1 mA. Moreover, it can be stretched by up to 30% without breaking (Fig. 1.5b) and hence can be worn around a human wrist to power an LED watch (Fig. 1.5c).

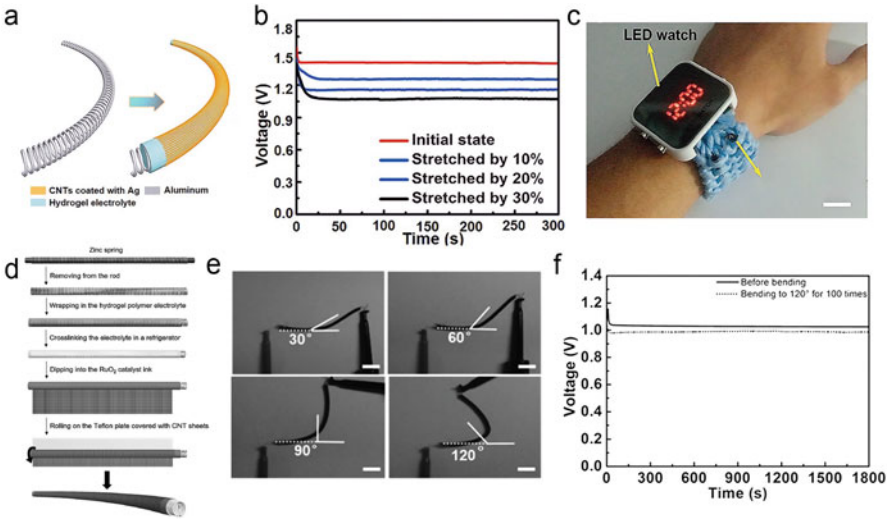

Fig. 1.5 (**a**) Schematic of a stretchable fiber Al-air battery with Al spring metal anode. (**b**) Discharge curves of the Al-air battery under stretching. (**c**) Two fiber Al-air battery is woven into a wrist strap to power a watch. (**a-c**) From [28]. Reprinted with permission from WILEY-VCH Verlag GmbH & Co. KGaA, Weinheim. (**d**) Schematic illustration of the fabrication of fiber Zn-air battery. (**e**) Photographs of a fiber Zn-air battery bent to increasing angles; scale bar: 1 cm. (**f**) Discharge curves of the fiber Zn-air battery with a length of 5 cm at a current density of 1 $A \cdot g^{-1}$ before and after bending to 120° for 100 cycles. (**d-f**) From [29]. Reprinted with permission from WILEY-VCH Verlag GmbH & Co. KGaA, Weinheim

1.3.3.2 Zinc-Air Batteries

Attracted by its intrinsic safety, environmental friend, low cost and high theoretical energy density of 1086 $Wh \cdot kg^{-1}$, fiber rechargeable Zn-air battery is particularly suitable for powering portable and wearable electronics [39]. The reaction mechanism of the Zn-air battery is described as:

$$\text{Metal anode} : Zn + 2OH^- \rightarrow Zn(OH)_2 + 2e^-$$

$$\text{Air cathode} : O_2 + 2H_2O + 4e^- \rightarrow 4OH^-$$

During discharge, ORR occurs at the air electrode while the metal ions react with the OH^- to produce $Zn(OH)_2$, while during the charging process, OH^- is oxidized to O_2 and Zn^{2+} is reduced to zinc metal [38]. Similar to the Al-air battery, a flexible fiber stretchable Zn-air battery can be fabricated by using a zinc spring instead of the aluminum spring. (Fig. 1.5d) To achieve a Zn-air battery with decent power density, a strong alkaline gel electrolyte is favored as it improves the dissolubility of the

$Zn(OH)_2$. Also, the air cathode is required to catalyze the ORR and OER efficiently. Therefore, a lot of efforts have been devoted to the improvement of the catalytic activity of the air electrode. For instance, RuO_2 was deposited on the dry-drawn CNT sheets to improve the OER. The produced fiber Zn-air battery without obvious damage in the structure under different bending angles (Fig. 1.5e) and the discharge voltage remained almost unchanged after bending to 120° for 100 cycles (Fig. 1.5f) [29].

Although significant progress has been made in fabricating flexible fiber metal-air batteries using dry-drawn CNT sheets, some challenges still need to be solved. For instance, the cycle life of the rechargeable metal-air batteries is relatively low. The CO_2 in the air reacts with the alkaline electrolyte, consuming the electrolyte and leading to the device failure. In short, great efforts are still needed to facilitate the real application of flexible fiber metal-air batteries.

1.3.4 Other Batteries

Sodium-ion batteries have recently received extension attentions, which are expected to be potential alternatives to lithium-ion batteries due to abundant natural reserves and low costs. Inspired by the fiber lithium-ion battery, an aqueous fiber sodium-ion battery was assembled by CNT/$Na_{0.44}MnO_2$ (NMO) and CNT/carbon-coated $NaTi_2(PO_4)_3$ (NTPO@C) hybrid fibers [40]. NMO and NTPO@C nanoparticle suspensions were impregnated into CNT sheets and then twisted into fiber electrodes. As shown in Fig. 1.6a, the CNT/NMO cathode had a potential window of 0–0.7 V, and the specific capacity was 44 $mAh{\cdot}g^{-1}$ at 0.1 $A{\cdot}g^{-1}$. CNT/NTPO@C cathode outputted a potential window of −0.9–0 V and a specific capacity of 105 $mAh{\cdot}g^{-1}$ at 0.1 $A{\cdot}g^{-1}$. After putting the hybrid electrodes in a tube containing 1 M Na_2SO_4 solution (Fig. 1.6b), the obtained fiber sodium-ion battery delivered a potential window of 0–1.6 V and a discharge specific capacity of 46 $mAh{\cdot}g^{-1}$ at a current density of 0.1 $A{\cdot}g^{-1}$. The galvanostatic charge-discharge curves of the fiber aqueous sodium-ion battery before and after bending displayed no noticeable difference, indicating its high flexibility (Fig. 1.6c). More critically, normal biocompatible saline and cell-culture medium act as electrolytes for this fiber aqueous sodium-ion battery, which provided an opportunity for its use in implantable electronic devices.

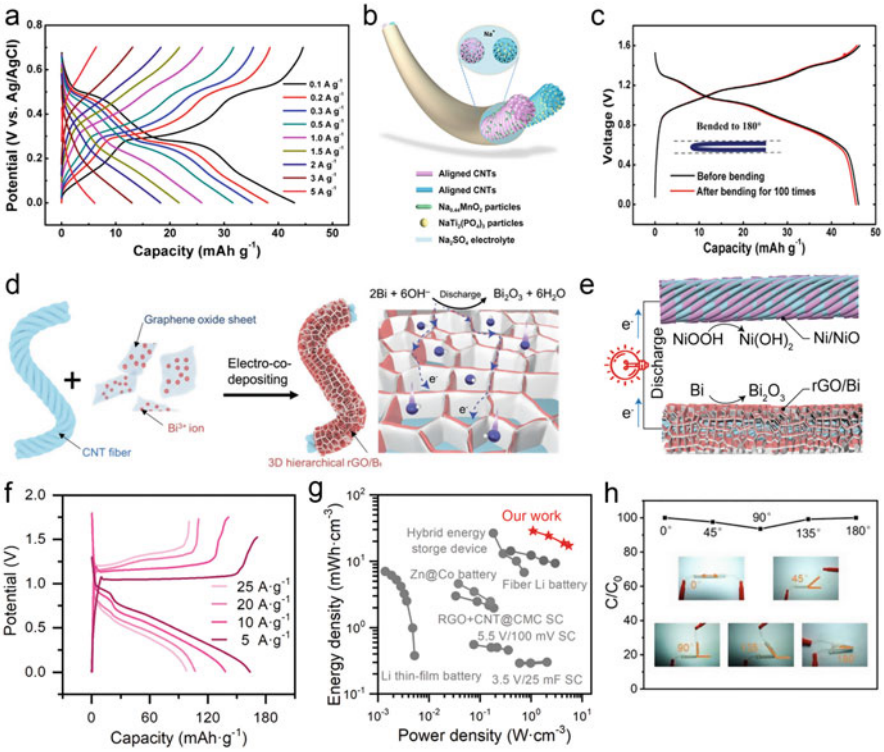

Fig. 1.6 (**a**) Galvanostatic charge-discharge curves of fiber CNT/NMO hybrid electrode. (**b**) Schematic illustration of the structure of the fiber sodium-ion battery. (**c**) Galvanostatic charge-discharge curves of the flexible fiber aqueous sodium-ion battery before and after bending at a current density of 0.2 $A \cdot g^{-1}$. (**a-c**) From [40]. Reprinted with permission from Elsevier. (**d**) Schematic diagram of preparing the rGO/Bi/CNT anode. (**e**) Schematic diagram of the working mechanism of the fiber Ni//Bi battery. (**f**) Galvanostatic charge-discharge profiles of fiber Ni//Bi battery. (**g**) Ragone plots by comparing the fiber Ni//Bi battery with the other energy storage devices. (**h**) Capacity retention of the fiber Ni//Bi battery under different bending conditions. (**d-h**) From [41]. Reprinted with permission from Wiley-VCH Verlag GmbH & Co. KGaA, Weinheim

Ni//Bi batteries that can combine high power density with high energy density are attracting attention in wearable electronics. A new type of fiber Ni//Bi battery was fabricated with rGO/Bi/CNT anode and rGO/Ni/NiO/CNT cathode [41]. The rGO/Bi/CNT anode preparation was carried out by electro-co-depositing rGO/Bi onto the CNT sheet. An interlaced rGO/Bi 3D structure was formed, which was beneficial for the ion diffusion and electron transport among the active materials (Fig. 1.6d). In comparison, the rGO/Ni/NiO/CNT cathode was prepared through a solution-based process. The rGO/Bi/CNT anode and rGO/Ni/NiO/CNT cathode

outputted operating voltage of −1.2–0 and 0–0.6 V, and a specific capacity of 147 $mAh{\cdot}g^{-1}$ and 115 $mAh{\cdot}g^{-1}$ at 5 $A{\cdot}g^{-1}$, respectively. The fiber Ni//Bi battery was assembled by pairing two electrodes in 1 M KOH (Fig. 1.6e). During discharging, NiOOH produced $Ni(OH)_2$ and OH^- while Bi reacted with OH^- to produce Bi_2O_3, while during the charging process, Ni^{2+} was oxidized to Ni^{3+} and Bi^{3+} was reduced to Bi. The Ni//Bi battery possessed a stable operating voltage of 1.8 V, a specific capacity of 164 $mAh{\cdot}g^{-1}$ at 5 $A{\cdot}g^{-1}$ (Fig. 1.6f), and the capacity could maintain 96.2% after 10,000 cycles. As shown in Fig. 1.6g, the maximal energy density of fiber Ni//Bi battery was remarkably higher than those of fiber-based aqueous lithium-ion batteries and thin-film lithium-ion batteries. The maximal power density was around 25 times higher than that of the CNT@CMC-based supercapacitor and 10 times higher than those of commercial supercapacitors. Besides, the fiber Ni//Bi battery had no noticeable damage in structure and capacity during bending and only 8.7% of its capacity was lost after 1000 bends (Fig. 1.6h).

1.4 Summary

This chapter highlights varioius flexible fiber batteries based on CNTs, including lithium-ion batteries, lithium-metal batteries and aqueous metal-air batteries. The preparation of CNTs and fiber electrodes, the assembly technology, and fiber batteries' performance are introduced in detail (Table 1.1). Benefitting from the excellent performance of CNT fiber electrode materials, fiber batteries exhibit unique properties, *e.g.*, miniaturization, flexibility, stretchability and weavability, which make them a prime choice for portable and wearable devices. However, there are still some formidable challenges of fiber batteries for practical applications. The first is to realize the large-scale production of fiber electrodes. At the same time, the electrical conductivity of aligned CNT fibers must be further enhanced. Finally, developing high-performance gel electrolytes for flexible fiber since safety is the last thing to be ignored.

Table 1.1 Performances of representative fiber rechargeable batteries

Battery	Cathode	Anode	Voltage (V)	Capacity ($mAh \cdot g^{-1}$)	Capacity retention	Energy density ($Wh \cdot kg^{-1}$)	Power density ($W \cdot kg^{-1}$)	Flexibility	Ref.
Li-metal	CNT/Si/CNT hybrid yarn	Li wire	3.4	107	87% after cycling for 100 cycles	242	–	Can be woven into flexible textile	[31]
LIB	CNT/LMO hybrid fiber	CNT/LTO hybrid fiber	2.5	138	85% after cycling for 100 cycles	27	880	Capacity remained at 97% after bending for 1000 cycles	[25]
LIB	CNT/LMO hybrid fiber	CNT/LTO hybrid fiber	2.2	92	78% after cycling for 100 cycles	30	830	Capacity remained at 88% at 600% strain	[27]
LIB	CNT/LMO hybrid fiber spring	CNT/LTO hybrid fiber spring	2.5	93	92.1% after cycling for 100 cycles	–	–	Capacity remained at 85% at 100% strain	[32]
Aqueous LIB	CNT/LMO hybrid fiber	CNT/PI hybrid fiber	1.4	123	100% after cycling for 1000 cycles	48.93	10,218	Can be woven into various flexible structures	[33]
Li-S	CNT/CMK-3@S hybrid fiber	Li wire	2.1	714	54% after cycling for 100 cycles	1500	–	Can light up a LED at bend state	[35]

Li-air	CNT sheet	Li wire	2.6	12,865	100% after cycling for 100 cycles	2457	250	Discharge voltage almost unchanged after bending to 90° for 100 cycles	[37]
Li-air	CNT sheet	Li wire	2.6	1000	Almost unchanged after cycling for 610 cycles	–	–	Charge/discharge curves almost unchanged after bending for 1000 cycles	[36]
Li-air	CNT sheet	Li wire	2.5	500	Negligible capacity loss after cycling for 380 cycles	3719	7884	–	[42]
Al-air	CNT sheet/Ag nanoparti-cles	Al spring	1.4	12,000	–	1168	20	The output voltage almost unchanged after stretching to 30%	[28]

(continued)

Table 1.1 (continued)

Battery	Cathode	Anode	Voltage (V)	Capacity ($mAh \cdot g^{-1}$)	Capacity retention	Energy density ($Wh \cdot kg^{-1}$)	Power density ($W \cdot kg^{-1}$)	Flexibility	Ref.
Zn-air	CNT sheet/RuO_2 nanoparticles	Zn spring	1.0	–	Discharge current density maintained for 30 cycles at the voltage plateau of 1.0 V	6 $Ah \cdot L^{-1}$	5.7 $Wh \cdot L^{-1}$	The discharge voltage almost unchanged after bending to 120° for 100 cycles	[39]
NIB	CNT/NMO hybrid fiber	CNT/NTPO@C hybrid fiber	1.1	46	76% after cycling for 100 cycles	–	–	GCD remained almost unchanged before and after bending	[40]
Ni//bi	rGO/Ni/NiO/CNT hybrid fiber	rGO/Bi/CNT hybrid fiber	1.0	164	96% after cycling for 10,000 cycles	43	6600	Capacity well maintained under bending conditions	[41]

References

1. Iijima, S.: Helical microtubules of graphitic carbon. Nature. **354**(6348), 56–58 (1991)
2. Dai, H.: Carbon nanotubes: opportunities and challenges. Surf. Sci. **500**(1–3), 218–241 (2002)
3. Ebbesen, T.W., Lezec, H.J., Hiura, H., et al.: Electrical conductivity of individual carbon nanotubes. Nature. **382**(6586), 54–56 (1996)
4. Yu, M.F., Files, B.S., Arepalli, S., et al.: Tensile loading of ropes of single wall carbon nanotubes and their mechanical properties. Phys. Rev. Lett. **84**(24), 5552–5555 (2000)
5. Kim, P., Shi, L., Majumdar, A., et al.: Thermal transport measurements of individual multiwalled nanotubes. Phys. Rev. Lett. **87**(21), 1–4 (2001)
6. Liao, M., Sun, H., Tao, X., et al.: Alignment of thermally conducting nanotubes making high-performance light-driving motors. ACS Appl. Mater. Interfaces. **10**(31), 26765–26771 (2018)
7. Jiang, K., Li, Q., Fan, S.: Nanotechnology: spinning continuous carbon nanotube yarns. Nature. **419**(6909), 801 (2002)
8. Li, Y.L., Kinloch, I.A., Windle, A.H.: Direct spinning of carbon nanotube fibers from chemical vapor deposition synthesis. Science. **304**(5668), 276–278 (2004)
9. Vigolo, B., Penicaud, A., Coulon, C., et al.: Macroscopic fibers and ribbons of oriented carbon nanotubes. Science. **290**(5495), 1331–1334 (2000)
10. Yoon, Y.H., Song, J.W., Kim, D., et al.: Transparent film heater using single-walled carbon nanotubes. Adv. Mater. **19**(23), 4284–4287 (2007)
11. Amama, P.B., Pint, C.L., Kim, S.M., et al.: Influence of alumina type on the evolution and activity of alumina-supported fe catalysts in single-walled carbon nanotube carpet growth. ACS Nano. **4**(2), 895–904 (2010)
12. Jia, J.J., Zhao, J.N., Xu, G., et al.: A comparison of the mechanical properties of fibers spun from different carbon nanotubes. Carbon. **49**(4), 1333–1339 (2011)
13. Zhang, Y.Y., Zou, G.F., Doorn, S.K., et al.: Tailoring the morphology of carbon nanotube arrays: from spinnable forests to undulating foams. ACS Nano. **3**(8), 2157–2162 (2009)
14. Li, Q.W., Zhang, X.F., DePaula, R.F., et al.: Sustained growth of ultralong carbon nanotube arrays for fiber spinning. Adv. Mater. **18**(23), 3160–3163 (2006)
15. Hata, K., Futaba, D.N., Mizuno, K., et al.: Water-assisted highly efficient synthesis of impurity-free single-walled carbon nanotubes. Science. **306**(5700), 1362–1364 (2004)
16. Zhang, S., Zhu, L., Minus, M.L., et al.: Solid-state spun fibers and yarns from 1-mm long carbon nanotube forests synthesized by water-assisted chemical vapor deposition. J. Mater. Sci. **43**(13), 4356–4362 (2008)
17. Huynh, C.P., Hawkins, S.C.: Understanding the synthesis of directly spinnable carbon nanotube forests. Carbon. **48**(4), 1105–1115 (2010)
18. Kuznetsov, A.A., Fonseca, A.F., Baughman, R.H., et al.: Structural model for dry-drawing of sheets and yarns from carbon nanotube forests. ACS Nano. **5**(2), 985–993 (2011)
19. Peng, H., Jai, M., Li, Q., et al.: Vertically aligned pearl-like carbon nanotube arrays for fiber spinning. J. Am. Chem. Soc. **130**, 1130–1131 (2008)
20. Wang, L., Xie, S., Wang, Z., et al.: Functionalized helical fibre bundles of carbon nanotubes as electrochemical sensors for long-term in vivo monitoring of multiple disease biomarkers. Nat. Biomed. Eng. **4**(2), 159–171 (2020)
21. Xu, X., Xie, S., Zhang, Y., et al.: The rise of fiber electronics. Angew. Chem. Int. Ed. **58**(39), 13643–13653 (2019)
22. Chen, P., Xu, Y., He, S., et al.: Hierarchically arranged helical fibre actuators driven by solvents and vapours. Nat. Nanotechnol. **10**(12), 1077–1083 (2015)
23. Ren, J., Li, L., Chen, C., et al.: Twisting carbon nanotube fibers for both wire-shaped micro-supercapacitor and micro-battery. Adv. Mater. **25**(8), 1155–1159 (2013)
24. Li, L., Wu, Z., Yuan, S., et al.: Advances and challenges for flexible energy storage and conversion devices and systems. Energy Environ. Sci. **7**(7), 2101–2122 (2014)
25. Ren, J., Zhang, Y., Bai, W., et al.: Elastic and wearable wire-shaped lithium-ion battery with high electrochemical performance. Angew. Chem. Int. Ed. **53**(30), 7864–7869 (2014)

26. Zhang, Y., Zhao, Y., Cheng, X., et al.: Realizing both high energy and high power densities by twisting three carbon-nanotube-based hybrid fibers. Angew. Chem. Int. Ed. **54**(38), 11177–11182 (2015)
27. Zhang, Y., Bai, W., Ren, J., et al.: Super-stretchy lithium-ion battery based on carbon nanotube fiber. J. Mater. Chem. A. **2**(29), 11054–11059 (2014)
28. Xu, Y., Zhao, Y., Ren, J., et al.: An all-solid-state fiber-shaped aluminum-air battery with flexibility, stretchability, and high electrochemical performance. Angew. Chem. Int. Ed. **55**(28), 7979–7982 (2016)
29. Xu, Y., Zhang, Y., Guo, Z., et al.: Flexible, stretchable, and rechargeable fiber-shaped zinc-air battery based on cross-stacked carbon nanotube sheets. Angew. Chem. Int. Ed. **54**(51), 15390–15394 (2015)
30. Miao, M., McDonnell, J., Vuckovic, L., et al.: Poisson's ratio and porosity of carbon nanotube dry-spun yarns. Carbon. **48**(10), 2802–2811 (2010)
31. Weng, W., Sun, Q., Zhang, Y., et al.: Winding aligned carbon nanotube composite yarns into coaxial fiber full batteries with high performances. Nano Lett. **14**(6), 3432–3438 (2014)
32. Zhang, Y., Bai, W., Cheng, X., et al.: Flexible and stretchable lithium-ion batteries and supercapacitors based on electrically conducting carbon nanotube fiber springs. Angew. Chem. Int. Ed. **53**(52), 14564–14568 (2014)
33. Zhang, Y., Wang, Y., Wang, L., et al.: A fiber-shaped aqueous lithium ion battery with high power density. J. Mater. Chem. A. **4**(23), 9002–9008 (2016)
34. Fang, X., Peng, H.: A revolution in electrodes: recent progress in rechargeable lithium-sulfur batteries. Small. **11**(13), 1488–1511 (2015)
35. Fang, X., Weng, W., Ren, J., et al.: A cable-shaped lithium sulfur battery. Adv. Mater. **28**(3), 491–496 (2016)
36. Wang, L., Pan, J., Zhang, Y., et al.: A Li–air battery with ultralong cycle life in ambient air. Adv. Mater. **30**(3), 1704378–1704376 (2017)
37. Zhang, Y., Wang, L., Guo, Z., et al.: High-performance lithium-air battery with a coaxial-fiber architecture. Angew. Chem. Int. Ed. **55**(14), 4487–4491 (2016)
38. Ye, L., Hong, Y., Liao, M., et al.: Recent advances in flexible fiber-shaped metal-air batteries. Energy Storage Mater. **28**, 364–374 (2020)
39. Ma, L., Chen, S., Wang, D., et al.: Super-stretchable zinc–air batteries based on an alkaline-tolerant dual-network hydrogel electrolyte. Adv. Energy Mater. **9**(12), 1803046 (2019)
40. Guo, Z., Zhao, Y., Ding, Y., et al.: Multi-functional flexible aqueous sodium-ion batteries with high safety. Chem. **3**(2), 348–362 (2017)
41. Wang, M., Xie, S., Tang, C., et al.: Making fiber-shaped Ni//bi battery simultaneously with high energy density, power density, and safety. Adv. Funct. Mater. **30**(3), 1905971 (2019)
42. Pan, J., Li, H., Sun, H., et al.: A lithium-air battery stably working at high temperature with high rate performance. Small. **14**(6), 1703454 (2018)

Chapter 2
Carbon Nanotube Dual-Material Gate Devices for Flexible Electronics

Li Xiang and Youfan Hu

Abstract Due to limited power supply and multifarious scenarios in practical applications, flexible electronic devices are expected to have low power consumption and functional configurability. In this chapter, a novel technology of dual-material gate (DMG) is demonstrated in flexible carbon nanotube (CNT) devices, which could modulate the energy-band structure in channel area of the devices by adopting two kinds of metals with different work functions, leading to low-power characteristics and functional configurability simultaneously. First, concept and principles of CNT-based DMG technology are introduced, followed by demonstrations of low-power characteristics of DMG devices under the transistor configuration. Then, after the exhibition of the devices under diode configuration, factors that could affect the electrical performances of DMG devices are identified. Finally, the flexibility of DMG devices and multifunctional integrated circuits (ICs) are demonstrated, together with the discussion of future perspectives of DMG technology.

Keywords Dual-material gate · Carbon nanotubes · Flexible electronics · Configurable devices · Multifunctional electronics · Integrated circuits

2.1 Introduction

Flexible electronics that can interface with complex curved surfaces and dynamic biological tissues have largely enhanced the capability of electronic devices in

L. Xiang
Key Laboratory for the Physics and Chemistry of Nanodevices, Department of Electronics and Center for Carbon-Based Electronics, Peking University, Beijing, China

College of Materials Science and Engineering, Hunan University, Changsha, China

Y. Hu (✉)
Key Laboratory for the Physics and Chemistry of Nanodevices, Department of Electronics and Center for Carbon-Based Electronics, Peking University, Beijing, China
e-mail: youfanhu@pku.edu.cn

F. Borghi et al. (eds.), *Nanoporous Carbons for Soft and Flexible Energy Devices*,
Carbon Materials: Chemistry and Physics 11,
https://doi.org/10.1007/978-3-030-81827-2_2

applications of smart sensing [1–6], healthcare monitoring [7–12] and advanced therapy [13–18]. Although tremendous efforts have been made to achieve much progress in this field, there are still some critical issues that need to be addressed to further push flexible electronics toward practical applications. One is reducing the power consumption of flexible devices. This is because that in most application scenarios of flexible electronics, the supplied power is limited. Achieving low-power flexible devices could yield an integrated system with a longer standby time or more functions with a restricted power supply [19–21]. Another one is enabling flexible devices to be functionally configurable, which has great advantages in providing superior adaptability to ever-changing and multifarious application scenarios [22–26].

Dual-material gate (DMG) technology, which has been well investigated in InGaP/InGaAs heterostructure FETs [27], bulk silicon MOSFETs [28] and silicon-on-insulator devices [29], has demonstrated promising characteristics in lowering power consumption and overcoming the short channel effect. For carbon nanotubes (CNTs), their ultrathin thickness, combined with high-k dielectrics to provide high gate efficiency, could demonstrate new electrical behaviors of functional configurability [30, 31]. Here, the high gate efficiency means a sufficient gate controlling ability of the energy band structure in channel area of the devices. Therefore, by adopting DMG technologies, CNT-based flexible devices could simultaneously exhibit low-power characteristics and functional configurability, which could give great impetus to the applications of flexible electronic devices. In this chapter, we first introduce the concept and principles of CNT-based DMG devices. Then, the low-power characteristics under the transistor configuration of DMG devices are presented in comparison with the characteristics of normal CNT devices, followed by a demonstration of the diode operation of flexible DMG devices. Next, factors that could affect the electrical performances of DMG devices are exhibited, including the length ratio and work function difference between two gate metals, gate dielectrics thickness and carbon nanotube diameters. Finally, the flexibility of DMG devices and multifunctional integrated circuits (ICs) is presented, and the future perspectives of this technology are discussed.

2.2 Principle of CNT-Based DMG Devices

Figure 2.1 depicts a comparison between a normal-gated (NG) device (Fig. 2.1a–c) and a DMG device (Fig. 2.1d–f) based on CNT thin films. As shown in Fig. 2.1a and b, the gate electrode of the NG device is constructed with only one kind of metal, while the DMG device adopts a dual-material gate electrode, which utilizes two kinds of metals (Fig. 2.1d and e) [30, 31]. In the dual-material gate electrode, the metal close to the source electrode should have a low work function (i.e., Al, Y, Ti, etc.), while a high-work-function metal (i.e., Pd, Au, etc.) should be chosen to serve as the other part of the gate close to the drain electrode [27–29]. When the gate electrodes have enough controlling ability to adjust the energy band

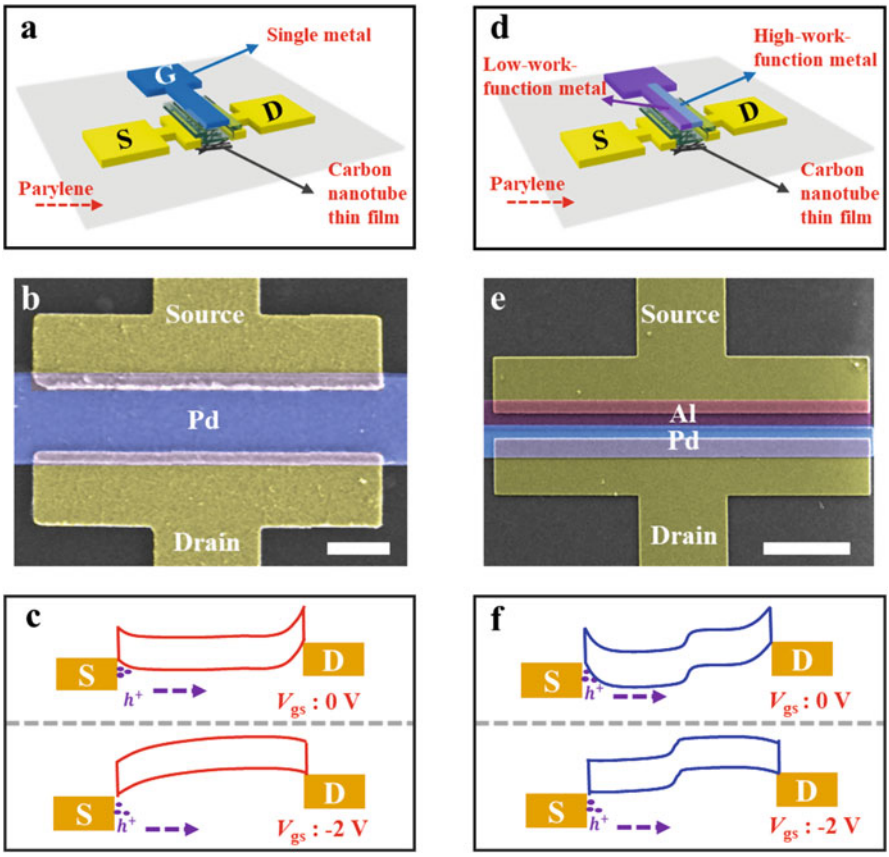

Fig. 2.1 Working principle and energy band diagrams of DMG and NG devices. (**a**), Structural illustration, (**b**), SEM image (scale bar: 1 μm), and (**c**), energy band diagram of NG devices. (**d**), Structural illustration, (**e**), SEM image (scale bar: 3 μm), and (**f**), energy band diagram of DMG devices. (Reproduced with permission from Ref. 31. Copyright 2020 Elsevier)

structure in channel area, here achieved by using ultrathin channel materials and high-k dielectrics, different gate electrode structures will lead to different energy band structures and thus different device behaviors [32]. In NG devices, the energy band in the channel area is symmetric (Fig. 2.1c), while the DMG devices have an asymmetric energy band structure (Fig. 2.1f) due to the modulation of different metals with different work functions in the dual-material gate electrode [31]. This asymmetry allows DMG devices to serve as a diode or a transistor with proper operation, as described in the subsequent part. Remarkably, due to the difference in energy band structures, the DMG devices have a smaller off-state current (I_{off}) than that of the NG devices when operating as a transistor. Such a smaller I_{off} indicate a smaller static power consumption, which is critical in wearable or portable applications [20, 33, 34]. In the off state (i.e., $V_{gs} = 0$ V), for DMG devices, due

to the step-like energy band structure caused by the dual-material gate electrodes, the energy barrier introduced near the source electrodes is increased compared to that in NG devices (Fig. 2.1f, top), resulting in enhanced blocking of holes and thus a decreased I_{off}. In the on state (i.e., $V_{gs} = -2$ V), for DMG devices (Fig. 2.1f, bottom), a negative voltage is applied to the gate electrode, which can reduce the height of the introduced barrier to a considerably low value, allowing holes transport easily from the source to the drain. Thus, the on-state current (I_{on}) in DMG devices is maintained at a similar level to that obtained in NG devices.

2.3 CNT-Based DMG Devices Under the Transistor Configuration for Low-Power Applications

Due to the introduced step-like energy band structure, DMG devices could have great advantages over NG devices in low-power applications. When the devices operate in the transistor configuration, the transfer characteristics under different voltage biases of a DMG device and an NG device are as shown in Fig. 2.2a and b, respectively. Here, the channel length ($L = 1$ μm), CNT purity (99.99%) and CNT density (~20 tubes/μm) in the DMG device and NG device are the same to verify the differences between the DMG and NG devices introduced by different gate structures. For the DMG device, Al (work function = 4.08 eV) and Pd (work function = 5.2 eV) serve as the metals of the gate electrodes, while for the NG device, the gate electrode is constructed with Pd only. When the supplied voltage increased from a small bias to a large bias (−2 V), different characteristics in the transfer curves between the NG device (Fig. 2.2a) and the DMG device (Fig. 2.2b) were observed, including the differences in the width-normalized off-state current I_{off}/W, current on/off ratio (I_{on}/I_{off}), subthreshold swing (SS) and threshold voltage (V_{th}).

As depicted in Fig. 2.2c, when the bias voltage (V_{ds}) increased from −0.1 V to −2 V, I_{off}/W of the NG devices dramatically increased from 8.2×10^{-12} A/μm to almost 10^{-7} A/μm, while that of the DMG device increased only from 1.4×10^{-12} A/μm to 8.2×10^{-11} A/μm. A much smaller I_{off}/W revealed a lower static power consumption, which indicates that DMG devices are more suitable for low-power applications than NG devices are. The current on/off ratio, I_{on}/I_{off}, which is a key parameter to characterize the switching properties, decreased rapidly in the NG device from 2×10^5 to 2.1×10^2 as V_{ds} increased, while that of the DMG device remained above 10^5 throughout the whole V_{ds} range (Fig. 2.2d). It should be noted that modern digital ICs require the I_{on}/I_{off} values of devices to be over 10^4 under a supplied voltage of over 0.7 V [34–37]. Therefore, the DMG devices have great advantages over the NG devices considering this requirement, especially when the device dimensions are continuously scaled down. This is because that much more difficulties would be encountered to switch off the devices due to the increased effect of drain-induced electrical field in short channel devices [27, 32,

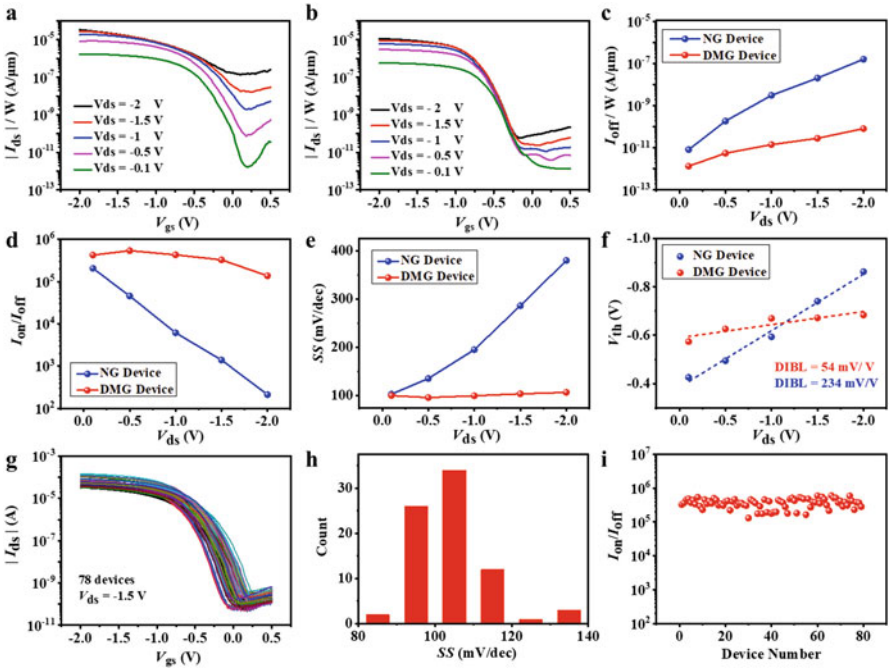

Fig. 2.2 Advantages of DMG devices in low-power applications under the transistor configuration. (**a**), Transfer characteristics of the NG device. (**b**), Transfer characteristics of the DMG device. Comparison of (**c**), width-normalized off-state current (I_{off}/W), (**d**), current on-off ratio (I_{on}/I_{off}), (**e**), subthreshold swing (*SS*), and (**f**), drain-induced barrier lowering (*DIBL*) between the NG device and DMG device. (**g**), Transfer characteristics of 78 DMG devices at $V_{ds} = -1.5$ V. Statistical distribution of (**h**), *SS* and (**i**), I_{on}/I_{off} of these 78 DMG devices. (Reproduced with permission from Ref. 31. Copyright 2020 Elsevier)

38]. Moreover, if the channel material is a single CNT or aligned CNT array, which has no or much fewer nanotube-nanotube junctions, the energy band modulation will be more efficient and can lead to a larger I_{on}/I_{off} of over 10^8 [30]. The *SS* is an important parameter used to characterize a device's switching-off properties, which should be as small as possible to enable device operation at a low supplied voltage, benefiting low-power applications [39]. As shown in Fig. 2.2e, when the supplied voltage was set at a relatively low value of $V_{ds} = -0.1$ V, both the DMG and NG devices had a similar *SS* of approximately 100 mV/dec. As the supplied voltage increased, the *SS* of the NG device obviously degraded from 100 mV/dec to 380 mV/dec, while that of the DMG device hardly changed (from 100 mV/dec to 106 mV/dec) in the full bias range. This result indicates that the DMG devices can still maintain efficient control over the channel even at a large bias voltage, which is also applicable for low-power devices. The drain-induced barrier lowering (DIBL), which is commonly observed in short channel devices [32], is depicted in Fig. 2.2f to compare the short channel effect in the DMG and NG devices. Here,

DIBL is measured by the V_{th} shift divided by the drain voltage difference. Because the DMG structure was originally designed to overcome the short channel effect in silicon MOSFETs [28, 29], similarly, when the channel material is CNTs, the DIBL obtained in DMG devices, as small as 54 mV/V, is greatly minimized compared to that obtained in the NG device (234 mV/V). This small DIBL in DMG devices is mainly attributed to the screening effect of the high-work function metal close to the drain [27], which effectively reduces the electrical field near the drain electrode. These results, including a lower I_{off}/W, larger I_{on}/I_{off} and smaller *SS,* indicate that the DMG devices have many advantages over the NG devices considering the low-power issues. Together with the reduction in the short channel effect, this superiority could be maintained if the device dimensions are further scaled down.

Additionally, these low-power advantages are not only realized in a single device but also achieved in scalable manufacturing [31]. As shown in Fig. 2.2g, 78 DMG devices were fabricated, and their transfer characteristics were measured under a large bias voltage of $V_{ds} = -1.5$ V, which demonstrated a narrow distribution with great uniformity. For example, the *SS* of these devices exhibited a statistical distribution of 103 ± 11.4 mV/dec (see Fig. 2.2h), while the statistical distribution of the I_{on}/I_{off} values of these devices was 5.5 ± 0.15 decades (see Fig. 2.2i), indicating good and uniform switching properties for low-power applications, which enables scalable integration based on these DMG devices.

2.4 DMG Devices Operated in the Diode Configuration

The DMG devices can not only serve as low-power transistors but also be configured as diodes due to their asymmetric electrical potential distribution in the channel. In this configuration, the source and drain electrodes of DMG devices are equivalent to the cathodes and anodes of diodes, respectively. As illustrated in Fig. 2.3a, due to the different energy band structures, the carrier transport properties in the channel are quite different between the DMG and NG devices [30]. For the DMG device, when a negative voltage is applied between the drain and source electrodes (i.e., $V_{ds} < 0$), as shown in the top panel of Fig. 2.3a, holes are blocked by the introduced energy barrier near the source electrode, resulting in a small current in the channel. Under this condition, the DMG devices can be regarded as a diode under reverse bias. When a positive voltage is applied between the drain and source electrodes (i.e., $V_{ds} > 0$), the holes can no longer be inhibited from transport from the drain to the source, leading to a large current in the channel, which is equivalent to a diode under forward bias conditions. For NG devices, because of the symmetric device and energy band structures, holes injected from the electrodes could transport easily in the channel under both reverse and forward biases. These results are verified by the experimental results presented in Fig. 2.3b. For the NG device (red curve in Fig. 2.3b), when V_{ds} was swept from negative (-1 V) to positive (1 V) voltages, a nearly symmetric *I-V* characteristic was demonstrated, with a rectification ratio of approximately 6. Here, the rectification ratio, a key parameter to characterize

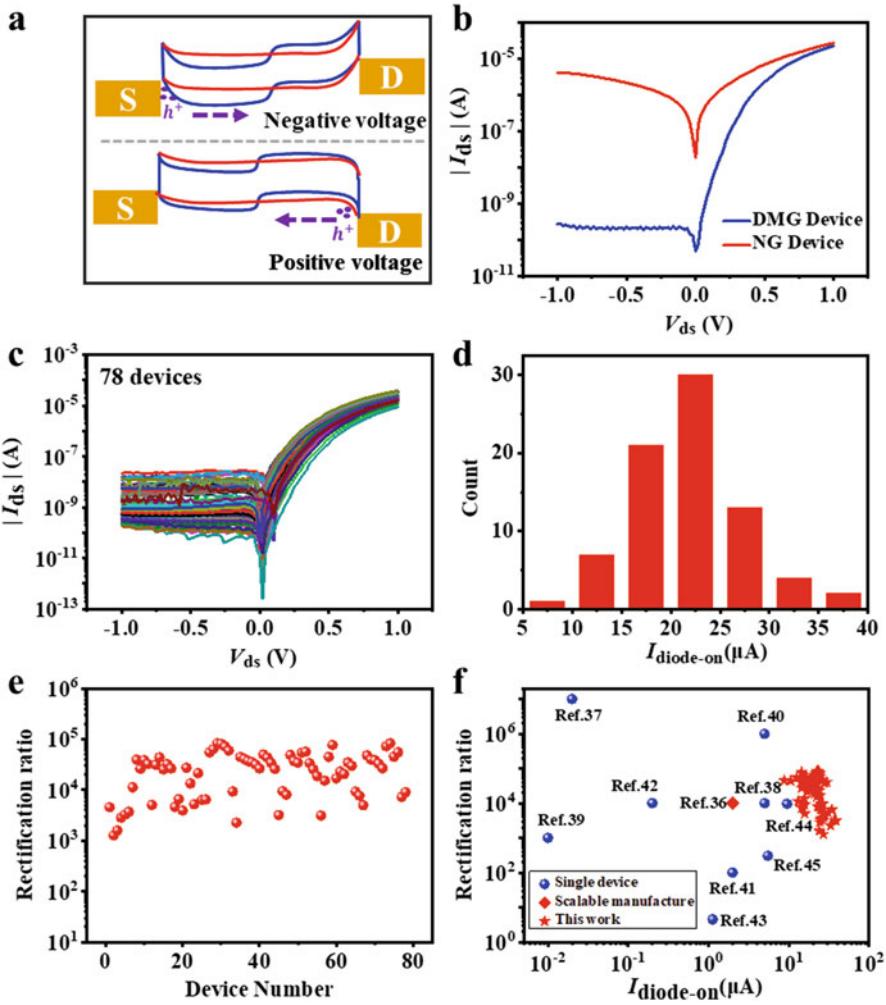

Fig. 2.3 DMG devices under the diode configuration. (**a**), Schematic energy band structure of NG and DMG devices under negative and positive V_{ds}. (**b**), *I-V* curves of the DMG and NG device. (**c**), *I-V* curves of 78 DMG devices under the diode configuration. Statistical distribution of (**d**), on-current of diode ($I_{diode\text{-}on}$) and (**e**), rectification ratios of these 78 DMG devices. (**f**), Comparison of $I_{diode\text{-}on}$ and the rectification ratio between DMG devices and other published CNT-based diodes. (Reproduced with permission from Ref. 31. Copyright 2020 Elsevier)

the rectifying performance of a diode, is defined as the current ratio between $V_{ds} = -1$ V and 1 V. In contrast to NG devices, the DMG device (blue curve in Fig. 2.3b) exhibited obvious asymmetric *I-V* characteristics with a rectification ratio of 8×10^4, which is a typical value that can be obtained for a rectifying diode [40, 41]. Another important parameter of diodes is the on-current ($I_{diode\text{-}on}$), which is defined by the current under forward bias (e.g., $V_{ds} = 1$ V). The $I_{diode\text{-}on}$ of the DMG device

here is approximately 26.5 μA, which is superior to almost all of the reported CNT-based diode values [40–49], indicating good driving ability. The *I-V* curves of 78 DMG devices in the diode configuration are depicted in Fig. 2.3c, which present obvious asymmetric behaviors that could be used for rectification. As shown in Fig. 2.3d, the $I_{\text{diode-on}}$ of these devices has a statistical distribution of 21.8 ± 5.8 μA. Moreover, the rectification ratios of these DMG devices (see Fig. 2.3e) are in the range of 10^3~10^5, with a statistical distribution of 4.28 ± 0.46 decades, which is adequate for them to serve as rectifying diodes. The $I_{\text{diode-on}}$ and rectification ratio of these DMG devices are summarized in Fig. 2.3f. Compared with other diodes based on CNT materials [40–49], the obtained DMG devices have a larger $I_{\text{diode-on}}$ and decent rectification ratios, indicating the better driving ability and smaller output resistance of the DMG devices in circuit integration.

2.5 Effect of Structural Parameters on the Characteristics of DMG Devices

The structural parameters of DMG devices, including the length ratio between two gate metals, work function difference between two gate metals, thickness of the gate dielectrics (t_{ox}), and diameter of the CNTs, all contribute to the modulation efficiency of the DMG structure and thus influence the electrical performances of the devices [30]. Therefore, to obtain the optimized configuration of the DMG structure, a more quantitative investigation should be carried out. Here, to make the system under investigation straightforward and clear, DMG devices based on single CNTs with different structure parameters are explored to eliminate the influence of nanotube-nanotube junctions in CNT networks.

First, devices in the transistor configuration with different length ratio of two gate metals were evaluated. By using Pd and Y to construct gate electrodes with different length ratios (L_{Pd}:L_{Y} = 3:1, 1:1, 1:3), DMG devices are fabricated on the same CNT with the same total gate length of 500 nm. The transfer characteristics of these DMG devices exhibit very little difference (see Fig. 2.4a), which indicates that the length ratio of the two metals in the gate electrode has a negligible effect on the performance of the device, providing high immunity against dimension variations introduced by fabrication deviations.

Then, DMG devices with different gate metal combinations are fabricated to explore the effect of the work function difference between the two gate metals. Here, Pd is fixed as the high-work-function metal near the drain electrodes, while metals with different work functions (Y, Ti, and Pd) are deposited as the other part of the gate electrodes close to the source electrodes in the DMG devices. The transfer characteristics shown in Fig. 2.4b indicate that $I_{\text{on}}/I_{\text{off}}$ of the device increases from 8.9×10^3 to 1.8×10^5 as the work function difference increases (changing from the Pd-Pd to Pd-Y combinations). The fundamental reason for this increase is mainly the increase in the introduced energy barrier height, which is positively correlated

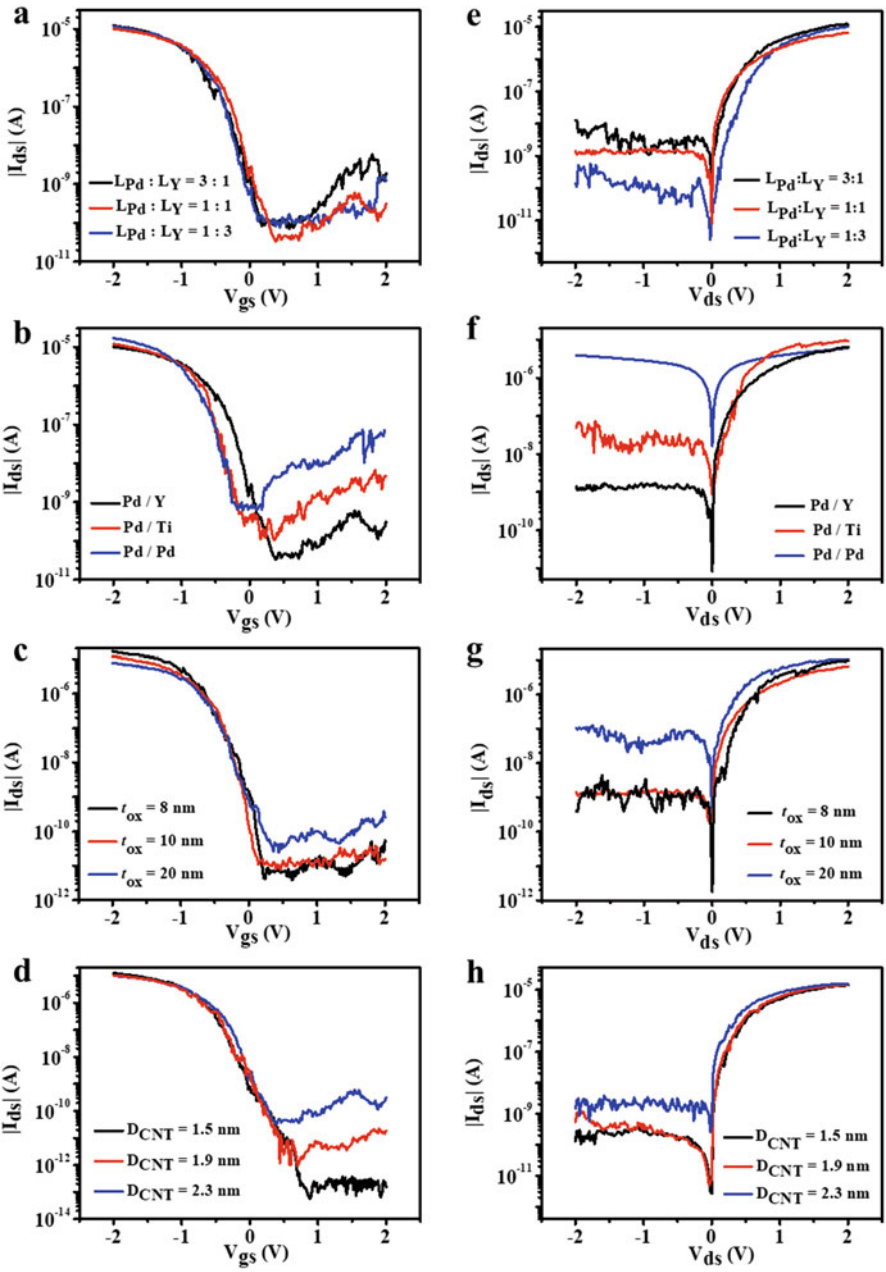

Fig. 2.4 Investigation of the effects of the structural parameters. Transfer characteristics of DMG devices under the transistor configuration with (**a**), different length ratios between a high-work-function metal and low-work-function metal, (**b**), different metal combinations of the gate electrode, (**c**), different dielectric thicknesses (t_{ox}), and (**d**), different CNT diameters. *I-V* curves of DMG devices under the diode configuration with (**e**), different length ratios between a high-work-function metal and low-work-function metal, (**f**), different metal combinations of the gate electrode, (**g**), different dielectric thicknesses (t_{ox}), and (**h**), different CNT diameters. (Reproduced from Ref. 30 with permission from The Royal Society of Chemistry)

with the work function difference between the metals used in the gate electrode, leading to the suppression of I_{off} and thus an increased I_{on}/I_{off}. Therefore, two metals used in the gate electrode of DMG devices are desired to have a larger work function difference to promote the effect of the DMG structure and obtain better electrical characteristics.

Gate capacitances are of great significance in the modulation efficiency of the energy band structure in the channel. For a certain dielectric, the gate capacitance is determined by the dielectric thickness. As shown in Fig. 2.4c, as the thickness of dielectrics (HfO_2 used here) decreases from 20 nm to 8 nm, I_{on}/I_{off} of the DMG devices increases from 2.4×10^5 to 1.8×10^6. This improvement mainly occurs because a thinner dielectric leads to a stronger coupling between the gate electrode and the CNT channel, resulting in a more efficient energy band structure modulation introduced by the DMG structure [32]. On the one hand, the improved efficiency yields a higher introduced energy barrier near the source electrodes with the same metal combination used in the gate electrode, resulting in a reduced $I_{off.}$ On the other hand, a thinner dielectric can also improve the electrostatic gate controlling efficiency, which can improve I_{on}. Therefore, I_{on}/I_{off} can be significantly elevated when the dielectric thickness is reduced in the DMG structure.

The bandgap of CNTs is also an important parameter that can significantly affect the I_{off} of CNT-based transistors, which is inversely proportional to the diameter of the CNTs [50]. To verify this influence, DMG devices with the same structural parameters were fabricated on different CNTs with diameters of 1.5 nm, 1.9 nm and 2.3 nm. When the CNT diameter decreases from 2.3 nm to 1.5 nm, I_{on}/I_{off} increases from 5.4×10^4 to 10^8, as shown in Fig. 2.4d. Notably, the large I_{on}/I_{off} of 10^8 is as good as the best reported result of CNT-based transistors [33], revealing that DMG technology is superior for low-power applications.

These structural parameters also impact the characteristics of DMG devices under the diode configuration. Figure 2.4e shows the *I-V* curves of DMG devices with different length ratios obtained by using Pd and Y to construct the gate electrode. As the length ratio of Pd to Y decreases from 3:1 to 1:3, the rectification ratio increases remarkably from 9.4×10^2 to 7.2×10^4. The length ratio of metals plays a more significant role when the DMG devices serve as diodes than as transistors because the introduced energy barrier that blocks the carrier transport is under the area of the low-work-function metal. When the length of the low-work-function metal increases, the width of the introduced energy barrier increases, resulting in a further suppressed current under negative bias in those devices in the diode configuration.

The influence of the work function difference between the two gate metals is presented in Fig. 2.4f. When the work function difference decreases as the metal combination changes from Pd-Y to Pd-Pd, the rectification ratio of the DMG devices decreases from 4.6×10^3 to 1.5, which is due to the decreased height of the introduced energy step and weakened asymmetry in the energy band structure. As shown in Fig. 2.4g, when the dielectric thickness is changed from 8 nm to 20 nm, the rectification ratio is reduced greatly from 4.6×10^3 to 98 due to the decreased coupling capacitance between the gate electrodes and the channel. The impact of

the diameters of the CNTs under the diode configuration is shown in Fig. 2.4h. As the diameters decrease from 2.3 nm to 1.5 nm, the rectification ratio of the DMG devices increases from 10^4 to 10 [5], as CNTs with a smaller diameter have a larger bandgap with which to suppress I_{off} and thus increase the rectification ratio.

Therefore, to optimize the performance of DMG devices in both the transistor and diode configurations, the following approaches could be taken: (i) the length ratio between the high- and low-work-function metals in the gate electrodes should be designed with a relatively small value to ensure that the width of the introduced energy barrier is wide enough; (ii) the work function difference between these two gate metals should be as large as possible to realize a larger energy barrier near the source electrode; (iii) the gate capacitance should be made as large as possible by adopting thin high-k dielectrics to elevate the energy band modulation efficiency; and (iv) CNTs with smaller diameters are better choices due to their larger bandgaps for suppressing the I_{off}.

2.6 Flexibility Test of DMG Devices

In practical applications, deformations may be introduced to electronic devices, which will affect the electrical performance of the devices [19]. Therefore, an investigation of the flexibility of DMG devices was carried out. As shown in Fig. 2.5a, the DMG devices fabricated on ultrathin flexible parylene-C substrates can be conformally laminated on human skin, and this intimate interface between the foil and human skin can be well maintained even when deformations of compression (Fig. 2.5b) and poking (Fig. 2.5c) are introduced [31]. As depicted in Fig. 2.5d, to quantitatively investigate mechanical deformation stability, DMG devices, together with ultrathin parylene foil, are mounted on a polyethylene terephthalate (PET) substrate with an adhesion layer of polydimethylsiloxane (PDMS), and cyclic bending tests are applied to them with a bending radius of curvature of 3.23 cm. After 4000 bending cycles, some wrinkles are generated in the DMG devices on the flexible parylene substrates, as shown in Fig. 2.5e. Figure 2.5f presents the transfer characteristics of a typical DMG device after different bending cycles when operated as a transistor. It is obvious that the electrical parameters, especially I_{off} and I_{on}/I_{off}, decline after 1000 bending cycles. The detailed changes in I_{on}/I_{off} exhibited in Fig. 2.5g show that I_{on}/I_{off} can be maintained at a large value of over 10^5 before 1000 bending cycles, after which it degrades gradually as the number of bending cycles increases. After 4000 bending cycles, I_{on}/I_{off} declines to near 1. Similarly, under the diode configuration, the *I-V* curves of DMG devices after different bending cycles show an obvious deteriorating trend, as depicted in Fig. 2.5h. As the number of bending cycles increases, the *I-V* characteristics of the DMG devices gradually convert from an asymmetric curve to a nearly symmetric one. The rectification ratio extracted from Fig. 2.5h is illustrated in Fig. 2.5i. Before reaching 1000 bending cycles, the rectification ratio of the DMG device is kept larger than 10^3 and decreases to 2.6 after 4000 bending cycles. These results indicate that

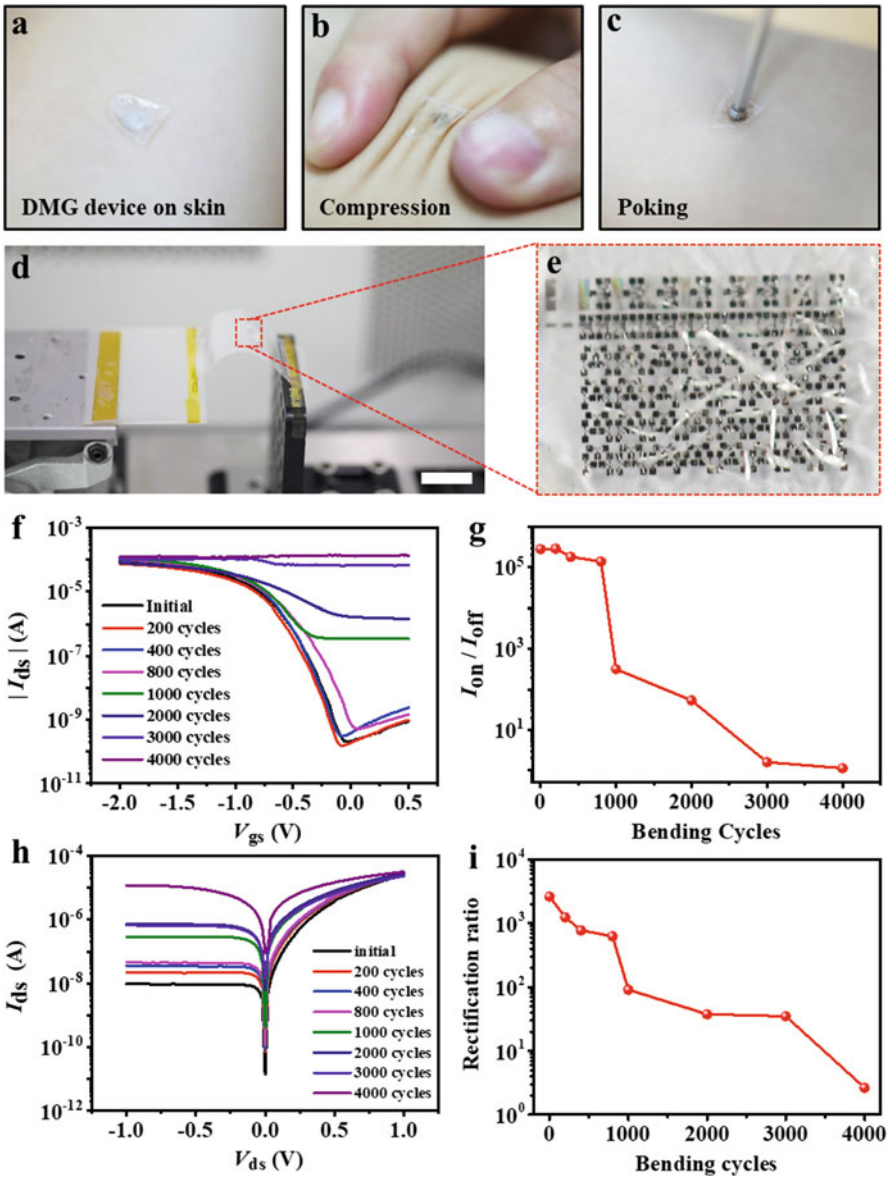

Fig. 2.5 Flexibility test of DMG devices. Optical images of the flexible DMG devices (**a**), laminated on human skin and under deformation: (**b**), compression and (**c**), poking. (**d**), Optical image of DMG devices attached to a curved PET substrate. (Scale bar: 2 cm). (**e**)**,** Magnified optical image of the DMG devices after 4000 bending cycles. (**f**)**,** Transfer characteristics and (**g**)**,** corresponding I_{on}/I_{off} of a DMG device in the transistor configuration after different numbers of cycles of the bending test. (**h**)**,***I-V* curves and (**i**)**,** corresponding rectification ratios of a DMG device in the diode configuration after different numbers of cycles of the bending test. (Reproduced with permission from Ref. 31. Copyright 2020 Elsevier)

the obtained DMG devices can withstand 1000 bending cycles and thus maintain decent performances in both the transistor and diode configurations. Although robust operation under 1000 bending cycles is sufficient for general applications, some further improvements, such as specialized mechanical structure design [18, 51–55] and material optimization [6, 56–58], can be adopted to further ameliorate the robustness of the electrical performances under deformations.

2.7 Multifunctional Integrated Circuits Constructed by the DMG Devices

Due to the configurable behaviors of DMG devices, multifunctional ICs can be constructed by using these devices. As shown in Fig. 2.6a, DMG devices are applied with a controlling bias on the gate electrodes, while the input signals are supplied on the drain electrodes. In this implementation, the controlling bias could modulate the energy band structure and thus change the functions of DMG devices on demand, which leads to different circuit functions dynamically. The corresponding mechanism is present in Fig. 2.6b. When the controlling bias on the gate electrode is set at a low level (e.g., $V_{gs} = 0$ V), simultaneously with a negative input signal on the drain electrode (i.e., $V_{ds} < 0$), the introduced step-like energy barrier near the source electrode can block the holes transported from the source to the drain, leading to a small current in the channel. While under a positive input signal on the drain electrode (i.e., $V_{ds} > 0$), holes can transport from the drain to the source easily with a large current in the channel. Therefore, with this low-level controlling bias, DMG devices operate as diodes with asymmetric *I*-*V* curves. However, as illustrated in Fig. 2.6c, when the controlling bias is set at a large negative bias (e.g., $V_{gs} = -2$ V), the introduced energy barrier can no longer block the holes either with negative (i.e., $V_{ds} < 0$) or positive input signals (i.e., $V_{ds} > 0$), leading to nearly symmetric carrier transport in the channel and thus symmetric *I*-*V* curves. This outcome was proved by the *I*-*V* curves under different controlling biases presented in Fig. 2.6d. When the controlling bias on the gate electrode changes from 0 to -1 V, the *I*-*V* curves of the DMG device gradually transform from an asymmetric curve with a rectification ratio of 5.2×10^4 to a nearly symmetric curve with a small rectification ratio of 6. Therefore, DMG devices can serve as asymmetric rectifying diodes under a small controlling bias or work as symmetric devices, i.e., resistors or transistors, when proper negative controlling biases are applied. As shown in Fig. 2.6e, based on the controllable operation of DMG devices, multifunctional ICs are constructed by integrating a DMG device with an on-chip resistor. Here, the controlling bias signal is applied to the terminal of $V_{g\text{-}in}$ (referring to the gate electrode of the DMG device), while the input signal is applied to the terminal of $V_{d\text{-}in}$ (referring to the drain electrode of the DMG device). The equivalent circuit diagram is illustrated in Fig. 2.6f. When the controlling bias is set at -2 V, the DMG device is equivalent to a resistor with a small resistance (top panel of Fig.

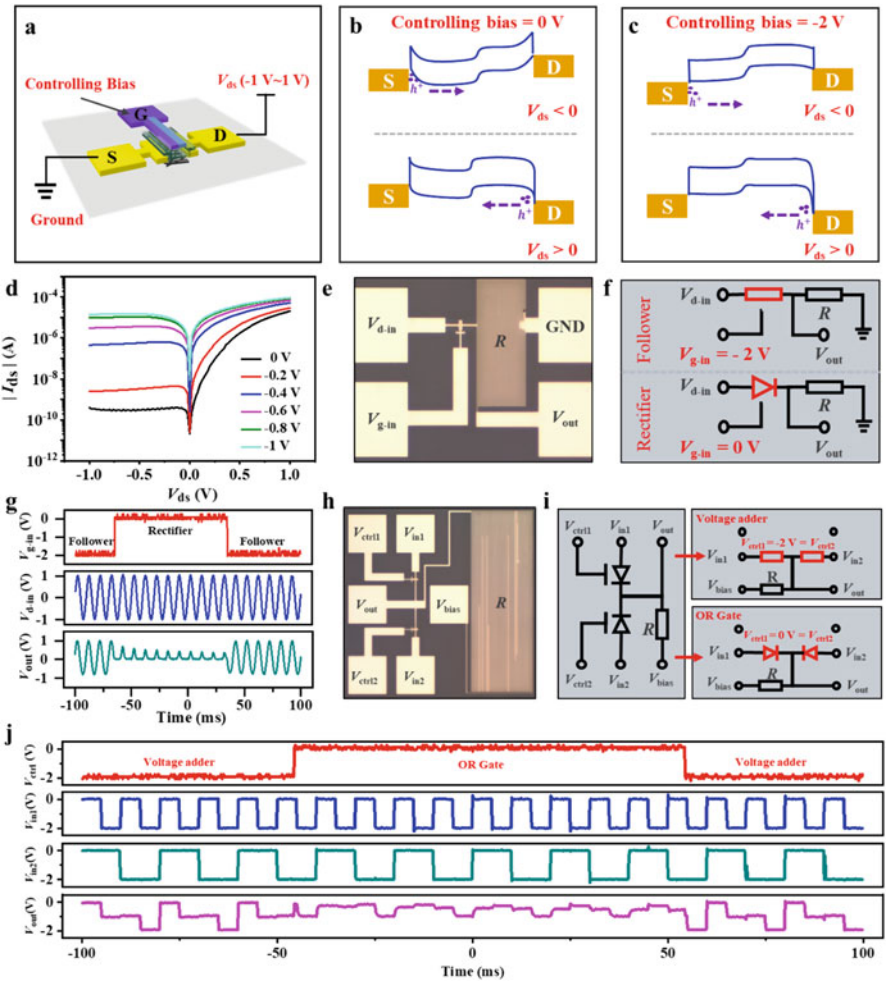

Fig. 2.6 Configurable multifunctional ICs based on DMG devices. (**a**)**,** Schematic illustration of the configuration of a DMG device integrated in circuits. Energy band structure of the DMG device applied with (**b**)**,** a small controlling bias of 0 V and (**c**)**,** a large negative controlling bias of −2 V. (**d**), *I-V* curves of a DMG device when applied with different controlling biases to the gate electrode. (**e**)**,** Optical image, (**f**)**,** equivalent circuit diagram, and (**g**)**,** dynamic input-output characteristics of a configurable one-device-one-resistor circuit. (**h**)**,** Optical image, (**i**)**,** equivalent circuit diagram and (**j**)**,** dynamic input-output characteristics of a configurable two-device-one-resistor circuit. (Reproduced with permission from Ref. 31. Copyright 2020 Elsevier)

2.6f). In this condition, input signals on the terminal of $V_{\text{d-in}}$ can propagate directly through this small resistor to the output terminal with very little amplitude loss, during which the circuits can be regarded as a signal follower. When the controlling bias is set to 0 V, the DMG device operates as a diode with a large rectification ratio; thus, the input signals applied to the terminal of $V_{\text{d-in}}$ are rectified, making the whole circuit operate as a rectifier, which is a basic element in analog ICs. The dynamic input-output characteristics of these circuits are shown in Fig. 2.6g, which reveals that the function of the circuit is successfully configured and switched by the controlling bias, either from follower to rectifier or vice versa.

A more complex circuit that integrates two DMG devices and one resistor is depicted in Fig. 2.6h, and the corresponding equivalent circuit diagram is presented in Fig. 2.6i. As shown in the left panel of Fig. 2.6i, controlling biases are applied to the terminals of V_{ctrl1} and V_{ctrl2}, while input signals are applied to the terminals of V_{in1} and V_{in2}. Similar to the circuit in Fig. 2.6f, because of the functional configurability of DMG devices, this two-device-one-resistor circuit can operate as a voltage adder (bottom of right panel in Fig. 2.6f) or an OR gate (top of right panel in Fig. 2.6f). The dynamic input-output characteristics shown in Fig. 2.6j prove this function switch. When the controlling biases of V_{ctrl1} and V_{ctrl2} are set at 0 V, the whole circuit can be equivalent to an OR gate, while when V_{ctrl1} and V_{ctrl2} are set at -2 V, this circuit operates as a voltage adder according to Kirchhoff's laws. It is expected that by further improving the integration scale of DMG devices, the functions of ICs can be further diversified in dynamic operation, and much better adaptability can be provided to the ever-changing application scenarios of flexible electronic devices.

2.8 Conclusions

In summary, this chapter introduces recent advances in exploring configurable flexible electronic devices based on CNTs. By using two metals with different work functions to construct the gate electrodes, together with the highly efficient gate modulation and ultrathin nature of CNTs, an asymmetric step-like energy band structure is generated in the CNT channel; thus, functional configurability and low-power characteristics can be simultaneously realized through this DMG technology. Compared to NG devices in the transistor configuration, DMG devices have great advantages over NG devices in low-power applications, with a smaller I_{off}, a larger $I_{\text{on}}/I_{\text{off}}$ and a smaller *SS*, and can maintain this superiority as the device dimensions are scaled down owing to their ability to overcome the short channel effect. Under the diode configuration, DMG devices can demonstrate large rectification ratios and on-currents at the same time. A proper length ratio and larger work function difference between two gate metals, thinner high-k dielectrics and smaller CNT diameters are desired to further optimize the performance of DMG devices. Based on the functional configurability of DMG devices, multifunctional ICs are demonstrated, which can be dynamically configured as a rectifier or a signal follower and as an OR

gate or a voltage adder. Continuous efforts are still in high demand to push DMG technology from proof-of-concept to practical applications. Adopting aligned CNT arrays, rather than randomly oriented CNT networks with many nanotube-nanotube junctions or single CNTs that are not scalable for mass production, could further improve the scalability and energy band modulation efficiency simultaneously. Additionally, adopting a more advanced circuit architecture rather than the current design of simply integrated DMG devices and resistors will greatly expand the functionality of configurable ICs with broadened applications. It is expected that many possibilities arising from the great advantages of DMG technologies will push this technology forward both in fundamental research and technical breakthroughs, enabling future flexible electronic devices to be more adaptive to ever-changing application scenarios.

References

1. Liu, Y., Pharr, M., Salvatore, G.A.: Lab-on-skin: a review of flexible and stretchable electronics for wearable health monitoring. ACS Nano. **11**(10), 9614–9635 (2017)
2. Yao, S., Ren, P., Song, R., Liu, Y., Huang, Q., Dong, J., O'Connor, B.T., Zhu, Y.: Nanomaterial-enabled flexible and stretchable sensing systems: processing, integration, and applications. Adv. Mater. **32**(15), 1902343 (2020)
3. Xiang, L., Zeng, X., Xia, F., Jin, W., Liu, Y., Hu, Y.: Recent advances in flexible and stretchable sensing systems: from the perspective of system integration. ACS Nano. **14**(6), 6449–6469 (2020)
4. Tian, X., Lee, P.M., Tan, Y.J., Wu, T.L.Y., Yao, H., Zhang, M., Li, Z., Ng, K.A., Tee, B.C.K., Ho, J.S.: Wireless body sensor networks based on metamaterial textiles. Nat. Electron. **2**(6), 243–251 (2019)
5. Xiang, L., Xia, F., Zhang, H., Liu, Y., Liu, F., Liang, X., Hu, Y.: Wafer-scale high-yield manufacturing of degradable electronics for environmental monitoring. Adv. Funct. Mater. **29**(50), 1905518 (2019)
6. Zhu, C., Chortos, A., Wang, Y., Pfattner, R., Lei, T., Hinckley, A.C., Pochorovski, I., Yan, X., To, J. W.-F, Oh, J.Y., Tok, J.B.-H., Bao, Z., Murmann, B.: Stretchable temperature-sensing circuits with strain suppression based on carbon nanotube transistors. Nat. Electron. **1**(3), 183–190 (2018)
7. Gao, W., Nyein, H.Y.Y., Shahpar, Z., Fahad, H.M., Chen, K., Emaminejad, S., Gao, Y., Tai, L.-C., Ota, H., Wu, E., Bullock, J., Zeng, Y., Lien, D.-H., Javey, A.: Wearable microsensor array for multiplexed heavy metal monitoring of body fluids. ACS Sens. **1**(7), 866–874 (2016)
8. Khan, Y., Garg, M., Gui, Q., Schadt, M., Gaikwad, A., Han, D., Yamamoto, N.A.D., Hart, P., Welte, R., Wilson, W., Czarnecki, S., Poliks, M., Jin, Z., Ghose, K., Egitto, F., Turner, J., Arias, A.C.: Flexible hybrid electronics: direct interfacing of soft and hard electronics for wearable health monitoring. Adv. Funct. Mater. **26**(47), 8764–8775 (2016)
9. Yang, Y., Gao, W.: Wearable and flexible electronics for continuous molecular monitoring. Chem. Soc. Rev. **48**(6), 1465–1491 (2019)
10. Pappa, A.-M., Parlak, O., Scheiblin, G., Mailley, P., Salleo, A., Owens, R.M.: Organic electronics for point-of-care metabolite monitoring. Trends Biotechnol. **36**(1), 45–59 (2018)
11. Dooley, E.E., Golaszewski, N.M., Bartholomew, J.B.: Estimating accuracy at exercise intensities: a comparative study of self-monitoring heart rate and physical activity wearable devices. JMIR Mhealth Uhealth. **5**(3), e34 (2017)

12. Sugiyama, M., Uemura, T., Kondo, M., Akiyama, M., Namba, N., Yoshimoto, S., Noda, Y., Araki, T., Sekitani, T.: An ultraflexible organic differential amplifier for recording electrocardiograms. Nat. Electron. **2**(8), 351–360 (2019)
13. Tasnim, F., Sadraei, A., Datta, B., Khan, M., Choi, K.Y., Sahasrabudhe, A., Vega Gálvez, T.A., Wicaksono, I., Rosello, O., Nunez-Lopez, C., Dagdeviren, C.: Towards personalized medicine: the evolution of imperceptible health-care technologies. foresight. **20**(6), 589–601 (2018)
14. Rogers, J.A.: Electronics for the human body. JAMA. **313**(6), 561 (2015)
15. Yu, Y., Nyein, H.Y.Y., Gao, W., Javey, A.: Flexible electrochemical bioelectronics: the rise of in situ bioanalysis. Adv. Mater. **32**(15), 1902083 (2020)
16. Lee, H., Choi, T.K., Lee, Y.B., Cho, H.R., Ghaffari, R., Wang, L., Choi, H.J., Chung, T.D., Lu, N., Hyeon, T., Choi, S.H., Kim, D.-H.: A graphene-based electrochemical device with thermoresponsive microneedles for diabetes monitoring and therapy. Nat. Nanotechnol. **11**(6), 566–572 (2016)
17. Sim, K., Ershad, F., Zhang, Y., Yang, P., Shim, H., Rao, Z., Lu, Y., Thukral, A., Elgalad, A., Xi, Y., Tian, B., Taylor, D.A., Yu, C.: An epicardial bioelectronic patch made from soft rubbery materials and capable of spatiotemporal mapping of electrophysiological activity. Nat. Electron., 1–10 (2020)
18. Han, M., Wang, H., Yang, Y., Liang, C., Bai, W., Yan, Z., Li, H., Xue, Y., Wang, X., Akar, B., Zhao, H., Luan, H., Lim, J., Kandela, I., Ameer, G.A., Zhang, Y., Huang, Y., Rogers, J.A.: Three-dimensional piezoelectric polymer microsystems for vibrational energy harvesting, robotic interfaces and biomedical implants. Nat. Electron. **2**(1), 26–35 (2019)
19. Myny, K.: The development of flexible integrated circuits based on thin-film transistors. Nat. Electron. **1**(1), 30–39 (2018)
20. Xiang, L., Zhang, H., Dong, G., Zhong, D., Han, J., Liang, X., Zhang, Z., Peng, L.-M., Hu, Y.: Low-power carbon nanotube-based integrated circuits that can be transferred to biological surfaces. Nat. Electron. **1**(4), 237–245 (2018)
21. Kim, Y., Lee, E.K., Oh, J.H.: Flexible low-power operative organic source-gated transistors. Adv. Funct. Mater. **29**(27), 1900650 (2019)
22. Mongillo, M., Spathis, P., Katsaros, G., Gentile, P., De Franceschi, S.: Multifunctional devices and logic gates with undoped silicon nanowires. Nano Lett. **12**(6), 3074–3079 (2012)
23. Weber, W.M., Heinzig, A., Trommer, J., Grube, M., Kreupl, F., Mikolajick, T.: Reconfigurable nanowire electronics-enabling a single CMOS circuit technology. IEEE Trans. Nanotechnol. **13**(6), 1020–1028 (2014)
24. Yan, H., Choe, H.S., Nam, S., Hu, Y., Das, S., Klemic, J.F., Ellenbogen, J.C., Lieber, C.M.: Programmable nanowire circuits for nanoprocessors. Nature. **470**(7333), 240–244 (2011)
25. Cheng, R., Wang, F., Yin, L., Wang, Z., Wen, Y., Shifa, T.A., He, J.: High-performance, multifunctional devices based on asymmetric van Der Waals Heterostructures. Nat. Electron. **1**(6), 356–361 (2018)
26. Weber, W.M., Heinzig, A., Trommer, J., Martin, D., Grube, M., Mikolajick, T.: Reconfigurable nanowire electronics - a review. Solid State Electron. **102**, 12–24 (2014)
27. Long, W., Ou, H., Kuo, J., Chin, K.K.: Dual-material gate (DMG) field effect transistor. IEEE Trans. Electron Devices. **46**(5), 865–870 (1999)
28. Saxena, M., Haldar, S., Gupta, M., Gupta, R.S.: Physics-based analytical Modeling of potential and electrical field distribution in dual material gate (DMG)-MOSFET for improved hot Electron effect and carrier transport efficiency. IEEE Trans. Electron Devices. **49**(11), 1928–1938 (2002)
29. Chaudhry, A., Kumar, M.J.: Investigation of the novel attributes of a fully depleted dual-material gate SOI MOSFET. IEEE Trans. Electron Devices. **51**(9), 1463–1467 (2004)
30. Xiang, L., Wang, Y., Zhang, P., Fong, X., Wei, X., Hu, Y.: Configurable multifunctional integrated circuits based on carbon nanotube dual-material gate devices. Nanoscale. **10**(46), 21857–21864 (2018)
31. Xiang, L., Xia, F., Jin, W., Zeng, X., Liu, F., Liang, X., Hu, Y.: Carbon nanotube dual-material gate devices for flexible configurable multifunctional electronics. Carbon. **161**, 656–664 (2020)

32. Sze, S.M., Ng, K.K.: Physics of Semiconductor Devices. Wiley (2006)
33. Qiu, C., Zhang, Z., Zhong, D., Si, J., Yang, Y., Peng, L.-M.: Carbon nanotube feedback-gate field-effect transistor: suppressing current leakage and increasing on/off ratio. ACS Nano. **9**(1), 969–977 (2015)
34. Auth, C., Allen, C., Blattner, A., Bergstrom, D., Brazier, M., Bost, M., Buehler, M., Chikarmane, V., Ghani, T., Glassman, T., Grover, R., Han, W., Hanken, D., Hattendorf, M., Hentges, P., Heussner, R., Hicks, J., Ingerly, D., Jain, P., Jaloviar, S., James, R., Jones, D., Jopling, J., Joshi, S., Kenyon, C., Liu, H., McFadden, R., McIntyre, B., Neirynck, J., Parker, C., Pipes, L., Post, I., Pradhan, S., Prince, M., Ramey, S., Reynolds, T., Roesler, J., Sandford, J., Seiple, J., Smith, P., Thomas, C., Towner, D., Troeger, T., Weber, C., Yashar, P., Zawadzki, K., Mistry, K.: A 22nm High Performance and Low-Power CMOS Technology Featuring Fully-Depleted Tri-Gate Transistors, Self-Aligned Contacts and High Density MIM Capacitors. In: 2012 Symposium on VLSI Technology (VLSIT), pp. 131–132 (2012)
35. International Roadmap for Devices and Systems (IRDS™) 2020 Edition https://irds.ieee.org/editions/2020. Accessed 2 Nov 2020
36. Jan, C., Agostinelli, M., Buehler, M., Chen, Z., Choi, S., Curello, G., Deshpande, H., Gannavaram, S., Hafez, W., Jalan, U., Kang, M., Kolar, P., Komeyli, K., Landau, B., Lake, A., Lazo, N., Lee, S., Leo, T., Lin, J., Lindert, N., Ma, S., McGill, L., Meining, C., Paliwal, A., Park, J., Phoa, K., Post, I., Pradhan, N., Prince, M., Rahman, A., Rizk, J., Rockford, L., Sacks, G., Schmitz, A., Tashiro, H., Tsai, C., Vandervoorn, P., Xu, J., Yang, L., Yeh, J., Yip, J., Zhang, K., Zhang, Y., Bai, P.: A 32nm SoC Platform Technology with 2nd Generation High-k/Metal Gate Transistors Optimized for Ultra Low Power, High Performance, and High Density Product Applications. In: 2009 IEEE International Electron Devices Meeting (IEDM), pp. 1–4 (2009)
37. Natarajan, S., Agostinelli, M., Akbar, S., Bost, M., Bowonder, A., Chikarmane, V., Chouksey, S., Dasgupta, A., Fischer, K., Fu, Q., Ghani, T., Giles, M., Govindaraju, S., Grover, R., Han, W., Hanken, D., Haralson, E., Haran, M., Heckscher, M., Heussner, R., Jain, P., James, R., Jhaveri, R., Jin, I., Kam, H., Karl, E., Kenyon, C., Liu, M., Luo, Y., Mehandru, R., Morarka, S., Neiberg, L., Packan, P., Paliwal, A., Parker, C., Patel, P., Patel, R., Pelto, C., Pipes, L., Plekhanov, P., Prince, M., Rajamani, S., Sandford, J., Sell, B., Sivakumar, S., Smith, P., Song, B., Tone, K., Troeger, T., Wiedemer, J., Yang, M., Zhang, K.: A 14nm Logic Technology Featuring 2nd-Generation FinFET, Air-Gapped Interconnects, Self-Aligned Double Patterning and a 0.0588 Mm2 SRAM Cell Size. In: 2014 IEEE International Electron Devices Meeting, pp. 3.7.1–3.7.3 (2014)
38. Long, W., Chin, K.K.: Dual Material Gate Field Effect Transistor (DMGFET). In: International Electron Devices Meeting, pp. 549–552. IEDM Technical Digest (1997)
39. Si, J., Xu, L., Zhu, M., Zhang, Z., Peng, L.-M.: Advances in high-performance carbon-nanotube thin-film electronics. Adv. Electron. Mater. **5**(8), 1900122 (2019)
40. Si, J., Liu, L., Wang, F., Zhang, Z., Peng, L.-M.: Carbon nanotube self-gating diode and application in integrated circuits. ACS Nano. **10**(7), 6737–6743 (2016)
41. Zhao, Y., Xiao, X., Huo, Y., Wang, Y., Zhang, T., Jiang, K., Wang, J., Fan, S., Li, Q.: Influence of asymmetric contact form on contact resistance and Schottky barrier, and corresponding applications of diode. ACS Appl. Mater. Interfaces. **9**(22), 18945–18955 (2017)
42. Hughes, M.A., Homewood, K.P., Curry, R.J., Ohno, Y., Mizutani, T.: An ultra-low leakage current single carbon nanotube diode with Split-gate and asymmetric contact geometry. Appl. Phys. Lett. **103**(13), 133508 (2013)
43. Huang, L., Chor, E.F., Wu, Y., Guo, Z.: Fabrication of single-walled carbon nanotube Schottky diode with gold contacts modified by asymmetric thiolate molecules. Carbon. **48**(4), 1298–1304 (2010)
44. Chen, C., Liao, C., Wei, L., Zhong, H., He, R., Liu, Q., Liu, X., Lai, Y., Song, C., Jin, T., Zhang, Y.: Carbon nanotube intramolecular P-i-n junction diodes with symmetric and asymmetric contacts. Sci. Rep. **6**(1), 22203 (2016)
45. Peng, N., Li, H., Zhang, Q.: Nanoscale contacts between carbon nanotubes and metallic pads. ACS Nano. **3**(12), 4117–4121 (2009)

46. Li, H., Zhang, Q., Marzari, N.: Unique carbon-nanotube field-effect transistors with asymmetric source and drain contacts. Nano Lett. **8**(1), 64–68 (2008)
47. Bandaru, P.R., Daraio, C., Jin, S., Rao, A.M.: Novel electrical switching behaviour and logic in carbon nanotube Y-junctions. Nat. Mater. **4**(9), 663–666 (2005)
48. Xu, H., Wang, S., Zhang, Z., Peng, L.-M.: Length scaling of carbon nanotube electric and photo diodes down to Sub-50 nm. Nano Lett. **14**(9), 5382–5389 (2014)
49. Yang, M.H., Teo, K.B.K., Milne, W.I., Hasko, D.G.: Carbon nanotube Schottky diode and directionally dependent field-effect transistor using asymmetrical contacts. Appl. Phys. Lett. **87**(25), 253116 (2005)
50. Zhou, X., Park, J.-Y., Huang, S., Liu, J., McEuen, P.L.: Band structure, phonon scattering, and the performance limit of single-walled carbon nanotube transistors. Phys. Rev. Lett. **95**(14), 146805 (2005)
51. Jang, K.-I., Han, S.Y., Xu, S., Mathewson, K.E., Zhang, Y., Jeong, J.-W., Kim, G.-T., Webb, R.C., Lee, J.W., Dawidczyk, T.J., Kim, R.H., Song, Y.M., Yeo, W.-H., Kim, S., Cheng, H., Rhee, S.I., Chung, J., Kim, B., Chung, H.U., Lee, D., Yang, Y., Cho, M., Gaspar, J.G., Carbonari, R., Fabiani, M., Gratton, G., Huang, Y., Rogers, J.A.: Rugged and breathable forms of stretchable electronics with adherent composite substrates for transcutaneous monitoring. Nat. Commun. **5**(1), 4779 (2014)
52. Xu, S., Yan, Z., Jang, K.-I., Huang, W., Fu, H., Kim, J., Wei, Z., Flavin, M., McCracken, J., Wang, R., Badea, A., Liu, Y., Xiao, D., Zhou, G., Lee, J., Chung, H.U., Cheng, H., Ren, W., Banks, A., Li, X., Paik, U., Nuzzo, R.G., Huang, Y., Zhang, Y., Rogers, J.A.: Assembly of micro/nanomaterials into complex, three-dimensional architectures by compressive buckling. Science. **347**(6218), 154–159 (2015)
53. Sim, K., Chen, S., Li, Z., Rao, Z., Liu, J., Lu, Y., Jang, S., Ershad, F., Chen, J., Xiao, J., Yu, C.: Three-dimensional curvy electronics created using conformal additive stamp printing. Nat. Electron. **2**(10), 471–479 (2019)
54. Zhang, Y., Wang, S., Li, X., Fan, J.A., Xu, S., Song, Y.M., Choi, K.-J., Yeo, W.-H., Lee, W., Nazaar, S.N., Lu, B., Yin, L., Hwang, K.-C., Rogers, J.A., Huang, Y.: Experimental and theoretical studies of serpentine microstructures bonded to Prestrained elastomers for stretchable electronics. Adv. Funct. Mater. **24**(14), 2028–2037 (2014)
55. Huang, Z., Hao, Y., Li, Y., Hu, H., Wang, C., Nomoto, A., Pan, T., Gu, Y., Chen, Y., Zhang, T., Li, W., Lei, Y., Kim, N., Wang, C., Zhang, L., Ward, J.W., Maralani, A., Li, X., Durstock, M.F., Pisano, A., Lin, Y., Xu, S.: Three-dimensional integrated stretchable electronics. Nat. Electron. **1**(8), 473–480 (2018)
56. Xu, S., Zhang, Y., Jia, L., Mathewson, K.E., Jang, K.-I., Kim, J., Fu, H., Huang, X., Chava, P., Wang, R., Bhole, S., Wang, L., Na, Y.J., Guan, Y., Flavin, M., Han, Z., Huang, Y., Rogers, J.A.: Soft microfluidic assemblies of sensors, circuits, and radios for the skin. Science. **344**(6179), 70–74 (2014)
57. Niu, S., Matsuhisa, N., Beker, L., Li, J., Wang, S., Wang, J., Jiang, Y., Yan, X., Yun, Y., Burnett, W., Poon, A.S.Y., Tok, J.B.-H., Chen, X., Bao, Z.: A wireless body area sensor network based on stretchable passive tags. Nat. Electron. **2**(8), 361–368 (2019)
58. Boutry, C.M., Kaizawa, Y., Schroeder, B.C., Chortos, A., Legrand, A., Wang, Z., Chang, J., Fox, P., Bao, Z.: A stretchable and biodegradable strain and pressure sensor for orthopaedic application. Nat. Electron. **1**(5), 314–321 (2018)

Chapter 3
Integration of Cost-Efficient Carbon Electrodes into the Development of Microbial Fuel Cells

Jiseon You, Iwona Gajda, John Greenman, and Ioannis A. Ieropoulos

Abstract Microbial fuel cells are a renewable energy technology that can generate electricity from organic fuel such as wastewater, whilst simultaneously treating it. In order to implement this technology at larger scale, a major challenge is the choice of suitable electrode material that determines system performance and cost. This chapter discusses carbon-based electrodes and characteristics of carbonaceous materials that are both high performing and cost-effective in light of the technology implementation at larger scale for practical applications. The focus is on the most recent findings and incorporation of lightweight, robust and biocompatible carbon fibre electrodes in the form of carbon veil both as the anode and cathode counterparts and their suitability in larger scale designs. The chapter also presents modification strategies of this substratum with microparticles such as activated carbon as another cost-effective approach that may assist in bringing this technology closer to market.

Keywords Microbial fuel cell · Carbon veil · Activated carbon · Electrode modification · Cost-effective · Electrode material

3.1 Introduction

Research on sustainable energy is now focusing on organic waste material as a renewable energy source. Waste products both organic (wastewater) and inorganic (CO_2, pollutants) are abundant, easily accessible and yet still require energy and resources to treat. Recent advances in treatment and processing of waste are shifting towards more sustainable methods of resource recovery that require novel,

J. You (✉) · I. Gajda · J. Greenman · I. A. Ieropoulos (✉)
Bristol BioEnergy Centre, Bristol Robotics Laboratory, T-Block, Frenchay Campus, UWE, Bristol, UK
e-mail: jiseon.you@uwe.ac.uk; iwona.gajda@uwe.ac.uk; john.greenman@uwe.ac.uk; ioannis.ieropoulos@brl.ac.uk

F. Borghi et al. (eds.), *Nanoporous Carbons for Soft and Flexible Energy Devices*, Carbon Materials: Chemistry and Physics 11,
https://doi.org/10.1007/978-3-030-81827-2_3

innovative ways of preserving natural resources with simultaneous biorefining of already polluted soil, air and water.

Bioelectrochemical energy conversion within the microbial fuel cell (MFC) technology brings new alternatives and novel opportunities to convert organic substrates in waste-streams into green electricity using living microorganisms as active biocatalysts. Hence, the use of MFCs in water quality improvement, which is related to wastewater treatment, has attracted attention over recent years. More importantly, MFCs can operate as self-powered wastewater treatment systems.

Microorganisms respire and capture energy for the production of ATP (adenosine triphosphate) through the oxidation of organic and inorganic matter and reduction of a terminal electron acceptor. The application of MFCs for wastewater treatment has become increasingly important due to the multiple benefits of recovering electrical energy from wastewater, reducing the organic content and recovering nutrient resources. Organic molecules can be continuously broken down by the bio-electrochemically active microbes leading to continuous operation of the MFC. These benefits open up opportunities for technology scale-up and with the advancement in material science, power output levels increase and come closer to those desired for practical applications.

3.2 Microbial Fuel Cells

Microbial fuel cell (MFC) is an energy transducer that coverts chemical energy into electrical energy using microbial metabolism. The earliest discovery of the link between metabolic processes of living organisms and electrical energy was made by Luigi Galvani who observed the bioelectrical properties of animal tissue in 1791. More than a century later, in 1911 an English botanist Michael C. Potter published the first MFC report on the ability of microorganisms to transform organic substrates (chemical energy) into electricity by demonstrating production of electrical energy from living cultures of either *Escherichia coli* and *Saccharomyces cerevisiae* [1]. Although there were several remarkable milestones in the MFC development history, such as Cohen's stack of multiple MFCs and the USA National Aeronautics and Space Administration (NASA)'s attempt to recycle human waste in space missions [2, 3], it was only in the last two decades that significant advancements in terms of power performance have been made.

Initially researchers started paying attention to the two main aspects of the MFC technology; electricity generation and organics degradation. Since almost any type of organic matter and some inorganic compounds can be used as an MFC substrate, the vast majority of MFC studies have been carried out with a focus on sustainable and effective waste/wastewater treatment [4, 5]. However, the range of applications of MFCs go beyond that; in the early 2000s, two robots, Chew-Chew and EcoBot I, both inspired by the MFC technology were developed [6, 7]. MFC powered robots can be goes truly autonomous with no maintenance requirements unlike most of the miniaturised mobile robots that are powered from standard primary or secondary

chemical batteries. They can also be less affected by latitude, location, time of day and weather, in comparison with (e.g.) photovoltaic panels. Moreover MFC powered biodegradable robots can be realised, so that they may decompose once the task at hand has been completed in 'release and forget' missions [8]. Sensing is another promising application of the MFC technology. Since the current flow of an MFC is affected by the surrounding environmental cues, such as concentration of organic substrate or toxicants, pH or temperature, the number of studies into MFC biosensors has been growing significantly [9, 10]. The potential use of MFC as a power source in implantable medical devices is a more recent interesting research avenue that is being explored [11]. Soft MFCs made of flexible materials for low-power electronics such as wireless communication system have also been suggested [12, 13].

MFCs usually consist of two compartments; an anode and a cathode separated by a membrane which facilitates ion flow. In the anode, electrochemically active microorganisms oxidise organic matter (fuel) and release CO_2, electrons and cations. Electrons produced in the anode flow towards the cathode via an external circuit as the result of electrophilic attraction from the cathode electrode, whilst protons migrate from the anode to the cathode through the separator between the two compartments. The electrons and protons subsequently combine with oxygen (final electron acceptor) and this reduction reaction completes the circuit. The electron flow through the external circuit results in current flow.

3.3 Cost-Effective Carbon Electrodes

For every MFC, regardless of its design or application, both the anode and cathode electrodes are essential components that determine performance and initial material cost [14]. For the successful choice of MFC electrodes, certain criteria need to be met such as high conductivity, large surface area, high porosity, good stability and durability as well as low cost. Considering that MFC anodes and some cathodes (i.e. bio-cathodes) act as hosts to microorganisms, biocompatibility is imperative. Moreover, minimising the environmental impact throughout the life cycle should be considered when selecting suitable electrode materials as well as easy accessibility and fabrication methods for the purpose of commercial applications.

A wide variety of MFC electrode including carbon-based and metal/metal oxide-based materials have been tested [14, 15]. Carbon-based materials such as carbon cloth [16], carbon paper [17], carbon veil [18] and granular activated carbon (GAC) [19] are mostly used as both anode and cathode due to the aforementioned properties. Carbon fibre brushes are also widely used as anodes due to their good surface area, however their cost has been reported as double that of carbon cloth [20]. Anodic carbon materials can significantly promote interfacial microbial colonisation and accelerate the formation of electroactive biofilms, which eventually improves power by providing a conductive microenvironment for extracellular electron transfer [21]. On the other hand, despite the excellent electrical conduc-

tivity, metals tend to suffer from corrosion and biocompatibility issues (for biotic electrodes) with a few exceptions [22, 23]. The high cost of metals also cannot be overlooked for system scale-up. Recent advances in the design and fabrication of MFC electrodes based on bio-derived carbon such as biochar and activated carbon as well as pyrolised natural raw materials such as corncob [24], sugarcane [25], coconut [26] or even bread [27] is worth noting. Utilisation of these bio-derived carbon substrata is an attractive strategy due to their sustainability, low cost and satisfactory performance. However, the stability and longevity are rarely reported to assess how the materials would behave in real environments over prolonged periods.

The benefits of the larger surface area therefore higher surface activity than that of solid materials are faster biochemical and electrochemical reaction rates and higher catalytic activity leading to improved system performance. Therefore, nanocomposite electrodes containing carbon nanotubes, graphene or polyaniline (PANI) have gained a great deal of attention in recent years. These nanomaterials have shown promising results, although poor stability, cellular toxicity, complex fabrication process and high cost prevents their use in commercial products [28–31].

One of the biggest hurdles that hinders commercialisation of the MFC technology is the high cost of materials [32, 33]. Therefore, continuous efforts should be made in searching for cost-effective but well performing and robust electrode materials for long-term operation.

This chapter presents one of the most cost-effective carbonaceous materials such as carbon fibre veil and activated carbon powder used as electrode material in both the anode and the cathode within various microbial fuel cell settings.

3.3.1 Carbon Veil

Carbon veil (CV) is a thin ply of continuous strands of fibres that are looped randomly throughout the material. The fibres are held together with a binder such as poly vinyl alcohol (PVA). The nonwoven structure allows excellent resin uptake that increases chemical stability and reduces the risk of micro-cracks forming on the composite surface. Therefore, it is widely used in a variety of industries worldwide, including aerospace, defence, automotive, construction, consumer electronics and energy. Carbon veil can also be used for grounding a composite structure, minimising the build-up of static electricity that could prove dangerous when in contact with explosive liquids and gases.

As an MFC electrode material, carbon veil has many advantages. It possesses a non-woven structure of smooth, long, cylindrical fibres (Fig. 3.1) forming a network with large (macro-size) gaps between fibres that determine the porosity of this type of carbonaceous substratum. Carbon veil structure even when convoluted, allows for permeation and interpenetration of liquid media within the structure due to macro-porosity [18], and as such has been explored as the material for mL- and L-scale MFCs including large scale applications. It has good electrical conductivity,

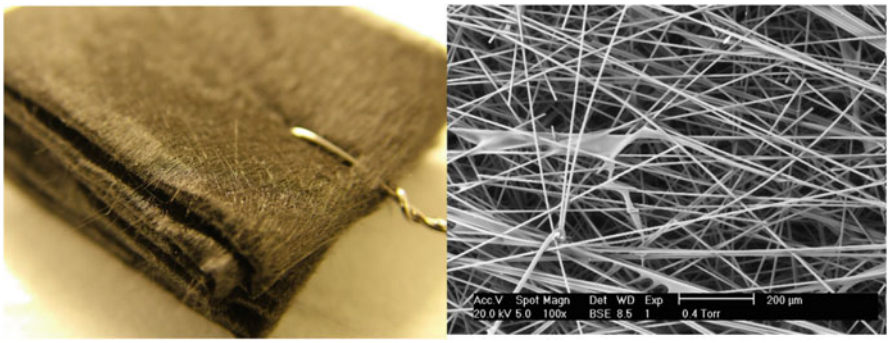

Fig. 3.1 A photo of folded 3D carbon veil material electrode (carbon loading: 20 g/m^2) (; left) and a scanning electron microscopy (SEM) image of the single layer at ×100 magnification (; right)

chemical resistance and higher porosity than woven carbon cloths. This lightweight, carbon-based nonwoven fabric, can be easily manipulated, folded, convoluted in any shape forming three dimensional (3D) structures for the bacterial attachment and formation of the electroactive biofilm. Also compared to other carbon-based fabric materials such as carbon cloth, the cost of carbon veil is much lower per unit area. Thus, it has been widely used as a 3D MFC electrode material.

As mentioned earlier, modification of the plain carbon veil is essential for enhanced performance, longevity and easy of scale-up. Thanks to the aforementioned properties (cost-effective and nonwoven structure that enables high chemical uptake) and high thermal stability, carbon veil is an ideal base material for electrode modification.

3.3.2 Activated Carbon

One of the most low-cost carbon-based materials are activated carbon and graphite which both show the lowest cost per mass [21]. Activated carbon (AC), also known as activated charcoal, is a carbonaceous, porous solid material with high specific surface area, relatively even pore size distribution and high-degree of surface reactivity. Due to its excellent adsorption properties, it has been widely used as an absorbent in many fields including hydrogen storage [34], medicine [35], water purification [36] and air filtration [37].

AC is produced from various carbonaceous materials such as wood, nutshells, fruit stones, peat, lignite, coal and petroleum pitch [38]. The process of AC synthesis usually consists of two steps, carbonisation and activation. Carbonisation is to reduce the volatile content of raw materials via pyrolysis of the carbon precursors in the temperature range of 300–900 °C. The following activation step is to improve the specific surface area or porosity through opening new pores and improving the existing pores. Properties of synthesised AC such as porosity, pore size, pore size

distribution and surface reactivity are affected by several factors including carbon precursors, activation pathways and activating agents [39].

Activated carbon electrodes have been widely used in bioelectrochemical systems, electrical energy storage as well as capacitive deionisation technologies due to the high storage capacity on the available large surface area, cost-effectiveness, availability and chemical stability. In MFCs, activated carbon is usually employed in granular, powder or woven form in either anodic or cathodic half-cell. However, it is primarily the powdered form that is used for in-house fabrication, modification and incorporation with other carbonaceous or metallic substrates. While the use of binding agents such as polyvinylidene difluoride (PVDF) or polytetrafluoroethylene (PTFE) is needed for AC powder attachment to the surface of the backbone, these binders can hinder ion access to the pore [40]. Currently, the choice of electrode core material and the method of surface modification is one of the main challenges undertaken in MFC research as it determines the system performance as well as technology cost for the purpose of future commercialisation.

3.3.3 Activated Carbon Doped Carbon Veil Anode

In order to enhance the bacterial adhesion as well as the electron transfer for efficient current collection, a strategy including the combination of carbonaceous scaffold decorated with a microporous agent can be successfully pursued [40], which can be followed utilising low-cost materials such as activated carbon as one of the most affordable and widely available forms of carbon [21]. Given the MFC anode is biotic, it is essential to give priority on pore size as well as the large surface area and high porosity. Surface topology has a direct influence on the formation and performance of electroactive biofilms [41]. This is important from the perspective of the mass transfer and diffusion limitations with regard to the substrate availability for the microbial biofilm grown on the surface of the electrode.

The clogging of pores in 3D porous carbon materials by the entrapment of bacterial cells can ultimately result in fast accumulation of inactive cells [42]. This may lead to a significant reduction of the power output levels. It has been reported that clogging most likely will happen if the diameter of the pore is smaller than 200 μm, and as a result mass transfer limitations would affect the bioanode performance [43].

Increasing the electrode macro area and electrode thickness by introducing multiple layers of carbon fibres provides a larger surface area for the electroactive biofilm to inhabit, but also a longer electron transfer path. Therefore the combination of macro- and micro-porosity has been introduced as a means of increasing the specific surface area in order to decrease the total (bulk) geometry [44].

The following sections describe some of the material parameters (Table 3.1) and show SEM images as well as data from real MFC experiments in which these materials were rigorously investigated; the methodology for experiments has been previously reported [44]. In summary, the MFCs were of cylindrical shape, made

Table 3.1 Material surface area and resistivity

Material	Surface area (m^a/g)[b]	Resistivity ($\Omega \cdot m$)[a]
Carbon veil	0.3183	9.2×10^{-4}
Activated carbon	672.1842	n.d.[c]
Modified anode	498.4422	7.7×10^{-4}

[a]measured using the four-wire resistance measurement
[b]measured by the Brunauer–Emmett–Teller (BET) method
[c]not determined

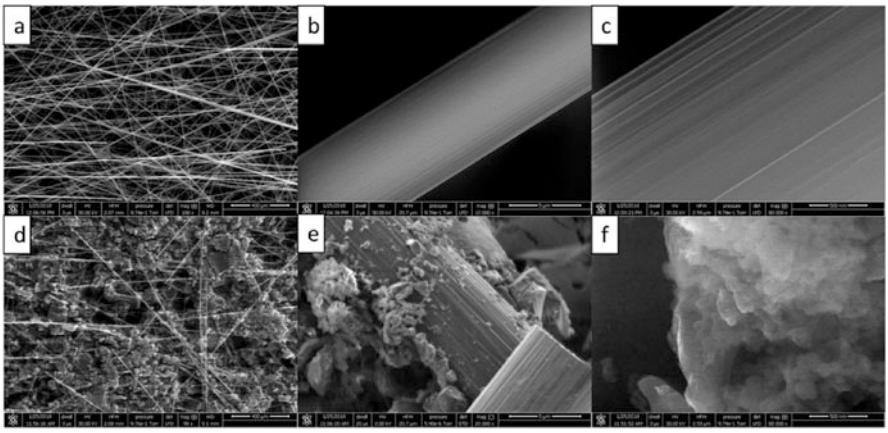

Fig. 3.2 Scanning electron microscopy observing plain carbon veil at (**a**) 100× (**b**) 10,000× (**c**) 80,000× and activated carbon doped carbon veil at (**d**) 99× (**e**) 20,000× (**f**) 80,000×. (Adapted from [44], Elsevier, under licence CC BY 4.0)

in house with terracotta clay and had an internal volume of 5 mL. The anode was a modified carbon veil with 5 mg/cm^2 of activated carbon powder and the cathodes were also modified carbon veil electrodes with 60 mg/cm^2 of activated carbon powder loading. In both cases, PTFE was used as the binding agent and it was 5% w/v for the anode and 20% w/v for the cathode. During the main parts of the experiment and for those data shown herewith, the external load connected to the MFCs was 100 Ω.

As shown in Table 3.1 and Fig. 3.2, AC particles attached on the smooth long fibres of plain carbon veil through the modification, created much higher surface area (1566 times) without losing the large void spaces. The additional micro- and nano-porous structures enhanced the surface roughness (Fig. 3.2e and f). The rough surface as a result of combination of macro, micro and nano pores should provide easier attachment for electroactive microorganisms compared to the smooth carbon fibres, hence higher cell population [45]. For bacterial attachment, the effect of electrode surface topology is predominant in macro-pores and grooves [46, 47], while the actual microbe-electrode interaction is determined by the microscopic roughness [47].

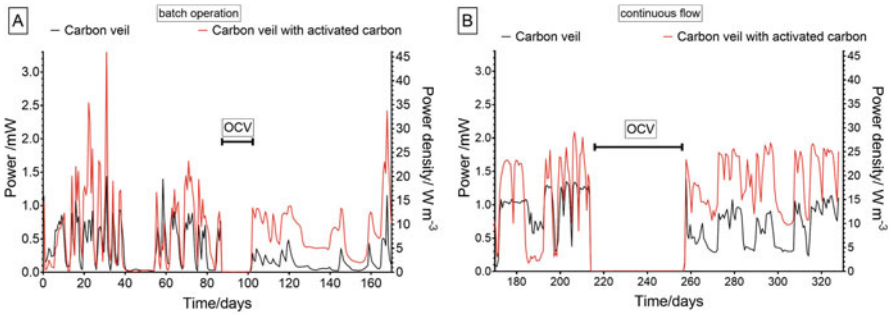

Fig. 3.3 Performance of activated carbon doped carbon veil anode in comparison to plain carbon veil both in batch operation (**a**) and under continuous flow feeding mode (**b**), OCV (open circuit voltage) depicts the period of time when the MFCs were operated under open circuit condition

Figure 3.3 illustrates 1-year performance of MFCs equipped with modified or unmodified, plain carbon veil electrodes. In Fig. 3.3a, the MFCs were operated in batch-fed mode and the maximum power performance of 3.2 mW was achieved by the modified anode MFCs, while the plain carbon veil showed up to 1.4 mW of power. Under continuous flow shown in Fig. 3.3b, MFCs with modified anodes stabilised at 1.8–2.0 mW, while MFCs with unmodified anodes showed output levels of 0.9–1.3 mW. The power fluctuations in this case were due to the cathode flooding by the continuously formed catholyte inside the cathode half-cells. The modification showed improved performance throughout the prolonged period of time and under various operating conditions including periodical feeding regime and long-term open circuit conditions (Fig. 3.3b). This shows both stability and resilience in the long term, which is sought after when implementing the technology in practical demonstrations. This is in line with the results obtained in the stack configuration [26].

These results show the enhanced surface area, surface topology, and electrical conductivity contribute to anode performance improvement. The results also demonstrate that the modified anode is suitable for long-term operation, showing no decrease in power generation performance for nearly one year of operation. In the literature, longevity is rarely reported which is connected to the performance stability within the lab, field trials and prototypes tested with real wastewater. The majority of materials and methodologies are unsuitable for practical implementations due to complex manufacturing processes, their scalability or high costs; moreover, the long-term stability of most tested materials is not given or is still unknown. Apart from the materials, scaling-up to multi-litre level brings about various challenges relating to design, stacking, fluidic and electrical complexities such as fuel starvation and voltage reversal. In this regard, the choice of materials for MFC assembly apart from electrodes as well as the choice of the semi-permeable membrane is of primary concern as it dictates technology performance and overall cost.

3.3.4 *Cathode Electrodes: Incorporation of Carbon Veil and Activated Carbon*

Carbon veil has also been a material of choice for the cathode in the biotic [48], synthetic [49], open to air cathode configurations [50], where the progress in material science and modification strategies are leading towards functionalisation of the carbon fibre matrix as a scaffold for the incorporation of microporous layers [51]. Cathode development is focusing on the improvement of air-breathing (open to air) cathode electrodes for the oxygen reduction reaction (ORR). The backbone of the carbon veil becomes a gas diffusion layer (GDL) and current collector where the active layer is directly attached to the scaffold and made of various carbon powder blends. This includes the carbon black and activated carbon. Activated carbon as the most affordable option was chosen for several lab-based studies as well as multiple prototypes tested in field trials of the technology. The powder of AC particles show micro-nano structure that promote electro-activity and enhances ORR while the carbon veil treated with hydrophobic agent such as PTFE allowing the air to permeate into the active layer (Fig. 3.2). Performance of the air-cathode that can be improved by developing an ORR catalyst with a high electrocatalytic activity, ensuring efficient transport, and enhancing oxygen diffusion.

The physico-chemical stability, robustness and cost of ceramics makes it particularly suitable for the technology advancement into larger scale and real-world applications. Optimum cathode modification results in better levels of performance, which can directly be used to power practical applications, as reported in [52]. As part of previous work, the modification was investigated under microscopy, which is now shown below in Fig. 3.4. Briefly, the MFCs were made of terracotta clay with 10 cm height, 3.6 cm inner diameter and a volume of 100 mL. Plain carbon veil (carbon loading: 20 g/m^2) was used as the anode and for the cathode, activated carbon/PTFE blend (20% w/w) was applied onto PTFE-treated carbon fibre veil. The MFCs were supplemented with a mixture of sludge and 0.1 M sodium acetate and tested in triplicates in batch-fed mode under 100 Ω external load.

In a different unpublished study, four types of carbon veil-based cathodes (10 cm^2) were tested as follows: i) plain carbon veil (20 g/m^2), ii) PTFE treated carbon veil, iii) thin layer of activated carbon paste with 20% PTFE content applied onto and iv) thick layer of AC paste applied onto the PTFE treated carbon veil backbone. The thickness of the thick AC was 3.0–3.5 mm, while the thin one was 1.5–1.6 mm. Carbon loading was 0.693 ± 0.03 g for the thin layer and 1.304 ± 0.05 g for the thick layer. The total of twelve MFCs were assembled as previously described [50].

Anode half-cells contained well matured anodes adapted from previous long-term MFC experiments operated for over 18 months. MFCs were assembled using 25 mL anode and 25 mL cathode chambers separated by a cation exchange membrane (CMI-7000, Membranes International Inc., New Jersey, USA) as previously described [48]. Anode electrodes were made of plain carbon fibre veil (20 g/m^2). MFC anodes were connected to the reservoir to recirculate the feedstock

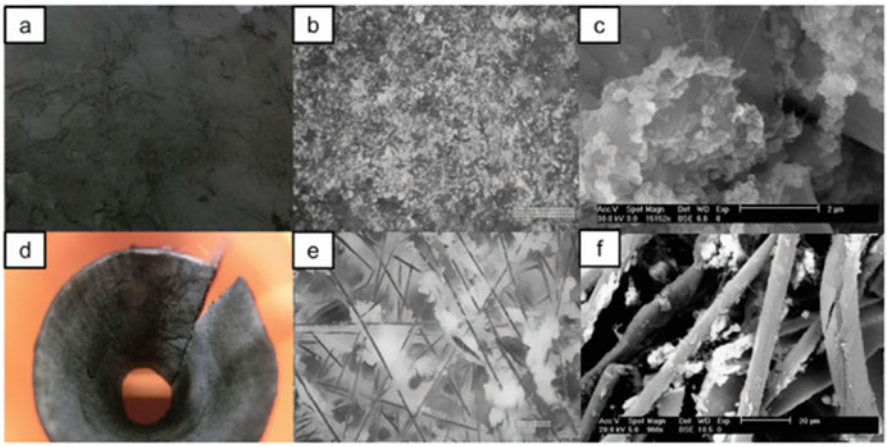

Fig. 3.4 Cathode electrode morphology. (**a**) Photograph illustrating AC layer; (**b**) digital microscope image using 400× magnification of AC; (**c**) SEM image of AC under high (15,152×) magnification; (**d**) photograph illustrating GDL on the air side; (**e**) digital microscope image at 400× magnification of GDL; (**f**) GDL under 960× magnification. (Adapted from [53], Elsevier, under licence CC BY 4.0)

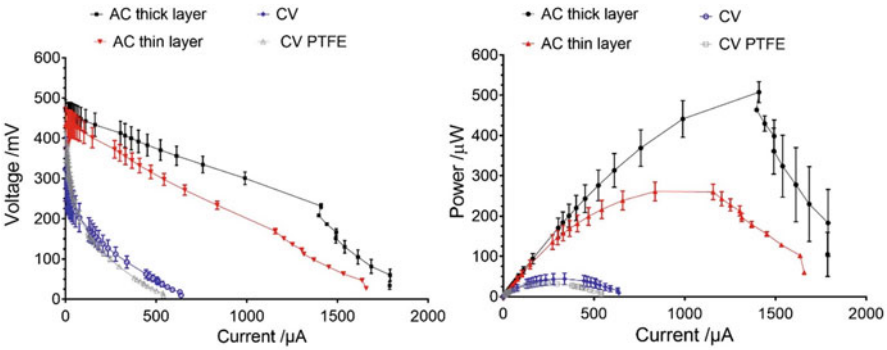

Fig. 3.5 Performance of thin and thick layer of activated carbon applied onto carbon veil cathode in comparison to plain carbon veil and PTFE treated carbon veil

(acetate/wastewater and urine) at a constant flow rate, while the external load connected was 300 Ω.

As can be seen in Fig. 3.5, the performance of the both AC-based cathodes was significantly higher than the unmodified plain CV both in PTFE treated and untreated versions. The maximum power achieved by the thick AC cathode was up to 500 μW, while the thin AC reached up to 260 μW, while the CV PTFE and CV produced only 32 μW and 43 μW respectively.

Figure 3.6 illustrates all MFC groups when tested under external load and two different feedstocks, namely wastewater supplemented with acetate and human

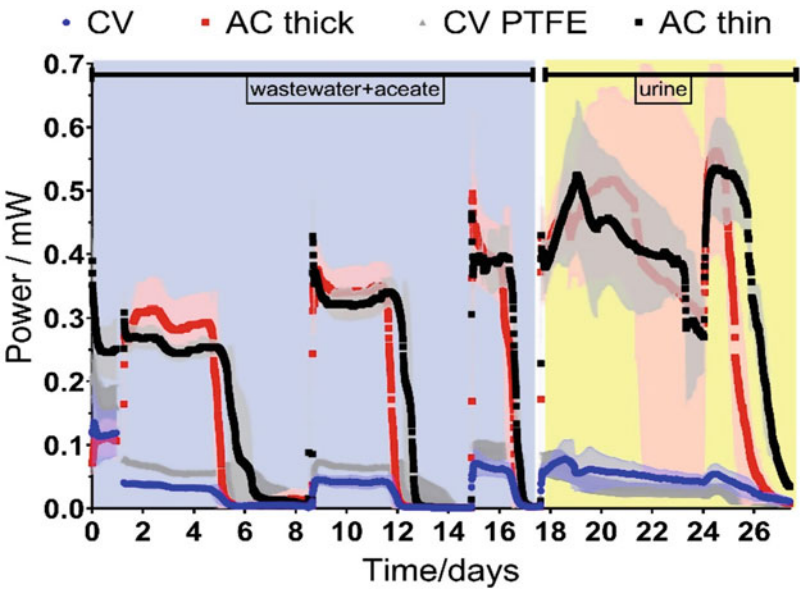

Fig. 3.6 Temporal behaviour of all four types of MFCs (n = 3, shaded areas illustrate error bars) when fed with sodium acetate/wastewater and when fed with neat human urine. Drop in performance shows feedstock depletion while the increase in power indicates fresh feedstock supply

urine. Although the MFCs were operated under constant recirculation mode between the anode and 1 L reservoir, the periodic feedstock depletion resulted in a decrease of power and subsequent feedstock replenishment resulted in restored and even improved output levels. Both thin and thick AC-modified cathode MFCs showed up to almost 400 μW when fed with acetate and over 500 μW when fed with urine, while the CV and CV PTFE reached up to 43 μW and 69 μW respectively when fed with acetate and 77 μW and 90 μW when urine was used as feedstock. The effect of AC-modification suggests an almost eightfold improvement. What is interesting to observe, both thin and thick AC modifications resulted in similar power performance, therefore higher carbon loading in this case did not improve the output.

In Fig. 3.7, both anodic and cathodic modifications are analysed in terms of performance and cost. It shows that for both anode and cathode, AC modification of the carbon veil is the most effective in terms of power to cost of material used (expressed in mW/£) reaching up to 7.4 mW/£. This is calculated using materials sourced in the United Kingdom, whereas both carbon veil and activated carbon are widely available and can be sourced worldwide even at more competitive prices when bought in bulk quantities. For the MFC experiments, both modifications of the core carbon veil are tailored for separate environments where the anode electrode is designed to accommodate biotic biofilm whereas the cathode is more compact,

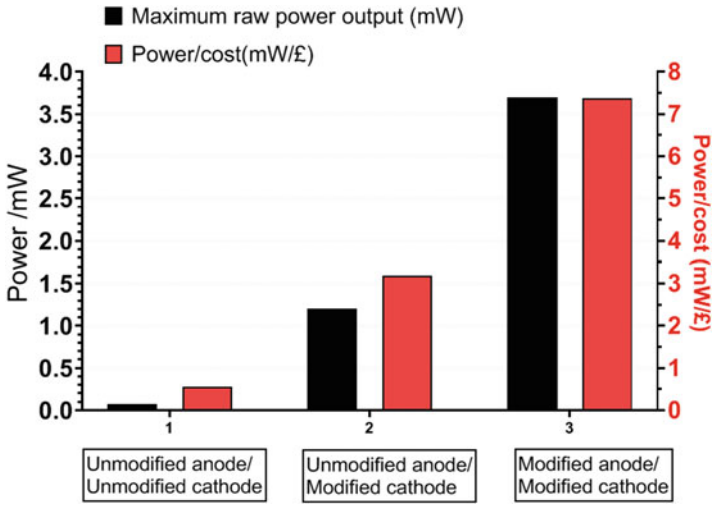

Fig. 3.7 Maximum power output and power/cost (in British pound sterling) comparison of the following anode/cathode configurations: 1) unmodified (plain) carbon veil anode and unmodified (plain) carbon cathode, 2) unmodified (plain) carbon veil anode and modified (with AC powder) carbon veil cathode, 3) modified (with AC powder) carbon veil anode and modified (with AC powder) carbon veil cathode. Please note that the 4th variation of modified anode/unmodified cathode was not tested. Costs of the PTFE binder material and fabrication are not included in power/cost comparison

hydrophobic (higher PTFE content) and abiotic for efficient ORR. Therefore, both methods of material preparation for the purpose of either cathode or anode assembly differ in binder content and in carbon loading because of the specific half-cell requirements. Power/cost ratio is particularly important when developing multi-modular stacks and prototypes for off-grid power production [54]. Therefore, further efforts in optimisation strategy with reducing overall cost and increasing MFC power output at the individual unit scale and from overall multi-unit stack can lead towards commercialisation of this technology.

3.4 Conclusions

The choice of electrode material is crucial for further development of the MFC technology as it determines its market readiness. Recent research had been directed towards anodic and cathodic modifications utilising high performing and affordable materials in order to enable scale-up and implementation. The combination of low-cost materials such as carbon fibre veil and activated carbon powder showed high power output, good longevity and improved power/cost ratio when implemented in both anode and in the cathode half-cells.

References

1. Potter, M.C.: Electrical effects accompanying the decomposition of organic compounds. Proc. R. Soc. B Biol. Sci. **84**, 260–276 (1911). https://doi.org/10.1098/rspb.1911.0073
2. Cohen, B.: The bacterial culture as an electrical half-cell. J. Bacteriol. **21**, 18–19 (1931)
3. Putnam, D.F.: Composition and Concentrative Properties of Human Urine, Washington, DC (1971)
4. Pandey, P., Shinde, V.N., Deopurkar, R.L., et al.: Recent advances in the use of different substrates in microbial fuel cells toward wastewater treatment and simultaneous energy recovery. Appl. Energy. **168**, 706–723 (2016). https://doi.org/10.1016/j.apenergy.2016.01.056
5. Gude, V.G.: Wastewater treatment in microbial fuel cells - an overview. J. Clean. Prod. **122**, 287–307 (2016)
6. Wilkinson, S.: "Gastrobots" - benefits and challenges of microbial fuel cells in food powered robot applications. Auton Robots. **9**, 99–111 (2000). https://doi.org/10.1023/A:1008984516499
7. Ieropoulos, I., Greenman, J., Melhuish, C.: Imitating metabolism: energy autonomy in biologically inspired robots. In: AISB '03, Second International Symposium on Imitation in Animals and Artifacts, pp. 191–194, Aberystwyth (2003)
8. Winfield, J., Chambers, L.D., Rossiter, J., et al.: Fade to green: a biodegradable stack of microbial fuel cells. ChemSusChem. **8**, 2705–2712 (2015). https://doi.org/10.1002/cssc.201500431
9. Abrevaya, X.C., Sacco, N.J., Bonetto, M.C., et al.: Analytical applications of microbial fuel cells. Part I: biochemical oxygen demand. Biosens. Bioelectron. **63**, 580–590 (2015). https://doi.org/10.1016/j.bios.2014.04.034
10. Abrevaya, X.C., Sacco, N.J., Bonetto, M.C., et al.: Analytical applications of microbial fuel cells. Part II: toxicity, microbial activity and quantification, single analyte detection and other uses. Biosens. Bioelectron. **63**, 591–601 (2015). https://doi.org/10.1016/j.bios.2014.04.053
11. Han, Y., Yu, C., Liu, H.: A microbial fuel cell as power supply for implantable medical devices. Biosens. Bioelectron. **25**, 2156–2160 (2010). https://doi.org/10.1016/j.bios.2010.02.014
12. Winfield, J., Chambers, L.D., Stinchcombe, A., et al.: The power of glove: soft microbial fuel cell for low-power electronics. J. Power Sources. **249**, 327–332 (2014). https://doi.org/10.1016/j.jpowsour.2013.10.096
13. Taghavi, M., Stinchcombe, A., Greenman, J., et al.: Wearable self sufficient MFC communication system powered by urine. In: Lecture Notes in Computer Science (including subseries Lecture Notes in Artificial Intelligence and Lecture Notes in Bioinformatics), pp. 131–138. Springer (2014)
14. Wei, J., Liang, P., Huang, X.: Recent progress in electrodes for microbial fuel cells. Bioresour. Technol. **102**, 9335–9344 (2011). https://doi.org/10.1016/j.biortech.2011.07.019
15. Palanisamy, G., Jung, H.-Y., Sadhasivam, T., et al.: A comprehensive review on microbial fuel cell technologies: processes, utilization, and advanced developments in electrodes and membranes. J. Clean. Prod. **221**, 598–621 (2019). https://doi.org/10.1016/J.JCLEPRO.2019.02.172
16. Luo, Y., Zhang, F., Wei, B., et al.: The use of cloth fabric diffusion layers for scalable microbial fuel cells. Biochem. Eng. J. **73**, 49–52 (2013). https://doi.org/10.1016/j.bej.2013.01.011
17. Zhang, Y., Sun, J., Hu, Y., et al.: Bio-cathode materials evaluation in microbial fuel cells: a comparison of graphite felt, carbon paper and stainless steel mesh materials. Int. J. Hydrog. Energy. **37**, 16935–16942 (2012). https://doi.org/10.1016/j.ijhydene.2012.08.064
18. Ieropoulos, I., Greenman, J., Melhuish, C.: Microbial fuel cells based on carbon veil electrodes: stack configuration and scalability. Int. J. Energy Res. **32**, 1228–1240 (2008). https://doi.org/10.1002/er.1419
19. Wu, S., Li, H., Zhou, X., et al.: A novel pilot-scale stacked microbial fuel cell for efficient electricity generation and wastewater treatment. Water Res. **98**, 396–403 (2016). https://doi.org/10.1016/j.watres.2016.04.043

20. Ge, Z., He, Z.: Long-term performance of a 200 liter modularized microbial fuel cell system treating municipal wastewater: treatment, energy, and cost. Environ. Sci. Water Res. Technol. **2**, 274–281 (2016). https://doi.org/10.1039/c6ew00020g
21. Li, S., Cheng, C., Thomas, A.: Carbon-based microbial-fuel-cell electrodes: from conductive supports to active catalysts. Adv. Mater. **29**, 1602547 (2017). https://doi.org/10.1002/adma.201602547
22. Yamashita, T., Yokoyama, H.: Molybdenum anode: a novel electrode for enhanced power generation in microbial fuel cells, identified via extensive screening of metal electrodes. Biotechnol. Biofuels. **11**, 39 (2018). https://doi.org/10.1186/s13068-018-1046-7
23. Beuth, L., Pfeiffer, C.P., Schröder, U.: Copper-bottomed: electrochemically active bacteria exploit conductive sulphide networks for enhanced electrogeneity. Energy Environ. Sci. **13**, 3102–3109 (2020). https://doi.org/10.1039/d0ee01281e
24. Li, M., Zhang, H., Xiao, T., et al.: Low-cost biochar derived from corncob as oxygen reduction catalyst in air cathode microbial fuel cells. Electrochim. Acta. **283**, 780–788 (2018). https://doi.org/10.1016/j.electacta.2018.07.010
25. Bose, D., Sridharan, S., Dhawan, H., et al.: Biomass derived activated carbon cathode performance for sustainable power generation from microbial fuel cells. Fuel. **236**, 325–337 (2019). https://doi.org/10.1016/j.fuel.2018.09.002
26. Gajda, I., Greenman, J., Ieropoulos, I.: Microbial fuel cell stack performance enhancement through carbon veil anode modification with activated carbon powder. Appl. Energy. **262** (2020). https://doi.org/10.1016/j.apenergy.2019.114475
27. Zhang, L., He, W., Yang, J., et al.: Bread-derived 3D macroporous carbon foams as high performance free-standing anode in microbial fuel cells. Biosens. Bioelectron. **122**, 217–223 (2018). https://doi.org/10.1016/j.bios.2018.09.005
28. Obreja, V.V.N.: On the performance of supercapacitors with electrodes based on carbon nanotubes and carbon activated material-a review. Phys. E Low-Dimensional Syst. Nanostruct. **40**, 2596–2605 (2008). https://doi.org/10.1016/j.physe.2007.09.044
29. Ren, H., Tian, H., Gardner, C.L., et al.: A miniaturized microbial fuel cell with three-dimensional graphene macroporous scaffold anode demonstrating a record power density of over 10000 W m-3. Nanoscale. **8**, 3539–3547 (2016). https://doi.org/10.1039/c5nr07267k
30. Xiao, L., Damien, J., Luo, J., et al.: Crumpled graphene particles for microbial fuel cell electrodes. J. Power Sources. **208**, 187–192 (2012). https://doi.org/10.1016/j.jpowsour.2012.02.036
31. Wu, X., Shi, Z., Zou, L., et al.: Pectin assisted one-pot synthesis of three dimensional porous NiO/graphene composite for enhanced bioelectrocatalysis in microbial fuel cells. J. Power Sources. **378**, 119–124 (2018). https://doi.org/10.1016/j.jpowsour.2017.12.023
32. Slate, A.J., Whitehead, K.A., Brownson, D.A.C., Banks, C.E.: Microbial fuel cells: an overview of current technology. Renew. Sust. Energ. Rev. **101**, 60–81 (2019). https://doi.org/10.1016/j.rser.2018.09.044
33. Trapero, J.R., Horcajada, L., Linares, J.J., Lobato, J.: Is microbial fuel cell technology ready? An economic answer towards industrial commercialization. Appl. Energy. **185**, 698–707 (2017). https://doi.org/10.1016/j.apenergy.2016.10.109
34. De La Casa-Lillo, M.A., Lamari-Darkrim, F., Cazorla-Amorós, D., Linares-Solano, A.: Hydrogen storage in activated carbons and activated carbon fibers. J. Phys. Chem. B. **106**, 10930–10934 (2002). https://doi.org/10.1021/jp014543m
35. Sarici-Özdemir, Ç., Önal, Y.: Study to observe the applicability of the adsorption isotherms used for the adsorption of medicine organics onto activated carbon. Part. Sci. Technol. **36**, 254–261 (2018). https://doi.org/10.1080/02726351.2016.1246497
36. Korotta-Gamage, S.M., Sathasivan, A.: A review: potential and challenges of biologically activated carbon to remove natural organic matter in drinking water purification process. Chemosphere. **167**, 120–138 (2017)
37. Suzuki, M.: Activated carbon fiber: fundamentals and applications. Carbon N Y. **32**, 577–586 (1994). https://doi.org/10.1016/0008-6223(94)90075-2
38. Marsh, H., Rodríguez-Reinoso, F.: Activated Carbon. Elsevier Ltd (2006)

39. Gao, Y., Yue, Q., Gao, B., Li, A.: Insight into activated carbon from different kinds of chemical activating agents: a review. Sci. Total Environ. **746**, 141094 (2020). https://doi.org/10.1016/j.scitotenv.2020.141094
40. Yang, X., Ma, X., Wang, K., et al.: Eighteen-month assessment of 3D graphene oxide aerogel-modified 3D graphite fiber brush electrode as a high-performance microbial fuel cell anode. Electrochim. Acta. **210**, 846–853 (2016). https://doi.org/10.1016/j.electacta.2016.05.215
41. Champigneux, P., Delia, M.L., Bergel, A.: Impact of electrode micro- and nano-scale topography on the formation and performance of microbial electrodes. Biosens. Bioelectron. **118**, 231–246 (2018)
42. Sun, D., Chen, J., Huang, H., et al.: The effect of biofilm thickness on electrochemical activity of Geobacter sulfurreducens. Int. J. Hydrog. Energy. **41**, 16523–16528 (2016). https://doi.org/10.1016/J.IJHYDENE.2016.04.163
43. Chen, S., Patil, S.A., Brown, R.K., Schröder, U.: Strategies for optimizing the power output of microbial fuel cells: transitioning from fundamental studies to practical implementation. Appl. Energy. **233–234**, 15–28 (2019). https://doi.org/10.1016/J.APENERGY.2018.10.015
44. Gajda, I., You, J., Santoro, C., et al.: A new method for urine electrofiltration and long term power enhancement using surface modified anodes with activated carbon in ceramic microbial fuel cells. Electrochim Acta. **136388** (2020). https://doi.org/10.1016/j.electacta.2020.136388
45. You, J., Santoro, C., Greenman, J., et al.: Micro-porous layer (MPL)-based anode for microbial fuel cells. Int. J. Hydrog. Energy. **39**, 21811–21818 (2014). https://doi.org/10.1016/j.ijhydene.2014.07.136
46. Bian, B., Shi, D., Cai, X., et al.: 3D printed porous carbon anode for enhanced power generation in microbial fuel cell. Nano Energy. **44**, 174–180 (2018). https://doi.org/10.1016/j.nanoen.2017.11.070
47. Lorenzetti, M., Dogša, I., Stošicki, T., et al.: The influence of surface modification on bacterial adhesion to titanium-based substrates. ACS Appl. Mater. Interfaces. **7**, 1644–1651 (2015). https://doi.org/10.1021/am507148n
48. Gajda, I., Greenman, J., Melhuish, C., Ieropoulos, I.: Photosynthetic cathodes for microbial fuel cells. Int. J. Hydrog. Energy. **38**, 11559–11564 (2013). https://doi.org/10.1016/j.ijhydene.2013.02.111
49. Ieropoulos, I., Greenman, J., Melhuish, C.: Improved energy output levels from small-scale microbial fuel cells. Bioelectrochemistry. **78**, 44–50 (2010). https://doi.org/10.1016/j.bioelechem.2009.05.009
50. Gajda, I., Greenman, J., Melhuish, C., et al.: Electro-osmotic-based catholyte production by microbial fuel cells for carbon capture. Water Res. **86**, 108–115 (2015). https://doi.org/10.1016/J.WATRES.2015.08.014
51. Papaharalabos, G., Greenman, J., Melhuish, C., et al.: Increased power output from micro porous layer (MPL) cathode microbial fuel cells (MFC). Int. J. Hydrog. Energy. **38**, 11552–11558 (2013). https://doi.org/10.1016/j.ijhydene.2013.05.138
52. Ieropoulos, I.A., Stinchcombe, A., Gajda, I., et al.: Pee power urinal – microbial fuel cell technology field trials in the context of sanitation. Environ. Sci. Water Res. Technol. **2**, 336–343 (2016). https://doi.org/10.1039/C5EW00270B
53. Gajda, I., Stinchcombe, A., Greenman, J., et al.: Microbial fuel cell - a novel self-powered wastewater electrolyser for electrocoagulation of heavy metals. Int. J. Hydrogen Energy, 1–7 (2016). https://doi.org/10.1016/j.ijhydene.2016.06.161
54. Jadhav, D.A., Das, I., Ghangrekar, M.M., Pant, D.: Moving towards practical applications of microbial fuel cells for sanitation and resource recovery. J. Water Process Eng. **38**, 101566 (2020). https://doi.org/10.1016/j.jwpe.2020.101566

Chapter 4
Bridging Electronics and Micro Energy Storage

Alexander Masson, Federico Poli, Francesca Soavi, and Clara Santato

Abstract The development of small, smart and remote objects requires microscale components and energy autonomy. Activated carbon electrodes with high specific surface areas, achieving high electrical double layer capacitances present an opportunity to associate electronic components and energy storage. Transistors are a key element in any integrated circuit and the use of carbon gate electrodes has proven efficient to achieve low-voltage (sub-1 V) current modulation, reducing the energy required to operate them. Furthermore, the monolithic integration of an ion-gated transistor and a supercapacitor allowed to store and reuse up to 50% of the energy used to switch on the transistor. This paves the path to low-power, durable and autonomous devices able to function on small ambient energy harvesters and/or energy storage units.

Keywords Ion-gated transistors · Carbon electrodes · High surface area · Electrochemical energy storage

4.1 On-Chip Technologies for Autonomous Systems

Energy autonomy is a key issue for remote sensors, small robotics, and wearable and bio-medical devices that require ultra-small, flexible, and compact components.

In the home, autonomous sensors are at work in security systems, thermostats, and intelligent lighting systems. In the factory and in other mechanical applications, sensors powered by engine vibrations enable the detection of defects in parts before they break, reducing downtime. In agriculture, sensors are expected to be needed

A. Masson · C. Santato (✉)
Department of Engineering Physics, Polytechnique Montreal, Montreal, Canada
e-mail: clara.santato@polymtl.ca

F. Poli · F. Soavi
Department of Chemistry "Giacomo Ciamician", Alma Mater Studiorum Universita' di Bologna, Bologna, Italy

F. Borghi et al. (eds.), *Nanoporous Carbons for Soft and Flexible Energy Devices*,
Carbon Materials: Chemistry and Physics 11,
https://doi.org/10.1007/978-3-030-81827-2_4

to monitor soil temperature and acidity level, wind speed and direction, and other variables. The bio-medical sector will require great numbers of monitors of vital signs, such as blood pressure, glucose levels, and cardiac function [1–4].

To be autonomous, these devices must be coupled with ambient energy harvesters (EHs) (photovoltaic (PV), thermoelectric, piezoelectric) or energy storage units (ESUs, secondary rechargeable batteries, supercapacitors, and dielectric capacitors). EH power output typically fluctuates over time and is often lower than that required for continuous operation of devices like wireless sensors. ESUs can be used to buffer EH output discontinuities. However, the low voltage and power of EH require that ESU are tailored designed for an efficient energy storage. In addition, their leakage currents are higher than those of small EHs.

Vast numbers of sensors, ESUs, and EHSs will need to be coupled through the internet of things (IoT). To meet this need, considerable research is focused on the integration of multiple functionalities on a single chip i.e., Systems on a Chip (SoC). Due to their low-voltage operational characteristics, ion-gated transistors (IGTs) are attractive candidates to be coupled to energy harvester/storage microsystems [5–14].

This chapter concerns carbon-based materials and architectures for autonomous SoC. The low cost, abundance and facile processing routes make carbon an ideal candidate for these purposes.

4.2 Fundamentals of Capacitance

The value of capacitance (Eq. (4.1)), expressed in Farad (F), corresponds to the amount of charge (dQ) that can be stored over a potential difference (dV). For ideal systems, C is constant.

$$C = \frac{dQ}{dV} \tag{4.1}$$

When an electrode is polarized, charge carriers can distribute into the bulk of the electrode over a relatively large distance (screening length) that is inversely related to the charge carrier density; this is called the space charge region (SCR) and ranges between 0.1 nm to 1 μm in semiconductors [15]. On the electrolyte side, a compact layer of ions of opposite polarity, the inner Helmholtz plane (IHP), forms in close proximity to the electrode surface, while a diffuse layer, the outer Helmholtz plane (OHP), forms at larger distances.

With the formation of an electrical double layer (EDL) at the electrode/electrolyte interface, the charge is distributed with potential gradients developing in the SCR, IHP, and OHP regions. These three potential gradients (Fig. 4.1 Φ_C, Φ_H, and Φ_{diff}) generate three capacitive components (C_C, C_H, and C_{diff}) that are connected in series and contribute to the EDL capacitance (C_{dl}). For

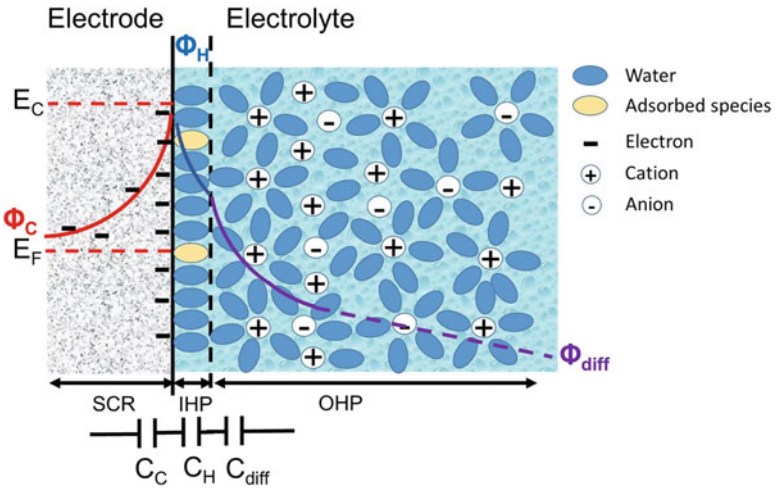

Fig. 4.1 Scheme of the electrical double layer at the electrode/electrolyte interface (for symbols, refer to main text). For electrolyte concentrations higher than 10^{-2} M, the typical total thickness of IHP and OHP is about 10 nm. EC and EF are the electrode conduction band edge and Fermi level, respectively. (Reproduced with permission from [16])

high conductivity electrodes and concentrated solutions, C_C and C_{diff} are high and the capacitance of the EDL is limited by C_H.

According to the Helmholtz model, for concentrated solutions (typically 1 M) the capacitance C_H is related to the surface area of the electrode (A) as stated in Eq. (4.2):

$$C_H = k_0 \varepsilon \frac{A}{\delta_{dl}} \tag{4.2}$$

where k_0 is the vacuum permittivity (8.85 10^{-12} F.m^{-1}), ε is the dielectric constant of the EDL region (that depends on solvent chemistry), and δ_{dl} is the thickness of the double layer (δ_{dl} is of the order of the nm). Carbon electrodes with a specific surface area up to 2000 m^2.g^{-1}, have a specific double layer capacitance in the order of 100–150 F.g^{-1}. Pore size and distribution in the electrode play an important role in the formation of the EDL. An optimal combination of micropores (< 2 nm), mesopores (2–50 nm), and macropores (> 50 nm) in the electrode structure minimizes ion transport resistance and maximizes the capacitance of the EDL. In the same way, ionic composition and concentration of the electrolyte are important parameters.

Faradaic (redox) processes bring about a higher charge accumulation at the IHP, paralleled by the increase of C_H with respect to the case of ideally polarized electrodes. When the redox processes are reversible, and determine the electrochemical signature of capacitive electrodes, i.e. they exhibit a linear dependence of the charge

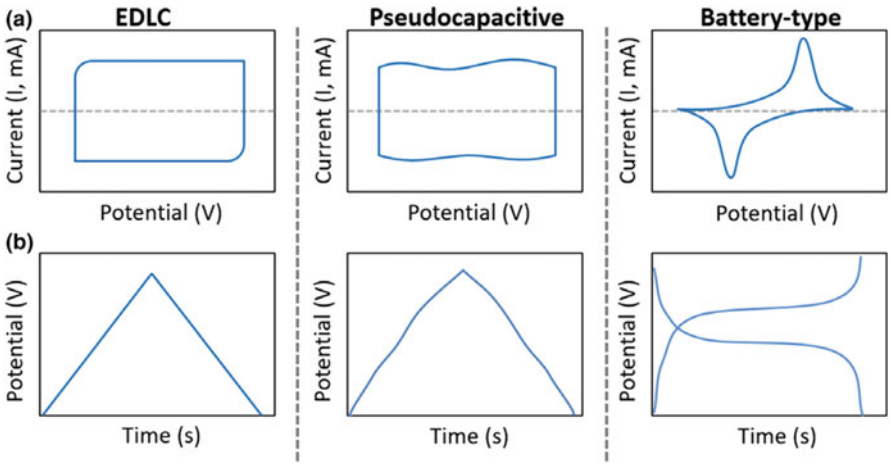

Fig. 4.2 Cyclic voltammetry and galvanostatic charge/discharge profiles of EDLC, pseudocapacitive, and exclusively faradaic battery-type electrodes. (Adapted with permission from [18])

stored with the width of the potential window (Fig. 4.2b), the electrodes can be defined as "pseudocapacitive" [17, 18].

Typical examples of pseudocapacitive materials are transition metal oxides (e.g. MnO_2 or RuO_2), and electronically conductive polymers (e.g. polythiophenes).

As for EDL capacitance, pseudocapacitance also depends on specific chemical interactions between the electrode material and electrolyte ions and accessibility of the electrode surface [19].

Capacitive, pseudocapacitive, and battery-type (exclusively faradaic) electrode materials are used in supercapacitors [20].

Different classes of supercapacitors making use of electrodes of different nature have been investigated. The most common supercapacitors are electrochemical double-layer capacitors (EDLCs) that use high surface area carbon electrodes, which store/deliver charge by an electrostatic process (no charge transfer occurs at the electrode surface). Pseudosupercapacitors feature electrodes (e.g., electronically conducting polymers and metal oxides) that are charged/discharged by fast and reversible redox processes. Pseudocapacitive electrodes provide electrochemical responses similar to those of high surface area carbons, i.e. box-shaped voltammetries and triangular galvanostatic charge/discharge profiles. Unlike pseudocapacitve electrode, battery-like electrodes feature the typical response of solid-state battery electrodes. Hybrid supercapacitors feature positive and negative electrode materials of different nature that are charged/discharged via different electrostatic and faradaic mechanisms.

High specific energy is achievable in supercapacitors by high capacitance values (C) and cell voltage which are dependent on the carbon electrode porosity and nanostructure, the electrochemical stability window of the electrolyte, and in the

case of pseudo or hybrid capacitors, the operating stability of the electrodes. The maximum specific energy E_{max} is:

$$E_{max} = \frac{1}{2}\frac{C(V_{max})^2}{m_{sc}} \tag{4.3}$$

where V_{max} is the maximum cell voltage and m_{sc} is the total electrode mass.

Further, high specific power is achieved at low ESR (equivalent series resistance), which in turn depends on the conductivity of the electrolyte, the electronic resistance of electrode materials, the interfacial resistance between the electrode and the current collector, Mhe ionic resistance of ions migrating and diffusing through small pores of the electrode. The maximum specific power P_{max} is:

$$P_{max} = \frac{1}{4}\frac{(V_{max})^2}{ESR\ m_{sc}} \tag{4.4}$$

The best performing commercially available EDLCs operate in organic electrolytes and feature $E_{max} < 5$ Wh.kg^{-1}, $P_{max} < 10$ kW.kg$_{-1}$, and $V_{max} < 2.7$ V [21].

4.3 Fundamentals of Transistors

The first transistor was fabricated in 1947 by John Bardeen, Walter Brattain, and William Shockley of Bell Labs who were jointly awarded the 1956 Nobel Prize in Physics [22]. Since then, transistors have continuously improved, and their size miniaturized to micro and nanometre scales. Gordon Moore proposed, in 1965, the empirical observation that the number of transistors in an integrated circuit doubled every year [23]. This concept, called Moore's law, is verified even today and modern smartphones are composed by over 11 billion transistors smaller than 5 nm [24].

Transistors are three-electrode devices acting as switches and amplifiers. A transistor consists of a semiconducting channel, three electrodes, and a gating medium (Fig. 4.3).

A semiconducting material has conductivity values (ranging from 10^{-6} to 10^4 S.cm^{-1}) between that of a conductor (metal) and an insulator (glass), and that value can be altered by doping to create an accumulation (or depletion) of positive (p-doping) or negative (n-doping) charge carriers in the semiconductor.

The three electrodes of a transistor are: source and drain electrodes, where charge carriers are injected into (or extracted from) the semiconducting transistor channel, and the gate electrode, where an electrical bias can be applied to modulate the doping, thus the conductivity, of the channel. The gating medium can consist of a wide range of dielectric materials, e.g. SiO_2 or HfO_2, or, in the case of ion-gated transistors (IGTs), ionic media, like aqueous saline solutions or ion gels [25]. The

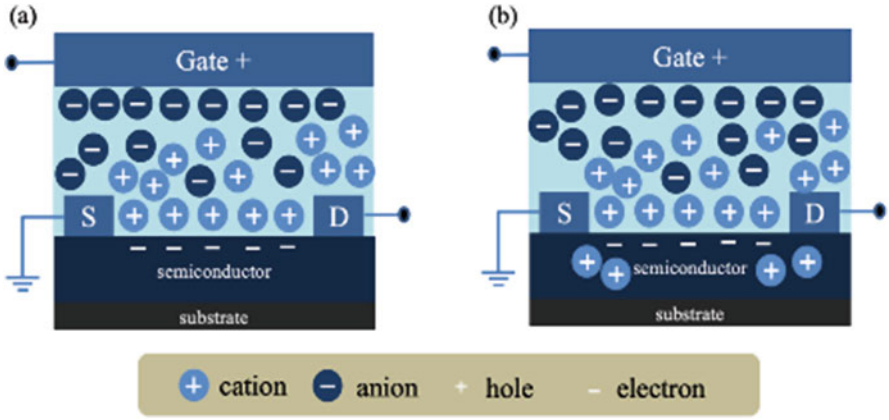

Fig. 4.3 Working mechanisms of IGTs: (**a**) in a purely electrostatic IGT ions from the gating medium do not penetrate the semiconductor channel but create a strong electric field at the interface, (**b**) in electrochemical IGTs doping (or de-doping) is achieved by permeation of ions in the semiconductor

gating medium is electronically insulating [7, 26]. IGTs exploit EDLs forming at the interface between the ionic medium and the channel, to modulate the electrical conductivity in the transistor channel. The high capacitance of thin EDLs (ca. 2–4 nm thick) enables high charge carrier density in the channel (ca. 10^{14} cm^{-2}), at operating voltages as low as 0.5 V [27].

As shown in Fig. 4.3, upon applying a potential to the gate electrode of the IGT, cations and anions preferentially distribute at the gate electrode/gating medium and gating medium/semiconductor interfaces doping the semiconductor through two possible mechanisms. A purely electrostatic IGT will behave as a field-effect transistor (FET), meaning that the accumulation of ions at the gating medium/semiconductor interface will create a strong electrostatic field that will attract charge carriers of opposite polarity in the semiconductor, modifying the charge carrier density. In an electrochemical transistor, ions reversibly permeate the gating medium/semiconductor interface and dope the semiconducting channel [7, 26].

Oxygen atom migration created by strong electric fields between the ionic liquid and the metal oxide channel have been invoked, as probed by X-ray photoelectron spectroscopy, to explain the working mechanism of IGTs making use of metal oxide channels [28].

Independent of the specific working mechanism, the arrangement of the ions upon application of an electrical bias at the gate electrode is an essential factor in establishing the behavior of IGTs. Fundamental aspects pertaining to such arrangements are complex and still under study. The complexity stems from the number of interactions, from electrostatic to van der Waals, contributing to the buildup of the ionic arrangement, possibly in the form of interfacial ionic layering [29].

Organic electrochemical transistors (OECTs) were first reported by Wrighton et al. [30] and have attracted growing attention for flexible electronic and bioelectronic applications, including synaptic devices [29]. OECTs are investigated in bioelectronics because of their low operating voltage, compatible with the electrochemical stability window of aqueous media, where biological processes take place [31]. Furthermore, the mechanical stability of OECTs, due to the softness of organic materials, make them particularly compatible with human tissues compared to rigid devices [32]. IGTs have been implanted in the human body [5, 33] and used for pH sensing through the presence of an analyte in the gating medium that affects the electrical response of the IGT [34, 35]. They have also been used to study electrophysiological signals from the human brain exploiting as signal the transistor transconductance (the change in source/drain current created by a small variation in the applied gate voltage) [36].

The use of dissolved ions in aqueous solvent at very low operational voltages in particular enables great biocompatibility and allows a wide range of in vivo applications [33].

Ionic liquids present a variety of properties that make them interesting candidates for IGT applications. They consist of salts with a relatively low fusion point (generally below 370 K) and are generally chemically and electrochemically stable, presenting optical transparency and low volatility. Ionic liquids can be created using a great pool of anions and cations; tailoring each pair allows a choice of interactions, such as electrostatic, van der Waals, and hydrogen bonding. This ensures the cohesion of the liquid impacting the physicochemical properties including ionic conductivity and viscosity. Finally, the use of a solvent allows further modification of the main interactions and properties [31].

The main technical challenge associated with ionic liquids is their outflow. The liquid state of these salts can cause packaging, portability, and leakage problems. Ion gels combine ionic liquids with polymers or inorganic materials to effectively immobilize them in a quasi-solid state by mixing the ionic liquid with the solid matrix or growing the matrix in situ. Ion gels are very stable over time and are resistant to pressure and temperature changes while keeping the properties of the original ionic liquid intact, making them ideal candidates for ion- gating media [37].

While the properties of ion gating media have been extensively studied, the specific role played by the gate electrode remains unclear. Most OECT devices rely on Pt, Au, Ag, or Ag/AgCl and patterned PEDOT:PSS for the gate electrode, but their respective impacts on device performance have yet to be investigated in depth [38, 39]. Using a Pt wire gate electrode with a polyacetylene ionomer based OECT, Lin et al. [40] studied the effect of the gate electrode geometric area on the performance of the device. They found that an increase in the capacitance of the gate electrode led to increased current modulation for comparable voltages. Cicoira et al. [41] studied the impact of faradaic reactions at the gate electrode by comparing Pt and Ag gate electrodes for PEDOT:PSS-based OECTs using halide electrolytes. The reaction between Ag electrode and halide electrolyte is proposed as the cause of the higher current modulation by Ag compared to Pt, for the same gate voltage.

4.4 Carbon Processing for Flexible Electronics

Deposition of electrochemically active materials on flexible substrates for energy storage and electronics has attracted growing attention due to the advent of wearable electronics [42–44], flexible displays [45], and medical applications for monitoring patient health [46]. Due to its electronic and mechanical properties, carbon is an ideal candidate for low-cost, environmentally friendly, flexible electrodes on strings [42, 47], substrates [48–50], or freestanding [51, 52]. In what follows, we explore deposition and fabrication techniques for flexible carbon electrodes.

Carbon presents multiple dimensionalities: from 1D carbon nanotubes (CNTs) to 2D graphene sheets and 3D carbon foams. These three possible dimensionalities for carbon technologies make them excellent candidates for a variety of electrodes.

4.4.1 Introduction to Microfabrication and Patterning of Electronic Devices

Microfabrication aims at creating micro and nanometre scale devices using precise, tunable, and reproducible techniques. These methods can be classified in three main categories depending on whether they add, shape, or remove materials. Most of the time, the device is constructed in a step-by-step process that builds a film on a rigid substrate (wafer) to ensure good stability during fabrication, followed by peeling off the film to achieve flexibility. In the following paragraph we give an overview of a few microfabrication techniques [53].

Additive techniques are used to deposit a new layer of material. This can be the active material that will then be patterned to comply with the desired device properties, or a secondary layer used to protect or shape the surface for a following step. A great variety of these additive techniques exist depending on the deposited material [54–56].

Spin-coating consists of initially drop-casting a small quantity of viscous fluid material on a substrate, followed by spinning to ensure homogeneity of film thickness and surface (step c of Fig. 4.4). The technique is suitable for deposition on flat surfaces of materials that can be incorporated in viscous solutions at room temperature; through drying or gentle thermal treatment the spin-coated films become solid. By adjusting the viscosity of the solution, volume of solution, and rotation speed and time, the thickness of the film can be tailored. This method is often used to deposit photoresist layers used for patterning and lift-off steps, as the thickness of the layer does not need to be extremely precise [57, 58].

Physical vapor deposition and chemical vapor deposition (PVD and CVD) are techniques used to create very uniform films whose thickness is precisely known and can be controlled by depositing materials directly on the wafer under vacuum conditions. Both methods use vapors of the material they wish to deposit to achieve controlled growth on the substrate. However, they present a few key differences:

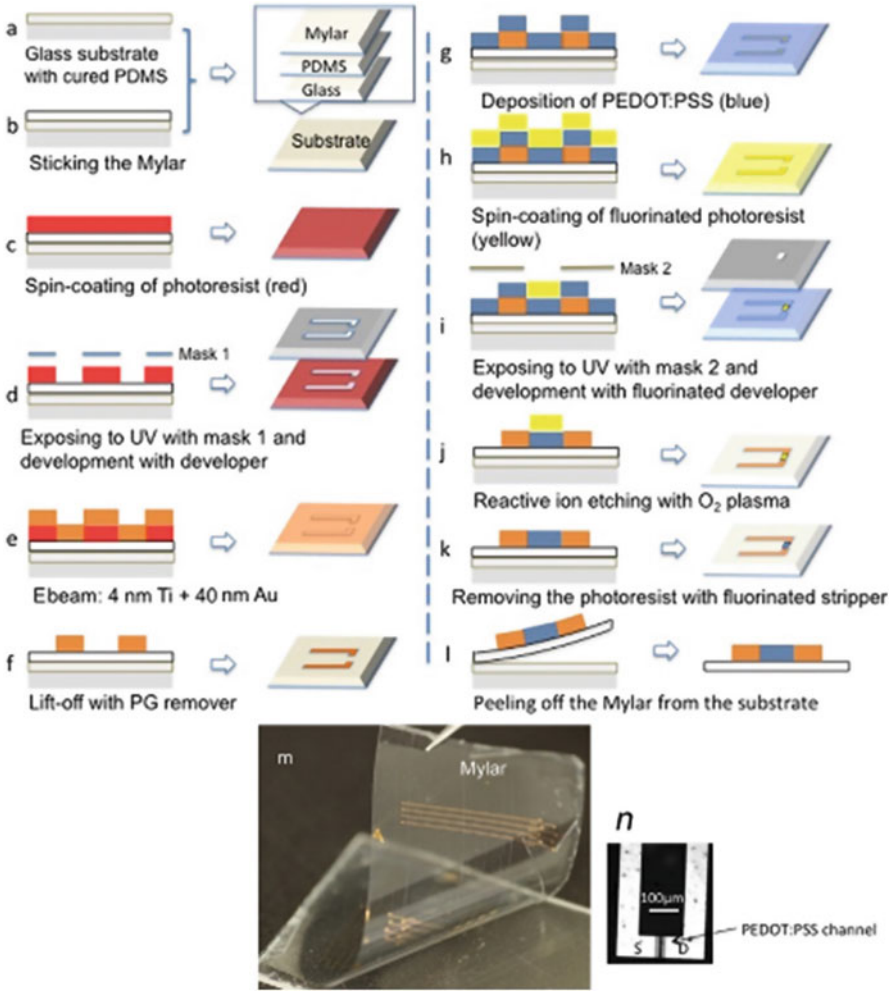

Fig. 4.4 The microfabrication process of a flexible transistor on polyethylene terephthalate (Mylar). (Reproduced with permission from [74])

PVD uses a solid material that is sublimed to allow its atoms to diffuse to the surface of the wafer at relatively low temperatures (500–700 K), whereas CVD materials are in gaseous form and react on the surface of the wafer to create the desired thin film at higher temperatures (700–1300 K). PVD comprises a wide range of techniques depending on the method used to sublime the material. Simple heating under vacuum is sometimes sufficient. Electron beams or plasma beams can also be used to bombard the material and eject its atoms (this is called sputtering deposition). PVD and CVD techniques have been used to grow ordered, flexible carbon thin films (step e of Fig. 4.4) [59–62].

Patterning methods are used to imprint a precise structure on the active material. Two main categories of patterning exist: optical and physicochemical. Optical methods use photoresists and light exposure to transfer the desired pattern from a mask to the thin film. Photoresists change molecular structure upon exposure to UV light leaving the pattern on selected regions of the wafer's outer layer (steps d and i of Fig. 4.4). The advantages of optical methods are rapidity and reproducibility; a single photomask can pattern a great number of devices with only a few minutes' exposure each. By choosing positive or negative photoresists, either the unexposed or exposed areas can be removed. This can be done in series or for several devices at a time. Simple optical methods reach the limit of their resolution as light diffraction at the mask creates a physical barrier of precision at about 2 μm for simple contact or proximity techniques, but that can be reduced to 200 nm using optical lenses (projection technique) and even 20 nm using X-rays instead of UV light [63–65].

Examples of high-resolution techniques include direct electron-beam lithography and nanoimprinting. Electron-beam lithography uses a focused electron beam to directly etch the desired pattern on the thin film, fully automated and without needing a mask, thus solving diffraction problems. Focused beams can achieve 10 nm resolution but is a trade-off for a much slower process [66]. Nanoimprinting uses solid molds to directly impress the desired pattern with a resolution that can reach 10 nm [67, 68].

Once the desired pattern has been transferred to the photoresist, one can choose from a few different removal techniques. Undesired layers can simply be peeled off (step l in Fig. 4.4) or removed by chemical or physical etching, namely wet and dry [53].

Physical dry etching is achieved by accelerating ions towards the surface under inert gas atmosphere. Chemical dry etching uses reactive gases that will remove the desired material through chemical reactions. These physical and chemical methods can also be combined. Wet etching is used for metals or silicon through oxidant or reducing solvents. Metals are oxidized ($M \rightarrow M^+ + \text{electron}$) and then can freely diffuse in solution. Silicon is a special case as the silicon-oxygen bond is very strong, requiring HF acid, leading to SiF_6 [69, 70].

In some cases, direct nanoprinting can conveniently replace these adding-patterning-etching steps, but not all materials can be printed, and each new material requires a custom-made ink. More details on nanoprinting can be found in [71–73].

4.4.2 One-Dimensional Flexible String Electrodes

One-dimensional string-like electrodes can be integrated in wearable electronics without altering the comfort or the texture of the fabric by knitting electrodes into the textiles [47]. There are two main approaches to the creation of durable, flexible, and resistant fiber electrodes: coaxial yarn electrodes [42] and deposition on an existing flexible and robust thread to make use of its mechanical properties [47, 48].

Wang et al. [42] have described the fabrication of a coaxial yarn asymmetric supercapacitor using CNT-MnO_2 composites and Fe_2O_3 on carbon fiber to achieve high energy densities (about 30 $Wh.kg^{-1}$) by introducing redox activity. Flexible CNT-MnO_2 nanosheets were constructed by floating catalyst-assisted CVD for CNT films, followed by immersion in $KMnO_4$ aqueous solution. The resulting composite was cut into strips and twisted into strong yarns (a single yarn resulting from a 5-mm-wide strip could hold 50 g) later coated in lithium-based electrolyte. The negative electrode made from Fe_2O_3 deposited on carbon fiber through a $FeCl_3$ aqueous solution was then rolled around the positive one creating an asymmetric supercapacitor.

Other techniques to create freestanding 1D carbon-based electrodes include wet-spinning [75] and dry-spinning of CNTs [76].

Another approach to fabricating resistant and flexible electroactive threads consists in coating metal fibers, cotton threads, rubber fibers, elastic polymers, and carbon fibers [77–79] using simple dipping-drying [77] or hydrothermal [47] methods. These methods have the advantage of making use of the mechanical properties of the substrate. For instance, shape-memory supercapacitor threads [78]. Zhou et al. [47] reported the fabrication of a graphene oxide (GO) and CNT-based supercapacitor on cotton threads. The GO/CNT composite was deposited by dipping a bovine serum albumin coated cotton thread in an acidic (pH 3–4) GO/CNTs suspension and maintaining it at 450 K in an autoclave. The supercapacitor was fabricated by twisting two threads together after dipping them in a gel electrolyte to achieve good capacitance (about 100 μF/cm), electrical stability (95% capacitance retention after 8000 charge-discharge cycles), and mechanical stability (90% capacitance retention after 500 continuous bending cycles).

4.4.3 Two-Dimensional Flexible Thin Film Electrodes

Thin film electrodes are garnering considerable attention in the field of wearable electronics, flexible displays, and medical sensors, and a number of methods have been considered in the past decade, such as printing, spraying, and dipping [48, 51, 80].

Key challenges when processing carbon on flexible substrates are adhesion and electronic contact with the substrate throughout the patterning. Huang et al. [51] focused on silicon compatibility with carbon-derived thin films that concentrated on developing a wafer-scale magnetron sputtering technique with low energy densities. They deposited a titanium carbide (TiC) film several microns thick, followed by chlorination to create a carbide-derived-carbon film on the surface (after removal of titanium chloride) while maintaining the TiC current collector and adhesion with the silicon wafer.

Santato's group [50] worked on creating flexible electrodes by combining the electrochemical properties of carbon and bio-sourced redox molecules. Using a parylene C film, patterned by photolithography, they were able to construct a

carbon-black/melanin composite electrode on a gold/titanium current collector and polyethylene terephthalate (PET) flexible substrate. First, gold and titanium were deposited by electron beam evaporation, then a carbon-black/melanin slurry was drop casted on the wafer and the parylene C film was peeled off to achieve patterning of the carbon/melanin electrodes.

McCreery's group [49] reported a very stable (unchanged performance after 10^7 current-voltage cycles) and flat carbon electrode allowing for good molecular junction to create a gold/carbon/anthraquinone/carbon/gold (in vertical order) supercapacitor on (undoped) silicon and silicon oxide. Carbon was deposited on the gold contact through electron-beam evaporation, creating amorphous carbon with an extremely smooth surface (<0.4 nm root mean square roughness from atomic force microscopy measurements) and allowing for strong C-C bonds with anthraquinone. The group adapted the technique to achieve deposition on PET using chrome/gold contact to add flexibility and transparency to the supercapacitor.

Other vapor deposition techniques of carbon have been reported [48, 80]. PVD was used to deposit amorphous carbon on metal oxide-coated carbon cloth to achieve $NiCo_2O_4$/carbon composite flexible electrodes [80]. $NiCo_2O_4$ was deposited on carbon cloth through hydrothermal deposition followed by standard PVD of carbon on the coated cloth. The obtained electrode exhibits a 750 mAh/g capacity and could be used to replace graphene in lithium- or sodium-ion batteries.

Gogotsi's group studied spray coating techniques for titanium carbide MXene ($Ti_3C_2T_x$) and reduced graphene oxide (rGO) electrodes [81]. MXenes are two-dimensional inorganic compounds consisting of a-few-atoms-thick layers of carbides (carbon-metal), nitrides (nitrogen-metal) or carbonitrides (combination of both). For this process, a mask was used to successively spray rGO and $Ti_3C_2T_x$ with a hot air gun to ensure quick drying of a pre-patterned structure on PET substrate. These two asymmetrical electrodes were covered by a gel electrolyte to form a supercapacitor bendable up to 90°, exhibiting 97% retention after 10,000 cycles and an energy and power density of 8.6 mWh/cm^3 and 0.2 W/cm^3. Spray coating methods are attractive due to their simplicity, scalability [81], amenability to deposition on non-flat surfaces and precise control of the amount deposited [82]. By controlling the physical and chemical parameters of deposition properties, such as wettability of the substrate, spraying pitch, height of nozzle, and gas flow rate, uniformity and density of the deposition can be controlled [82].

Printing techniques have been studied to facilitate automatic and large-scale device manufacturing [46, 83]. However, printing techniques, such as inkjet and aerosol printing, require pre-processing and thermal post-processing that are not suitable for all materials. Gandhiraman et al. [46] reported an atmospheric pressure printing technique for multi-walled carbon nanotube (MWCNT) electrodes on commercial paper. Standard aerosol printing was enhanced by plasma to improve density of MWCNTs on a paper substrate and a dielectric barrier was used to reduce the temperature at the nozzle to adapt to the lower glass transition temperature of MWCNTs. Improved printing techniques can produce a complete supercapacitor instead of a simple electrode. Direct ink writing can be used to print a single-walled

carbon nanotube (SWCNT) supercapacitor without mask, transfer, and alignment steps, thus increasing productivity [83]. SWCNTs were dissolved in deionized water with sodium n-dodecyl sulfate surfactant and the direct ink writing was conducted by layer-by-layer deposition through a needle close to a moving platform.

4.4.4 Three-Dimensional and Freestanding Flexible Electrodes

3D carbon-based electrodes make use of microporous flexible materials such as sponges [48] or porous carbon [84] to coat macropores in the active material of interest. Wu et al. [84] reported on a flexible 3D carbon electrode based on the pyrolysis of pomelo peels to achieve a honeycomb-like structure onto which were coated rGO and CNTs to produce a hybrid carbon film (Activated Carbon/rGO/CNTs) presenting high specific capacitance of 214 F/g.

A different approach to making flexible carbon-based electrodes is to take advantage of the mechanical properties of carbon and construct freestanding electrodes instead of relying on deposition on a substrate. The carbide-derived carbon (CDC) electrode constructed by Huang et al. [51] can be further chlorinated up to complete consumption of the titanium carbide layer to be able to peel off the CDC layer, making a freestanding flexible carbon electrode.

Other approaches are even more direct and make use of the flexible properties of some forms of carbon, such as graphene sheets [85]. Graphene sheets were used as a base for freestanding carbon-based electrodes by creating a graphene/polymer composite via in situ anodic electropolymerization of aniline onto graphene paper to overgrow a polyaniline (PANI) thin film. The resulting composite sheet exhibited remarkable flexibility, tensile strength, and excellent specific capacitance (233 F/g) due to very lightweight materials and the absence of a substrate.

Cheng et al. [52] used three-step carbonization of a graphene/PANI to create a richly nitrogen-doped flexible freestanding electrode. The three-step pyrolysis was conducted by progressively heating a furnace to 420 K under argon atmosphere for 5 h, followed by a slow warming to 720 K before progressing to 970 K for 3 h. This slow carbonization allowed for strong nitrogen doping (10%) bringing about increased energy density even under 180° bending.

Several other techniques have been developed to create freestanding carbon electrodes adapted to a variety of dimensionalities. String-like electrodes were obtained by wet [75] and dry [76] spinning of CNTs, thin film electrodes have been created by vacuum filtration [86], casting of carbon ink followed by peeling off the film [87], CVD [88], and dry drawing [89].

4.5 Ion-Gated Transistors (IGTs) and Advantages of Using Carbon-Based Gate Electrodes in IGTs

A number of channel materials have been used in IGTs and depending on their nature, different doping mechanisms have been taken into account. IGTs making use of organic polymers mainly rely on faradaic doping. In this case, the charge and pseudocapacitance stemming from the doping surpasses those of electrostatically doped, non-porous materials by about two orders of magnitude. In these polymer channels, current modulation is achieved by varying the doping level. The faradaic nature of this doping depends on the electrochemical potential of the channel. Thus, careful monitoring of the channel potential is crucial to the optimization of current modulation in polymer IGTs and requires an additional reference electrode. The potential of the channel must be compatible with the electrochemical stability window of the electrolyte.

IGTs have also made use of a wide range of gate electrode materials., The impact of the nature of the material on the performance of the device is yet to be fully understood and is at the heart of recent studies [41, 90]. Nevertheless, it is possible to improve the device stability by using certain gate electrode materials to limit undesirable electrochemical reactions. Furthermore, high specific surface area in gate electrodes permits to achieve high current modulations in organic polymer channels that are prone to bulk electrochemical doping. These electrodes have high double layer specific capacitances enabling them, within a narrow potential excursion, to supply a non-limiting charge to efficiently dope organic polymer transistor channels. The charges are stored via highly reversible fast, electrostatic processes following $Q = mC\Delta V$, where m the mass of the electrode material, Q is the stored charge, C the specific capacitance (optimized high surface area carbon can reach ca. 100–200 $F.g^{-1}$) and ΔV the potential excursion of the electrode.

4.5.1 Enabling Low Voltage and Simple Design

Activated carbons are ideal gate electrode materials for IGTs. Indeed, their high gravimetric and areal capacitance permits them to store electrostatically and within a relatively low ΔV (a few hundreds of mV), the amount of charge required to effectively dope the channel. Furthermore, the low ΔV permits the carbon gate electrode to act as a quasi-reference electrode. High surface area activated carbon gate electrodes present an interesting opportunity to lower the voltage required for channel modulations. Nevertheless, low-voltage IGTs require a compatible redox activity of the channel material that must take place at sufficiently low potentials vs. the quasi reference carbon electrode [14].

We reported on an ionic liquid-gated organic transistor based on MEH-PPV semiconducting polymer for the channel and activated carbon for the gate electrode (Fig. 4.5) [91].

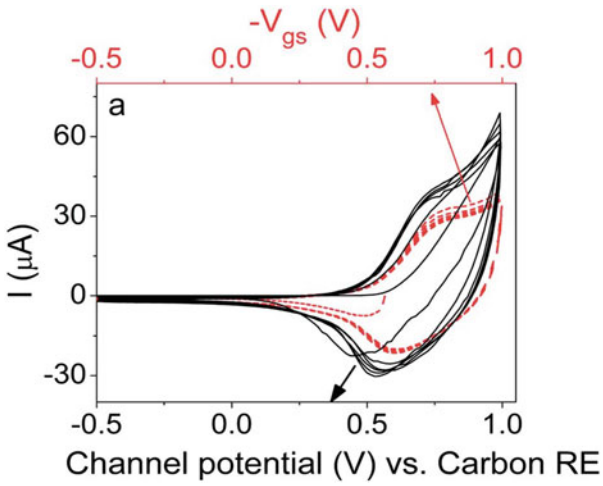

Fig. 4.5 Electrochemical characteristics of [EMIM][TFSI]-gated MEH-PPV transistors. Cyclic voltammetry at 50 mV.s-1 obtained using the polymer film as the working electrode, the activated carbon gate electrode as the counter electrode and i) a second activated carbon electrode as the quasi-reference electrode (black, solid line) or ii) the carbon gate electrode itself as both the counter and the quasi-reference electrode (red dotted line). In the latter case, the potential of the transistor channel corresponds to Vgs (the gate–source voltage). (Reproduced with permission from [91])

The channel/ionic medium/gate stacking of IGTs can be viewed as a 2-electrode electrochemical cell where $|V_{gs}|$ is the difference of the gate (V_{gate}) and channel (V_{ch}) electrode potentials (vs. a given reference).

$$\left|V_{gs}\right| = \left|V_{gate} - V_{ch}\right| \tag{4.5}$$

The potential difference of the gate electrode vs. channel material (and vice versa) has to be properly set to optimize current modulation in IGTs based on redox channels.

When a V_{gs} bias is applied, both channel and gate electrode potentials change as described in Fig. 4.6. Eq. (4.5) suggests that even the electrochemical behavior of the gate is affecting IGTs' current modulation. Developing low voltage (low V_{gs}) IGTs, positively affecting power consumption and device stability, requires that the redox activity of the channel takes place at low potentials vs. gate potential (i.e. $V_{ch} \cong V_{gate}$), and that channel and gate potential excursions are as narrow as possible. Being a bulk process, the doping of redox channels involves a high doping charge ($Q_{ch.}$) and pseudocapacitance (C_{ch}), which can be up to two orders of magnitude larger than those involved in the electrostatic polarization of a flat surface/ionic medium interface. Channels with high pseudocapacitance ($C_{ch} \cong$ 100–200 $F.g^{-1}$) typically exhibit narrow ΔV_{ch}:

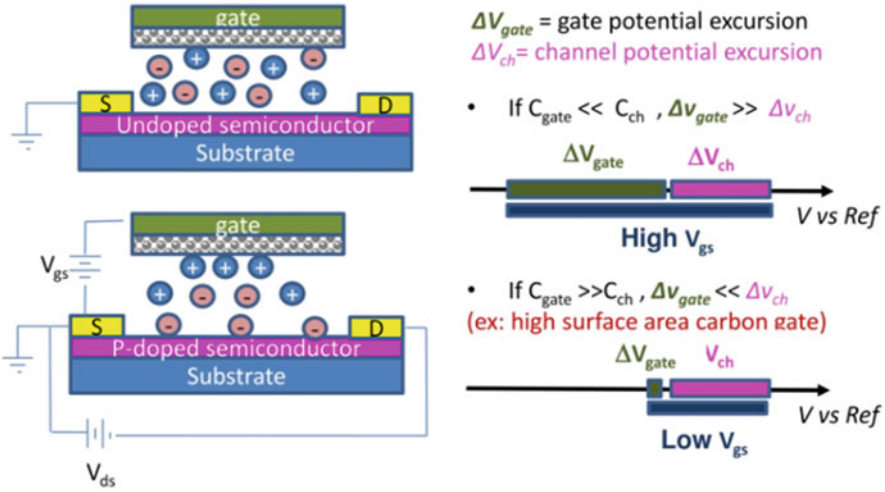

Fig. 4.6 Schematic description of the effect of the gate capacitance (C_{gate}) on the operation of low-voltage IGTs. (Reproduced with permission from [92])

$$C_{ch} = \frac{Q_{ch}}{\Delta V_{ch}} \tag{4.6}$$

The channel doping charge has to be counterbalanced by the gate, i.e.:

$$Q_{ch} = Q_{gate} \tag{4.7}$$

and

$$C_{ch}\Delta V_{ch} = C_{gate}\Delta V_{gate} \tag{4.8}$$

Conventional metal gates like Pt, of low gate capacitance (C_{gate}), are not capable of effectively counterbalancing the doping processes occurring at redox channels within a narrow ΔV_{gate}. On the other hand, gate electrodes based on high surface area carbons with high double-layer capacitance ($\cong$ 100 $F.g^{-1}$), can store/deliver a noticeable amount of charge Q_{gate} by a fast and reversible electrostatic process within a relatively low $\Delta V_{gate.}$, thus enabling an overall narrow ΔV_{gs} [92]. These concepts are described in Fig. 4.6.

Tang et al. (Fig. 4.7) used an activated carbon (AC) gate electrode in an OECT and proved it can provide large current modulation with low voltages and act as a replacement for the reference electrode used to monitor the channel potential. They concluded that the very high double layer capacitance of the AC electrode and its intrinsic property to act as quasi-reference were responsible for the behavior [39]. Indeed, cyclic voltammetry (CV) shows that the high specific capacitance of the AC counter electrode (CE) permits the potential excursion of the CE to be kept within a few tenths of mV during PEDOT:PSS doping/dedoping. The overlap of

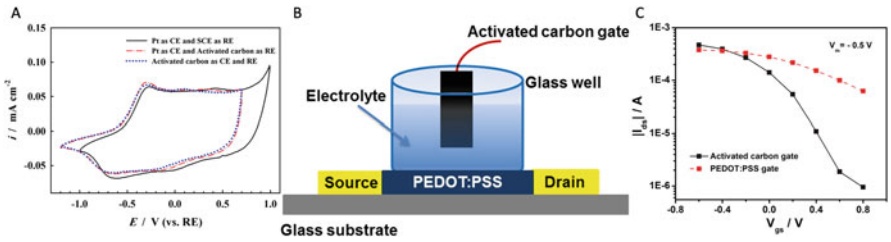

Fig. 4.7 (**a**) Cyclic voltammograms where a doped (pristine) PEDOT:PSS film acts as the working electrode (WE), and different counter electrodes (CE) and reference electrodes (RE) are compared. The electrolyte is a 0.01 M aqueous solution of NaCl. Solid black line: three-electrode configuration with a Pt wire CE and a saturated calomel electrode (SCE) RE; red dashed curve: three-electrode configuration with a Pt wire CE and an AC electrode RE; blue dotted curve: two-electrode configuration with an AC electrode acting as CE and RE. (**b**) Scheme of the architecture of OECTs using an activated carbon (AC) gate electrode and a conducting polymer channel made of PEDOT:PSS. (**c**) Transfer characteristics of PEDOT:PSS OECTs using an AC (black line) and a PEDOT:PSS gate electrode (red line). (Reproduced with permission from [39])

the CV curves in Fig. 4.7a indicates that the AC electrode is able to effectively dope/dedope the PEDOT:PSS channel, while simultaneously acting as a quasi-reference electrode. When the CV is performed in a two-electrode configuration (Fig. 4.7a, dotted blue curve), the potential applied between the working electrode (PEDOT:PSS) and the AC quasi-reference corresponds to $-V_{gs}$ in PEDOT:PSS OECTs making use of an AC gate electrode. Therefore, our results indicate that a V_{gs} range between -0.6 to $+0.8$ V enables safe switching of the OECT from the ON to the OFF state (Fig. 4.7c).

4.5.2 *Monolithic Integration of Supercapacitor and Ion-Gated Transistor: TransCap*

In what follows we try to evaluate the energy and power required to operate IGTs. The energy required to drive IGTs (E_{IGT}) consists of two terms: that required to dope the channel (E_{gs}) and that required for the source/drain current to flow through the channel (E_{ds}) over a certain time (t), i.e.:

$$E_{IGT} = E_{gs} + E_{ds} \tag{4.9}$$

The doping energy is related to V_{gs} and Q_{ch} by:

$$E_{gs} = \left| V_{gs} Q_{ch} \right| \tag{4.10}$$

This is why low-V_{gs} IGTs are promising for low-power devices.

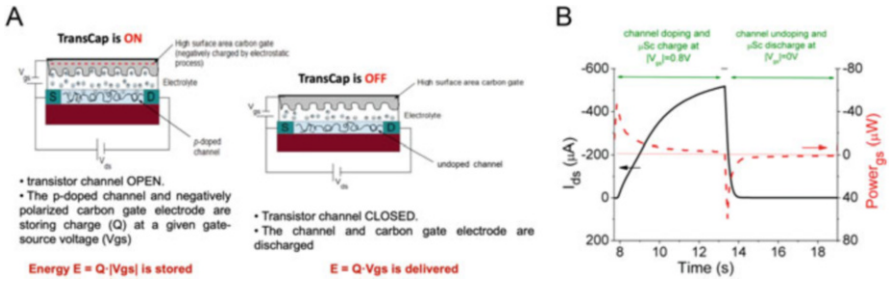

Fig. 4.8 (**a**) Scheme of the ON/OFF switching mechanism and (**b**) evolution of I_{ds} and P_{gs} as a function of time for charge (ON) and discharge (OFF) conditions of the TransCap. For meaning of symbols, please refer to the main text. (Reproduced with permission from [14])

E_{ds} depends on the power flowing through the channel, in turn related to I_{ds}, and t:

$$E_{ds} = P_{ds}t \tag{4.11}$$

where:

$$P_{ds} = |I_{ds}V_{ds}| \tag{4.12}$$

Table 4.1 reports the energy and power of IGTs making use of organic polymer and inorganic semiconductors as the channel materials, ionic liquids, possibly mixed with propylene carbonate, as the gating media, and high surface area carbon gate.

The channel/ionic medium/gate stacking of IGTs can be viewed as a 2-electrode electrochemical cell where the capacitive channel and carbon gate components reversibly store charge at given V_{gs}. Specifically, the channel/ionic medium/carbon gate stacking is analogous to that of a hybrid supercapacitor where channel and gate electrodes are charged/discharged by a faradaic and an electrostatic process, respectively. This means that E_{gs} used to dope the channel is stored and then is ready to be delivered when the IGT is switched OFF. The percentage of stored energy can be described as $E_{stored} = 100\ E_{gs}/E_{IGT}$ (Table 4.1). I_{ds}, I_{gs}, and the IGT power demand depend on geometric parameters like channel thickness and area.

Table 4.1 also shows the performance of a TransCap, a device which seamlessly integrates an IGT and a micro-supercapacitor [14]. The TransCap whose characteristics are shown in Table 4.1 featured an MEH-PPV channel, a gate based on an AC layer deposited on carbon paper, and the ionic liquid N_{1113}TFSI as gating media [14]. Figure 4.8b shows the power stored upon channel doping ($P_{gs} = I_{gs}\ V_{gs}$) and delivered upon channel dedoping. The integration of P_{gs} over time provides E_{gs} of ca. 0.02 μWh stored during switch ON and delivered with an efficiency of 99.5%.

Furthermore, the storage capability of the TransCap permits the transistor channel to be kept open even when the transistor is not connected to a power supply. This storage capability can be affected by the presence of leakage currents, resulting in discharging of the device. This was demonstrated by an [N_{1113}][TFSI]-gated

Table 4.1 Electrical and energy characteristics of IGTs and TransCap making use of high surface area carbon gate and ionic liquid-based gating media. Q_{ch} is the doping charge obtained from the voltammetric scan of V_{gs} up to the value reported in the table during the transfer curve at a V_{gs} sweeping rate of 10 $mV.s^{-1}$; the ON/OFF ratio is deduced from the forward sweep of the transfer curves. I_{ds} is the saturation current flowing through the channel at the V_{ds} shown in the table and evaluated by the output curves at the highest $|V_{gs}|$. E_{ds} is calculated for 5 s switch-on time. For TransCap, the Q_{ch} and energy and power values have been obtained from Fig. 4.8b

Channel	Ionic liquid	$\|Q_{ch}\|$ μC	$\|V_{gs}\|$ V	ON/ OFF	I_{ds} μA	$\|V_{ds}\|$ V	E_{gs} μWh	P_{ds} μW	E_{ds} μWh	E_{EGT} μWh	E_{stored} %
EGT											
MEHPPV	EMIMTFSI	170	1.0	$2–3.10^3$	1200	0.25	0.05	300	0.40	0.45	11
	BMIMTFSI	230	1.0	$2–3.10^3$	2500	0.25	0.07	625	0.80	0.87	8
	$PYR_{14}TFSI$	180	1.0	$2–3.10^3$	1200	0.25	0.05	300	0.40	0.45	11
	PC-$PYR_{14}TFSI$	95	1.0	$1.8.10^3$	170	0.15	0.03	25	0.03	0.06	50
WO_3	$PYR_{14}TFSI$	300	1.2	100	500	0.7	0.10	350	0.49	0.59	17
TransCap											
MEHPPV	$N_{1113}TFSI$	70	0.8	2.10^3	500	0.3	0.02	150	0.2	0.22	9

Adapted with permission from [14, 91, 93]

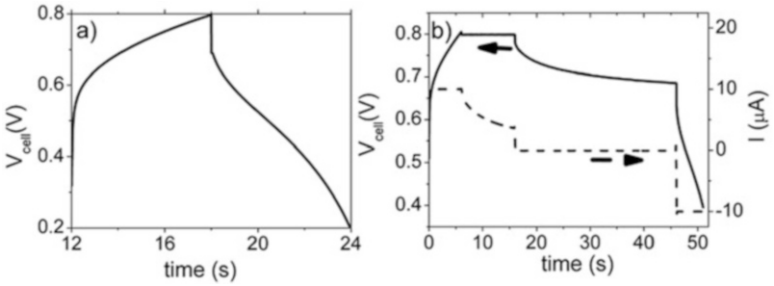

Fig. 4.9 Supercapacitor characteristics of the [N1113][TFSI]-gated MEH-PPV TransCap: (**a**) voltage profile vs time when the device is galvanostatically charged/discharged at ±10 μA up to 0.8 V (data taken during the second cycle of a sequential type of acquisition: 6 s TransCap ON followed by 6 s TransCap OFF); (**b**) voltage (left axis) and current (right axis) vs time upon galvanostatic charging at 10 μA up to 0.8 V, followed by 10 s at 0.8 V, 30 s rest in open circuit conditions, and galvanostatic discharge at −10 μA. (Reproduced with permission from [14])

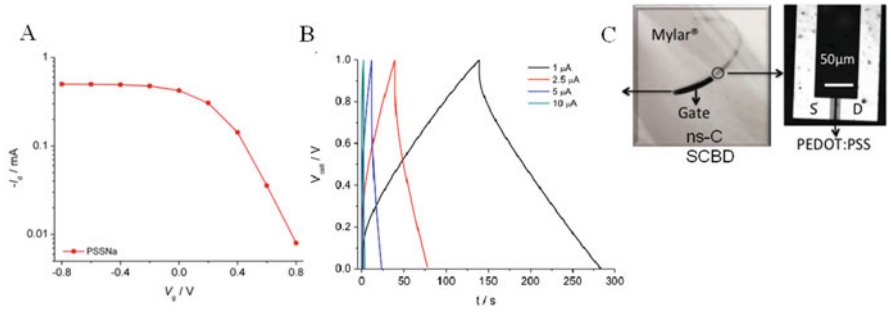

Fig. 4.10 (**a**) Transfer curves of micron-sized (L = 5 μm, W = 80 μm) OECTs making use of a PEDOT:PSS channel, a nanostructure carbon (ns-C) gate deposited at room temperature by supersonic cluster beam deposition (SCBD) and a PSSNa-based gel electrolyte. $V_{ds} = -0.5$ V. (**b**) Voltage profile over time for galvanostatic charge-discharge cycles at different currents from 1 to 10 μA for the TransCap. (**c**) Devices patterned on Mylar® during peel off from the PDMS-glass support for later use. SEM image of a microscale device. (Reproduced with permission from [74])

MEH-PPV TransCap. Figure 4.9 shows the voltage behavior over time during the OFF step proving that the supercapacitor can keep its charge within a voltage drop of 1.4% after 0.2 s (high resolution plot not shown here). Afer 30 s, the voltage decreases by 30% of its initial value. This result suggests that the TransCap can operate without being connected to an electric grid for relatively short times and that the transistor channel is still open (doped) at relatively long times.

The TransCap concept was further demonstrated by a flexible, planar OECT using PEDOT:PSS as the channel material and nanostructured carbon as the gate electrode material and poly(sodium 4-styrenesulfonate (PSSNa) gel as the gating media. The electrical characteristics of the system reveal good current modulation at low voltages, while demonstrating efficient charge retention and satisfying energy storage characteristics (Fig. 4.10; Table 4.2).

Table 4.2 Discharge Time (t), Capacitance (C), Delivered Energy (E), and Power (P) of Type I OECTs/Supercapacitors at Different Values of the Current (I), Normalized to the Geometric Area and Volume (Footprint) of the PEDOT:PSS Electrode (0.16 cm^2 with a thickness of 470 nm). Reproduced with permission from [74]

I (μA)	t (s)	C (mF/cm^2)	E ($\mu Wh/cm^2$)	P ($\mu W/cm^2$)	C (F/cm^3)	E (mWh/cm^3)	P (W/cm^3)
1	143.5	1.08	0.10	2.48	23.0	2.1	0.05
2.5	39.3	0.87	0.06	5.25	18.5	1.2	0.11
5	11.7	0.61	0.03	8.56	13.0	0.6	0.18
10	1.6	0.25	0.005	10.56	5.32	0.1	0.22

4.6 Conclusions

Flexible carbon electrodes represent a key component to bridge electronic and micro energy storage. Indeed, their good volumetric capacitance can be exploited for different devices, which, if properly designed and connected, could bring about a miniaturized autonomous system. Carbon electrodes can be used to process sub-1 V IGT components and to design novel architectures for new multifunction energy storage elements. Specifically, nanostructured carbon electrodes can be used as gates in IGTs and TransCaps assembled with both organic and aqueous electrolytes, the latter of interest for biosensing applications. The integration of transistor and capacitor provides a very efficient and low-cost energy system of great interest for autonomous flexible/stretchable electronics and bioelectronics. Furthermore, the charge storage properties of the channel and the gate electrodes of the OECTs permit the operation of the OECT without power supply for short periods of time.

References

1. Newman, P.: The Internet of Things 2020 (2020)
2. *AGRICULTURAL IOT WILL SEE A VERY RAPID GROWTH OVER THE NEXT 10 YEARS*. IoT forecast tool 2016 [cited 2021; Available from: https://machinaresearch.com/news/agricultural-iot-will-see-a-very-rapid-growth-over-the-next-10-years/]
3. Meola, A.: IoT Healthcare in 2020: Companies, devices, use cases and market stats. 2020 [cited 2021; Available from: https://www.businessinsider.com/iot-healthcare]
4. Danova, T.: THE CONNECTED-HOME REPORT: Forecasts and growth trends for one of the top 'Internet of Things' markets. 2015 [cited 2021; Available from: https://www.businessinsider.com/connected-home-forecasts-and-growth-2014-9?r=DE&IR=T]
5. Spyropoulos, G.D., Gelinas, J.N., Khodagholy, D.: Internal ion-gated organic electrochemical transistor: a building block for integrated bioelectronics. Sci. Adv. **5**(2), eaau7378 (2019)
6. Jo, Y.J., Kwon, K.Y., Khan, Z.U., Crispin, X., Kim, T.-i.: Gelatin hydrogel-based organic electrochemical transistors and their integrated logic circuits. ACS Appl. Mater. Interfaces. **10**(45), 39083–39090 (2018)
7. Bisri, S.Z., Shimizu, S., Nakano, M., Iwasa, Y.: Endeavor of iontronics: from fundamentals to applications of ion-controlled electronics. Adv. Mater. **29**(25), 1607054 (2017)
8. Zeglio, E., Inganäs, O.: Active materials for organic electrochemical transistors. Adv. Mater. **30**(44), 1800941 (2018)

9. Li, S., Pan, N., Zhu, Z., Li, R., Li, B., Chu, J., Li, G., Chang, Y., Pan, T.: Paper electronics: all-in-one iontronic sensing paper. Adv. Func. Mater. **29**(11), 1970072 (2019)
10. Arbring Sjöström, T., Berggren, M., Gabrielsson, E.O., Janson, P., Poxson, D.J., Seitanidou, M., Simon, D.T.: A decade of iontronic delivery devices. Adv. Mater. Technol. **3**(5), 1700360 (2018)
11. Yang, C.-S., Shang, D.-S., Liu, N., Fuller, E.J., Agrawal, S., Talin, A.A., Li, Y.-Q., Shen, B.-G., Sun, Y.: All-solid-state synaptic transistor with ultralow conductance for neuromorphic computing. Adv. Funct. Mater. **28**(42), 1804170 (2018)
12. Yang, J.-T., Ge, C., Du, J.-Y., Huang, H.-Y., He, M., Wang, C., Lu, H.-B., Yang, G.-Z., Jin, K.-J.: Artificial synapses emulated by an electrolyte-gated tungsten-oxide transistor. Adv. Mater. **30**(34), 1801548 (2018)
13. Ren, X., Wang, Y., Xie, Z., Xue, F., Leighton, C., Frisbie, C.D.: Gate-tuned insulator–metal transition in electrolyte-gated transistors based on Tellurene. Nano Lett. **19**(7), 4738–4744 (2019)
14. Sayago, J., Shafique, U., Soavi, F., Cicoira, F., Santato, C.: TransCap: a monolithically integrated supercapacitor and electrolyte-gated transistor. J. Mater. Chem. C. **2**(48), 10273–10276 (2014)
15. Bard, A.J., Faulkner, L.R.: Electrochemical methods: Fundamentals and applications, New York: Wiley, 2001, 2nd ed. Russ. J. Electrochem. **38**(12), 1364–1365 (2002)
16. Caizán-Juanarena, L., Borsje, C., Sleutels, T., Yntema, D., Santoro, C., Ieropoulos, I., Soavi, F., ter Heijne, A.: Combination of bioelectrochemical systems and electrochemical capacitors: principles, analysis and opportunities. Biotechnol. Adv. **39**, 107456 (2020)
17. Brousse, T., Bélanger, D., Long, J.: To be or not to be pseudocapacitive? J. Electrochem. Soc. **162**, A5185–A5189 (2015)
18. Jiang, Y., Liu, J.: Definitions of pseudocapacitive materials: a brief review. Energy Environ. Mater. **2**(1), 30–37 (2019)
19. Frackowiak, E., Béguin, F.: Carbon materials for the electrochemical storage of energy in capacitors. Carbon. **39**(6), 937–950 (2001)
20. Pandolfo, A.G., Hollenkamp, A.F.: Carbon properties and their role in supercapacitors. J. Power Sources. **157**(1), 11–27 (2006)
21. Béguin, F., Presser, V., Balducci, A., Frackowiak, E.: Carbons and electrolytes for advanced supercapacitors. Adv. Mater. **26**(14), 2219–2251 (2014)
22. NobelPrize.org. The Nobel Prize in Physics 1956. [cited 2020 October 18th]; Available from: https://www.nobelprize.org/prizes/physics/1956/summary/]
23. Moore, G.E.: Cramming more components onto integrated circuits. In: Readings in computer architecture, pp. 56–59. Morgan Kaufmann Publishers Inc (2000)
24. Apple, Apple Event, October 13th 2020, at 28:00. Uploaded October 13th 2020. Accessed on 19 Oct 2020. Available at https://www.apple.com/apple-events/october-2020/
25. Lan, T., Soavi, F., Marcaccio, M., Brunner, P.L., Sayago, J., Santato, C.: Electrolyte-gated transistors based on phenyl-C61-butyric acid methyl ester (PCBM) films: bridging redox properties, charge carrier transport and device performance. Chem. Commun. (Camb.). **54**(43), 5490–5493 (2018)
26. Tarabella, G., Mahvash Mohammadi, F., Coppedè, N., Barbero, F., Iannotta, S., Santato, C., Cicoira, F.: New opportunities for organic electronics and bioelectronics: ions in action. Chem. Sci. **4**(4), 1395–1409 (2013)
27. Lan, T., Soavi, F., Marcaccio, M., Brunner, P.-L., Sayago, J., Santato, C.: Electrolyte-gated transistors based on phenyl-C61-butyric acid methyl ester (PCBM) films: bridging redox properties, charge carrier transport and device performance. Chem. Commun. **54**(43), 5490–5493 (2018)
28. Jeong, J., Aetukuri, N., Graf, T., Schladt, T.D., Samant, M.G., Parkin, S.S.P.: Suppression of metal-insulator transition in VO2 by electric field–induced oxygen vacancy formation. Science. **339**(6126), 1402 (2013)

29. Barbosa, S.M., Balke, N., Tsai, W.Y., Santato, C., Orlandi, M.O.: Structure of the electrical double layer at the interface between an ionic liquid and tungsten oxide in ion-gated transistors. J. Phys. Chem. Lett. **11**(9), 3257–3262 (2020)
30. White, H.S., Kittlesen, G.P., Wrighton, M.S.: Chemical derivatization of an array of three gold microelectrodes with polypyrrole: fabrication of a molecule-based transistor. J. Am. Chem. Soc. **106**(18), 5375–5377 (1984)
31. Yi, Z., Natale, G., Kumar, P., Mauro, E.D., Heuzey, M.-C., Soavi, F., Perepichka, I.I., Varshney, S.K., Santato, C., Cicoira, F.: Ionic liquid–water mixtures and ion gels as electrolytes for organic electrochemical transistors. J. Mater. Chem. C. **3**(25), 6549–6553 (2015)
32. Wang, H., Yang, M., Tang, Q., Zhao, X., Tong, Y., Liu, Y.: Flexible, conformal organic synaptic transistors on elastomer for biomedical applications. Adv. Funct. Mater. **29**(19), 1901107 (2019)
33. Subramanian, A., George, B., Bobbara, S.R., Valitova, I., Ruggeri, I., Borghi, F., Podestà, A., Milani, P., Soavi, F., Santato, C., Cicoira, F.: Ion-gated transistors based on porous and compact TiO2 films: effect of Li ions in the gating medium. AIP Adv. **10**(6) (2020)
34. Gumyusenge, A., Xu, T., Wang, X., Mei, J.: Organic-based transistors and sensors. In: Flexible and stretchable medical devices, pp. 60–63. Wiley Online Books (2018)
35. Scheiblin, G., Coppard, R., Owens, R.M., Mailley, P., Malliaras, G.G.: Referenceless pH sensor using organic electrochemical transistors. Adv. Mater. Technol. **2**(2), 1600141 (2017)
36. Leleux, P., Rivnay, J., Lonjaret, T., Badier, J.-M., Bénar, C., Hervé, T., Chauvel, P., Malliaras, G.G.: Organic electrochemical transistors for clinical applications. Adv. Healthc. Mater. **4**(1), 142–147 (2015)
37. Chen, N., Zhang, H., Li, L., Chen, R., Guo, S.: Ionogel electrolytes for high-performance lithium batteries: a review. Adv. Energy Mater., **8**(12) (2018)
38. Valitova, I., Kumar, P., Meng, X., Soavi, F., Santato, C., Cicoira, F.: Photolithographically patterned TiO2 films for electrolyte-gated transistors. ACS Appl. Mater. Interfaces. **8**(23), 14855–14862 (2016)
39. Tang, H., Kumar, P., Zhang, S., Yi, Z., Crescenzo, G.D., Santato, C., Soavi, F., Cicoira, F.: Conducting polymer transistors making use of activated carbon gate electrodes. ACS Appl. Mater. Interfaces. **7**(1), 969–973 (2015)
40. Lin, F., Lonergan, M.C.: Gate electrode processes in an electrolyte-gated transistor: non-faradaically versus faradaically coupled conductivity modulation of a polyacetylene ionomer. Appl. Phys. Lett. **88**(13), 133507 (2006)
41. Tarabella, G., Santato, C., Yang, S.Y., Iannotta, S., Malliaras, G.G., Cicoira, F.: Effect of the gate electrode on the response of organic electrochemical transistors. Appl. Phys. Lett. **97**(12) (2010)
42. Wang, Q., Ma, Y., Liang, X., Zhang, D., Miao, M.: Flexible supercapacitors based on carbon nanotube-MnO2 nanocomposite film electrode. Chem. Eng. J. **371**, 145–153 (2019)
43. Wang, C., Xia, K., Wang, H., Liang, X., Yin, Z., Zhang, Y.: Advanced carbon for flexible and wearable electronics. Adv. Mater. **31**(9), 1801072 (2019)
44. Wu, Z., Wang, Y., Liu, X., Lv, C., Li, Y., Wei, D., Liu, Z.: Carbon-nanomaterial-based flexible batteries for wearable electronics. Adv. Mater. **31**(9), 1800716 (2019)
45. Zhang, H., Li, A., Wang, J., Zhang, Y., Zhao, Z., Zhao, H., Cheng, M., Wang, C., Wang, J., Zhang, S., Wang, J.: Graphene integrating carbon fiber and hierarchical porous carbon formed robust flexible "carbon-concrete" supercapacitor film. Carbon. **126**, 500–506 (2018)
46. Gandhiraman, R.P., Singh, E., Diaz-Cartagena, D.C., Nordlund, D., Koehne, J., Meyyappan, M.: Plasma jet printing for flexible substrates. Appl. Phys. Lett. **108**(12) (2016)
47. Zhou, Q., Jia, C., Ye, X., Tang, Z., Wan, Z.: A knittable fiber-shaped supercapacitor based on natural cotton thread for wearable electronics. J. Power Sources. **327**, 365–373 (2016)
48. Liu, L., Niu, Z., Chen, J.: Flexible supercapacitors based on carbon nanotubes. Chin. Chem. Lett. **29**(4), 571–581 (2018)
49. Morteza Najarian, A., Szeto, B., Tefashe, U.M., McCreery, R.L.: Robust all-carbon molecular junctions on flexible or semi-transparent substrates using "process-friendly" fabrication. ACS Nano. **10**(9), 8918–8928 (2016)

50. Kumar, P., Di Mauro, E., Zhang, S., Pezzella, A., Soavi, F., Santato, C., Cicoira, F.: Melanin-based flexible supercapacitors. J. Mater. Chem. C. **4**(40), 9516–9525 (2016)
51. Huang, P., Lethien, C., Pinaud, S., Brousse, K., Laloo, R., Turq, V., Respaud, M., Demortiere, A., Daffos, B., Taberna, P.L., Chaudret, B., Gogotsi, Y., Simon, P.: On-chip and freestanding elastic carbon films for micro-supercapacitors. Science. **351**(6274), 691–695 (2016)
52. Cheng, M., Meng, Y., Meng, Q., Mao, L., Zhang, M., Amin, K., Ahmad, A., Wu, S., Wei, Z.: A hierarchical porous N-doped carbon electrode with superior rate performance and cycling stability for flexible supercapacitors. Mater. Chem. Front. **2**(5), 986–992 (2018)
53. Madou, M.: Fundamentals of microfabrication and nanotechnology. 3rd édition ed. Vol. II. (2012)
54. Xiao, H., Zeng, P., Ren, X.,Wang, F.: Three-dimensional microfabrication of copper column by localized electrochemical deposition. In: 2016 17th International Conference on Electronic Packaging Technology (ICEPT). (2016)
55. Li, J., Zhu, M., An, Z., Wang, Z., Toda, M., Ono, T.: Constructing in-chip micro-supercapacitors of 3D graphene nanowall/ruthenium oxides electrode through silicon-based microfabrication technique. J. Power Sources. **401**, 204–212 (2018)
56. Koutsouras, D.A., Gkoupidenis, P., Stolz, C., Subramanian, V., Malliaras, G.G., Martin, D.C.: Impedance spectroscopy of spin-cast and electrochemically deposited PEDOT:PSS films on microfabricated electrodes with various areas. ChemElectroChem. **4**(9), 2321–2327 (2017)
57. Breshike, C.J., Furstenberg, R., Dominguez, D., Kusterbeck, A., Kozak, D., Stievater, T., McGill, R.A.: Gas chromatography using a spin-coated stationary phase and a molded elastomer micro-channel. J. Chromatogr. A. **2020**, 460555 (1610)
58. Nielsen, L.H., Keller, S.S., Boisen, A.: Microfabricated devices for oral drug delivery. Lab Chip. **18**(16), 2348–2358 (2018)
59. Stassin, T., Rodríguez-Hermida, S., Schrode, B., Cruz, A.J., Carraro, F., Kravchenko, D., Creemers, V., Stassen, I., Hauffman, T., De Vos, D., Falcaro, P., Resel, R., Ameloot, R.: Vapour-phase deposition of oriented copper dicarboxylate metal–organic framework thin films. Chem. Commun. **55**(68), 10056–10059 (2019)
60. Larrazábal, G.O., Shinagawa, T., Martín, A.J., Pérez-Ramírez, J.: Microfabricated electrodes unravel the role of interfaces in multicomponent copper-based CO2 reduction catalysts. Nat. Commun. **9**(1), 1477 (2018)
61. Martín-Palma, R.J., Lakhtakia, A.: Chapter 15 - Vapor-deposition techniques. In: Lakhtakia, A., Martín-Palma, R.J. (eds.) Engineered Biomimicry, pp. 383–398. Elsevier, Boston (2013)
62. del Val, J., Comesaña, R., Riveiro, A., Lusquiños, F., Quintero, F., Boutinguiza, M., Pou, J.: Laser direct writing of co-superalloy lines for micro-fabrication applications. Surf. Coat. Technol. **345**, 76–88 (2018)
63. Pavel, E., Marinescu, V., Lungulescu, M.: Graphene nanopatterning by quantum optical lithography. Optik. **203**, 163532 (2020)
64. Ramadan, S., Bowen, L., Popescu, S., Fu, C., Kwa, K.K., O'Neill, A.: Fully controllable silicon nanowire fabricated using optical lithography and orientation dependent oxidation. Appl. Surf. Sci. **523**, 146516 (2020)
65. Lee, S.H., Seo, S.E., Kim, K.H., Lee, J., Park, C.S., Jun, B.-H., Park, S.J., Kwon, O.S.: Single photomask lithography for shape modulation of micropatterns. J. Ind. Eng. Chem. **84**, 196–201 (2020)
66. Gaag, B.P.V.D., Scherer, A.: Microfabrication below 10 nm. Appl. Phys. Lett. **56**(5), 481–483 (1990)
67. Balla, T., Spearing, S.M., Monk, A.: An assessment of the process capabilities of nanoimprint lithography. J. Phys. D. Appl. Phys. **41**(17), 174001 (2008)
68. Zhang, Y., Lu, J., Zhou, H., Itoh, T., Maeda, R.: Application of nanoimprint technology in MEMS-based micro direct-methanol fuel cell (μ-DMFC). J. Microelectromech. Syst. **17**(4), 1020–1028 (2008)
69. Romano, L., Vila-Comamala, J., Jefimovs, K., Stampanoni, M.: High-aspect-ratio grating microfabrication by platinum-assisted chemical etching and gold electroplating. Adv. Eng. Mater. **n/a**(n/a), 2000258

70. Cozzi, C., Polito, G., Kolasinski, K.W., Barillaro, G.: Controlled microfabrication of high-aspect-ratio structures in silicon at the highest etching rates: the role of H2O2 in the anodic dissolution of silicon in acidic electrolytes. Adv. Funct. Mater. **27**(6), 1604310 (2017)
71. Gupta, T., Strelcov, E., Holland, G., Schumacher, J., Yang, Y., Esch, M.B., Aksyuk, V., Zeller, P., Amati, M., Gregoratti, L., Kolmakov, A.: Electron and X-ray focused beam-induced cross-linking in liquids: toward rapid continuous 3D Nanoprinting and interfacing using soft materials. ACS Nano. (2020)
72. Bougdid, Y., Sekkat, Z.: Voxels optimization in 3D laser Nanoprinting. Sci. Rep. **10**(1), 10409 (2020)
73. Dietrich, P.I., Blaicher, M., Reuter, I., Billah, M., Hoose, T., Hofmann, A., Caer, C., Dangel, R., Offrein, B., Troppenz, U., Moehrle, M., Freude, W., Koos, C.: In situ 3D nanoprinting of free-form coupling elements for hybrid photonic integration. Nat. Photonics. **12**(4), 241–247 (2018)
74. Yi, Z., Bettini, L.G., Tomasello, G., Kumar, P., Piseri, P., Valitova, I., Milani, P., Soavi, F., Cicoira, F.: Flexible conducting polymer transistors with supercapacitor function. J. Polym. Sci. B Polym. Phys. **55**(1), 96–103 (2017)
75. Mukai, K., Asaka, K., Wu, X., Morimoto, T., Okazaki, T., Saito, T., Yumura, M.: Wet spinning of continuous polymer-free carbon-nanotube fibers with high electrical conductivity and strength. Appl. Phys. Express. **9**(5), 055101 (2016)
76. Di, J., Zhang, X., Yong, Z., Zhang, Y., Li, D., Li, R., Li, Q.: Carbon-nanotube Fibers for wearable devices and smart textiles. Adv. Mater. **28**(47), 10529–10538 (2016)
77. Hao, T., Sun, J., Wang, W., Yu, D.: MWCNTs-COOH/cotton flexible supercapacitor electrode prepared by improvement one-time dipping and carbonization method. Cellulose. **25**(7), 4031–4041 (2018)
78. Deng, J., Zhang, Y., Zhao, Y., Chen, P., Cheng, X., Peng, H.: A shape-memory supercapacitor Fiber. Angew. Chem. Int. Ed. **54**(51), 15419–15423 (2015)
79. Nagaraju, G., Sekhar, S.C., Yu, J.S.: Utilizing waste cable wires for high-performance Fiber-based hybrid supercapacitors: An effective approach to electronic-waste management. Adv. Energy Mater. **8**(7), 1702201 (2018)
80. Wang, K., Huang, Y., Wang, M., Yu, M., Zhu, Y., Wu, J.: PVD amorphous carbon coated 3D NiCo2O4 on carbon cloth as flexible electrode for both sodium and lithium storage. Carbon. **125**, 375–383 (2017)
81. Couly, C., Alhabeb, M., Van Aken, K.L., Kurra, N., Gomes, L., Navarro-Suárez, A.M., Anasori, B., Alshareef, H.N., Gogotsi, Y.: Asymmetric flexible MXene-reduced graphene oxide micro-supercapacitor. Adv. Electron. Mater. **4**(1) (2018)
82. Woo, J.S., Lee, G.-W., Park, S.-Y., Han, J.T.: Realization of transparent conducting networks with high uniformity by spray deposition on flexible substrates. Thin Solid Films. **638**, 367–374 (2017)
83. Chen, B., Jiang, Y., Tang, X., Pan, Y., Hu, S.: Fully packaged carbon nanotube supercapacitors by direct ink writing on flexible substrates. ACS Appl. Mater. Interfaces. **9**(34), 28433–28440 (2017)
84. Wu, K., Fu, J., Zhang, X., Peng, X., Gao, B., Chu, P.K.: Three-dimensional flexible carbon electrode for symmetrical supercapacitors. Mater. Lett. **185**, 193–196 (2016)
85. Wang, D.-W., Li, F., Zhao, J., Ren, W., Chen, Z.-G., Tan, J., Wu, Z.-S., Gentle, I., Lu, G.Q., Cheng, H.-M.: Fabrication of graphene/polyaniline composite paper via in situ anodic Electropolymerization for high-performance flexible electrode. ACS Nano. **3**(7), 1745–1752 (2009)
86. Yang, Y., Ng, S.-W., Chen, D., Chang, J., Wang, D., Shang, J., Huang, Q., Deng, Y., Zheng, Z.: Freestanding lamellar porous carbon stacks for low-temperature-foldable supercapacitors. Small. **15**(48), 1902071 (2019)
87. Du, J., Mu, X., Zhao, Y., Zhang, Y., Zhang, S., Huang, B., Sheng, Y., Xie, Y., Zhang, Z., Xie, E.: Layered coating of ultraflexible graphene-based electrodes for high-performance in-plane quasi-solid-state micro-supercapacitors. Nanoscale. **11**(30), 14392–14399 (2019)

88. He, S., Zhang, C., Du, C., Cheng, C., Chen, W.: High rate-performance supercapacitor based on nitrogen-doped hollow hexagonal carbon nanoprism arrays with ultrathin wall thickness in situ fabricated on carbon cloth. J. Power Sources. **434**, 226701 (2019)
89. Malik, R., Zhang, L., McConnell, C., Schott, M., Hsieh, Y.-Y., Noga, R., Alvarez, N.T., Shanov, V.: Three-dimensional, free-standing polyaniline/carbon nanotube composite-based electrode for high-performance supercapacitors. Carbon. **116**, 579–590 (2017)
90. Bhat, S.N., Pietro, R.D., Sirringhaus, H.: Electroluminescence in ion-gel gated conjugated polymer field-effect transistors. Chem. Mater. **24**(21), 4060–4067 (2012)
91. Sayago, J., Soavi, F., Sivalingam, Y., Cicoira, F., Santato, C.: Low voltage electrolyte-gated organic transistors making use of high surface area activated carbon gate electrodes. J. Mater. Chem. C. **2**(28), 5690–5694 (2014)
92. Soavi, F., Bettini, L.G., Piseri, P., Milani, P., Santoro, C., Atanassov, P., Arbizzani, C.: Miniaturized supercapacitors: key materials and structures towards autonomous and sustainable devices and systems. J. Power Sources. **326**, 717–725 (2016)
93. Meng, X., Quenneville, F., Venne, F., Di Mauro, E., Işık, D., Barbosa, M., Drolet, Y., Natile, M.M., Rochefort, D., Soavi, F., Santato, C.: Electrolyte-gated WO3 Transistors: electrochemistry, structure, and device performance. J. Phys. Chem. C. **119**(37), 21732–21738 (2015)

Chapter 5
Nanoporous Composite Sensors

Adebayo Eisape, Bohan Sun, Jing Li, and Sung Hoon Kang

Abstract Nanoporous composite sensors provide great opportunities to tune their characteristics for specific functions beyond the intrinsic properties of constituent materials. To make nanoporous composites, one needs to mix matrix materials with fillers and introduce small scale pores. While many different classes of materials can be utilized for the synthesis of nanonporous composites, we will focus on carbon-based materials as they are the most common and widely utilized materials. In this chapter, carbon-based filler and matrix materials will be introduced to inform selection based on sensor application and environment, followed by fabrication methods to control the internal and external structure of the composites to have desired properties. Finally, we will conclude by discussing current challenges and future opportunities.

Keywords Piezoresistive · Carbon-based · Nanocomposite · Microstructure · Nanostructure

5.1 Introduction

Sensors are used in many aspects of modern life to collect information about environments, health conditions, and machines, as they provide quantitative information about various stimuli (e.g. pressure, strain, temperature) which can be used as guides for monitoring and decision making. One typically chooses a sensor based on requirements such as sensing capability (e.g. types of signals to detect, sensitivity, sensing range) and associated mechanical, thermal, chemical,

A. Eisape · B. Sun · S. H. Kang (✉)
Department of Electrical and Computer Engineering, Johns Hopkins University, Baltimore, MD, USA
e-mail: shkang@jhu.edu

J. Li
School of Mechanical Engineering, Hubei University of Technology, Wuhan, Hubei, P. R. China

F. Borghi et al. (eds.), *Nanoporous Carbons for Soft and Flexible Energy Devices*,
Carbon Materials: Chemistry and Physics 11,
https://doi.org/10.1007/978-3-030-81827-2_5

and electrical properties. In this regard, nanoporous composites provide great opportunities for sensor applications, as their properties can be tuned for specific applications, rather than relying on the inherent properties of the materials used.

To tune the properties of a sensor, mechanisms such as the control of compositions, constituent materials, and porosity have been utilized for the manipulation of the mechanical/electrical/electrochemical properties of composites. These mechanisms are also used to adjust the associated sensitivity and sensing range of the devices fabricated with these composite materials.

Beyond tunability, such sensors have other desirable attributes including low cost, scalability, light weight, and ease of fabrication and shaping. As a result, there have been many studies exploring the use of nanoporous composites for sensing applications such as the measurement of strain [1], pressure [2], physiological signals [3], gas [4], humidity [5, 6], and antibiotic agents [7]. In particular, they have been actively studied for applications where flexibility and elasticity are desirable, such as wearable electronics, human-machine interfaces, health monitoring devices, and soft robotics.

While there are multiple mechanisms by which sensing can be achieved, including change of capacitance and charge generation, change of resistivity or resistance associated with stimuli such as pressure and strain is the most commonly used mechanism. And, it is the effect by which the composites discussed in this chapter are able to achieve sensing. As such, it is prudent to provide a brief introduction of this sensing mechanism.

The piezoresistive effect is the effect by which a material changes its resistivity with the application of a mechanical strain or stress. It is widely utilized for sensing mechanical signals, and it is particularly well-suited for pressure sensing applications because it is based on absolute pressure, as opposed to changes in pressure (as is the case for piezoelectric sensing elements, for example). This allows sensors utilizing this effect to provide an accurate measurement of slowly varying pressures, such as those experienced due to changing atmospheric conditions, descending into the ocean, or measuring body movements/joint articulation. The piezoresistive effect is realized as the modification (both creation and destruction) of electrically conducting pathways throughout the sensing material.

Conductive pathways can be established due to close proximity of conductive elements in the matrix. Tunneling channels are responsible for variations in conductivity when the distances between conductive elements are small enough (on the order of 10^0 to 10^1 nm [8, 9]) such that charges can tunnel from one conductive element to another. Conductive pathways can be also modulated due to the change of direct physical contact between conductive elements, as shown in Fig. 5.1a. The reversibility of this process can be ensured by the incorporation of an architected structure. Conductive pathways can be (permanently) destroyed due to ripping/tearing/damage to conductive elements or to the additive-matrix interface, leading to a permanent increase in the base resistance of the composite material and as a result, a permanent decrease in the performance of the sensor. The effects of this damage (pull-out effects) will be discussed in Sect. 5.3.

While incorporating conductive fillers into a matrix will increase the electrical response of the formed composite, the sensitivity of a bulk material will always

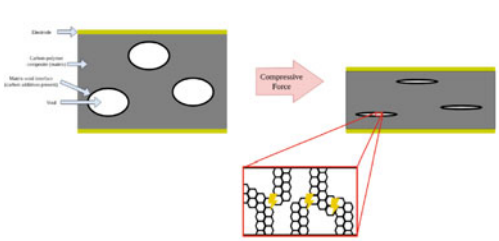

(a) Mechanism of conductive pathway formation.

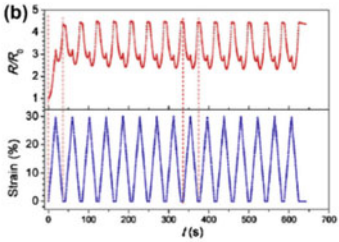

(b) Shift of electrical response due to pull-out effects. Reprinted from Ref. [10]. Copyright 2012, with permission from Elsevier.

Fig. 5.1 Piezoresistive nanocomposites [10]. (**a**) Mechanism of conductive pathway formation. (**b**) Shift of electrical response due to pull-out effects. (Reprinted from Ref. [10]. Copyright 2012, with permission from Elsevier)

be limited, as the only mechanisms for conductive pathway modification in such a system are charge tunneling and damage to the filler or filler-matrix interface. As such, microstructures can be introduced to provide more control over the interactions of conductive elements. The microstructures discussed in this chapter will be pores of varying geometries, with their associated methods of fabrication also being discussed. While the fabrication method will vary based on the constituents of the composite, the degree of the desired porosity, and the mechanical and electrical properties and response of the desired sensor, they share common principles and fabrication approaches.

In general the fabrication of all nanoporous composites requires the mixing of one or more matrix materials with fillers and the introduction of small scale pores. To ensure the uniform mixing of matrix and filler, and to introduce pores in a desired size range and fraction, there have been many studies to facilitate the process by overcoming challenges such as agglomeration and segregation. While many different classes of materials can be utilized for the synthesis of nanoporous composites, we will focus on carbon-based materials as they are the most common and widely utilized materials.

In this chapter, different filler and matrix materials will be introduced to inform selection based on sensor application and environment, followed by a discussion of structure properties and morphology and fabrication methods to control the internal and external structure of the composites to improve their properties. Finally, we will conclude by discussing current challenges and future opportunities.

5.2 Materials

In this section, we will provide information about popular carbon-based filler and matrix materials used for composite sensors, as a guide for material selection for different sensor applications and environments. Composites consisting of polymeric matrices and carbon-based conductive fillers (e.g. carbon black, carbon nanotube,

graphene, graphite) can provide the integration of the electrical conductivity of carbon fillers and the mechanical compliance of flexible matrices [11, 12].

Carbon Black Carbon black (abbreviated CB) is carbon in a nanoparticulate form, and is a widely used filler with outstanding electrical properties, with a resistivity in the range of 10^{-2}–$10^{1}\ \Omega\,\text{cm}$ [13] and a high surface area to volume ratio [14]. Controlling the concentration of carbon black in a polymer offers a mechanism of tuning sensitivity when applied in pressure sensing applications by changing the modulus and the conductivity of the composite.

Carbon black has been explored widely for use as a 0D conductive filler in various applications to significantly improve the electrical conductivity of polymer materials via incorporation [13]. CB can be directly mixed with soft polymers such as polydimethylsiloxane (PDMS), Ecoflex, silicone rubber or thermoplastic polyurethane (TPU) to fabricate piezoresistive composite sensors using methods including drop-casting, compression moulding or spin-coating [15–18] to name a few. Besides the common carbon black/polymer composites, rubber-band (RB)/CB/PDMS composite piezoresistive sensors have been demonstrated with high sensitivity (Gauge factor $\approx$ 242.6 (ϵ = 38.8–71.4%), see Sect. 5.3 and equation 5.1 for more information about the Gauge factor) and good reliability and repeatability for human motion monitoring [19].

As shown in Fig. 5.2a, the pre-swollen RB is soaked in CB suspension to adsorb CB particles onto its surface, followed by PDMS casting. Therefore, the added CB fillers form a shell-like microstructure inside the PDMS matrix, and at different stretching states the microstructure of the conductive CB layer on the RB surface is gradually cracked, resulting in a significantly increased resistance. Additionally, it is reported that the use of ionic liquids (IL) inside the polymer matrix can improve filler dispersion and rubber-filler interaction (Fig. 5.2b) [20]. The reported sensitivity of CB/rubber composite with IL/CB (ratio of 1 to 1.5) is about 6 times higher than the composite without IL.

Graphite Graphite, a crystalline form of the element carbon with its atoms arranged in a hexagonal structure [21], can be randomly dispersed in flexible polymeric matrices to fabricate piezoresistive graphite/polymer composite sensors with very limited sensitivity [22]. To overcome the poor sensitivity of polymeric composites with graphite powders, a number of synthesis methods have been proposed to prepare graphite nanosheets [23–25]. Taking advantage of the continuous 2D sheet form, the contact area changes are enlarged upon external mechanical loading, leading to a high sensitivity for human motion monitoring (Fig. 5.3) [26].

Carbon Nanotube Carbon nanotubes (CNTs) are layered cylindrical molecules of rolled-up carbon atoms which exhibit high electrical conductivity and exceptional mechanical properties [27]. These tubes may form with a single rolled-up sheet of carbon atoms (single-walled carbon nanotube, SWCNT) or with multiple rolled-up sheets of carbon atoms (multiwalled carbon nanotube, MWCNT) and can have length to diameter ratios exceeding 1,000,000 [28]. CNTs are widely utilized in pressure and strain sensing, owing to their excellent electrical and mechanical

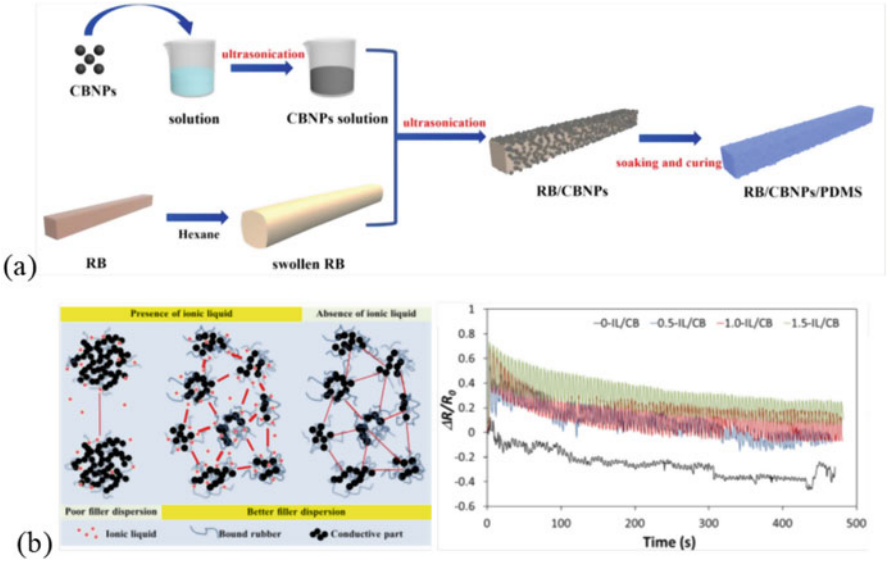

Fig. 5.2 (**a**) Schematic of the fabrication process of the RB/CBNPs/PDMS piezoresistive composite. (Reprinted from Ref. [19] with permission from Elsevier). (**b**) The improved sensitivity and rubber-filler interaction of CB/rubber composite by adding ionic liquid. (Reprinted from Ref. [20] with permission from Elsevier)

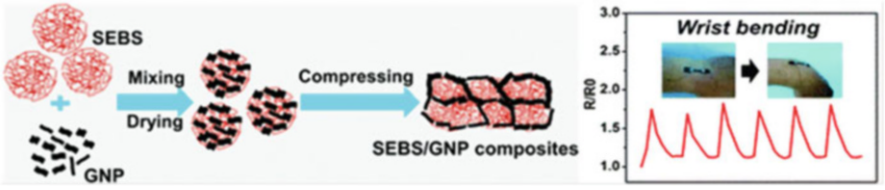

Fig. 5.3 Styrene-b-(ethylene-co-butylene)-b-styrene (SEBS) triblock copolymer/graphite nanoplatelet (GNP) composites with enhanced sensitivity for human motion monitoring. (Reprinted from Ref. [26] with permission from Royal Society of Chemistry)

properties including high electrical conductivity (as high as 10^6 to 10^7 S/m for pure CNT [29]), good flexibility, and high thermal conductivity (6000 W/mK for SWCNT and 3000 W/mK for MWCNT [30]). These outstanding properties make them widely used as conductive fillers for polymeric composite-based piezoresistive sensors.

The most popular CNT/polymer composite synthesis method is to randomly disperse CNTs in a PDMS matrix [31]. In order to imitate stretchability of human skin, ultra-soft Ecoflex has been widely used to synthesize CNT/Ecoflex composites for electronic skin applications [34]. Moreover, CNT/polymer composites with various characteristics have been developed using different polymer matrices, such as versatile thermoplastic PU, high-strength epoxy and transparent PMMA [35–37].

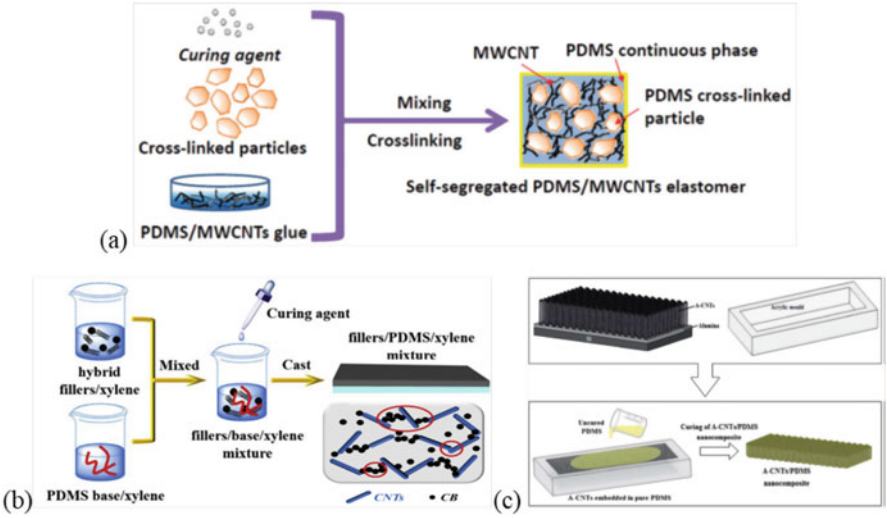

Fig. 5.4 The schematic of the fabrication process of (**a**) self-segregated CNTs/PDMS composite. (Reprinted from Ref. [31] with permission from Royal Society of Chemistry), (**b**) hybrid CNTs-CBs/PDMS composite. (Reprinted from Ref. [32] with permission from Elsevier), (**c**) CNT-arrays/PDMS composite for piezoresistive sensing applications. (Reprinted from Ref. [33] with permission from Royal Society of Chemistry)

Remarkably, with the increasing popularity of the development of high performing self-powered sensors for portable electronics, polyvinylidene fluoride (PVDF), a piezoelectric polymer, has served as the matrix material for CNT-based composites as well [38]. However, due to the nanoscale size and large aspect ratio, the randomly dispersed CNT fillers are prone to agglomeration, forming clusters throughout the composite [39]. The agglomeration negatively influences the sensitivity of CNT/polymer composites and impedes the capability of the composite to detect pressures in the tactile pressure range ($\leq$1 kPa). Therefore, many methods have been applied for the uniform distribution of CNT fillers. For instance, self-segregated structures have been constructed to form dense conductive CNT networks in PDMS. As shown in Fig. 5.4a, the self-segregated CNT/PDMS composite exhibits a sensitivity 7.4 times higher than that of conventional samples and shows a more prominent compression modulus and strength [31]. Another approach is to hybridize CNTs with high surface area to volume ratio CBs. Such implementations combine PDMS with hybrid CNT-CB conductive fillers using a mixing-casting method. CNTs and CBs overlap and entangle, forming a bridged structure, resulting in improved sensitivity and electrical conductivity for human joint motion detection (Fig. 5.4b) [32]. Furthermore, a novel piezoresistive CNT-based composite with aligned CNT-arrays in a PDMS matrix has also been proposed for stretchable sensor applications (Fig. 5.4c) with the resulting composite possessing not only outstanding electromechanical sensitivity, but also excellent elasticity [33].

Graphene Graphene is a two-dimensional (2D) carbon allotrope, consisting of a monolayer of carbon atoms arranged in a honeycomb lattice [40] and is a base unit for other graphitic materials and the assembly of carbon nanomaterials in other dimensions. It can be assembled as 0D buckyballs by wrapping, 1D nanotubes by rolling, or 3D graphite by stacking [41]. The conduction bands of graphene make it a semimetal, with unusual mechanical, electrical, and thermal properties that are best described by theories for massless relativistic particles [41]. The scaled-up and reliable production of graphene derivatives, such as graphene oxide (GO) and reduced graphene oxide (rGO), offers a wide range of possibilities to synthesize functional graphene-based materials for various applications [42].

Graphene exhibits great mechanical, electrical, and thermal properties. Graphene stands out both as an individual material and as a reinforcing agent in composites owing to its impressive mechanical properties including modulus of elasticity equal to 1000 ± 100 GPa, an intrinsic strength (σ_{int}) of 130 GPa and critical stress intensity factor (K_C) of 4.0 ± 0.6 MPa [43, 44]. For thermal properties, graphene has very high in-plane thermal conductivity exceeding 3000 W $(mK)^{-1}$ and thermoelectric effects [44, 45].

Graphene has a very high electrical conductivity, with a low sheet resistance of around 10 Ω/sq [46] and an electron mobility of 250,000 $cm^2/V\,s$ [43]. It is widely utilized in various tactile pressure sensing applications. For graphene-based composite sensors, graphene is incorporated into well-known polymeric matrices, such as PDMS, Ecoflex, PLA, PVDF, PU, and rubber for wearable sensors and biocompatible materials including PLA, PDMS, and Poly (ethylene-glycol) for biomedical and implanted sensing applications [47–50].

Due to the high carrier mobility and large surface area of graphene, graphene-based composite sensors possess higher sensitivity compared to other carbon-based composite sensors [51, 52]. Remarkably, it has been shown that the lightly cross-linked Silly Putty polymer matrix with highly viscous properties can enable high mobility of graphene nanosheets, resulting in outstanding electromechanical properties, such as dramatic changes in resistivity with mechanical strain and temporal relaxation of electric resistance [53].

A PDMS sponge with graphene embedded as a filler material can enable pressure sensors with a remarkable sensitivity of 2.2 MHz/kPa, wide operating range to 500 kPa, fast response time of around 7 ms, and a low detection limit of 5 kPa (Fig. 5.5a) [54]. As shown in Fig. 5.5b, adding conductive metal nanoparticles to a graphene/polymer mixture by drop-casting to make a nanoparticle-bridged graphene/polymer composite can further increase sensitivity for both subtle and intensive human activity detection [55]. To address the drawbacks of simply overlapping 2D graphene in composite materials, architected 3D graphene structures have been utilized as an effective reinforcing agent to enhance the linear sensing range and sensitivity of graphene/polymer composite-based sensors as well [56, 57].

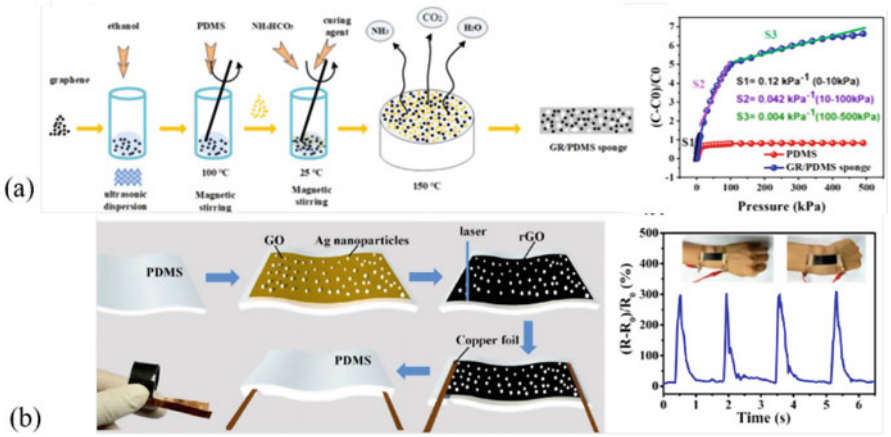

Fig. 5.5 (**a**) Graphene-based polymeric composite with PDMS sponge matrix, exhibiting high piezoresistive sensitivity. (Reprinted from Ref. [54] with permission from Springer Nature). (**b**) Metal nanoparticle-bridged graphene/polymer composite sensors for detecting subtle and intensive human activities. (Reprinted from Ref. [55] with permission from American Chemical Society)

5.3 Structure

In carbon-based piezoresistive pressure sensors, the principle mechanism of resistance modification is conductive pathway modulation. By controlling the size, shape, and fraction of microstructures in a composite, it is possible to tune the electrical response, sensitivity, and mechanical properties of the sensor, with a decreased dependence on the intrinsic characteristics of the constituent materials. This facilitates a more robust implementation and finer control of specific properties of the resultant composite.

For example, consider a composite material X, consisting of an elastomeric matrix material and a conductive filler, and a sensor A, made with bulk material X. Consider another sensor B, made with the same material X, as well as having incorporated microstructures. For sensor A, if the sensitivity or conductivity of the sensor is to be increased, the loading of the conductive phase must also be increased. This cannot be done to an arbitrary degree, as excessive increases in conductivity would cause decreases in sensitivity (Gauge Factor, GF), given by equation 5.1, where ΔR is resistance change (upon application of a given strain ϵ), R_0 is the initial resistance of the sensor, ϵ is the strain, ΔL is the length change, and L_0 is the initial length.

$$GF = \frac{\frac{\Delta R}{R_0}}{\epsilon} \qquad \epsilon = \frac{\Delta L}{L_0} \tag{5.1}$$

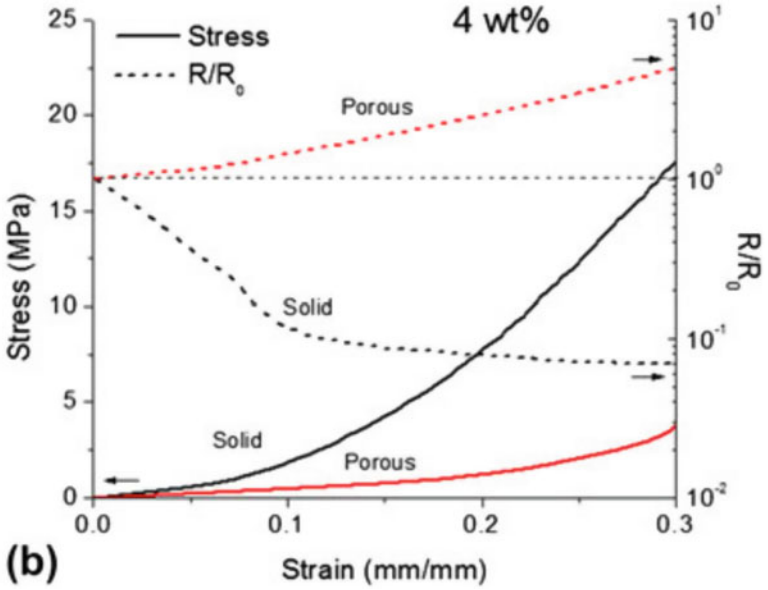

Fig. 5.6 Mechanical and electrical response of a TPU/multi-walled carbon nanotube composite, with and without porosity. (Reprinted with permission from Ref. [62]. Copyright 2013 Cambridge University Press)

Additionally, increase in the amount of the conductive phase will result in an increase in the stiffness of the overall composite, as increasing the filler loading ratio will cause the properties of the composite to tend towards those of the filler material [58–60].

If these effects could be decoupled, finer tuning of sensor performance and more control over material properties could be achieved. It is possible to do this (implementing sensor B in the example above) by leveraging microstructures such as nanoscale pores [2, 61, 62]. The concentration of these pores is given by equation 5.2, where f is the fraction of pores, M is the mass of fillers, V is the volume of the fillers, and ρ_0 is the density of the fillers.

$$f = 1 - \frac{M}{V\rho_0} \tag{5.2}$$

This relationship can be clearly seen in Fig. 5.6, where not only are the electrical and mechanical properties of the composite material made more linear (a beneficial trait for sensors in general), but the electrical response with respect to deformation is inverted, with the resistance increasing instead of decreasing when pressure is applied, tracking the applied stress well.

Yet another factor to be mindful of when developing sensing composites is the percolation threshold of the filler in the matrix. Percolation is the phenomenon by

which a significant change (typically an increase) in one or more properties of a system occurs. It is estimated by equation 5.3 where σ is the conductivity of the composite material, Φ is the volume fraction of the filler in the composite, Φ_C is the volume fraction of the filler that is the percolation threshold (or the critical value of the filler fraction) [63]. The exponent t is a fitting parameter based on dimensionality, and has been shown empirically and theoretically to be between 1 and 4 for polymer-carbon nanoparticle systems [64].

$$\sigma \propto (\Phi - \Phi_C)^t \tag{5.3}$$

This proportionality can be represented as a scaling factor applied to a base value, as shown in equation 5.4 where the base value σ_0 is the conductivity of the conductive filler [64].

$$\sigma = \sigma_0(\Phi - \Phi_C)^t \tag{5.4}$$

The percolation threshold is the volume fraction of a filler material in a matrix such that long range connectivity is established, and can be derived algebraically from equation 5.4, as shown in equation 5.5

$$\Phi_C = \Phi - \sqrt[t]{\frac{\sigma}{\sigma_0}} \tag{5.5}$$

As such, the loading (Φ) of a conductive phase in a composite should be above the percolation threshold (Φ_C) of the system in order to ensure that sufficient conductivity will be established. However, because percolation is statistical in nature, the percolation threshold describes the concentration of filler at which the likelihood of the existence of a conductive network throughout the composite becomes very high.

However, this does not necessarily preclude the existence of conductive pathways at filler loadings below Φ_C, nor does it necessarily guarantee the existence of conductive pathways above Φ_C. As such, it is advisable for some safety margin to be added to Φ_C in order to shift the loading of the system by a safe amount from the threshold, where chance and slight variations have a more pronounced effect.

The formation of this network causes the conductivity of the composite to increase sharply, as a filler network is established throughout the composite, increasing the likelihood that a charge will be able to travel from any point to any other. The percolation threshold and network formation of fillers provide yet another method for the modification of sensor properties.

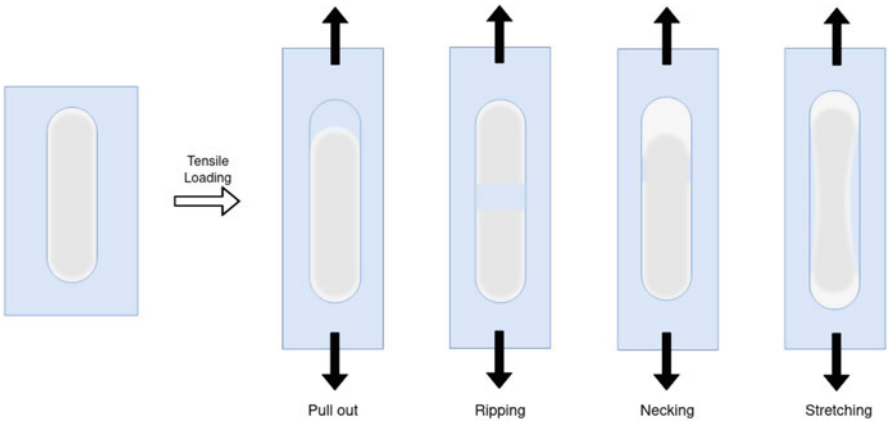

Fig. 5.7 Pull out effects that cause damage to the matrix-filler interface

5.3.1 Effects of Deformation

The degree to which deformation causes a shape change in a sample is a function of both the moduli and relative concentrations of the matrix and the filler. When choosing a matrix material, the use case of the final composite should be taken into account (i.e. anticipated strain and environmental compatibility).

Additionally, the forces from deformation that the matrix experiences are transferred to the filler material via the matrix-filler interface. As such, the relative stiffness of these phases, as well as the strength of their interface, is particularly important. If the filler material is much stiffer than the matrix and not allowed to deform, or if the strength of the interface is insufficient for the loads experienced, damage to the interface may occur. Specifically, filler slipping, buckling, ripping, necking, etc. may occur, as illustrated in Fig. 5.7. This causes a permanent decrease in sensitivity as a result of the damage to the composite.

Since excessive deformation can cause damage to fillers, and thus degradation of sensor performance, care should be taken when selecting a conductive phase. A way of alleviating this concern is to architect the structure of the material, allowing the potentially damaging loads from being borne by the fillers or their interface with the matrix, which will be covered in the following section.

5.3.2 Structure Morphology

As non-planar microstructures reside in the bulk material between sensor faces, the bulk is leveraged to increase the change of interfacial area in response to applied strain, thus creating more sites for conductive pathway modification. While these sensors can be very sensitive, they also have a low, narrow pressure range that they

are sensitive in, with greater pressures leading to no significant change in the output signal (saturation). From this point on, any further change in resistance is due to the piezoresistive properties of the bulk material, because the microstructures have collapsed and the composite subsequently behaves as a bulk material. As discussed, the piezoresistive performance of bulk materials is typically low. Since any change in resistance is ultimately due to the increased or decreased proximity of conductive elements in the matrix, the only way for this change to occur in a bulk material is by damaging the filler or straining the bulk-filler interface (see Sect. 5.3.1).

In the following sections, a distinction will be made between *subtractive* and *formed* voids, as their fabrication methods and resulting behaviors can be grouped. For the purposes of this discussion, the terminology *subtractive voids* will be used to refer to porosity that has been introduced by the removal of some sacrificial phase. *Formed voids* will be used to refer to porosity that has been introduced via the forming/molding/deposition of the material.

As discussed in Sect. 5.1, the mechanism by which the resistance through a composite material is changed with respect to pressure is based on the proximity (and contact) of the introduced conductive filler. Based on the cell structure and fabrication process, a composite can be synthesized such that its resistance increases or decreases with an applied strain. Composites that exhibit a decrease in resistance with applied pressure typically employ a fabrication process that exposes the filler to voids throughout the bulk. As such, when these voids are progressively collapsed by an applied pressure, the conductive elements exposed at the void interface are allowed to make contact, decreasing the resistance of the material. Composites that exhibit an increase in resistance when an external pressure is applied are typically fabricated such that the conductive elements throughout the composite are encased in the matrix material. In this case, when a pressure is applied, conductive pathways throughout the material are made longer, as the deformation of the pores causes the elements and the paths surrounding those pores bow, becoming disjointed.

5.3.2.1 Subtractive Voids

Voids can be introduced with different geometries, depending on the method of pore induction. It has been shown that sensitivity increases as porosity increases – that is, as the volume fraction of the space that is occupied by voids in the material increases [2]. This can be accomplished by increasing the pore fraction of the composite. While the porosity can also be increased by increasing the size of the pores, this method would not increase the sensitivity of the composite. Even through the porosity is being increased, in this case, the increased size of the pores decreases the number of conductive pathway modification sites present, causing an overall decrease in sensitivity. Depending on the fabrication method, the porosity of these composites can be adjusted, allowing sensors made with them to observe different ranges of pressures, potentially with modified sensitivities.

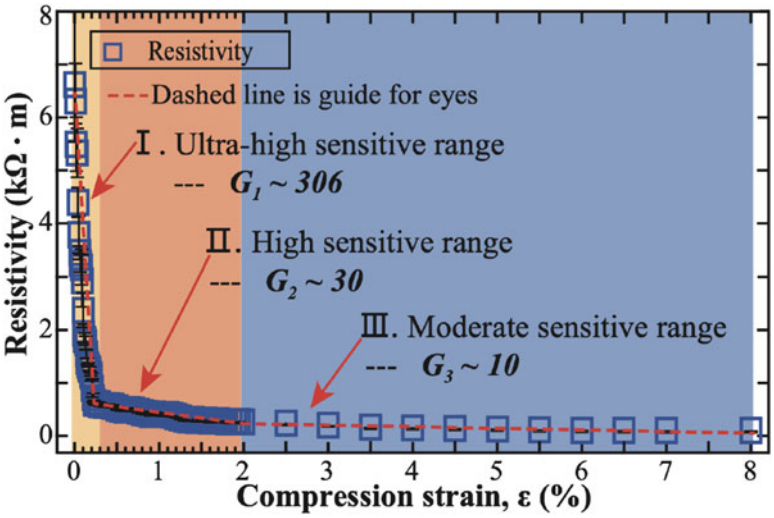

Fig. 5.8 Resistivity change of the CNT/PDMS porous nanocomposite under compression strain (pressure). (Reproduced from Ref. [2] with permission from The Royal Society of Chemistry)

An effective method for the implementation of such composites typically involves the removal of some place-holding element, whose removal introduces a void. Fabrication techniques for these kinds of sensors include freeze casting (Sect. 5.4.2) and cast etching (Sect. 5.4.3). Due to the nature of the fabrication process, conductive elements are typically available at the faces of the internal voids, causing the resistivity of the composite to decrease with an applied pressure (Fig. 5.8).

As composites with low pore density are primarily comprised of the bulk material, they retain more of the properties of the bulk material. As such, these composites are appropriate for use in applications where higher loads are expected, and reduced sensitivity is acceptable. They are also beneficial in applications where the load may not be well-known beforehand, as the composite is less likely to be compromised by strains that are not damaging to the bulk material. This is in contrast to composites that have more empty space, as the reduced amount of bulk material (per unit volume) is responsible for the transmission of the same amount of energy.

In addition, the aspect ratio of the pores can also be modified with an appropriate fabrication process. Composites containing non-isometric pores exhibit different behaviors when the pores are aligned (with respect to their principle axes) as opposed to being randomly oriented throughout the sample [61]. Such a composite potentially possesses a mechanism for the detection of loading direction.

5.3.2.2 Formed Voids

Foams are popular because they provide high surface area via typically simple fabrication methods such as dip coating [65] and gas foaming [62]. The coating of foam scaffolds, with either a conductive phase or conductive phase suspended in an elastomeric carrier, is popular due to the ease of fabrication and high sensitivity achieved. When coated, these sensors provide an open-cell structure and a high surface area, which results in an increased number of sites throughout the composite for the modification of electrical pathways.

However, these sensors do not gain much strength or rigidity from their conductive fillers (as it is typically a thin surface coating). So, they can only detect strains similar to those the foam scaffold is able to withstand. Furthermore, if excessive force is applied, it is possible to irreversibly damage the foam structure and/or coating, compromising the sensor. As such, these sensors are best suited for applications where high sensitivity and known, relatively low loads are to be measured.

Gas foaming is also a popular method for creating foams. The created foams can have either an open- or closed-cell structure, controlled by a heating and quenching process. Such foams can be tuned to have more or less porosity, allowing the mechanical and electrical response of the material to be finely controlled. The Fig. 5.9 shows the porosity that is introduced into a TPU/MWCNT nanocomposite by a gas forming process [66]. Since the interfaces of the pores and matrix were not defined by the removal of a sacrificial phase, it is the case that these voids have well-defined boundaries. As such, there typically are not exposed conductive elements at these boundaries. As a result, the majority of the electrical response of such a composite is due to the contact between the internal conductive elements, which can cause the resistance of the composite to increase with an applied pressure due to disruption of the conductive filler network [66].

Such a sensor is appropriate for when either high or low loading is expected, as the materials that can be used have a wider range of moduli and the amount of porosity introduced can be limited to preserve the strength of the reinforced bulk.

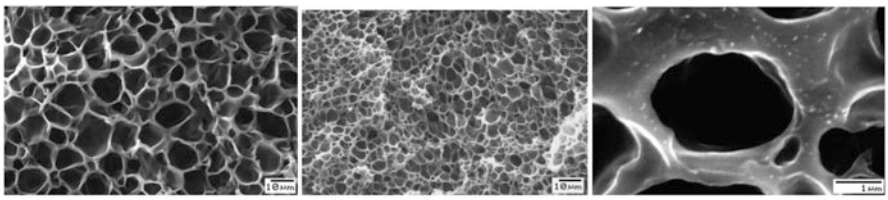

Fig. 5.9 TPU/MWCNT foam fabricated with CO_2 foaming. SEM images shows MWCNTs surrounding pores. (Reprinted from Ref. [66]. Copyright 2014, with permission from AIP Publishing)

5.4 Fabrication

The fabrication method used to synthesize a composite material varies based on the nature of its constituents, but primarily the matrix material, as carbon fillers are typically very stable and non-reactive (and are thus compatible with a wide range of processes and treatments). The fabrication method will dictate not only the morphology of the composite, but also its mechanical properties, as different fabrication techniques introduce differing levels of porosity and control. It is also important to note that the fabrication technique for one composite system may not be appropriate for another, and may even cause damage to the matrix. Note the effect of the use of hydrochloric acid on PDMS (little to none) versus TPU (high degradation) in an etching-based process as an example.

5.4.1 Mixing and Dispersion

Homogeneous dispersion of the filler in the matrix is important for any fabrication method used to develop porous composite sensors. As such, thorough mixing is crucial. Mixing facilitates thorough incorporation of fillers, ensuring homogeneity and uniform properties throughout the composite and making characterization of, and measurements with, the material reproducible and reliable. Inadequate dispersion can lead to varying electrical responses and material properties throughout the material, making characterization of the composite and measurements performed with sensors made of the composite difficult. Carbon fillers are typically hydrophilic, owing to the strength of carbon-carbon bonds (among the strongest in nature). Because of this, carbon fillers do not tend to readily mix with most matrix materials. As such, adequate dispersion is needed. This is typically done in one of two ways: (1) mechanically, through the addition of energy (mixing, ultrasonication) to promote the separation of filler agglomerates, or (2) chemically, through the addition of hydrophilic groups to the carbon fillers, which will be further described below.

5.4.1.1 Ultrasonication

Carbon-carbon bonds are very strong and as such, carbon fillers are very stable and do not readily dissolve in solvents or disperse in a matrix. Thus, mechanical mixing/dispersion is required to ensure uniform dispersion of the filler. Ultrasonication is commonly used for its ability to deliver mechanical energy to fillers in solution. This energy can serve to break up or disentangle nanotube bundles, nanoparticle clumps, and exfoliate (separate) layered graphitic structures. It is also important to note, however, that the quality, duration, and degree of this separation depends both on the nature of the filler (functionalization, geometry, etc.), the solvent in which the

mixing occurs (polar, organic, etc.), and their interaction. Also of consideration is the fitness of the method of energy delivery with respect to the nature of the system, i.e. a metallic ultrasonic horn would be a poor choice for use in a system where the solvent is strongly corrosive to that type of metal.

5.4.1.2 Filler Functionalization

Because of the tendency of carbon fillers to not readily disperse due to the stability of its carbon-carbon bonds, it may be desirable to chemically treat them so as to add functional groups to their carbon structure. These functional groups promote dispersion by interacting with the surrounding fluid during fabrication. While this means that the carbon filler itself is still not interacting with the solvent, the functional groups allow it to remain suspended in solution through the repulsion that occurs between the functional elements attached to filler particles, as well as the size of the functional group preventing the carbon-based fillers from coming too close together. These effects prevent $\pi - \pi$ stacking and van der Waals force from causing the filler to agglomerate, allowing it to remain suspended [67, 68].

While this promotes dispersion, it also diminishes the exceptional electrical and mechanical properties of the carbon filler, as some of the carbon bonds that give rise to the exceptional electrical and mechanical properties of carbon fillers are broken to add functional groups (in the case of covalently bonded functional groups) [67, 68]. While a comprehensive discussion of the nature and methods of carbon functionalization is beyond the scope of this chapter, it is prudent to highlight that functional groups can be added either covalently or non-covalently.

When adding groups covalently, the filler is chemically treated such that the valence electrons of the filler and the functional group are shared. A notable subclass of this approach is doping, whereby carbon atoms in the filler are replaced with atoms of other elements, providing a degree of tunability of the electrical behavior of the filler. When adding functional groups noncovalently, the groups are affixed via $\pi - \pi$ bonds, van der Walls force, or other attractive forces. While each has its advantages based on application, it is important to note that carbon-based fillers that have functional groups covalently bonded generally posses decreased conductivity, which may be important from the standpoint of the implementation of a pressure sensor (to be weighed against the effect and benefits of homogeneity in a given application).

5.4.2 Freeze Casting

When using freeze casting to induce porosity, the process is two-fold: (1) template the composite (in liquid form) with ice, and (2) remove the ice, leaving behind a porous structure. When freezing the solution, a temperature gradient needs to be established. This enables the controlled growth of ice crystals in the solution,

which provides control over the morphology of the pores. Of special importance is the relationship between the rate at which ice is formed in the solution and the displacement of the composite material by those ice crystals [69]. In order for the composite material to be displaced by the formed ice, the inequality presented in equation 5.6 must be satisfied, where γ_{cs} and γ_{cl} are the free energies that exist between the composite material and the solid and liquid phases of the solvent respectively, and γ_{sl} is the free energy that exists at the boundary of the solid and liquid phases of the solvent.

$$\Delta\gamma_0 = \gamma_{cs} - (\gamma_{cl} + \gamma_{sl}) > 0 \tag{5.6}$$

Equally important is the control of the velocity of the ice front, v, relative to the critical ice front velocity, v_{cr}. This critical velocity is the threshold at which the composite material in the solution is not displaced quickly enough to remain external to the ice formed. It is given by equation 5.7, where d is the thickness of the layer of unfrozen solvent that exists between the solvent ice and the composite, η is the viscosity of the liquid-phase solvent, r is the radius of the particle (in the particle model illustrated in Fig. 5.10), α_0 is the distance between particles, and n is a correction factor [69].

If energy is removed too slowly ($v \ll v_{cr}$), a planar ice front (rather than discrete crystals) will propagate in the desired direction. This ice front will displace all of the composite material ahead of it, leading to little or no porosity being induced. If the solution is frozen too quickly ($v \geq v_{cr}$), the ice crystals will form rapidly throughout the solution, encasing the composite material throughout (see Fig. 5.10d). When the velocity of the ice front is in the appropriate range for the system of interest (Fig. 5.10c), well defined structures of ice will form and grow in the composite, effectively displacing the composite material and templating the solution, as shown in Fig. 5.11.

$$v_{cr} = \frac{\delta\gamma_0 d}{3\eta r}\left(\frac{\alpha_0}{d}\right)^n \tag{5.7}$$

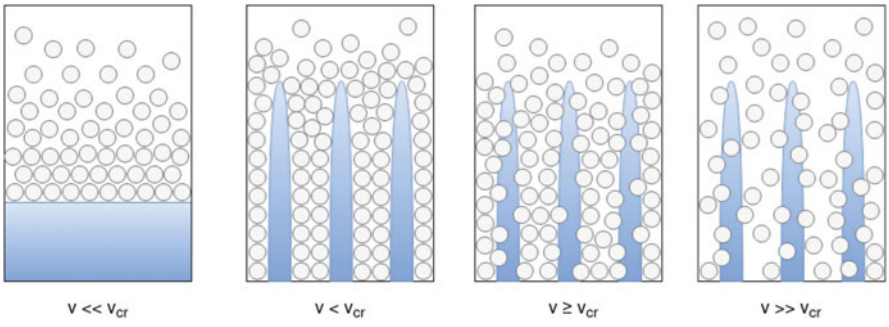

Fig. 5.10 Particle model schematic of ice front dynamics during freeze casting

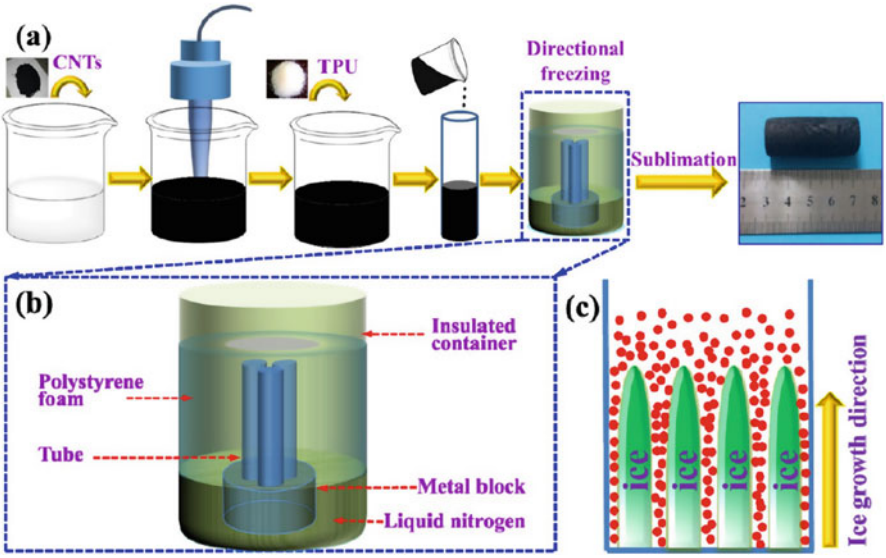

Fig. 5.11 Freeze casting schematic for the fabrication of porous, carbon-based nanocomposites. (Reprinted with permission from Ref. [61]. Copyright 2017 American Chemical Society)

After the entire sample is frozen, the ice is then removed via freeze-drying. During this process, the sample is placed in a chamber, in which a vacuum is then established (based on the phase diagram of the solvent used). When the pressure is sufficiently low, the ice in the sample will be able to sublimate (change phase from solid to gas, without becoming liquid) and be removed in its gaseous state. This is crucial, as the ice serves as a template for the to-be-made sample. If the ice that was formed transitions through a liquid before becoming gaseous, the sample will lose the imposed structure, leading to no porosity being induced.

5.4.3 Sacrificial Cast-Etching

In sacrificial cast etching, the sacrificial filler is mixed into a polymer (or its precursor), and then selectively removed after curing, typically through the use of solvents that act only, or preferentially, on the sacrificial filler (see Fig. 5.12). The porosity can be controlled through both the size of the sacrificial particles and the amount of this sacrificial phase that is introduced.

The particle properties can be chosen based on matrix and response to solvent. Because the removal of the sacrificial particle is most typically performed by a solvent, care should be taken with respect to nanoparticle selection such that the solvent of the particle does not inadvertantly degrade the matrix material (as the

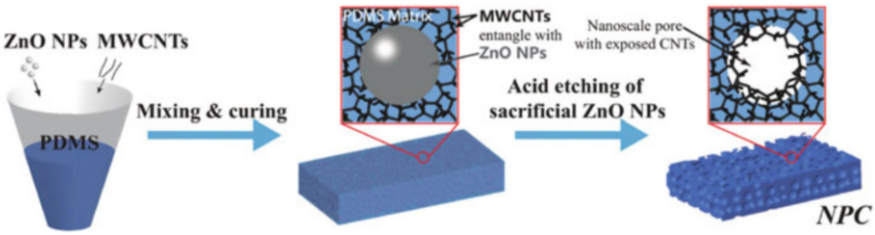

Fig. 5.12 Schematic of sacrificial cast-etching. (Reproduced from Ref. [2] with permission from The Royal Society of Chemistry)

case for hydrochloric acid and TPU, for example). Furthermore, while it might seem obvious, it is critical for the success of this fabrication method that the solvent is able to reach the particles that are to be removed. If the structure of the porosity induced is not an open-cell structure, the matrix, in addition to being resistant to the solvent used, must also be permeable to it.

5.4.3.1 Gas Foaming

Gas foaming describes the use of a gas for the induction of pores in a matrix. Though CO_2 is most widely used, other gasses (such as N_2, Ar, or other inert gasses) can be used [70, 71]. For example, the sample composite material is immersed in supercritical CO_2. The CO_2 then dissolves into the polymer, forming a solid solution. It is important to note the glass transition temperature (T_g) of many polymers drops with an increase in pressure. As such, the polymer that has dissolved CO_2 present throughout is also likely to be near its transition point. The sample is then pressure quenched as the saturation chamber is rapidly de-pressurized. As the pressure is released, the dissolved CO_2 leaves the supercritical regime (becoming a gas) while the polymer matrix is still able to be easily deformed. Simultaneously, the matrix material leaves its glass regime with the decrease in pressure, causing the gaseous CO_2 and deformable matrix material to coexist for a very brief amount of time. This combination of conditions causes nanoscale pores (nucleation sites for future porosity) to form (see Fig. 5.13).

To increase the size of the pores, thermally induced phase separation is used. The sample can be introduced to an environment (typically liquid) or bath above T_g, causing the matrix to become deformable while simultaneously causing the precipitation of the dissolved CO_2 out of the solid solution (at the nucleation sites developed during pressure quenching). This combination causes the matrix material to foam as the pores increase in size. This pore growth can be stopped by thermally quenching the sample.

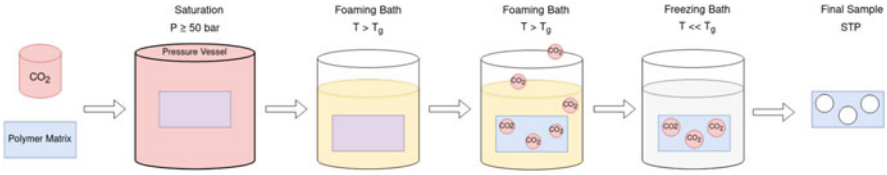

Fig. 5.13 A schematic example of the gas-foaming process

5.5 Discussion

In this section, we will discuss some of the challenges and future opportunities of nanoporous composite sensors.

5.5.1 Challenges

While there is exciting development and progress in the field, there are also challenges, including scalable fabrication approaches for composite sensors with sophisticated structures and environmental operation ranges for composite-based sensors.

As discussed in Sect. 5.3 (Structure), incorporation of internal or external structures to composites can improve the sensitivity of devices implemented with them, and can be used to modulate their properties. For some types of complex structures, there are challenges of fabrication in terms of scalability, time, and cost. To address these challenges, one can potentially consider approaches such as nanoimprinting and self-assembly for parallel patterning of large areas in a cost-effective manner.

Besides the fabrication challenges, each composite has a range of environments that it can be used in, as composites can change or lose their functionality in extreme environments such as high/low temperatures and high humidity. For example, polymers exhibit significant changes of their mechanical properties around their glass transition temperature, T_g. If the sensor based on a polymer matrix will be used for a wide range of temperatures, one needs to consider the effect of an environment on the matrix of the composite. Moreover, polymers can degrade or melt at elevated temperatures, which will damage the composite and the sensor. Polymers can also become quite brittle at a very low temperature. So, depending on the environment in which the sensor will be utilized, one need to choose a polymer matrix with suitable thermal stability. These issues can be also mitigated by encapsulation.

5.5.2 *Opportunities*

Beyond the current capability of composite sensors, there are potential opportunities for further improvement. Nature and its many organisms are a constant source of inspiration for scientists and engineers. One can learn from natural organisms for expanding the types of information to sense, as well as improving the sensitivity of sensors.

For example, many insects and fish use hair-like structures for detecting flow, vibration, and sound [72, 73]. Incorporating structures with adequate bending stiffness or resonance can be used as a method for sensing a specific range and type of signal, informing the detection of stimuli ranging from flow rate of a fluid to propioception (knowledge of the relative position or orientation of body parts) in robotic applications.

One can glean inspiration for multifunctional sensors, such as skins, that can detect multiple stimuli such as temperature, pressure, and strain [74] and utilize filler materials that change their resistivity as a function of temperature, pressure, and strain for detecting multiple stimuli by decoupling contributions from each environmental stimulus, an aspect where advanced signal processing algorithms or machine learning can help.

The use of soft matrices, such as elastomers, provides additional opportunities such as usage in high pressure environments including underwater from their incompressibility and durability. In addition, the fact that the matrix material changes its properties can be utilized as sensing mechanisms of, for example, temperature and/or humidity.

5.6 Conclusion

Nanoporous composites are attractive materials for sensor applications due to their desirable characteristics including tunability, low cost, light weight, ease of shaping, and scalability. As nanoporous composites allow us to modulate the properties of materials for applications and required sensing capabilities (e.g. types of signals to detect, sensitivity, sensing range) and associated mechanical and electrical properties, there have been many studies to investigate compositions, constituent materials, and the internal/external structures for controlling mechanical/electrical/electrochemical properties of composites, as well as the associated sensitivity and sensing range of the devices fabricated from these composites.

To provide guidance for synthesis of nanoporous composites, we first compared various materials then described structural features to enhance and/or tune sensing capability and associated fabrication methods. To ensure uniform mixing of matrix and filler and introduce pores with desirable size range and fraction, there have been many studies to facilitate the process by overcoming challenges such as clumping and segregation. Then, we discussed the challenges and opportunities for future studies.

Currently, nanoporous composite-based sensors are utilized for measuring signals such as strain, pressure, temperature, physiological conditions, gas, humidity, and antibiotic agent detection. They can be found in various applications including flexible/wearable devices, human-machine interfaces, health/environment monitoring devices, and soft robotics. We envision that future studies can expand the sensing capability of nanoporous composite-based sensors by enhancing sensitivity, increasing the sensing range, and enabling detection of multiple signals in cost-effective ways.

Acknowledgments This work was partially supported by the Office of Naval Research (Award No.: N00014-19-1-2673, Program Manager: Dr. Reginald Beach) and the start-up funds from the Whiting School of Engineering at Johns Hopkins University and the Natural Science Foundation of Hubei Province (No. 2020CFB391).

References

1. Cho, D., Park, J., Kim, J., Kim, T., Kim, J., Park, I., Jeon, S.: Three-dimensional continuous conductive nanostructure for highly sensitive and stretchable strain sensor, ACS Appl. Mater. Interfaces **9**(20), 17369–17378 (2017)
2. Li, J., Orrego, S., Pan, J., He, P., Kang, S.H.: Ultrasensitive, exible, and low-cost nanoporous piezoresistive composites for tactile pressure sensing, Nanoscale **11**(6), 2779–2786 (2019)
3. Zhao, X.-H., Ma, S.-N., Long, H., Yuan, H., Tang, C.Y., Cheng, P.K., Tsang, Y.H.: Multifunctional sensor based on porous carbon derived from metal–organic frameworks for real time health monitoring, ACS Appl. Mater. Interfaces **10**(4), 3986–3993 (2018)
4. Travlou, N.A., Bandosz, T.J.: Nanoporous carbon-composites as gas sensors: Importance of the specific adsorption forces for ammonia sensing mechanism, Carbon **121**, 114–126 (2017)
5. Xiao, S.H., Xu, H.J., Hu, J., Jiang, W.F., Li, X.J.: Structure and humidity sensing properties of barium strontium titanate/silicon nanoporous pillar array composite films, Thin Solid Films **517**(2), 929–932 (2008)
6. Miglio, S., Bruzzi, M., Scaringella, M., Menichelli, D., Leandri, E., Baldi, A., Bongiorno, G., Piseri, P., Milani, P.: Development of humidity sensors based on nanostructured carbon films, Sens. Actuat. B: Chem. **111–112**, 140–144 (2005)
7. Guo, W., Umar, A., Alsaiari, M.A., Wang, L., Pei, M.: Ultrasensitive and selective label-free aptasensor for the detection of penicillin based on nanoporous ptti/graphene oxide-fe3o4/mwcnt-fe3o4 nanocomposite, Microchem. J. **158**, 105270 (2020)
8. Zare, Y., Rhee, K.Y.: Expression of characteristic tunneling distance to control the electrical conductivity of carbon nanotubes-reinforced nanocomposites, J. Mater. Res. Technol. **9,** 22–32 (2020).
9. Zare, Y., Rhee, K.Y.: Effects of network, tunneling, and interphase properties on the operative tunneling resistance in polymer carbon nanotubes (cnts) nanocomposites, Poly. Comp. **41**(7), 2907–2916 (2020)
10. Zhang, R., Deng, H., Valenca, R., Jin, J., Fu, Q., Bilotti, E., Peijs, T.: Carbon nanotube polymer coatings for textile yarns with good strain sensing capability, Sens. Actuat. A: Phys. **179**, 83–91 (2012)
11. Li, J., Fang, L., Sun, B., Li, X., Kang, S.H.: Review—Recent Progress in Flexible and Stretchable Piezoresistive Sensors and Their Applications, J. Electrochem. Soc. **167**(3), 037561 (2020)
12. Harris, P.J.: Carbon nanotube composites, Int. Mater. Rev. **49**(1), 31–43 (2004)

13. Spahr, M.E., Gilardi, R., Bonacchi, D.: In: Rothon, R. (ed.) Fillers for Polymer Applications, pp. 375–400. Springer International Publishing, Cham, (2017)
14. Huang, J.C.: Carbon black filled conducting polymers and polymer blends, Adv. Poly. Technol. **21**(4), 299–313 (2002)
15. Chang, X., Sun, S., Sun, S., Liu, T., Xiong, X., Lei, Y., Dong, L., Yin, Y.: ZnO nanorods/carbon black-based exible strain sensor for detecting human motions, J. Alloys Comp. **738**, 111–117 (2018)
16. Shintake, J., Piskarev, E., Jeong, S.H., Floreano, D.: Ultrastretchable Strain Sensors Using Carbon Black-Filled Elastomer Composites and Comparison of Capacitive Versus Resistive Sensors, Adv. Mater. Technol. **3**(3), 1–8 (2018)
17. Shang, S., Yue, Y., Wang, X.: Piezoresistive strain sensing of carbon black /silicone composites above percolation threshold, Rev. Sci. Instrum. **87**(12), 1–6 (2016)
18. Duan, L., Spoerk, M., Wieme, T., Cornillie, P., Xia, H., Zhang, J., Cardon, L., D'hooge, D.R.: Designing formulation variables of extrusion-based manufacturing of carbon black conductive polymer composites for piezoresistive sensing, Comp. Sci. Technol. **171**, 78–85 (2019)
19. Chen, Y., Wang, L., Wu, Z., Luo, J., Li, B., Huang, X., Xue, H., Gao, J.: Super-hydrophobic, durable and cost-effective carbon black/rubber composites for high performance strain sensors, Comp. Part B: Eng. **176**, 107358 (2019)
20. Narongthong, J., Das, A., Le, H.H., Wießner, S., Sirisinha, C.: An efficient highly exible strain sensor: Enhanced electrical conductivity, piezoresistivity and exibility of a strongly piezoresistive composite based on conductive carbon black and an ionic liquid, Comp. Part A: Appl. Sci. Manuf. **113**, 330–338 (2018)
21. Chung, D.D.: Review: Graphite, J. Mater. Sci. **37**(8), 1475–1489 (2002)
22. Nag, A., Afasrimanesh, N., Feng, S., Mukhopadhyay, S.C.: Strain induced graphite/PDMS sensors for biomedical applications, Sens. Actuat. A: Phys. **271**, 257–269 (2018)
23. Luo, S., Liu, T.: Graphite nanoplatelet enabled embeddable fiber sensor for in situ curing monitoring and structural health monitoring of polymeric composites, ACS Appl. Mater. Interfaces **6**(12), 9314–9320 (2014)
24. Chen, L., Chen, G., Lu, L.: Piezoresistive behavior study on finger-sensing silicone rubber/graphite nanosheet nanocomposites, Adv. Funct. Mater. **17**(6), 898–904 (2007)
25. Chen, G., Wu, C., Weng, W., Wu, D., Yan, W.: Preparation of polystyrene/graphite nanosheet composite, Polymer **44**(6), 1781–1784 (2003)
26. Shen, Z., Feng, J.: Mass-produced SEBS/graphite nanoplatelet composites with a segregated structure for highly stretchable and recyclable strain sensors, J. Mater. Chem. C **7**(30), 9423–9429 (2019)
27. Yao, Z., Postma, H.W.C., Balents, L., Dekker, C.: Carbon nanotube intramolecular junctions, Nature **402**(6759), 273–276 (1999)
28. Gupta, N., Gupta, S.M., Sharma, S.K.: Carbon nanotubes: synthesis, properties and engineering applications, Carbon Lett. **29**(5), 419–447 (2019)
29. Wang, Y., Weng, G.J.: In: Micromechanics and Nanomechanics of Composite Solids, pp. 123–156. New York: Springer (2018)
30. Nasiri, A., Shariaty-Niasar, M., Rashidi, A.M., Khodafarin, R.: Effect of cnt structures on thermal conductivity and stability of nanofluid, Int. J. Heat Mass Transf. **55**(5–6), 1529–1535 (2012)
31. Wang, M., Zhang, K., Dai, X.X., Li, Y., Guo, J., Liu, H., Li, G.H., Tan, Y.J., Zeng, J.B., Guo, Z.: Enhanced electrical conductivity and piezoresistive sensing in multi-wall carbon nanotubes/polydimethylsiloxane nanocomposites: Via the construction of a self-segregated structure, Nanoscale **9**(31), 11017–11026 (2017)
32. Zheng, Y., Li, Y., Dai, K., Wang, Y., Zheng, G., Liu, C., Shen, C.: A highly stretchable and stable strain sensor based on hybrid carbon nanofillers/polydimethylsiloxane conductive composites for large human motions monitoring, Comp. Sci. Technol. **156**, 276–286 (2018)
33. Sepúlveda, A.T., Guzman De Villoria, R., Viana, J.C., Pontes, A.J., Wardle, B.L., Rocha, L.A.: Full elastic constitutive relation of non-isotropic aligned-CNT/PDMS exible nanocomposites, Nanoscale **5**(11), 4847–4854 (2013)

34. Mai, H., Mutlu, R., Tawk, C., Alici, G., Sencadas, V.: Ultra-stretchable MWCNT–Eco ex piezoresistive sensors for human motion detection applications, Comp. Sci. Technol. **173**, 118–124 (2019)
35. Akindoyo, J.O., Beg, M.D., Ghazali, S., Islam, M.R., Jeyaratnam, N., Yuvaraj, A.R.: Polyurethane types, synthesis and applications-a review, RSC Adv. **6**(115), 114453–114482 (2016)
36. Domun, N., Hadavinia, H., Zhang, T., Sainsbury, T., Liaghat, G.H., Vahid, S.: Improving the fracture toughness and the strength of epoxy using nanomaterials-a review of the current status, Nanoscale **7**(23), 10294–10329 (2015)
37. Mahar, B., Laslau, C., Yip, R., Sun, Y.: Development of Carbon Nanotube-Based Sensors—A Review, IEEE Sens. J. **7**(2), 266–284 (2007)
38. Gu, H., Zhao, Y., Wang, M.L.: A wireless smart PVDF sensor for structural health monitoring, Struct Control Health Monitor **12**(3–4), 329–343 (2005)
39. Gong, S., Zhu, Z.H., Meguid, S.A.: Carbon nanotube agglomeration effect on piezoresistivity of polymer nanocomposites, Polymer **55**(21), 5488–5499 (2014)
40. Geim, A.K.: Graphene: status and prospects, Science **324**(5934), 1530–1534 (2009)
41. Novoselov, K.S., Geim, A.: The rise of graphene, Nat. Mater **6**(3), 183–191 (2007)
42. Huang, X., Qi, X., Boey, F., Zhang, H.: Graphene-based composites, Chem. Soc. Rev. **41**(2), 666–686 (2012)
43. Papageorgiou, D.G., Kinloch, I.A., Young, R.J.: Mechanical properties of graphene and graphenebased nanocomposites, Prog. Mater. Sci. **90**, 75–127 (2017)
44. Papageorgiou, D.G., Kinloch, I.A., Young, R.J.: Graphene/elastomer nanocomposites, Carbon **95**, 460–484 (2015)
45. Ling, Y., Pang, W., Li, X., Goswami, S., Xu, Z., Stroman, D., Liu, Y., Fei, Q., Xu, Y., Zhao, G., others: Laserinduced graphene for electrothermally controlled, mechanically guided, 3d assembly and human–soft actuators interaction, Adv. Mater. **32**(17), 1908475 (2020)
46. Ling, Y., Zhuang, X., Xu, Z., Xie, Y., Zhu, X., Xu, Y., Sun, B., Lin, J., Zhang, Y., Yan, Z.: Mechanically assembled, three-dimensional hierarchical structures of cellular graphene with programmed geometries and outstanding electromechanical properties, ACS Nano **12**(12), 12456–12463 (2018)
47. Jing, Z., Guang-Yu, Z., Dong-Xia, S.: Review of graphene-based strain sensors, Chin. Phys. B **22**(5), 057701 (2013)
48. Mehmood, A., Mubarak, N.M., Khalid, M., Walvekar, R., Abdullah, E.C., Siddiqui, M.T., Baloch, H.A., Nizamuddin, S., Mazari, S.: Graphene based nanomaterials for strain sensor application - A review, J. Environ. Chem. Eng. **8**(3), 103743 (2020)
49. Kumar, R., Singh, R., Hui, D., Feo, L., Fraternali, F.: Graphene as biomedical sensing element: State of art review and potential engineering applications, Comp. Part B: Eng. **134**, 193–206 (2018)
50. Sun, B., McCay, R.N., Goswami, S., Xu, Y., Zhang, C., Ling, Y., Lin, J., Yan, Z.: Gas-permeable, multifunctional on-skin electronics based on laser-induced porous graphene and sugar-templated elastomer sponges, Adv. Mater. **30**(50), 1804327 (2018)
51. Nag, A., Mitra, A., Mukhopadhyay, S.C.: Graphene and its sensor-based applications: A review, Sens. Actuat. A: Phys. **270**, 177–194 (2018)
52. Xu, Y., Sun, B., Ling, Y., Fei, Q., Chen, Z., Li, X., Guo, P., Jeon, N., Goswami, S., Liao, Y., others: Multiscale porous elastomer substrates for multifunctional on-skin electronics with passive-cooling capabilities, Proc. Natl. Acad. Sci. **117**(1), 205–213 (2020)
53. Boland, C.S., Khan, U., Ryan, G., Barwich, S., Charifou, R., Harvey, A., Backes, C., Li, Z., Ferreira, M.S., Möbius, M.E., Young, R.J., Coleman, J.N.: Sensitive electromechanical sensors using viscoelastic graphene-polymer nanocomposites, Science **354**(6317), 1257–1260 (2016)
54. Kou, H., Zhang, L., Tan, Q., Liu, G., Dong, H., Zhang, W., Xiong, J.: Wireless wide-range pressure sensor based on graphene/pdms sponge for tactile monitoring, Sci. Rep. **9**(1), 1–7 (2019)

55. Yang, C., Li, L., Zhao, J., Wang, J., Xie, J., Cao, Y., Xue, M., Lu, C.: Highly Sensitive Wearable Pressure Sensors Based on Three-Scale Nested Wrinkling Microstructures of Polypyrrole Films, ACS Appl. Mater. Interfaces **10**(30), 25811–25818 (2018)
56. Wu, Z., Xu, C., Ma, C., Liu, Z., Cheng, H.M., Ren, W.: Synergistic Effect of Aligned Graphene Nanosheets in Graphene Foam for High-Performance Thermally Conductive Composites, Adv. Mater. **31**(19), 1–8 (2019)
57. Luo, N., Huang, Y., Liu, J., Chen, S.C., Wong, C.P., Zhao, N.: Hollow-Structured Graphene–Silicone-Composite-Based Piezoresistive Sensors: Decoupled Property Tuning and Bending Reliability, Adv. Mater. **29**(40), 1–9 (2017)
58. Tran, L., Kim, J.: A Comparative Study of the Thermoplastic Polyurethane/Carbon Nanotube and Natural Rubber/Carbon Nanotube Composites According to Their Mechanical and Electrical Properties, Fibers Poly. **19**(9), 1948–1955 (2018)
59. Rausch, J., Zhuang, R.C., Mäder, E.: Surfactant assisted dispersion of functionalized multi-walled carbon nanotubes in aqueous media, Comp. Part A: Appl. Sci. Manuf. **41**(9), 1038–1046 (2010)
60. Lan, Y., Liu, H., Cao, X., Zhao, S., Dai, K., Yan, X., Zheng, G., Liu, C., Shen, C., Guo, Z.: Electrically conductive thermoplastic polyurethane/polypropylene nanocomposites with selectively distributed graphene, Polymer **97**, 11–19 (2016)
61. Huang, W., Dai, K., Zhai, Y., Liu, H., Zhan, P., Gao, J., Zheng, G., Liu, C., Shen, C.: Flexible and Lightweight Pressure Sensor Based on Carbon Nanotube/Thermoplastic Polyurethane-Aligned Conductive Foam with Superior Compressibility and Stability, ACS Appl. Mater. Interfaces **9**(48), 42266–42277 (2017)
62. Rizvi, R., Naguib, H.: Porosity and composition dependence on electrical and piezoresistive properties of thermoplastic polyurethane nanocomposites, J. Mater. Res. **28**(17), 2415–2425 (2013)
63. Balberg, I., Azulay, D., Toker, D., Millo, O.: Percolation and tunneling in composite materials, Int. J. Modern Phys. B **18**(15), 2091–2121 (2004)
64. Bauhofer, W., Kovacs, J.Z.: A review and analysis of electrical percolation in carbon nanotube polymer composites, Comp. Sci. Technol. **69**(10), 1486–1498 (2009)
65. Zhong, W., Ding, X., Li, W., Shen, C., Yadav, A., Chen, Y., Bao, M., Jiang, H., Wang, D.: Facile fabrication of conductive graphene/polyurethane foam composite and its application on exible piezoresistive sensors, Polymers **11**(8), 16–19 (2019)
66. Rizvi, R., Naguib, H.: Development and characterization of piezoresistive porous TPU-MWNT nanocomposites, AIP Conf. Proc. **1593**, 383–387 (2014)
67. Kuila, T., Bose, S., Mishra, A.K., Khanra, P., Kim, N.H., Lee, J.H.: Chemical functionalization of graphene and its applications, Prog. Mater. Sci. **57**(7), 1061–1105 (2012)
68. Yang, G.-H., Bao, D.-D., Liu, H., Zhang, D.-Q., Wang, N., Li, H.-T.: Functionalization of Graphene and Applications of the Derivatives, J. Inorg. Organometal. Poly. Mater. **27**(5), 1129–1141 (2017)
69. Shao, G., Hanaor, D.A.H., Shen, X., Gurlo, A.: Freeze casting: From low-dimensional building blocks to aligned porous structures—a review of novel materials, methods, and applications, Adv. Mater. **32**(17), 1907176 (2020)
70. Dehghani, F., Annabi, N.: Engineering porous scaffolds using gas-based techniques, Curr. Opin. Biotechnol. **22**(5), 661–666 (2011)
71. Santos-Rosales, V., Iglesias-Mejuto, A., García-González, C.A.: Engineering porous scaffolds using gas-based techniques, Polymers **12**(3), 533 (2020)
72. McHenry, M.J., van Netten, S.M.: The exural stiffness of superficial neuromasts in the zebrafish (danio rerio) lateral line, J. Exp. Biol. **210**(23), 4244–4253 (2007)
73. Pokroy, B., Epstein, A.K., Persson-Gulda, M.C., Aizenberg, J.: Fabrication of bioinspired actuated nanostructures with arbitrary geometry and stiffness, Adv. Mater. **21**(4), 463–469 (2009)
74. Xu, K., Lu, Y., Takei, K.: Multifunctional skin-inspired exible sensor systems for wearable electronics, Adv. Mater. Technol. **4**(3), 1800628 (2019)

Chapter 6
Laser-Induced Graphene and Its Applications in Soft (Bio)Sensors

Alexander Dallinger, Kirill Keller, and Francesco Greco

Abstract In recent years the technological importance of graphene increased significantly also in the field of soft, flexible and wearable electronics. In this chapter a simple one step process to create 3D porous graphene structures into flexible polymer films is highlighted. By laser scribing polymer precursor substrates with commercially available laser scribing setups the polymer is converted into so-called Laser-Induced Graphene (LIG) via a photothermal conversion. The properties of this material and the influence of different processing parameters on its composition and structure are introduced. Different transfer methods for stretchable applications are discussed. Three main application fields of LIG for soft (bio)sensors are identified: piezoresistive, electrophysiological and electrochemical sensors. Each of the application fields is highlighted more in detail and an overview of recent publications is given. Concluding with an outlook on the future of LIG – including improvement of patterning resolution and the use of renewable, bio-derived precursors – this chapter provides a broad overview of LIG for soft and flexible sensor devices.

Keywords Laser-induced graphene · Porous carbon · Biosensors · Piezoresistive · Electrophysiological · Electrochemical

A. Dallinger · K. Keller
Institute of Solid State Physics, NAWI Graz, Graz University of Technology, Graz, Austria
e-mail: dallinger@tugraz.at; keller@tugraz.at

F. Greco (✉)
Institute of Solid State Physics, NAWI Graz, Graz University of Technology, Graz, Austria

The Biorobotics Institute, Scuola Superiore Sant'Anna, Pontedera, Italy
e-mail: francesco.greco@santannapisa.it

F. Borghi et al. (eds.), *Nanoporous Carbons for Soft and Flexible Energy Devices*,
Carbon Materials: Chemistry and Physics 11,
https://doi.org/10.1007/978-3-030-81827-2_6

6.1 Introduction

Traditional synthesis of porous carbon involves high temperatures (up to 1200 °C) and an inert atmosphere for thermal decomposition of organic precursors (resins, pitches) [1].

A fairly new method to produce 3D nanoporous graphene, first discovered and investigated by Lin et al., utilizes commercially available CO_2 laser scribing systems to convert insulating polyimide (PI) and other synthetic polymers into conductive Laser-Induced Graphene (LIG), thanks to a photothermal pyrolysis process [2]. This process (schematically depicted in Fig. 6.1) benefits from the absence of any chemicals, no need for inert atmosphere, full and easy customization, and the possibility of converting an insulating polymer substrate into a conductive material while simultaneously patterning it with a desired design. Over the last few years the research interest on LIG has grown steadily, with a focus on the basic understanding of the process, elucidation of its composition and morphology, characterization of its properties, as well as on a myriad of applications, especially in sensing and power storage [3, 4]. Up to date several applications of LIG in devices have been proposed. One of the first devices demonstrated was a microsupercapacitor fabricated from PI [2] followed by stackable [5] and even stretchable supercapacitors [6–8]. Other LIG based devices have been demonstrated, such as: acoustic sensors [9, 10], strain sensors [11–15], gas sensors [16–18], electrophysiological sensors [14, 19, 20] and electrochemical sensors [17, 18, 21–31].

Advancements in applications emerged in parallel with the progresses achieved in the investigation of these materials and of the laser processing required for synthesis. Tuning of composition, surface morphology and properties (i.e. surface, electrical, mechanical) of LIG is achieved by changing the parameters of laser rastering, and mainly the laser fluence H ($J\,cm^{-2}$), defined as the optical energy scribed per surface area [2, 32]. Such control makes it possible to pattern areas of a substrate with specific tailored properties with only one technique. This is

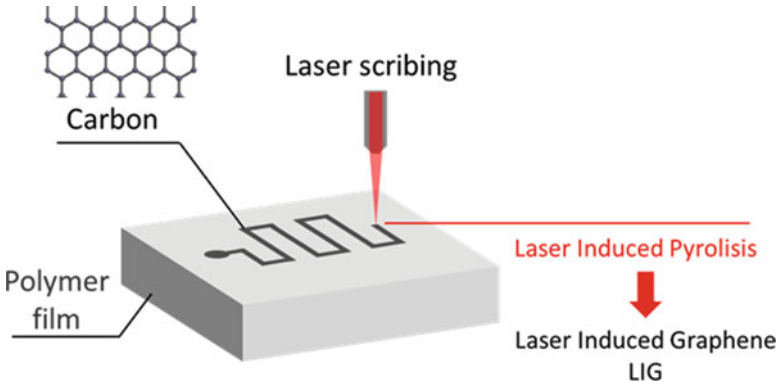

Fig. 6.1 Schematics of laser-induced pyrolysis and LIG creation by laser scribing

especially useful in soft (bio)sensors, where a variety of different requirements have to be fulfilled. Traditional biosensors are electrochemical sensors which can sense biologically relevant substances such as glucose, urea, lactate, among others, with high selectivity, high sensitivity, and low detection limits [33]. Typically, these sensors are developed onto flexible polymer substrates. However, soft biosensors to be deployed in smart skin applications for personal health monitoring do not only need to be flexible but preferably also stretchable and/or conformable. Moreover, in this scenario of skin-worn devices other electrophysiological and piezoresistive sensors are needed, as they can give important information about the health of a person, in addition to the aforementioned biochemical sensing.

A typical sensor consists of a sensing part (transducer) and an electrical interconnection to some wiring or amplification stage. Different sensors have different requirements for the sensing area; for example, in the case of electrochemical sensors often a transducer with high surface area is desired. The transducer is functionalized to achieve the desired sensitivity and selectivity for the target analyte. On the other hand, the electrical connections should have high conductivity. For soft sensors, which can be deformed and bent, the sensing part and the electrical connection should be resistant to changes induced by stress or strain. Even more constraints are given for skin-worn sensors. In addition to the aforementioned resistance to strain the materials should be also biocompatible, adhesive, preferably thin (few μm) and gas (e.g. moisture) permeable. This ensures that the wearable device retains conformability to the epidermis and feels like a second skin for the user.

The following sections of this chapter review the mechanism used to convert polymers into 3D porous graphene and the transfer onto stretchable substrates for the application in soft and epidermal sensors. A detailed survey of the application of LIG in three selected scenarios is then provided: piezoresistive, electrophysiological, electrochemical/gas soft sensors.

6.2 Conversion into 3D Porous Graphene: LIG

Although conversion of PI into amorphous carbon by UV pulsed laser was already known [32], in 2014 Lin et al. accidentally turned some polyimide (PI) into a black conductive porous material by lasering it with a commercial CO_2 laser, routinely used for laser cutting/engraving. This was ascribed to a photothermal pyrolisis process induced by the IR laser scribing in which the polymer precursor, PI, is converted into carbon. The recorded Raman Spectrum of this material unexpectedly showed the characteristic bands associated with graphene instead of typical features of amorphous carbon. A detailed investigation with scanning electron microscopy (SEM), transmission electron microscopy (TEM), X-ray diffraction (XRD), X-ray photoelectron spectroscopy (XPS) and Fourier-Transform infrared spectroscopy (FT-IR) permitted to identify this material as 3D porous graphene which was then named Laser-Induced Graphene (LIG) [2].

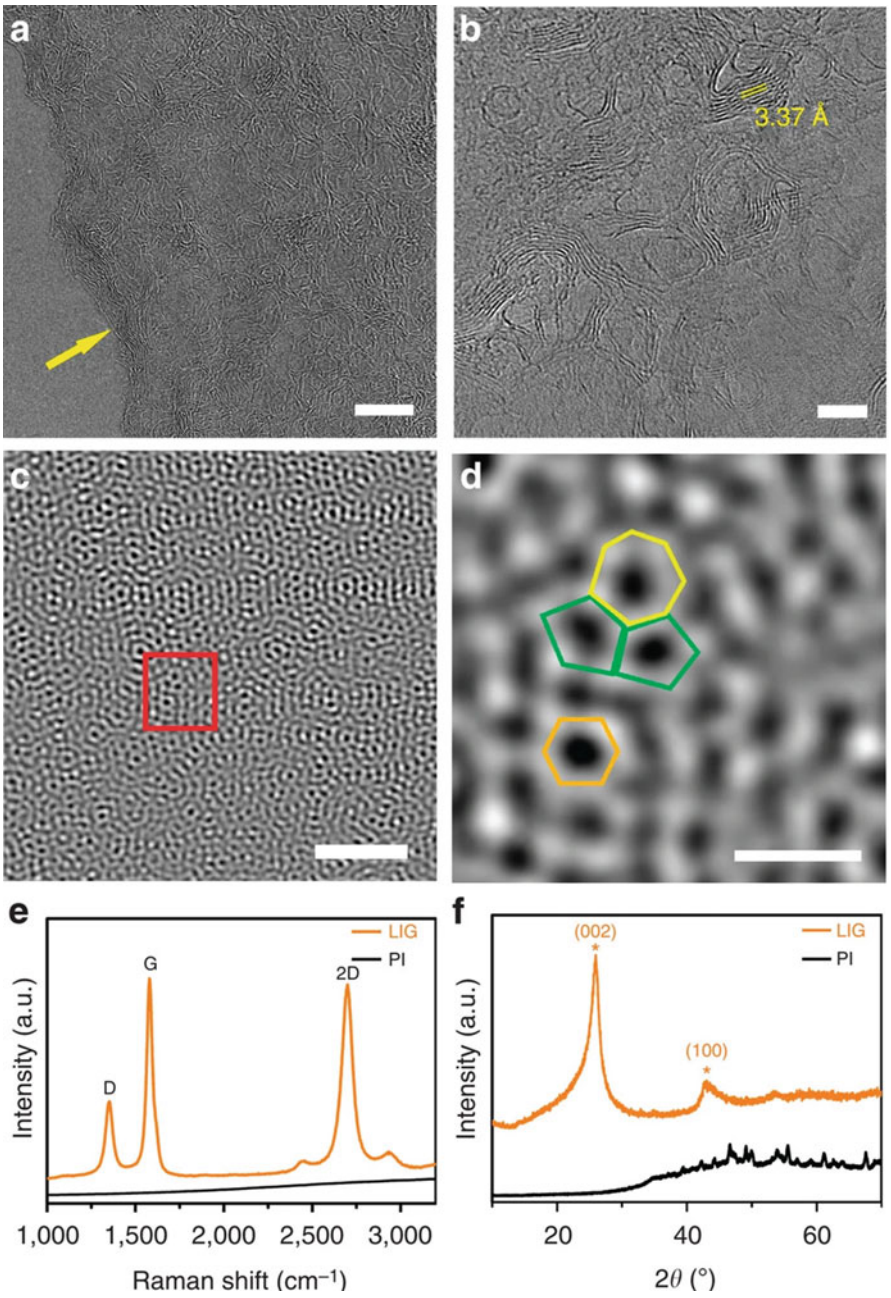

Fig. 6.2 (**a**) TEM image showing wrinkled structures on a cross section of a LIG flake (scale bar: 10 nm); (**b**) detailed view of (**a**) showing a lattice distance of 3.4 Å (scale bar: 5 nm); (**c**, **d**) TEM image showing different types of carbon rings – heptagons, pentagons and hexagons (scale bar: 5 Å); (**e**) Raman Spectrum of LIG scribed into PI; (**f**) XRD for LIG powder from PI. (Reprinted from [2] with permission from Springer Nature)

Further investigations with TEM and XRD showed an average lattice spacing of ≈ 3.4 Å, corresponding to the (002) planes of graphitic materials (Fig. 6.2a, b) [2]. High resolution TEM images revealed that not only the 6-member rings of graphene, but also defective 5- and 7-member rings were present (Fig. 6.2c, d). A typical Raman spectrum for LIG is shown in Fig. 6.2e. In this spectrum one can find three main bands; the first is the D band at ≈1350 cm^{-1}, which is an indicator for defects or bent sp^2 carbon bonds. The second feature, the G band, is located at ≈1580 cm^{-1} while the third feature, the 2D band, is located at ≈2700 cm^{-1}. The 2D band is associated with single layer graphene, the larger width of the band comes from randomly stacked graphene layers. The intensity ratio of D and G bands, I_D/I_G can be used to estimate the degree of crystallinity (graphitization) of the LIG [2].

Investigations with XPS showed that after laser scribing LIG into PI the amount of C-C bonds increased, while the number of C=O, C-O, and C-N bonds decreased (Fig. 6.2f). The data also showed that the carbon is dominated by the sp^2-species, which is in agreement with the Raman and XRD results [2].

Typically the LIG photothermal synthesis is carried out by laser rastering with a CO_2 pulsed laser operating at a 10.6 μm wavelength, commonly used for laser cutting/engraving of various materials. These laser scribing systems comprise focusing optics attaining a typical laser spot size of around 30–100 μm. This size is in fact limiting the resolution of the LIG scribing process. However later studies demonstrated how also UV semiconductor lasers with a wavelength of 405 nm can be used to successfully convert polymers to LIG [25, 34, 35]. With such laser sources smaller beam spot size, and thus improved LIG patterns resolution, is attainable, as recently demonstrated [35].

The photothermal process for creation of LIG depends on the laser energy delivered on the precursor surface during the laser rastering. A characteristic figure used to describe the laser process is thus the laser fluence H, which is calculated as follows, from the laser scribing parameters which can be set in the laser scribing system [14, 32]:

$$H = \frac{P}{s \cdot v \cdot PPI} \tag{6.1}$$

Here the laser fluence H is calculated from the power (P), the laser spot size (s), the scribing speed (v) and the spots per length unit (points per inch, PPI). As the laser fluence is gradually increased, the polymer precursor is increasingly damaged by heat. However the precursor is not turned into LIG until a certain threshold is reached: the critical fluence H_{cr}. For $H < H_{cr}$ no LIG is formed and the material stays an insulator or is simply ablated. Since most of the studies involved PI as a LIG precursor, we will refer to it in the following. For PI, depending on the method of calculation (observed or theoretical spot size) the critical fluence value ranges from $H_{cr} \approx 5\,J\,cm^{-2}$ [32] to $\approx 25\,J\,cm^{-2}$ [14]. For $H > H_{cr}$ LIG is formed and, with increasing fluence, the electrical resistance is correspondingly reduced, up to a point where oxidation starts to play an important role and the resulting gain in reduced resistance gets smaller [2]. For $H > 80\,J\,cm^{-2}$ the PI substrate

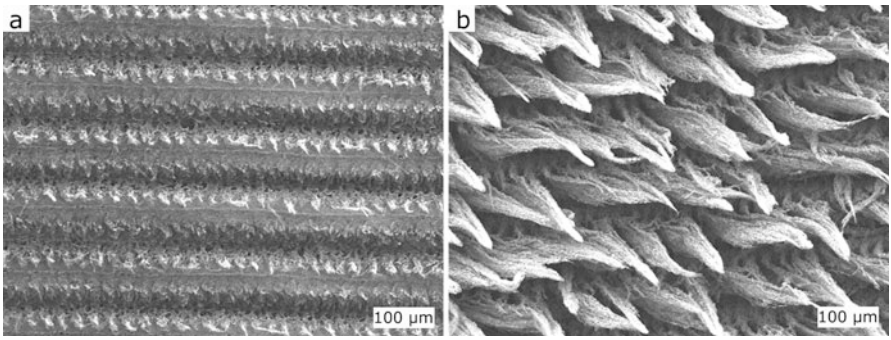

Fig. 6.3 SEM images of flat porous LIG (**a**) (low fluence, H = 25 J cm^{-2}) and fibrous LIG (**b**) (high fluence, H = 50 J cm^{-2}). (Adapted from [14], Copyright © 2020 American Chemical Society, licensed under CC-BY)

gets totally destroyed [14]. Duy et al. investigated how the thickness of scribed LIG was related to the laser fluence H. It was found that with increasing H the thickness of the converted LIG increased [32]. Another parameter affecting much the structure and composition of LIG is the scribing resolution, the combination of PPI (along rastering direction x) and LPI (lines per inch, perpendicular direction to rastering, y) in the so-called raster mode. Duy et al. found that at a scribing resolution of 1000 PPI × 1000 LPI the upper layer of LIG got destroyed because the single laser spots were overlapping. When instead a lower scribing resolution of 500 PPI × 500 LPI was used, fiber-like structures with a length up to 1 mm were emerging from the surface [32]. Dallinger et al. investigated the change of surface morphology by fixing the scribing resolution and changing H. It was found that a threshold $H_{cr} \approx 25\,J\,cm^{-2}$ should be overcome to convert the PI into a flat porous LIG layer (Fig. 6.3a). With $H > 45\,J\,cm^{-2}$ LIG fibers (Fig. 6.3b) started to emerge from the surface; the length of fibers could be varied by changing H. Higher fluence led to longer fibers (up to 1 mm). These individual fibers, with a diameter of around 50 nm to 100 nm, were forming macroscopic bundles of fibers [2, 14] arranged into a so-called "forest".

While a description of the structure and composition of various forms of LIG and how this can be varied by different laser scribing settings has been proposed by several groups, a complete understanding of the LIG formation mechanism is still missing. Molecular dynamics simulations showed that LIG formation happens under high temperature (>2400 K) and pressure (GPa), due to localized laser heating [36]. At these conditions the polymer precursor is decomposed and volatile gases such as CO and H_2 are removed. Depending on the presence of heteroatoms in the pristine macromolecular structure or as additives in the polymer precursor, other compounds can be formed and removed as well. Apart from PI which has a high temperature and chemical resistance and has been the first and more intensively investigated polymer precursor so far, many other polymers were investigated for conversion into LIG. These include Polyetheretherketone (PEEK) [37–39], phenolic

resins [34] and PEI [2]. Poly- or heterocyclic structures seem to be more prone for LIG formation. As the rings break up and the other elements are removed as gases, the sp^3 carbon atoms are converted into sp^2 carbons and create defective graphene structures composed of 5-, 6- and 7-membered carbon rings. The abundance of defective structure could be justified by the kinetics of the process: the system cannot rearrange into an ordered graphitic structure before it is cooled down [40, 41]. Besides many synthetic polymers (for a more complete list the reader is referred to [42]), other biologically derived materials have been successfully converted into LIG. Examples comprise lignin from wood in inert or reducing gas atmosphere [43], wood impregnated with metal salts [44] and lignin from cork, coconut shells and potato skins by multiple lasering [45].

6.3 Properties of LIG

The morphology of LIG has some interesting features arising from the laser scribing process. The laser is rastering over the polymer precursor, while heating and converting it into LIG. The laser beam transversal intensity profile is described by a Gaussian function. Thus, the fluence in the middle of the laser spot is higher than in the outer rim. This results in increased ablation at the center of scribed lines and production of trenches along the laser scribing direction. Also the LIG formed in the middle of the trenches was found to have an higher degree of cristallinity with respect to the one formed at the edges of the trenches, because of such transversal laser fluence gradient [45].

This reflects on the electrical properties of LIG. The electrical resistance measured along the scribing direction is typically lower than the one measured perpendicularly to it [14]. The sheet resistance can be as low as 15 Ω/□ for the flat porous LIG, which gives a conductivity of ≈25 S cm^{-1}, for an estimated homogenous LIG thickness of ≈25 μm [2]. By changing the scribing resolution not only the morphology (from porous to fibers) but also the properties of LIG are changed. By lowering the scribing resolution to obtain fibers, the overlapping of laser pulses and therefore the conductive pathways got less, which resulted in a higher sheet resistance [32].

Another property of LIG which is strongly affected by changing the laser scribing parameters is its surface area. Measurements with the Brunauer–Emmett–Teller (BET) analysis resulted in a surface area for porous LIG of 342 m^2 g^{-1} (pore size <9 nm [2]) and for fibrous LIG of 70 m^2 g^{-1} [32]; in both cases LIG was obtained from PI. The lower surface area of fibrous LIG is due to the fact that the fiber bundles on the surface don't have any pores, while the bulk area has pores formed by the 3D arranged graphene slabs. LIG made from lignin/poly(vinyl acetate) (PVA) films showed a surface area of 338 m^2 g^{-1} and can compete with LIG from PI [46].

Surface wettability of LIG can be changed by tuning the laser parameters. Nasser et al. investigated the change of LIG water wettability depending on the scribing resolution. It was shown that by lowering the resolution from 1000 PPI

to 100 PPI, the wettability of LIG dramatically changed from hydrophilic (full wetting, contact angle (CA) of 0°) to superhydrophobic, with a CA = 161°. XPS and Energy-dispersive X-ray spectroscopy (EDS) investigations showed that by lowering the PPI the oxygen content of produced LIG was decreased. At high resolution scribing the surface was relatively flat and promoted the impregnation of the porous LIG; moreover, the higher oxygen content on the LIG surface promoted its hydrophilic behaviour. Viceversa, at low resolution the emerging LIG fiber pillars create a surface with high roughness at the micro- and nano-scale; additionally, a lower oxygen content is produced. These two combined contributions promote the observed (super)hydrophobic behaviour, according to either a Cassie-Baxter or a Wenzel model [47]. A very interesting finding was that the contact angle was almost negligibly depending on the laser scribing power. However, the sheet resistance could be decreased by 90 % by increasing the laser scribing power [48].

Wu et al. used a two step LIG process for mimicking the taro leaf structure and its peculiar surface properties. The taro leaf's surface structure consists of microscale hexagonal shapes, protruding round shapes and petal-like nanostructures. By recreating this surface pattern by lasering with a Nd:YAG laser at 1064 nm the superhydrophobic behaviour of the taro leaf (CA = 159 ± 2°) could be reproduced (CA = 152°). This was done in a two-steps process: (i) pre-carbonizing the whole PI surface by scribing the PI with a low fluence, and then (ii) laser scribing the pattern onto the surface with a higher fluence [49].

Wettability of LIG depends also on the gas atmosphere used during the laser-induced pyrolysis. Li et al. used a custom chamber equipped with an infrared transparent ZnSe window to scribe PI while flowing different gases (Ar and H_2) through the chamber; the results were then compared with those obtained with scribing in air. The wettability of LIG could be changed from hydrophilic (CA = 0°) in air to superhydrophobic (CA = 157°) in the case of Ar. Investigations with XPS showed that in the case of the (super)hydrophobic samples, made in the reducing (H_2) or inert (Ar) atmosphere, the content of O and C-O in the LIG was lower than in case of scribing in air, and correlated with the higher contact angles [50].

6.4 From Flexible to Stretchable: Transfer onto Substrate

Most polymer precursors which can be converted to LIG are thin enough to be easily bendable and have very good mechanical properties as regards to resistance to repeated mechanical cycling. However they are rather stiff and have a very limited stretchability (up to a few % strain) before showing plastic deformation or even fatal damage/breaking. Thus, flexible sensors can be readily produced by directly scribing LIG circuits and electrodes, but different strategies are required for soft/stretchable (bio)sensors. This is relevant for all those applications where the use of soft and stretchable substrates is required, such as in the case, for example, of epidermal devices. Indeed, applications regarding the placement of sensors on skin require a substrate matching the skin's own mechanical properties.

Moreover, they need to be thin for a conformable application, and have a high water vapor transmission rate (WVTR) in order to let the skin breath and prevent inflammation and discomfort. Currently these requirements can't be fulfilled by any precursor material used for LIG. Therefore, various strategies have been designed and proposed to transfer the conductive LIG pattern onto other soft and stretchable substrates, more suitable for the envisioned applications.

One possible strategy is the embedding of LIG formed on a non stretchable precursor (like PI) into a liquid polymer mixture which can be subsequently crosslinked into a solid elastomeric matrix, like poly-dimethyl siloxane (PDMS) or other thermoset silicones [7, 12, 15, 18, 21, 52]. Here the transfer is achieved by simply submerging the LIG, still anchored to PI, in the elastomer prepolymer mixture, or by blade or spin coating of the latter on top of scribed PI. The liquid can infiltrate into the porous structure of LIG and, after curing, LIG is stably embedded inside the elastomer matrix, forming a composite which can be peeled off from the PI surface (Fig. 6.4a). Luong et al. showed that with this embedding method LIG can be transferred not only onto elastomers but also onto a variety of other materials including solid hydrocarbons, epoxy resins, cement, and geopolymers. This enabled the creation of composite conductive tracks into insulating materials or a local change of wettability of different materials [52].

Some different and very promising strategies have been recently demonstrated. A composite from PDMS and PI particles [53] was prepared. Then an IR laser irradiation caused the conversion in LIG of just the PI phase, and the LIG remained embedded into the soft PDMS matrix. Direct conversion of PDMS into LIG was also demonstrated, but only when operating with a 405 nm UV laser diode [25].

Another method, already known from graphene exfoliation from a block of graphite with a simple scotch tape, is to transfer the LIG from PI with an adhesive surface. By placing the adhesive surface on top of the scribed LIG and applying a pressure, the LIG is transferred from the PI surface to the new one (Fig. 6.4b). This approach was recently used to transfer LIG conductive tracks onto a soft and transparent medical grade polyurethane (PU), enabling various sensing applications on skin [14]. This method can be generalized for allowing the transfer onto almost any solid surface with an adhesive. Here however, differently from the above-mentioned approach of LIG embedded into an elastomer matrix (Fig. 6.4a), the LIG is rather anchored on the elastomer surface and its whole surface can be placed in contact with other target surfaces (as skin) or exposed to analytes (Fig. 6.4b), in case of chemical/biochemical sensors.

Additionally, Li et al. demonstrated a method for industrial scale embedding of LIG into polymer sheets to create several composites. By hot-laminating LIG scribed on PI and thermoplastic sheets (polypropylene, polystyrene, thermoplastic polyurethane and polyvinyl chloride, among others) in a roll-to-roll fashion, different composites were created (Fig. 6.4c) [51].

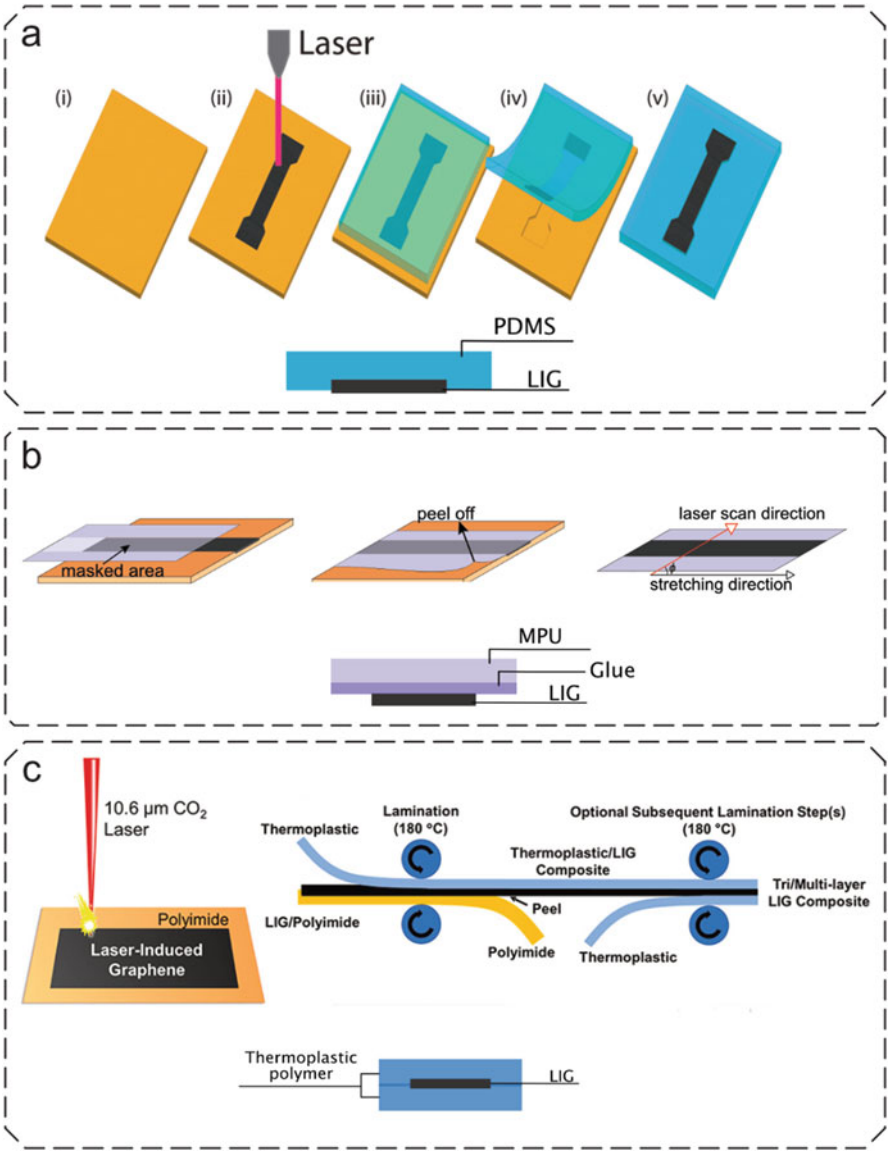

Fig. 6.4 (**a**) Embedding of LIG in PDMS: applying PI tape onto PET sheet (i), scribing of LIG into PI (ii), embedding of LIG it into PDMS (iii), peeling off PDMS with embedded LIG after crosslinking (iv, v). (Adapted with permission from [15] Copyright © 2015 American Chemical Society); (**b**) scribing of LIG into PI and transferring it onto medical polyurethane (MPU). (Adapted from [14] 2020 American Chemical Society, licensed under CC-BY); (**c**) demonstration of roll-to-roll fabrication and lamination for LIG composites. (Adapted from [51], Copyright © 2020 American Chemical Society)

6.5 Applications

The number of studies and proposed applications of LIG has been increasing enormously in the last few years. Some reviews provide a good introduction to the topic and overview of LIG preparation [42], and present its applications in various fields, especially in power storage [54], sensors [3, 4]. Here, given the focus of this chapter, we identified three fields of applications for 3D porous LIG in soft (bio)sensors that will be discussed in more detail: piezoresistive, electrophysiological and electrochemical sensors.

6.5.1 Piezoresistive Sensors

Piezoresistive sensors use the change in resistance observed when the sensor is stretched or compressed. The typical figure that is related to this behaviour is the so-called Gauge Factor (GF),

$$GF = \frac{\Delta R/R}{\Delta L/L} = \frac{\Delta R/R}{\epsilon}. \tag{6.2}$$

The GF sets the change in resistance ($\Delta R/R$ with $\Delta R = R - R_0$) in relation with the change in length, or strain ($\Delta L/L = \epsilon$ with $\Delta L = L - L_0$) of the piezoresistive material structure used as a sensor.

LIG conductors can show a marked piezoresistive behaviour because of crack formation in the conductive matrix during stretching [14, 21]. By changing the laser process parameters (like the fluence H) it is possible to change LIG morphology, which, in turn, results in tuning the GF. Dallinger et al. showed the tuning of GF of LIG-based strain sensors operating under tension and made from medical polyurethane. A porous LIG (LIG-P) produced at low fluence was prone to crack formation and therefore resulted in a higher GF. A fibrous LIG (LIG-F) produced at higher fluence showed a much smaller GF [14]. Another possible strategy for tuning of the GF is to modify the orientation of scribed LIG features with respect to the stretching direction. Scribed LIG lines are more or less prone to crack formation, depending on their orientation. LIG lines scribed parallel to the stretching direction are more prone to irreversible crack formation than those orientated perpendicular to it, as evidenced in some tensile testing experiments [14]. This effect is much dependent on the LPI parameter and thus on the actual separation between consecutively scribed LIG lines. By tuning the LPI parameter the GF can be tuned to some extent.

Another important factor to be considered is the substrate onto which the LIG is transferred and its mechanical properties. While Dallinger et al. used a medical polyurethane, showing a small range of elastic behaviour and an overall pronounced viscoelastic behaviour, Chhetry et al., Wu et al. and Rahimi et al. used PDMS as

a transfer stretchable matrix for LIG. Due to the very good elastic behaviour of PDMS, this resulted in nearly hysteresis-free sensing behaviour [12, 15, 16]. Xuan et al. investigated the influence of the LIG design shape (straight, serpentine) on the GF. A serpentine shape has a significant lower GF than the straight shape, as expected due to geometrical factors impacting on the overall stress applied to the conductor during the application of a tensile strain [21].

The piezoresistive properties of aforementioned LIG composites have found application in biosensing. LIG based piezoresistive epidermal sensors have been demonstrated by wrist pulse detection (Fig. 6.5a) [12, 16], tactile sensing (Fig. 6.5b) [14, 16], measuring the bending angle of a finger (Fig. 6.5c) [12, 15, 16], respiration rate detection [14] and pressure sensing with a sandwich of LIG/PU and polystyrene microspheres [55]. In all these cases, besides the good piezoresistive behaviour, the sensors demonstrated a stable adhesion on skin.

6.5.2 Electrophysiological Sensors

Electrophysiology uses the electrical signals produced by the body, to monitor the body's condition, functioning of organs, muscles, among others. Often this is done with surface (on skin) signal recording, by means of dedicated skin-contact electrodes in so called surface electrophysiology (sEP) recordings [56]. The strongest (larger amplitude) sEP signals come from muscle activation, detected in electromyography (EMG); the heart generates smaller signals measured with electrocardiography (ECG); the smallest and more challenging to detect signals come from brain activity, studied in electroencephalography (EEG). Other electrophysiological techniques exist but we will refer in the following to just these main techniques as they represent the majority of elctrophysiology biosensors presented so far. Commonly Ag/AgCl gel electrodes are used as transducers for sEP, connected to external signal amplification and recording devices. These electrodes use a wet interface to connect to the skin which comes with some major constraints in use, especially for long term recording (manual placement of gel, drying out of gel interface in some hours, interelectrode crosstalk, limited wearing comfort). A possible solution is to use hybrid interfaces (wet/dry) or dry interfaces to connect to the skin. In recent years thin metal films/meshes [57] or tattoo based electrodes based on the conductive polymer poly(3,4-ethylenedioxythiophene):polystyrene sulfonate (PEDOT:PSS) were used [58, 59]. Due to the possibility to embed LIG in flexible and soft/stretchable polymer matrices and to easily pattern them in the desired shape, LIG-based electrodes have been recently tested in this application. Dallinger et al. demonstrated an EMG electrode based on LIG transferred onto medical PU which was worn for 72 h and survived exercising and showering (Fig. 6.6a) with no loss of functionality. The LIG based electrodes could be connected/disconnected multiple times from wiring to external acquisition devices, without suffering from delamination or breaking. The combination of porous LIG and breathable medical polyurethane resulted in an electrode that had high wearing comfort and prevented skin inflammation [14]. Sun et al. embedded LIG into a sugar templated elastomer

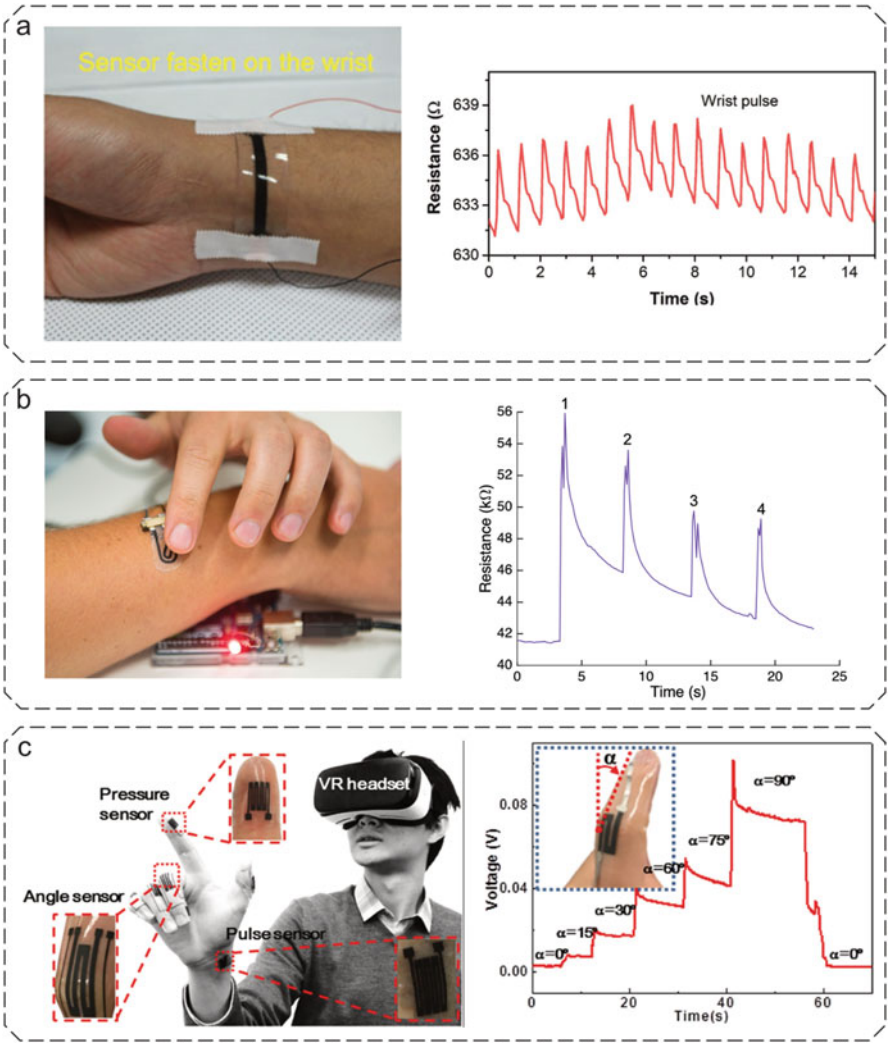

Fig. 6.5 (**a**) Piezoresistive wrist pulse detection by LIG embedded in PDMS. (Adapted from [12], Copyright © 2019 American Chemical Society); (**b**) tactile on-skin button realized with LIG transferred on PI utilizing the piezoresistive effect. (Adapted from [14], Copyright © 2020 American Chemical Society, licensed under CC-BY); (**c**) demonstration of piezoresistive sensor based on LIG/PDMS composite for grip pressure, finger bending angle and pulse sensing. (Reprinted from [16], Copyright © 2018 Elsevier)

sponge with a high water-vapor permeability; these electrodes were used to measure EEG, ECG and EMG in combination with a hydration and temperature sensor (Fig. 6.6b) [19].

Table 6.1 Comparison of the contact impedance at 100 Hz for four different kinds of skin-contact electrodes

Type of electrode	Contact impedance @ 100 Hz	Typology	Reference
Ag/AgCl	12 kΩ	Wet	[19]
	80 kΩ	Wet	[58]
Au Nanomesh	140 kΩ	Dry	[19]
LIG	17 kΩ	Dry	[19]
PEDOT:PSS	100 to 200 kΩ	Dry	[58]

An ECG sensor demonstrated by Zahed et al. used LIG scribed onto PI and spray coating of PEDOT:PSS to sense the heartbeat when placing a thumb of one hand, and the index and middle fingers of another hand on the sensor and pressing against it (Fig. 6.6c). Thus, this approach is very different from those reviewed so far, since it doesn't imply embedding of LIG electrodes into a wearable. The spray coating of LIG with PEDOT:PSS significantly enhanced the adhesion to PI and the mechanical resistance against rubbing [20].

Comparing the contact impedance of different types of electrodes at 100 Hz (as relevant in several electrophysiology techniques) shows that LIG electrodes are performing as good as other types (Table 6.1).

6.5.3 Electrochemical Sensors

Analysis of many biofluids, biomolecules and even cells and bacteria can rely on powerful electrochemical analysis methods. Electrochemical sensors could be single or multielectrode systems. The most dominant are three electrode sensors which include working electrode (WE), counter electrode (CE) and reference electrode (RE) [60]. In most cases CE is just a conductor several times larger than WE to reduce the resistance at solution/WE interface. RE consists of the material with known electrochemical potential and is used to compare the potential of the WE. In wearable applications RE is commonly made of Ag/AgCl. Ag/AgCl electrodes are easy to fabricate with multiple methods; they are based on solid state chemical equilibrium and suitable for use in water-based environments such as body fluids (e.g. sweat) as relevant for many health monitoring, ex vivo as well as in vivo, both inside the body (implanted sensors) or surface (sensors mounted on skin).

In an electrochemical sensor the WE is responsible for selective sensing of the analyte. The WE is usually made of conductive material functionalized with some solvent resistant species. The huge surface area of LIG in combination with its good intrinsic conductivity allows to easily modify it, adding an extremely wide range of selective functionality. So far there are many reports of adapting LIG for electrochemical sensors. The simplest example of an electrochemical LIG-sensor can include only a single electrode. Zhang et al. presented an electrochemical

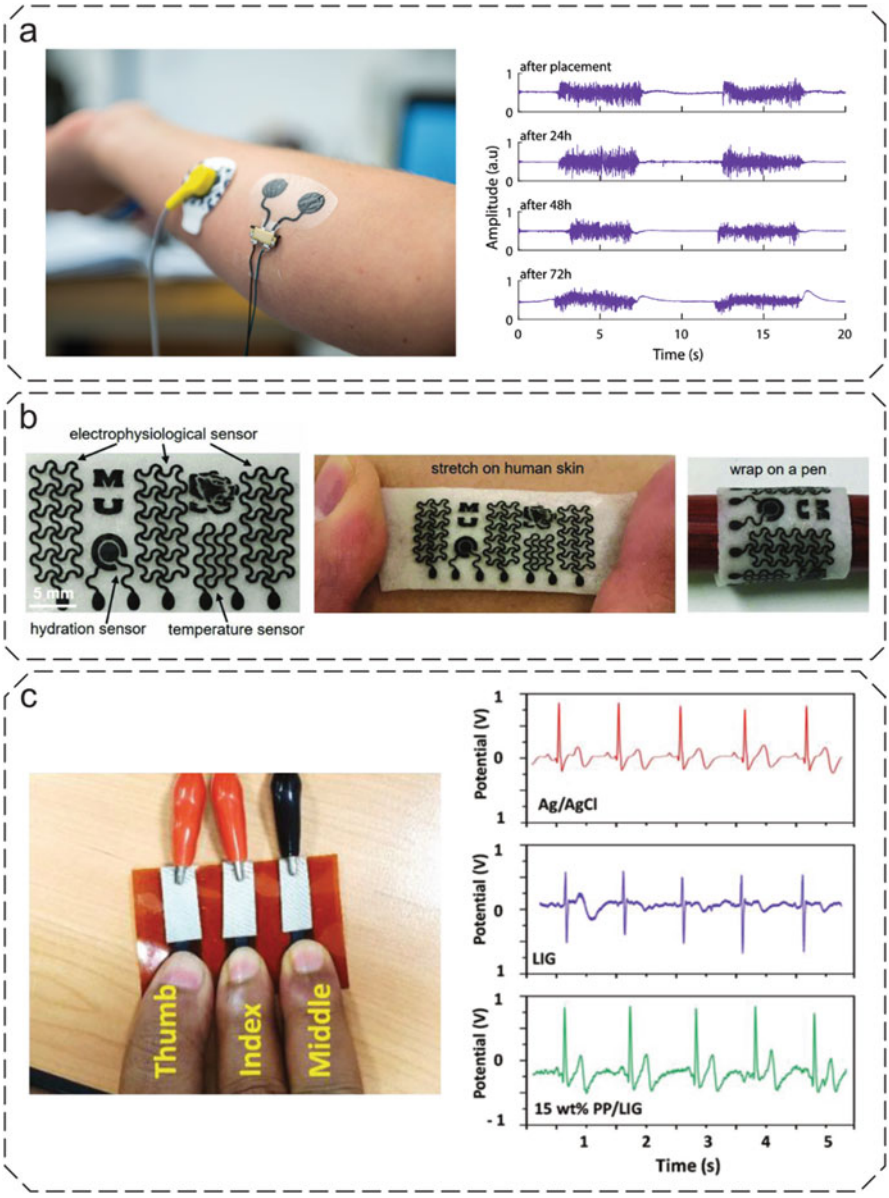

Fig. 6.6 (**a**) Electromyography (EMG) sensor based on LIG transferred onto medical polyurethane. (Adapted from [14], Copyright © 2020 American Chemical Society, licensed under CC-BY); (**b**) electrophysiological sensor based on sugar-templated elastomer sponge with embedded LIG. (Adapted from [19], Copyright © 2018 WILEY-VCH Verlag GmbH & Co. KGaA, Weinheim); (**c**) LIG/PEDOT:PSS composite for electrocardiography (ECG) recording on finger tips. (Reprinted from [20], Copyright © 2020 Elsevier)

sensor for detection of trans-resveratrol (TRA), a natural polyphenol isomer found in many plants, including grapes. The sensor was used to quantitatively determine the content of TRA in red wines. It was composed of a pure LIG electrode lasered from PI sheet [30]. The sensor wasn't functionalized at all, but before use it needed activation with several cycles of cyclic voltammetry (CV) sweeping in PBS solution to remove organic impurities from inside the porous structure. Even such simple configuration could be used to determine TRA concentration with differential pulse voltammetry (DPV). A similar concept was used in [31], where laser parameters were tuned to incorporate more nitrogen atoms into graphene composition and form N-doped LIG with improved sensitivity; the sensor was used to analyse micro-RNA molecules with limit of detection (LOD) of 10 fmol. Recently LIG electrodes formed on PI were functionalized with antibodies (Fig. 6.7a) for detection of *S. enterica* bacteria [27]. This sensor showed high selectivity for target bacteria even in complex media and broad range of detection from 25 CFU/mL to 10×10^5 CFU/mL (colony-forming unit). Bacteria concentration was measured using electrochemical impedance spectroscopy.

Multielectrode sensors on LIG include skin pH sensors where the function of WE and CE are combined into a single electrode [21, 22]. The WE is electrochemically functionalized mainly with polyaniline (PANI) aqueous solution because it is non-toxic, skin-friendly and has high pH-sensitivity. Demonstrated sensors exhibit high pH-response (66 in [21] and 75 in [22] mV/pH) in the range 4 pH to 7 pH.

Using complex electrochemical analysis techniques such as CV requires implementing full three electrodes design. More sophisticated sensors could be functionalized with enzymes which exchange the electrons with the target molecule under applied potential. For example for glucose sensors glucose oxidase (GOx) is widely used [62], and most of the work aimed on improving electromechanical properties of fabricated devices. One of the first examples of GOx-based sensors on LIG was shown by Zhang et al. [34]. All three electrodes were lasered from the spin-coated phenolic resin film "doped" with $FeCl_3$. Afterwards the GOx with ferrocene acting as an electron-transfer mediator, were encapsulated onto WE in a chitosan hydrogel. Presented biosensor showed good sensitivity to glucose (LOD 0.2 mmol), however selectivity was not tested. One way to improve the sensor's limit of detection is to reduce the resistivity of the LIG. Currently, most common way is to use the combination of metal nanoparticles electroplating (Fig. 6.7b) inside the LIG pores and some solution-based additive for the interface modification, including: PEDOT:PSS spraying [22], and treatment with acetic acid to increase the content of C-C bonds [23]. Lately, the first attempts to solve the wearability issue of such electrochemical glucose sensors were demonstrated by Xuan et al. by coupling of LIG with PDMS by silver nanowires (AgNW) [21]. AgNW provided better piezoresistive properties up to 40 % strain with the R/R_0 ratio reaching thousands percent. The electrochemical properties were also enhanced by electroplating of Au/Pt nanoparticles inside LIG pores which improved electron-transfer rate. Apart from glucose biosensors, three electrode design are also suitable for detection of other organic molecules, e.g. chloramphenicol – an important antibiotic contaminant

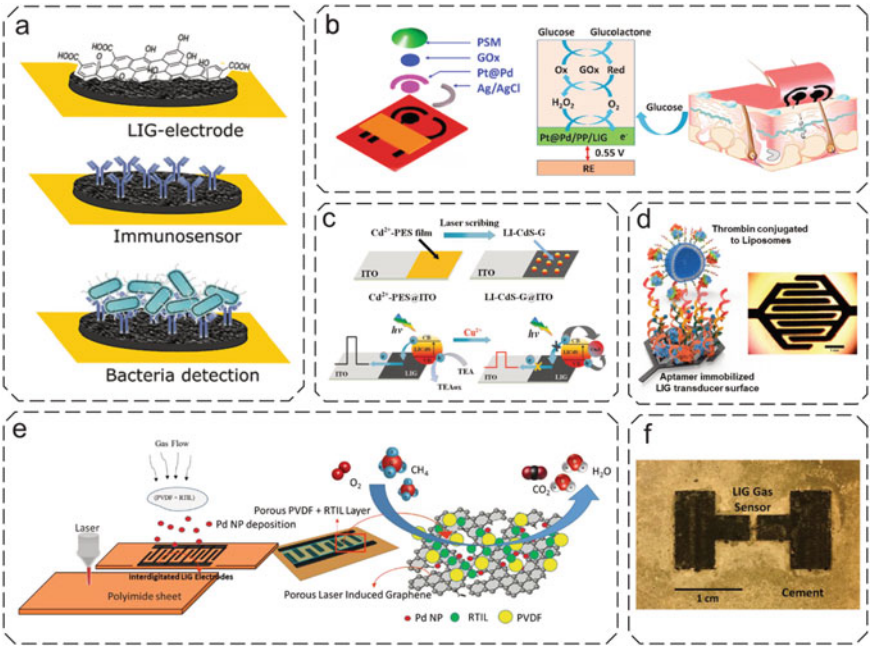

Fig. 6.7 LIG-based bio-, electrochemical and gas sensors; (**a**) LIG imunosensor functionalized with antibodies for bacteria detection. (Adapted with permission from [27] Copyright © 2020, American Chemical Society); (**b**) illustration of LIG-based glucose biosensor assembly and working principle. (Reprinted with permission from [22], Copyright © 2020 Elsevier); (**c**) LIG photoelectrode fabrication and working principle. (Adapted from [61] with permission from © 2019 WILEY-VCH Verlag GmbH & Co. KGaA, Weinheim); (**d**) LIG IDEs for thrombin detection. (Reprinted permission from [29], Copyright © 2020 Elsevier); (**e**) electrochemical methane LIG-sensor. (Reprinted with permission from [26], Copyright © 2019, American Chemical Society); (**f**) LIG gas sensor embedded into cement. (Adapted with permission from [17], Copyright © 2019 American Chemical Society)

in agriculture [28]. WE in the presented device was modified with a molecularly imprinted polymer and had a LOD 0.62 nmol.

Non-enzymatic LIG-based sensors have started to emerge recently. A method was developed to produce the decorated LIG from the mixture of liquid polymer precursors and metal complexes. First example of the photoelectrode made of LIG was formed from a mixture of Ti^{4+} and poly(amic acid) (PAA) solution [63]. Furthermore, this concept was employed for fabrication of metal sulfide doped LIG from polyethersulfone precursor as a photoelectrode, which could also be adapted for selective photoelectrochemical sensing of Cu^{2+} (Fig. 6.7c) [61]. One of the most promising is the photoelectrode-based glucose sensor made by direct lasering of PES membrane mixed with Cd/Ni complexes [24]. Resulting LIG was already doped with metal ions which act as photocatalytic sites for glucose oxidation.This

sensor is simpler in production since it doesn't need additional electrodes and demonstrates a LOD in the order of micromoles.

Special cases of sensors with electrochemical nature are interdigitated electrodes (IDEs) made of LIG. These sensors (Fig. 6.7d) could be used for capacitive detection of thrombin, upon surface functionalization of LIG [29]. Dosi et al. studied application of LIG IDEs decorated with Pd nanoparticles for alkane sensing (Fig. 6.7e) [26]. Pd-doped LIG covered with solid polymer electrolyte promotes electrooxidation of methane gas. The LOD of the sensor is quite low and is around 9 ppm, however the sensor is also sensitive to interfering low-molecular weight alkanes which affects the accuracy in complex gaseous mixtures. LIG decorated with nanostructured ZnO is interesting because of its active UV sensing capabilities [64]. In this case LIG electrodes are treated with UV/ozone to improve wetting and allow drop-casted ZnO dispersion to evenly distribute inside the pores of the carbon structure. Sensor performance was tested by measuring the photocurrent under UV light and it was found that the sensitivity is highly dependent on the geometry of IDEs.

6.5.4 Gas Sensors

A special class of LIG-based sensing devices are flexible and embeddable gas sensors. The already demonstrated decoration of LIG with nanoparticles, in combination with other physical concepts might help in creation of so called "artificial nose" in future.

LIG decorated with Pd NPs was demonstrated to be an accurate hydrogen sensor with sensitivity at room temperature down to 600 ppm [25]. The sensing mechanism is based on the well known catalytic effect of Pd and on its structural changes upon adsorption of H_2. Another approach relies on decoration of LIG with reduced graphene (rGO)/MoS_2 particles [18]. The formed composite electrode acts as a chemiresistor which exhibits an ultrasensitive detection of NO_2 gas with LOD of 1.5 ppb.

One of the most accurate and selective sensors so far are sensors based on thermal conductivity of gases, known as thermal conductivity detectors or katharometers. Very thin channel (50–60 μm) is lasered between 2 electrodes and when potential is applied the channel starts heating [17]. This causes the change in resistance which depends on the thermal conductivity of surrounding gas. With these sensors it is possible to detect CO_2, O_2, N_2 from a binary gas mixture (He, Ar) with sensitivity down to 1000–3000 ppm and response time around 8 s. Due to the ability to transfer the LIG onto different surfaces, the katharometer LIG-based sensor was transferred onto cement (Fig. 6.7f) allowing to deploy it in extreme conditions.

6.6 Outlook

In the previous sections we have shown how in recent years the conversion of polymers into LIG by direct laser writing gained a lot of interest for both fundamental and applied research. Here we aim to highlight some current and future challenges that could permit to develop even further the LIG preparation and its use in devices. Improvements in LIG processing can still be achieved by lowering the minimum feature size of LIG by using a UV laser [35]. Lasering with CO_2 lasers actually causes direct heating and "burn" of the polymer, which results in a LIG feature larger than the actual laser spot size. Compared to this, UV lasers locally heat the substrate by absorption and thus a smaller LIG features can be obtained. In order to minimize the price and environmental footprint of LIG-based materials, it will be important to find alternative precursors (preferably bioderived) for LIG conversion. An already demonstrated possible route is the use of an inert atmosphere (e.g. N_2) during laser scribing of biologically derived materials [43]. A very promising approach is the use of lignin as a precursors for LIG, either as a composite consisting of poly(ethylene oxide) (PEO) [65, 66] or poly(vinyl acetate) (PVA) [46, 67] and lignin. Edberg et al. demonstrated an ink based on lignin and cellulose (2-HEC) which was used for screen printing patterns on top of surfaces which were afterwards converted to LIG via scribing with a CO_2 laser [68].

Another way to scale up LIG preparation into industrial scale production is represented by a roll-to-roll (R2R) production. Li et al. showed that it is possible to create composites with LIG by just using a commercially available thermal laminator. Sheets of polypropylene, polystyrene, polyurethane and other thermoplastic materials were laminated to composites with LIG [51]. By further improving the aforementioned approaches, LIG can become a cheap, scalable and reliable technology for sensor fabrication. The laser scribing process allows for an easy and local tuning of properties which enables the creation of a multifunctional device in one go (e.g. electrophysiological, temperature and hydration [19]). The highly porous nature of LIG makes it the perfect base for electrochemical sensors, due to the high surface area which can be utilized for surface functionalization. By using different functionalization chemicals and methods, multifunctional electrochemical sensors can be achieved (e.g. pH and glucose [21, 22]). LIG shows as well a great potential to act as an electrode for supercapacitors, especially in flexible [69–71] and stretchable/wearable supercapacitors [5–7] . Further improving the supercapacitors performance, in combination with wireless communication and powering (such as NFC or RFID) can enable wearable devices to be self powered. As regards future directions in bioapplications, first toxicity assessments on LIG have been carried out on zebrafish [72], suggesting that LIG could be safely used in biological/biomedical applications. Additionally, by finding alternative (e.g. biodegradable, edible) precursors, LIG could be used in the development of next generation transient [73] and even edible electronics [45, 74].

References

1. Inagaki, M.: New Carbons Control of Structure and Functions. Elsevier Science, Amsterdam/New York (2000)
2. Lin, J., Peng, Z., Liu, Y., Ruiz-Zepeda, F., Ye, R., Samuel, E.L.G., Yacaman, M.J., Yakobson, B.I., Tour, J.M.: Laser-induced porous graphene films from commercial polymers. Nat. Commun. **5**, 5714 (2014)
3. Huang, L., Su, J., Song, Y., Ye, R.: Laser-induced graphene: En route to smart sensing. Nano-Micro Lett. **12**, 157 (2020)
4. Wan, Z., Nguyen, N.-T., Gao, Y., Li, Q.: Laser induced graphene for biosensors. Sustainable Mater. Technol. **25**, e00205 (2020)
5. Peng, Z., Lin, J., Ye, R., Samuel, E.L.G., Tour, J.M.: Flexible and stackable laser-induced graphene supercapacitors. ACS Appl. Mater. Interfaces **7**, 3414–3419 (2015)
6. Lamberti, A., Clerici, F., Fontana, M., Scaltrito, L.: A highly stretchable supercapacitor using laser-induced graphene electrodes onto elastomeric substrate. Adv. Energy Mater. **6**, 1600050 (2016)
7. Song, W., Zhu, J., Gan, B., Zhao, S., Wang, H., Li, C., Wang, J.: Flexible, stretchable, and transparent planar microsupercapacitors based on 3D porous laser-induced graphene. Small **14**, 1702249 (2018)
8. Tehrani, F., Beltrán-Gastélum, M., Sheth, K., Karajic, A., Yin, L., Kumar, R., Soto, F., Kim, J., Wang, J., Barton, S., Mueller, M., Wang, J.: Laser-induced graphene composites for printed, stretchable, and wearable electronics. Adv. Mater. Technologies **4**, 1900162 (2019)
9. Tao, L.-Q., Tian, H., Liu, Y., Ju, Z.-Y., Pang, Y., Chen, Y.-Q., Wang, D.-Y., Tian, X.-G., Yan, J.-C., Deng, N.-Q., Yang, Y., Ren, T.-L.: An intelligent artificial throat with sound-sensing ability based on laser induced graphene. Nat. Commun. **8**, 14579 (2017)
10. Zhang, P., Tang, X., Pang, Y., Bi, M., Li, X., Yu, J., Zhang, J., Yuan, M., Luo, F.: Flexible laser-induced-graphene omnidirectional sound device. Chem. Phys. Lett. **745**, 137275 (2020)
11. Carvalho, A.F., Fernandes, A.J.S., Leitão, C., Deuermeier, J., Marques, A.C., Martins, R., Fortunato, E., Costa, F.M.: Laser-induced graphene strain sensors produced by ultraviolet irradiation of polyimide. Adv. Funct. Mater. **28**, 1805271 (2018)
12. Chhetry, A., Sharifuzzaman, M., Yoon, H., Sharma, S., Xuan, X., Park, J.Y.: MoS2-decorated laser-induced graphene for a highly sensitive, hysteresis-free, and reliable piezoresistive strain sensor. ACS Appl. Mater. Interfaces **11**, 22531–22542 (2019)
13. Liu, W., Huang, Y., Peng, Y., Walczak, M., Wang, D., Chen, Q., Liu, Z., Li, L.: Stable wearable strain sensors on textiles by direct laser writing of graphene. ACS Appl. Nano Mater. **3**, 283–293 (2020)
14. Dallinger, A., Keller, K., Fitzek, H., Greco, F.: Stretchable and skin-conformable conductors based on polyurethane/laser-induced graphene. ACS Appl. Mater. Interfaces **12**, 19855–19865 (2020)
15. Rahimi, R., Ochoa, M., Yu, W., Ziaie, B.: Highly stretchable and sensitive unidirectional strain sensor via laser carbonization. ACS Appl. Mater. Interfaces **7**, 4463–4470 (2015)
16. Wu, Y., Karakurt, I., Beker, L., Kubota, Y., Xu, R., Ho, K.Y., Zhao, S., Zhong, J., Zhang, M., Wang, X., Lin, L.: Piezoresistive stretchable strain sensors with human machine interface demonstrations. Sens. Actuators A **279**, 46–52 (2018)
17. Stanford, M.G., Yang, K., Chyan, Y., Kittrell, C., Tour, J.M.: Laser-induced graphene for flexible and embeddable gas sensors. ACS Nano **13**, 3474–3482 (2019)
18. Yang, L., Yi, N., Zhu, J., Cheng, Z., Yin, X., Zhang, X., Zhu, H., Cheng, H.: Novel gas sensing platform based on a tretchable laser-induced graphene pattern with self-heating capabilities. J. Mater. Chem. A **8**, 6487–6500 (2020)
19. Sun, B., McCay, R.N., Goswami, S., Xu, Y., Zhang, C., Ling, Y., Lin, J., Yan, Z.: Gas-permeable, multifunctional on-skin electronics based on laser-induced porous graphene and sugar-templated elastomer sponges. Adv. Mater. **30**, 1804327 (2018)

20. Zahed, M.A., Das, P.S., Maharjan, P., Barman, S.C., Sharifuzzaman, M., Yoon, S.H., Park, J.Y.: Flexible and robust dry electrodes based on electroconductive polymer spray-coated 3D porous graphene for long-term electrocardiogram signal monitoring system. Carbon **165**, 26–36 (2020)
21. Xuan, X., Kim, J.Y., Hui, X., Das, P.S., Yoon, H.S., Park, J.-Y.: A highly stretchable and conductive 3D porous graphene metal nanocomposite based electrochemical-physiological hybrid biosensor. Biosens. Bioelectron. **120**, 160–167 (2018)
22. Zahed, M.A., Chandra Barman, S., Das, P.S., Sharifuzzaman, M., Yoon, H.S., Yoon, S.H., Park, J.Y.: Highly flexible and conductive poly (3, 4-ethylene dioxythiophene)-poly (styrene sulfonate) anchored 3-dimensional porous graphene network-based electrochemical biosensor for glucose and pH detection in human perspiration. Biosens. Bioelectron. **160**, 112220 (2020)
23. Yoon, H., Nah, J., Kim, H., Ko, S., Sharifuzzaman, M., Barman, S.C., Xuan, X., Kim, J., Park, J.Y.: A chemically modified laser-induced porous graphene based flexible and ultrasensitive electrochemical biosensor for sweat glucose detection. Sens. Actuators B **311**, 127866 (2020)
24. Li, H., Guo, C., Liu, C., Ge, L., Li, F.: Laser-induced graphene hybrid photoelectrode for enhanced photoelectrochemical detection of glucose. Analyst **145**, 4041–4049 (2020)
25. Zhu, J., Cho, M., Li, Y., Cho, I., Suh, J.-H., Orbe, D.D., Jeong, Y., Ren, T.-L., Park, I.: Biomimetic turbinate-like artificial nose for hydrogen detection based on 3D porous laser-induced graphene. ACS Appl. Mater. Interfaces **11**, 24386–24394 (2019)
26. Dosi, M., Lau, I., Zhuang, Y., Simakov, D.S.A., Fowler, M.W., Pope, M.A.: Ultrasensitive electrochemical methane sensors based on solid polymer electrolyte-infused laser-induced graphene. ACS Appl. Mater. Interfaces **11**, 6166–6173 (2019)
27. Soares, R.R.A., Hjort, R.G., Pola, C.C., Parate, K., Reis, E.L., Soares, N.F.F., McLamore, E.S., Claussen, J.C., Gomes, C.L.: Laser-induced graphene electrochemical immunosensors for rapid and label-free monitoring of Salmonella Enterica in chicken broth. ACS Sensors **5**, 1900–1911 (2020)
28. Cardoso, A.R., Marques, A.C., Santos, L., Carvalho, A.F., Costa, F.M., Martins, R., Sales, M.G.F., Fortunato, E.: Molecularly-imprinted chloramphenicol sensor with laser-induced graphene electrodes. Biosens. Bioelectron. **124–125**, 167–175 (2019)
29. Yagati, A.K., Behrent, A., Beck, S., Rink, S., Goepferich, A.M., Min, J.,Lee, M.-H., Baeumner, A.J.: Laser-induced graphene interdigitated electrodes for label-free or nanolabel-enhanced highly sensitive capacitive Aptamer-based biosensors. Biosens. Bioelectron. **164**, 112272 (2020)
30. Zhang, C., Ping, J., Ying, Y.: Evaluation of trans-resveratrol level in grape wine using laser-induced porous graphene-based electrochemical sensor. Sci. Total Environ. **714**, 136687 (2020)
31. Wan, Z., Umer, M., Lobino, M., Thiel, D., Nguyen, N.-T., Trinchi, A., Shiddiky, M.J., Gao, Y., Li, Q.: Laser induced self-N-doped porous graphene as an electrochemical biosensor for femtomolar miRNA detection. Carbon **163**, 385–394 (2020)
32. Duy, L.X., Peng, Z., Li, Y., Zhang, J., Ji, Y., Tour, J.M.: Laser-induced graphene fibers. Carbon **126**, 472–479 (2018)
33. Zhai, Q., Cheng, W.: Soft and stretchable electrochemical biosensors. Mater. Today Nano **7**, 100041 (2019)
34. Zhang, Z., Song, M., Hao, J., Wu, K., Li, C., Hu, C.: Visible light laser-induced graphene from phenolic resin: a new approach for directly writing graphene-based electrochemical devices on various substrates. Carbon **127**, 287–296 (2018)
35. Stanford, M.G., Zhang, C., Fowlkes, J.D., Hoffman, A., Ivanov, I.N., Rack, P.D., Tour, J.M.: High-resolution laser-induced graphene. Flexible electronics beyond the visible limit. ACS Appl. Mater. Interfaces **12**, 10902–10907 (2020)
36. Dong, Y., Rismiller, S.C., Lin, J.: Molecular dynamic simulation of layered graphene clusters formation from polyimides under extreme conditions. Carbon **104**, 47–55 (2016)
37. Lamberti, A., Serrapede, M., Ferraro, G., Fontana, M., Perrucci, F., Bianco, S., Chiolerio, A., Bocchini, S.: All-SPEEK flexible supercapacitor exploiting laser-induced graphenization. 2D Mater. **4**, 035012 (2017)

38. Zhu, C., Zhao, D., Wang, K., Dong, X., Duan, W., Wang, F., Gao, M., Zhang, G.: Direct laser writing of graphene films from a polyether ether ketone precursor. J. Mater. Sci. **54**, 4192–4201 (2019)
39. Yang, W., Zhao, W., Li, Q., Li, H., Wang, Y., Li, Y., Wang, G., Fabrication of smart components by 3D printing and laser-scribing technologies. ACS Appl. Mater. Interfaces **12**, 3928–3935 (2020)
40. Vashisth, A., Kowalik, M., Gerringer, J., Ashraf, C., van Duin, A.C., Green, M.J.: ReaxFF simulations of laser-induced graphene (LIG) formation for multifunctional polymer nanocomposites, ACS Appl. Nano Mater. **3**, 1881–1890 (2020)
41. Chen, Y., Long, J., Zhou, S., Shi, D., Huang, Y., Chen, X., Gao, J., Zhao, N., Wong, C.-P.: UV laser-induced polyimide-to-graphene conversion: modeling, fabrication, and application. Small Methods **3**, 1900208 (2019)
42. Wang, F., Wang, K., Zheng, B., Dong, X., Mei, X., Lv, J., Duan, W., Wang, W.: Laser-induced graphene: preparation, functionalization and applications. Mater. Technol. **33**, 340–356 (2018)
43. Ye, R., Chyan, Y., Zhang, J., Li, Y., Han, X., Kittrell, C., Tour, J.M.: Laser-induced graphene formation on wood. Adv. Mater. **29**, 1702211 (2017)
44. Han, X., Ye, R., Chyan, Y., Wang, T., Zhang, C., Shi, L., Zhang, T., Zhao, Y., Tour, J.M.: Laser-induced graphene from wood impregnated with metal salts and use in electrocatalysis. ACS Appl. Nano Mater. **1**, 5053–5061 (2018)
45. Chyan, Y., Ye, R., Li, Y., Singh, S.P., Arnusch, C.J., Tour, J.M.: Laser-induced graphene by multiple lasing: toward electronics on cloth, paper, and food. ACS Nano **12**, 2176–2183 (2018)
46. Zhang, W., Lei, Y., Ming, F., Jiang, Q., Costa, P.M.F.J., Alshareef, H.N.: Lignin laser lithography: a direct-write method for fabricating 3D graphene electrodes for microsupercapacitors. Adv. Energy Mater. **8**, 1801840 (2018)
47. Quéré, D.: Wetting and roughness. Annu. Rev. Mater. Res. **38**, 71–99 (2008)
48. Nasser, J., Lin, J., Zhang, L., Sodano, H.A.: Laser induced graphene printing of spatially controlled super-hydrophobic/hydrophilic surfaces. Carbon **162**, 570–578 (2020)
49. Wu, W., Liang, R., Lu, L., Wang, W., Ran, X., Yue, D.: Preparation of superhydrophobic laser-induced graphene using Taro leaf structure as templates. Surf. Coat. Technol. **393**, 125744 (2020)
50. Li, Y., Luong, D.X., Zhang, J., Tarkunde, Y.R., Kittrell, C., Sargunaraj, F., Ji, Y., Arnusch, C.J., Tour, J.M.: Laser-induced graphene in controlled atmospheres: from superhydrophilic to superhydrophobic surfaces. Adv. Mater. **29**, 1700496 (2017)
51. Li, J.T., Stanford, M.G., Chen, W., Presutti, S.E., Tour, J.M.: Laminated laser-induced graphene composites. ACS Nano **14**, 7911–7919 (2020)
52. Luong, D.X., Yang, K., Yoon, J., Singh, S.P., Wang, T., Arnusch, C.J., Tour, J.M.: Laser-induced graphene composites as multifunctional surfaces. ACS Nano **13**, 2579–2586 (2019)
53. Parmeggiani, M., Zaccagnini, P., Stassi, S., Fontana, M., Bianco, S., Nicosia, C., Pirri, C.F., Lamberti, A.: PDMS/polyimide composite as elastomeric substrate for multifunctional laser-induced graphene electrodes. ACS Appl. Mater. Interfaces **11**, 33221–33230 (2019)
54. Ye, R., James, D.K., Tour, J.M.: Laser-induced graphene. Acc. Chem. Res. **51**, 1609–1620 (2018)
55. Tian, Q., Yan, W., Li, Y., Ho, D.: Bean pod-inspired ultra-sensitive and self-healing pressure sensor based on laser induced graphene and polystyrene microspheres sandwiched structure. ACS Appl. Mater. Interfaces **12**, 9710–9717 (2020)
56. Searle, A., Kirkup, L.: A direct comparison of wet, dry and insulating bioelectric recording electrodes. Physiol. Meas. **21**, 271–283 (2000)
57. Miyamoto, A., Lee, S., Cooray, N.F., Lee, S., Mori, M., Matsuhisa, N., Jin, H., Yoda, L., Yokota, T., Itoh, A., Sekino, M., Kawasaki, H., Ebihara, T., Amagai, M., Someya, T.: Inflammation-free, gas-permeable, lightweight, stretchable on-skin electronics with nanomeshes. Nat. Nanotechnol. **12**, 907–913 (2017)
58. Ferrari, L.M., Sudha, S., Tarantino, S., Esposti, R., Bolzoni, F., Cavallari, P., Cipriani, C., Mattoli, V., Greco, F.: Ultraconformable temporary tattoo electrodes for electrophysiology. Adv. Sci. **5**, 1700771 (2018)

59. Zucca, A., Cipriani, C., Sudha, Tarantino, S., Ricci, D., Mattoli, V., Greco, F.: Tattoo conductive polymer nanosheets for skin-contact applications. Adv. Healthc. Mater. **4**, 983–990 (2015)
60. Arduini, F., Micheli, L., Moscone, D., Palleschi, G., Piermarini, S., Ricci, F., Volpe, G.: Electrochemical biosensors based on nanomodified screen-printed electrodes: Recent applications in clinical analysis. TrAC Trends Anal. Chem. **79**, 114–126 (2016). Past, Present, Future Challenges of Biosensors and Bioanalytical Tools in Anal. Chem.: A Tribute to Prof Marco Mascini
61. Ge, L., Hong, Q., Li, H., Liu, C., Li, F.: Direct-laser-writing of metal sulfide-graphene nanocomposite photoelectrode toward sensitive photoelectrochemical sensing. Adv. Funct. Mater. **29**, 1904000 (2019)
62. Zhu, Z., Garcia-Gancedo, L., Flewitt, A.J., Xie, H., Moussy, F., Milne, W.I.: A critical review of glucose biosensors based on carbon nanomaterials: carbon nanotubes and graphene. Sensors **12**, 5996–6022 (2012)
63. Ge, L., Hong, Q., Li, H., Li, F.: A laser-induced TiO 2-decorated graphene photoelectrode for sensitive photoelectrochemical biosensing. Chem. Commun. **55**, 4945–4948 (2019)
64. Samouco, A., Marques, A.C., Pimentel, A., Martins, R., Fortunato, E.: Laser-induced electrodes towards low-cost flexible UV ZnO sensors. Flex. Print. Electron. **3**, 044002 (2018)
65. Mahmood, F., Zhang, C., Xie, Y., Stalla, D., Lin, J., Wan, C.: Transforming lignin into porous graphene via direct laser writing for solid-state supercapacitors. RSC Adv. **9**, 22713–22720 (2019)
66. Mahmood, F., Zhang, H., Lin, J., Wan, C.: Laser-induced graphene derived from Kraft lignin for flexible supercapacitors. ACS Omega **5**, 14611–14618 (2020)
67. Lei, Y., Alshareef, A.H., Zhao, W., Inal, S.: Laser-scribed graphene electrodes derived from lignin for biochemical sensing. ACS Appl. Nano Mater. **3**, 1166–1174 (2019)
68. Edberg, J., Brooke, R., Hosseinaei, O., Fall, A., Wijeratne, K., Sandberg, M.: Laser-induced graphitization of a forest-based ink for use in flexible and printed electronics. npj Flex. Electron. **4**, 1–10 (2020)
69. Peng, Z., Ye, R., Mann, J.A., Zakhidov, D., Li, Y., Smalley, P.R., Lin, J., Tour, J.M.: Flexible boron-doped laser-induced graphene microsupercapacitors. ACS Nano **9**, 5868–5875 (2015)
70. Li, L., Zhang, J., Peng, Z., Li, Y., Gao, C., Ji, Y., Ye, R., Kim, N.D., Zhong, Q., Yang, Y., Fei, H., Ruan, G., Tour, J.M.: High-performance pseudocapacitive microsupercapacitors from laser-induced graphene. Adv. Mater. **28**, 838–845 (2016)
71. Li, X., Cai, W., Teh, K.S., Qi, M., Zang, X., Ding, X., Cui, Y., Xie, Y., Wu, Y., Ma, H., Zhou, Z., Huang, Q.-A., Ye, J., Lin, L.: High-voltage flexible microsupercapacitors based on laser-induced graphene. ACS Appl. Mater. Interfaces **10**, 26357–26364 (2018)
72. d'Amora, M., Lamberti, A., Fontana, M., Giordani, S.: Toxicity assessment of laser-induced graphene by zebrafish during development. J. Phys.: Mater. **3**, 034008 (2020)
73. Cheng, H., Vepachedu, V.: Recent development of transient electronics. Theor. Appl. Mech. Lett. **6**, 21–31 (2016)
74. Wu, Y., Ye, D., Shan, Y., He, S., Su, Z., Liang, J., Zheng, J., Yang, Z., Yang, H., Xu, W., Jiang, H.: Edible and nutritive electronics: materials, fabrications, components, and applications. Adv. Mater. Technol. **5**, 2000100 (2020)

Chapter 7
Production of Carbon Nanofoam by Pulsed Laser Deposition on Flexible Substrates

Alessandra Maffini, Andrea Pazzaglia, David Dellasega, Valeria Russo, and Matteo Passoni

Abstract Nanostructured, ultra-low density carbon materials known as "carbon nanofoams" are attracting a growing interest for novel applications in many fields, from hydrogen storage and catalysis to advanced targets for laser-driven particle acceleration. Pulsed laser deposition has emerged as one of the most promising and versatile techniques for the synthesis of nanofoam, especially whenever a flexible substrate is required. Here we will review the most recent advances about the production and charaterization of carbon nanofoams by means of the pulsed laser deposition with nanosecond laser pulses. In particular, we will address the process of foam growth starting from the aggregation of carbon nanoparticles in fractal-like structures, demonstrating how it is possible to control nanofoam properties exploiting unconventional process parameters such as the laser repetition rate. Finally, the deposition of carbon nanofoams on flexible substrates for superintense laser-matter interaction is discussed as an illustrative example of the potential of the technique.

Keywords Nanofoam · Carbon nanoparticles · Pulsed laser deposition · Ultra-low density · Fractal aggregation · Laser-driven acceleration

7.1 Introduction

Carbon (C) films, and in particular films with high sp^3 content, can be deposited by many Chemical Vapor Deposition [1] and Physical Vapor Deposition (PVD) [2, 3] techniques. In this frame, in addition to well-established deposition techniques such as magnetron sputtering, also Pulsed Laser Deposition (PLD) has shown its ability in depositing compact carbon coatings with different fractions of sp^2 and sp^3 carbon

A. Maffini (✉) · A. Pazzaglia · D. Dellasega · V. Russo · M. Passoni
Department of Energy, Politecnico di Milano, Milan, Italy
e-mail: alessandro.maffini@polimi.it

F. Borghi et al. (eds.), *Nanoporous Carbons for Soft and Flexible Energy Devices*,
Carbon Materials: Chemistry and Physics 11,
https://doi.org/10.1007/978-3-030-81827-2_7

atoms [4–7]. In PLD laser pulses are shot on a target placed in a vacuum chamber, causing the evaporation of target surface layers. The ablated species expand in a controlled background atmosphere and are finally collected on a substrate. By properly tuning the deposition conditions it is possible to tailor the properties of the depositing film down to the nanometer scale. Thanks to its peculiar features, PLD is practically the only PVD technique that has been extensively used in the deposition of nanostructured porous carbon films with controlled densities in the range of 2–1000 mg/cm^3 [8–11].

Nanostructured materials characterized by a ultra-low density (1-100 mg/cm^3), a large fraction of submicrometric voids and/or pores (typically ~90%), and a disordered fractal-like structure constitute a broad class of materials known as *nanofoam*. Their ultra-low density as well as the extremely high surface-to-volume ratio make nanofoam the material of choice for many research fields of great societal and technological importance, such as hydrogen storage [12], next generation supercapacitors [13] and catalysts [14], water treatment [15], gas sensing [9], and medicine [16]. Among them, carbon nanofoams have attracted an impressive amount of research efforts because of their unusual and appealing features, like an unconventional ferromagnetic behavior [17], giant optical absorption [18], and an increased adsorption and storage capability [19], together with the unique carbon capability of forming chemical bonds that are very different in their nature (i.e., sp^1, sp^2, and sp^3 hybridization).

Carbon nanofoams are essentially void-rich, fractal-like structures made of carbon nanoparticles, with an average diameter ranging from a few nanometers up to tens of nanometers [8, 9, 20–22]. Due to the interaction with the background gas the nanoparticles are deposited on the substrate in a low energy regime. This allows the deposition of several micron thick carbon nanofoam films on thin metallic films [23, 24] and flexible substrates with a lateral dimension of about hundreds of cm^2. The first carbon nanofoams films produced by PLD are reported in the works of Rode et al. [8, 20, 25]. There, an unconventional set of deposition parameters, namely high values of fluence (~120 J/cm2), Ar pressure (~10^4 Pa) and repetition-rate (kHz) have been exploited in the attempt to get a material having a significant sp^3 bonding content and densities around 2–10 mg/cm^3.

In the work of Zani et al. [10] the role of ambient gas, Ar or He, and pressure in the range 0–1000 Pa was assessed with respect to density, thickness, surface uniformity and adhesion of foam layers. A complete scan of average mass density as a function of pressure for different ambient gases was made showing how the morphological and structural properties of the foams change as a function of the main process parameters. In particular, it was highlighted how the role of the atomic weight of the ambient gas determined a completely different morphology of the deposited foam.

The dynamics of the nanoparticle aggregation into a foam-like structure as well as the evolution of nanofoam morphology through different stages of growth, characterized by an increasing number of laser shots was explored by Maffini et al. [11]. The authors show that the peculiar nanofoam structure is given by the coalescence of aggregates in a snowfall-like process and correlate the aggregate size

with the aggregation timescale demonstrating how it is possible to control nanofoam morphology and density by acting on the laser repetition rate.

In addition to the already mentioned applications the possibility to produce carbon foams with controlled and reproducible mean density (tens of mg/cm^3), area (several cm^2) and thickness (4-18 μm), deposited on a micrometric solid flexible substrate has been proven to be of pivotal importance for the development of advanced target concepts in superintense laser-driven ion acceleration experiments [23, 24].

In the following of the chapter the features of the deposition of carbon nanofoams by PLD will be presented and main process parameters will be addressed. Morphology, structure, and composition of the resulting deposited films will be discussed (Sect. 7.2). Since the features of the deposited films are strictly related to the PLD deposition, in Sect. 7.3 a focus will be made with respect to the growth dynamics of carbon foam aggregates. The quantification of the extremely low density of the carbon nanofoam represents an experimental challenge that needs the development of ad-hoc characterizations. In Sect. 7.4 a new tool that exploits the features of energy dispersion spectroscopy to assess the areal density of the carbon foam will be discussed. Finally, in Sect. 7.5 the production of carbon foam on flexible substrate for laser-driven acceleration experiments will be presented.

7.2 Pulsed Laser Deposition of Nanostructured Carbon Films

In PLD the power source that leads to the ejection of the depositing species from the target is constituted by a short (from tens of nanosecond to tens of femtosecond) laser pulse that is focused on a carbon target material (usually graphite) that is placed in a proper vacuum chamber. The use of a graphite target prevents one of the main issues related to PLD that is the ejection of liquid droplet that solidifies on the growing film forming macroscopic defects. In the following, unless otherwise specified, we will refer to PLD with nanosecond pulses (or ns-PLD in short), since it is the most established deposition regime.

The features of the deposited film result from a complex interplay among many experimental parameters, such as laser wavelength, laser fluence (i.e. pulse energy on target per unit surface), target-to-substrate distance, laser repetition rate (i.e. the inverse of shot-to-shot time interval) and background gas composition and pressure. Differently from many other PVD techniques that require the presence of a specific gas atmosphere to function properly, in PLD it is possible to change background atmosphere in terms of composition (typically argon, helium, oxygen, nitrogen or hydrogen in different ratios) and pressure in the range 10^{-4}-10^4 Pa. The background pressure is indeed a crucial parameter in order to govern the PLD process, since it allows to control the nature of the species arriving on the substrate (either atoms, atomic clusters, or nanoparticles), their kinetic energy,

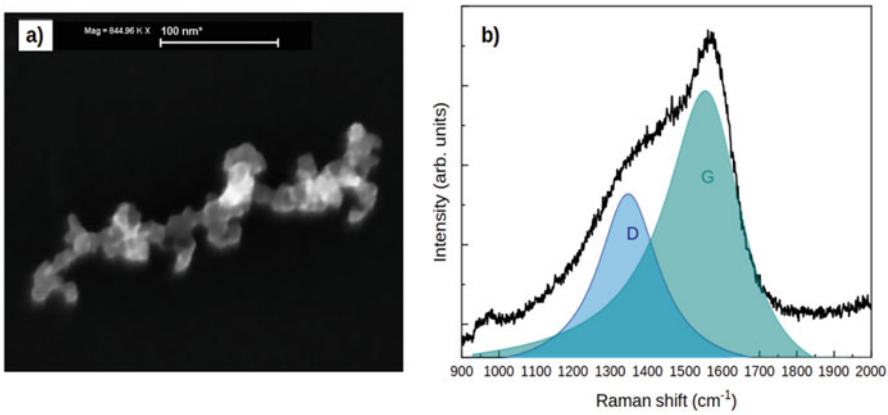

Fig. 7.1 (**a**) HR-STEM of a C nanoparticle aggregate *deposited by PLD at background gas pressure of 700 Pa Ar.* (**b**) Raman spectrum of a typical *C nanostructure (background pressure 1000 Pa Ar).* Fit curves, Lorentzian for D peak and BWF for G peak, are also depicted

and -in the case of nanoparticles- their aggregation dynamics. In presence of a sufficiently high pressure the ablated species can condense into nanoparticles while they expand in the deposition chamber. During the expansion, the nanoparticles can stick together and finally reach the substrate in the form of aggregates (more details about the deposition process dynamics are given below and in the next sections). In the specific case of carbon nanofoams an unconventional regime is exploited, characterized by moderate laser fluence (1.5 – 2.1 J/cm^2) and high background pressure (up to 1000 Pa).

A structure made of C nanoparticles produced by PLD is shown in the High Resolution *S*canning Transmission Electron Microscopy (HR-STEM) image reported in Fig. 7.1a. The synthesis of these nanoparticles, that represent the elementary constituents of nanostructured C films grown by PLD, occurs within the ablation plume starting from small carbon clusters and atoms ablated by the laser. Raman spectroscopy gives further insights about carbon nanoparticles and nanostrucured films, providing information concerning the sp^2 (graphite-like) and sp^3 (diamond-like) content, ordering and clustering, which in turn determine most physical properties of carbon-based materials. Raman data for pulsed laser deposited nanoparticles are reported in Fig. 7.1b. The spectrum is typical of amorphous carbon, with prominent broad G and D peaks. Using a fitting procedure involving an asymmetric Breit–Wigner–Fano (BWF) function for the G peak and a Lorentzian function for the D peak (also depicted in the figure), quantitative significant parameters can be deduced, such as the G position (relative to the maximum of the BWF curve) and the ratio of the peak heights I(D)/I(G). Based on these data and following a well-established interpretation for Raman spectra of disordered carbon materials [26], the nanoparticle structure can be described as a nearly pure sp^2 network of topologically disordered graphitic domains, with few chain-like structures and extremely low sp^3 content.

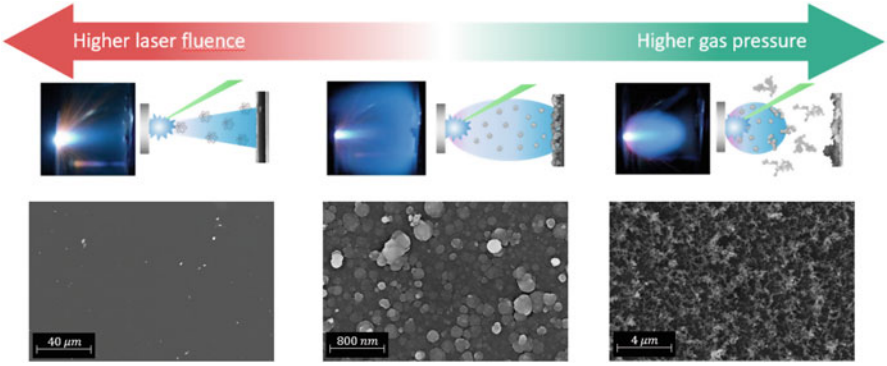

Fig. 7.2 Scheme of the film morphologies which can be produced by Pulsed-Laser Deposition (top) with the relative SEM images (bottom). At higher laser fluence and lower gas pressure, compact amorphous films are deposited. At intermediate values, more porous films grow. At low laser fluence and high gas pressure, very porous and fractal films, called nanofoams, are produced. Details about the depositions can be found in references [11, 28]

The nanoparticles form films with peculiar structures dependent on the dynamics of the deposition.

In particular the momentum of the nanoparticles and the properties of the ambient gas play the major role in determining it, since the shape of the trajectories and the eventual sticking before landing determine which growth mechanism and film nanostructure takes, as schematically shown in Fig. 7.2.

If the ablated material is composed by atoms or ions, the film grows as compact amorphous carbon. Conversely, if nanoparticles are synthesized during the plume expansion, different growth mechanisms -and hence different film morphologies- can be distinguished as a function of the nanoparticles motion. In the case of high momentum nanoparticles and relatively low ambient gas pressure (few Pa), the trajectories can be approximated by straight lines and the film is formed by the so-called Ballistic Aggregation (BA) [27]. This mechanism produces slightly porous films composed by a random assembling of the nanoparticles. In this case the nanoparticle can stick to the substrate or to other pre-landed ones with some residual thermal energy and may also result in a rearrangement of the crystal structure in a 'cauliflower' shape (see Fig. 7.2, bottom central SEM image) [28].

Increasing the gas pressure or reducing the initial momentum of nanoparticles (by diminishing the laser fluence) makes the nanoparticle to collide more frequently with the gas atoms and reaching a thermal equilibrium with it. In this condition, due to the intrinsic collision stochasticity, the nanoparticles move in random directions with a Brownian motion [29]. The phenomenon continues until the nanoparticles reach the substrate or the growing film and irreversibly stick to them. This growth mechanism is well described by the Diffusion Limited Aggregation model (DLA) [30], called in this way because the limiting phenomenon for the system formation is the Brownian diffusion.

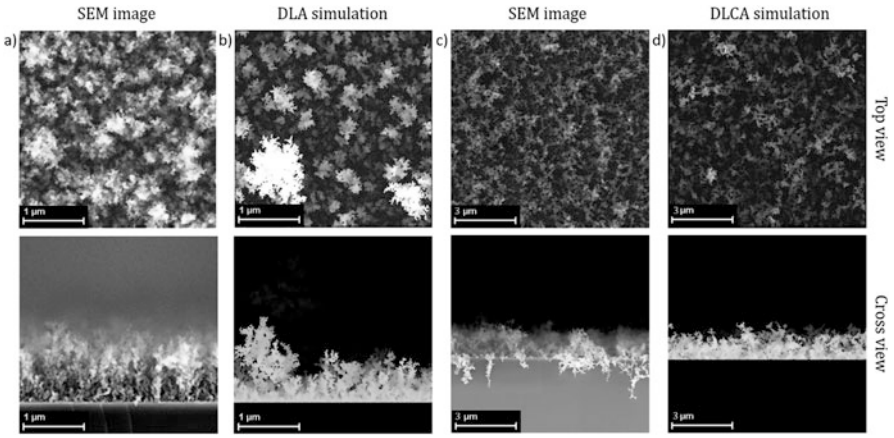

Fig. 7.3 top view (upper panel) and cross view (bottom panel) SEM images (**a,c**) of low-density fractal films, compared to Diffusion Limited Aggregation (DLA) film simulation (**b**) and Diffusion Limited Cluster-Cluster Aggregation (DLCA) film simulation (**d**)

DLA can be easily implemented in a computer simulation to reproduce the film structure which should be obtained within the model hypotheses. As shown in Fig. 7.3a-b, DLA algorithm generates a 'trees' structure which looks like the experimentally observed nanostructures. It can be appreciated that these film exhibit a fractal pattern, i.e. show auto-similarity at different scales of observation. Fractals can be described in terms of their fractal dimension D_f, which is a measure of the complexity of a pattern and how its details change with the scale at which they are observed. In general, D_f is equal to the number of the space dimensions for non-fractal objects (e.g. 1 for lines, 2 for squares, 3 for cubes), while lower values are found for fractal objects.

The radius of gyration R_g is another useful quantity in describing fractal patterns, being defined as the radius at which a number of filled spaces equal to that of the entire pattern would have to be placed to have the same moment of inertia.

One peculiar properties of fractals is that they obey a power scaling law which, for nanoparticles aggregates, reads as [31]:

$$N = K\left(\frac{R_g}{R_{np}}\right)^{D_f} \tag{7.1}$$

where N is the number of particles composing the fractal, K a pre-factor in the order of unity, R_g the radius of gyration, R_p the nanoparticle radius and D_f the fractal dimension. Equation 7.1 shows that the higher is D_f, the higher is the complexity of the pattern and lower is its space-filling capacity.

Strictly speaking about the DLA mechanism, the fractal properties arise from the Brownian motion, which makes the probability that a nanoparticle sticks to the outer branches of the 'tree' higher than sticking to the substrate or to the inner body of the

structure. The DLA branching shape is characterized by a fractal dimension around 2.4, considering isolated 'trees' in three dimensions [32]. Since this value is lower than the 3D space dimensions, the structure fills a lower volume and it is therefore more porous with respect to BA, with densities about tens times lower than the bulk one, showing also a high surface area, useful for some applications.

DLA can even occur onto a 2D surface, to produce fractals with $D_f = 1.7$ [33]. This mechanism can experimentally take place when few nanoparticles reach a hot substrate, which makes them to move with random motion onto the surface [34].

Nonetheless, DLA is not the only mechanism which enables to produce fractal films. A further increase in the background pressure results in the confinement of the nanoparticles in a smaller volume and in the occurring of a new phenomenon: the nanoparticle-nanoparticle collision and irreversible sticking. Due to the higher concentration, the nanoparticles are able to aggregate with a mechanism called Diffusion Limited Cluster-Cluster Aggregation (DLCA). The cluster (nanoparticle) trajectories are Brownian as in DLA, but, since they can irreversibly stick together, they can produce fractal aggregates before their landing onto the substrate. The DLCA mechanism produce patterns with fractal dimension roughly equal to 1.8 [35], which makes these aggregates more porous than the DLA ones. Higher fractal dimension values can be found for slightly different growth mechanisms. For example, if the nanoparticles sticking probability is approaching zero, the aggregation is dominated by the sticking reaction and not by the Brownian diffusion. In this case we speak of Reaction Limited Cluster-Cluster Aggregation (RLCA), which is featured by a 2.1 fractal dimension [36]. In natural systems, the aggregation mechanism is frequently a combination or an intermediate case of DLCA and RLCA [37].

DLCA/RLCA can be easily implemented in numerical codes to reproduce the structure of films obtained when these aggregation mechanisms take place, such as nanofoams. Due to the low fractal dimension nanofoam are characterized by an ultra-low density, down to few thousandth of the bulk density (hence more than 99,5% of vacuum fraction), and by a very high surface area to mass ratio. As shown in Fig. 7.3 c-d, the DLCA simulation is able to precisely reproduce the nanofoam morphology, and its fractal features.

In the next section we will discuss in details the process that leads to nanofoam growth in PLD experiments and the role of deposition parameters on the nanofoam morphology.

7.3 Growth Dynamics of PLD Carbon Nanofoam

In the previous section we have shown how different nanoparticle aggregation mechanisms give rise to different aggregate morphologies and hence to different features for the resulting films. Understanding the aggregation and growth dynamics of a nanostructured PLD film is therefore instrumental in achieving a full control over its properties. In this section we will describe in details the growth dynamics

of PLD carbon nanofoams by reviewing and expanding the snowfall-like model proposed in reference [11].

By looking at the striking similarities between the morphology of a pulsed laser deposited nanofoam (Fig. 7.3c) and the simulation under DLCCA hypotesis (Fig. 7.3d) one can deduce that the DLCCA is the dominant aggregation mechanism responsible for aggregation of carbon nanoparticle into a nanofoam structure. In this context, two different scenarios -distinguished according to where the nanoparticle aggregation takes place- have been proposed: *on substrate* rather than *on flight*. To each scenario corresponds a specific dimensionality, namely 2D (or *in-plane*) for the former, 3D (*or in-space*) to the latter.

One can draw an illustrative analogy between the growth of fractal nanostructured materials in PVD techniques and deposition of ice from the water vapor present in the atmosphere. Both frost and snow can be considered fractal structures made of I_c ice. They differ in how they grow: hoar frost grows from the direct condensation (also called de-sublimation) of water vapor onto a cold surface (as on-substrate aggregation), while snow flakes aggregate in clouds, before landing to the ground (on-fligh aggregation).

Examples of PLD experiments where nanoparticle aggregation occurs mostly on substrate are given in [34, 38]. There, a pulsed ultrashort (<100 fs) laser is used to directly ablate Ti and TiO2 nanoparticles, and the two-dimensional nature of the aggregation process is demonstrated by observing how a change in the substrate affects the aggregate morphology. However, as firstly noted in [39], this scenario does not match well with experimental evidences about PLD depostion of carbon nanofoam with nanosecond pulses.

Firstly, as can be appreciated by the SEM image in Fig. 7.4, nanofoam aggregates are three-dimensional. The height of a single aggregate can be tens or even hundreds of times the size of a single nanoparticle. This means that, in a on-substrate aggregation scenario, a nanoparticle diffusing on the substrate would have to jump tens of times its size to climb up to the top of the aggregate and stick there. Such an event is very unlikely in comparison to a nanoparticle sticking in-plane to the edge of the aggregate (and that is the reason why structures originated by DLA on substrate are essentially flat).

Second, the aggregate morphology is not significantly affected by the properties of the substrate. Nanofoam aggregates deposited with the same conditions onto three different substrates (bulk silicon, amorphous carbon and nanocrystalline rhodium) are shown in Fig. 7.5a-c.

Despite the fact that the three substrates possess substantial differences in their chemical and physical properties the aggregates show a remarkable similarity. This fact stands in sharp contrast to what is expected in the case of on-substrate aggregation, as pointed out in [34]. Also, the aggregation process does not seem to be influenced by the chemical affinity between substrate and nanoparticles (as in the case of aC substrate) or by the presence of droplets on the Rh surface that could have acted as nucleation seeds if diffusion-limited aggregation on substrate were the dominant aggregation mechanism at play.

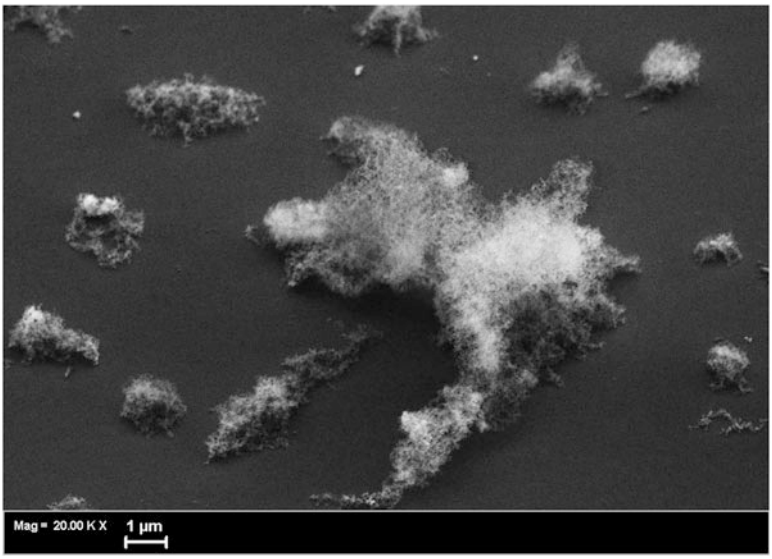

Fig. 7.4 SEM image of C aggregates taken with type II secondary electrons (SE2). Three-dimensional nature of the aggregates can be appreciated

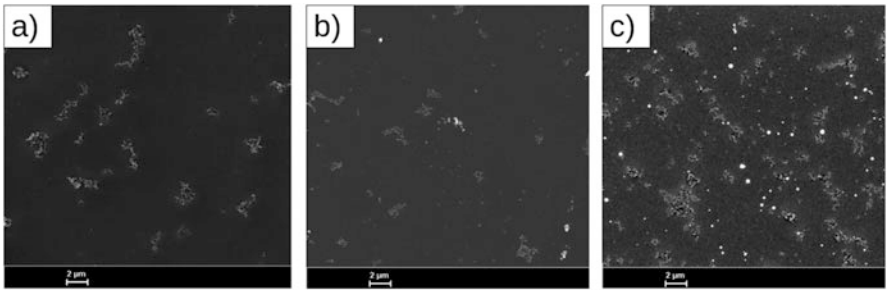

Fig. 7.5 SEM images of the deposited C aggregates after 10 laser shots for: (**a**) silicon substrate, (**b**) amorphous carbon substrate, and (**c**) rhodium substrate. The bright, spherical features observed in the case of Rh substrate are droplets of molten Rh ejected by the target during the Rh film deposition; the textured background is due to the different orientation of Rh crystallites. Background pressure is 700 Pa Ar, target to substrate distance is 4.5 cm, laser fluence is 1.7 J/cm^2, repetition rate is 1 Hz. Adapted with permission from reference [11] (Copyright 2019) (American Physical Society)

On-flight aggregation hypothesis can be further supported by considering the evolution of aggregate morphology and number with the number of laser shots, i.e. with the amount of ablated material. In a scenario where on-substrate aggregation is dominant, one should expect the average aggregate size to be increasing with of the number of shots, since each laser shot produces a certain number of nanoparticles that start diffusing on the substrate until sticking to an aggregate, increasing its

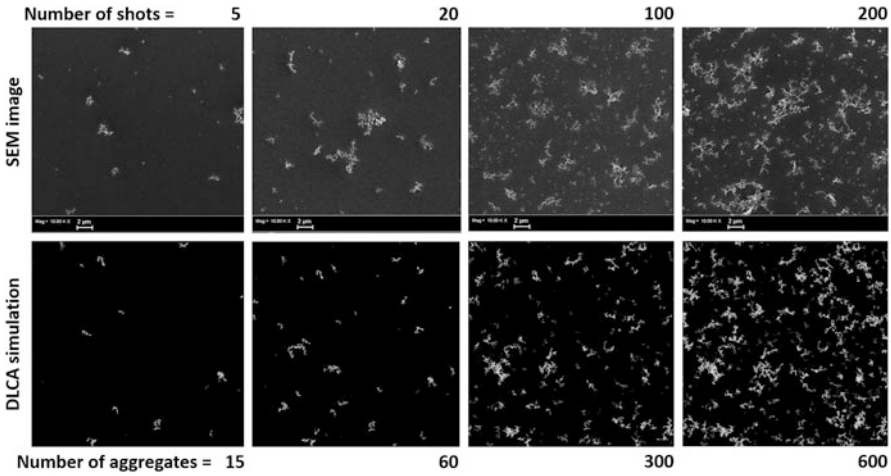

Fig. 7.6 Evolution of aggregate morphology. Above SEM images with an increasing number of laser shots. Below: simulations under the hypotheses of three dimensional DLCCA aggregation as a function of the number of aggregates

size. In the light of the analogy with frost, the size of the crystalline ice spicules depends on the amount of water vapor and how long they have been growing. On the contrary, if aggregates are formed before landing, their size has to be constant but their number should increase linearly with each shot. The same goes for snowfalls: the size of a single flake depends on the atmospheric conditions and does not change upon landing; the height of the snow blanket depends on the number of flakes that have fallen.

Figure 7.6 shows how the aggregate morphology changes with increasing number of laser shots, compared with the results of numeric simulations under the hypotheses of three dimensional DLCCA aggregation. The striking similarities between the morphology of PLD nanofoam and simulated materials together with the fact that aggregate size does not increase significantly with the number of shot -while the aggregate number does- lead us to conclude that in the case of ns-PLD nanofoam the aggregation of C nanoparticles occurs "in flight", i.e. inside the deposition chamber before the aggregate landing.

To summarize, we have seen how the growth of PLD carbon nanofoam bears some similarities to what happens during a snowfall: a low density nanofoam layer (the snow blanket) grows because of the coalescence of fractal, void-rich aggregates (the snowflakes). Each aggregate increases its size by clustering of smaller nanoparticles (supercooled water droplets) while is free to float in a nanoparticle-rich atmosphere (supersaturated air masses). The characteristic timescale of the aggregation dynamics τ_{agg} corresponds to the amount of time that an aggregate (snowflake) spends in the PLD background atmosphere (earth atmosphere) before being finally deposited on the substrate (the ground).

Once we have understood that a snowfall-like process is responsible for the nanofoam growth, we can try to investigate what is the aggregation timescale τ_{agg} and how it can be controlled by acting on the PLD process parameters. As already mentioned, is well known from the theory of fractal aggregation [40, 41] that the aggregation kinetics possesses some universal features which can be expressed in the form of scaling laws relating the aggregates properties with the aggregation time. In particular, the average gyration radius R_g should depend on the aggregation time following a power law:

$$R_g \propto {\tau_{agg}}^b \tag{7.2}$$

where b is a power-law exponent whose value depends on the specific aggregation mechanism and on the fractal dimension [40–42].

Considering a PLD deposition there are two natural timescales consistent with the hypothesis of "in-flight" aggregation, each one corresponding to a different physical description of the aggregation process. The first one is the "travel time" τ_{trav}, i.e. the time that an aggregate takes -on the average- to travel from the region where nanoparticles originate to the substrate under the push provided by the laser-generated shock wave. The other is the time between two subsequent shock waves, namely the "shot-to-shot time" T_{STS}, which is readily available as the inverse of the laser repetition rate. In order to check whether τ_{agg} corresponds either to τ_{trav} or T_{STS} we follow a two-step procedure: firstly, we theoretically estimate how the PLD process parameters are related to the proposed timescales and -by virtue of (Eq. 7.2)- to the average gyration radius R_g, then we experimentally investigate the dependence of R_g on said parameters and make a comparison with the theoretical estimations.

The motion of an aggregate in the background gas is described, in principle, by an advection-diffusion equation, where the advection part accounts for the transport by the fluid flow and the diffusion part is a Brownian motion. Since the fluid velocity of the gas is unknown it is practically impossible to find an exact solution. Also, in an advection-diffusion picture the aggregate parameters (such as mass and gyration radius) are constant, thus it cannot describe coalescence during the motion. Nevertheless, one can derive simple estimations considering separately an "advection timescale" τ_{adv} and a "diffusion timescale" τ_{diff}, and supposing that τ_{trav} lies somewhere between τ_{adv} and τ_{diff}.

Advection timescale can be estimated as the time required to travel a target-to-substrate d_{TS} distance moving with velocity u_f, which corresponds to the fluid velocity after the passage of the laser-generated shock wave. Shocked fluid velocity can be derived from Rankine-Hugoniot relations; exact analytical solutions, however, exist only under strong simplifying assumption. Here we assume that $u_f = c_s/k$, where c_s is the speed of sound in the background gas and $k > 1$ is a numerical factor few times the unity, obtaining:

$$\tau_{adv} = k\frac{d_{TS}}{c_s} \tag{7.3}$$

Diffusion timescale is related to the diffusion coefficient D by the Einstein's theory of the Brownian motion:

$$\tau_{dif\ f} = \frac{{d_{TS}}^2}{2D} \tag{7.4}$$

Putting (Eq. 7.3) and (Eq. 7.4) in (Eq. 7.2) one gets:

$$R_g \propto (d_{TS})^{yb} \tag{7.5}$$

Where y ranges from 1 (pure advection) to 2 (pure diffusion). Thus, the "travel time" hypothesis predicts a power-law relation between the average aggregate radius and the target-to-substrate distance.

Another possibility is that the nanoparticles generated by the n^{th} laser shot are free to aggregate in the vacuum chamber for a timescale T_{STS}, i.e. until the shockwave generated by the subsequent $(n + 1)^{th}$ laser shot drags them toward the substrate within a timescale τ_{adv}. Since T_{STS} is typically in the order of hundreds of milliseconds, much greater than τ_{adv} (in the order of millisecond or less), this scenario corresponds to the assumption $\tau_{agg} = T_{sts}$, which put in (Eq. 7.2) gives a power-low dependence of Rg on T_{STS}:

$$R_g \propto (T_{STS})^b \tag{7.6}$$

Coming back to the snowfall analogy, this hypothesis is equivalent to say that the size of a snowflake is determined by the amount of time it spends floating in the supercooled atmosphere rather than the amount of time it takes to fall to the ground, being the latter much smaller than the former. Incidentally, this mechanism is quite similar to the one at play in actual snowfalls. An experimental benchmark is obtained with two series of depositions, one where d_{TS} is varied from 35 mm to 65 mm, and the other where T_{STS}, is varied from 0.1 s to 10 s, all the other parameters being fixed. The corresponding results are shown in Fig. 7.7:

While the aggregate diameter is essentially independent from the target-to-substrate distance, it shows a marked dependence on the shot-to-shot time. The experimental points are nicely fitted by the power-law relation given by Eq. 7.6, thus confirming that the growth of carbon nanofoam is described by a in-flight process where the dominant aggregation timescale is the interval of time between two subsequent laser shots.

7.4 Measurement of Nanofoam Density

One of the most important nanofoam properties to be measured is the mean density.

At a first sight, one could imagine that it is a quite simple task: the sample can be weighted and the density can be retrieved by dividing the total film mass

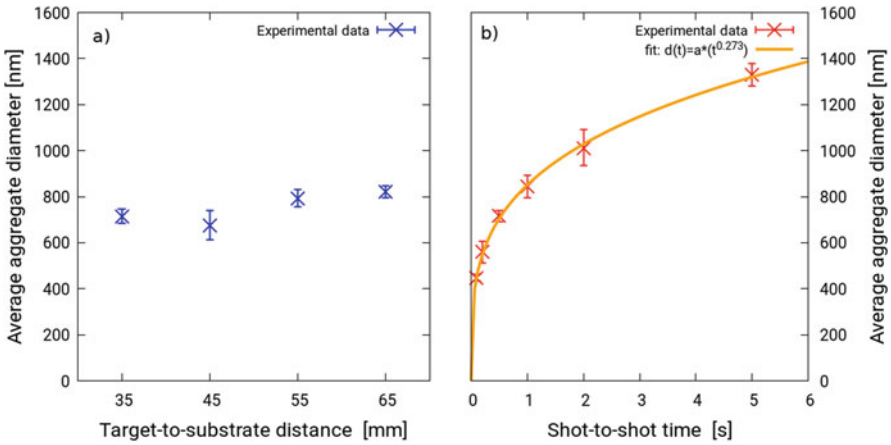

Fig. 7.7 Average aggregate radius as a function of (**a**) target-to-substrate distance (**b**) shot-to-shot time. Ten laser shots for each experimental point, with background pressure of 700 Pa Ar and laser fluence 1.6 J/cm2. The shot-to-shot time in (**a**) is 1 s, the target-to-substrate distance in (**b**) is 45 mm. Red solid line: Fitting power-law curve for the average radius. The coefficients a $\approx$ 810 and b $\approx$ 0.27 are obtained with with a Levenberg-Marquardt least square algorithm

by its volume, calculated from the cross section SEM image and the side length. Nevertheless, this method is not sufficiently accurate, as can be shown by this simple calculation.

Considering a nanofoam with density of 10 mg/cm^3 (which is an ultra-low value but not the minimum that can be achieved by PLD) deposited onto a squared substrate with 1 cm of side length, and with thickness of about 10 μm. The total nanofoam mass is about 0.01 mg, yet the accuracy of a high-precision analytical balance is limited to about 0.1 mg, leading to an unsensitive measurement.

The only type of standard laboratory instrument which is capable to measure lower values of mass is the Quartz Crystal Microbalance (QCM) which has an extraordinary sensitivity, down to 0.1 ng. This technique uses the Quartz crystal as piezoelectric oscillator and exploits the changes in resonance frequency of the crystal to measure the mass on the surface. Nevertheless, an important issue arises if we try to measure the nanofoam mass by the QCM. Due to its fractal structure, the foam deposited onto the oscillating crystal does not move as a rigid body with the crystal, yet it quenches the oscillations along the vertical axis, through chain vibrations. This phenomenon could be compared to the motion of trees during an earthquake, where the branches oscillate with a phase different from the ground. For this reason the QCM fails in determining accurate values of nanofoam mass and should not be used for this kind of nanostructures.

Thus, measuring the foam density is a challenging issue which can be tackled only by non conventional techniques. One possible method is given by the quantitative Electron Probe Microanalysis (EPMA), which exploits the Energy Dispersive X-ray Spectroscopy (EDS) to measure the mass thickness τ (which is equal to the

density ρ times the thickness *t*) of thin films [43]. Quantitative EPMA is of a great interest for our scope, because it is non-destructive, it uses a common apparatus (a scanning electron microscope, SEM, with an energy dispersive X-ray spectrometer, EDS), and the film roughness does not affect the measurement. The technique consists in measuring characteristic X-rays excited by the SEM electron beam, and then calculating the so-called k-ratio of the X-rays emitted from the film/substrate and the ones produced in homogeneous reference sample of known composition. To derive the film mass thickness from the k-ratio, we have to know the so-called $\Phi(\rho z)$ curve, which is defined as the distribution of the production of characteristic X-rays as a function of the depth z. In particular two equation can be used (see scheme of Fig. 7.8), depending if the reference sample has the same composition of the film (coating method) or the substrate (substrate method) [44]:

$$K_c = \frac{I_{C,i}}{I_{C,i}^{ref}} = \frac{\int_0^{\tau} c_{C,i}\ \Phi_{C,i}(\rho z)\ \exp\left(-\chi_{C,i}\rho z\right)\ \mathrm{d}(\rho z)}{\int_0^{\infty} c_{ref,i}\ \Phi_{ref,i}(\rho z)\ \exp\left(-\chi_{ref,i}\rho z\right)\ \mathrm{d}(\rho z)} \tag{7.7}$$

$$K_S = \frac{I_{S,i}}{I_{S,i}^{ref}} = \frac{\exp\left(-\tau\ \chi_{C,i}\right)\int_0^{\tau} c_{C,i}\ \Phi_{C,i}(\rho z)\ \exp\left[-\chi_{C,i}\ (\rho z-\tau)\right]\ \mathrm{d}(\rho z)}{\int_0^{\infty} c_{ref,i}\ \Phi_{ref,i}(\rho z)\ \exp\left(-\chi_{ref,i}\ \rho z\right)\ \mathrm{d}(\rho z)} \tag{7.8}$$

where I is the X-ray measured intensity, c the atomic concentration, $\chi = (\mu/\rho)/\cos(\alpha)$ is the X-rays mass attenuation factor obtained from the absorption coefficient μ and the angle α of the detector with respect to the interface of the sample; the subscripts refer to the element i and the analysed sample *C/S* or the reference sample *ref*.

Thus, the knowledge of the $\Phi(\rho z)$ distribution is of crucial importance in the determination of the mass thickness τ, even if it is not trivial to determine, since its shape depends on the complex phenomena of electrons multiple scattering and characteristic X-rays generation.

Semi-empirical models have been exploited to obtain reasonable measurements of the foam density, see Fig. 7.8 [44]. In addition, the figure shows that the EPMA results are in agreement with the QCM for high value of density, hence for quite compact Carbon films, while for lower density values EPMA is able to obtain more accurate measurements than QCM.

Nevertheless, the use of semi-empirical models for $\Phi(\rho z)$ suffers from important limitations: the measurement procedure which assures the highest accuracy needs EDS measurements of a standard reference sample having the same composition of the substrate or the film, which is not always available, and it also needs many acquisitions at different accelerating voltages, which therefore involves time-consuming measurements.

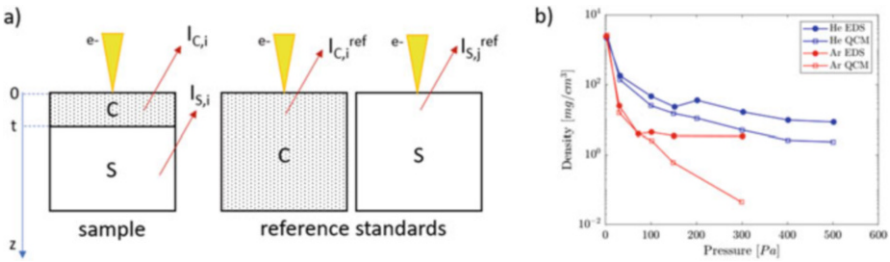

Fig. 7.8 (**a**) scheme of the quantitative Electron Probe Micro-Analysis technique (EPMA). A monoenergetic electron beam (1-30 keV) is focused on a sample and characteristic X-rays are emitted. The ratio of the measured intensities with the ones of reference sample (either with the same composition of the coating C, or the substrate S) are used to determine the coating thickness. (**b**) nanofoam mean density measured by quantitative EPMA (full markers) and by Quartz Crystal Microbalance (QCM, open markers), as a function of the Pulsed-Laser Deposition gas (Helium/Argon) and pressure. For lower density samples, the QCM measures unreasonably low values due to the oscillations damping in the fractal structure. Adapted with permission from reference [44] (Copyright 2015 under the terms Creative Commons CC BY license)

Only recently attempts to derive theoretically $\Phi(\rho z)$ have been carried out. A Monte Carlo code, called PENEPMA [45], is able to describe the electron multiple scattering and X-ray production physics with high accuracy. Nonetheless, as all Monte Carlo codes, it suffers from statistical errors which can be reduced only by a high number of simulated trajectories and long simulation times. Another recent solution consists in the numerical solution of the electron transport equation in cylindrical symmetry. This last method, called EDDIE [46], is able to theoretically determine the $\Phi(\rho z)$ distribution of multilayer samples and the consequent X-ray generation. This description is more accurate than semi-empirical models, and consequently it enables to determine film mass thickness without the need of a reference sample, by using the K-ratio (with the capital letter to distinguish from the standard k-ratio). It is defined as the ratio of the X-ray intensity from the film elements to the ones of the substrate. The mass thickness is therefore retrieved by numerically solving the following equation:

$$K_{i,j} = \frac{I_{C,i}}{I_{S,j}} = \frac{\varepsilon_i c_{C,i} \int_0^{\tau} \Phi_{C,i}(\rho z) \exp\left(-\chi_{C,i}, \rho z\right) \mathrm{d}(\rho z)}{\varepsilon_j c_{S,j} \exp\left(-\tau\ \chi_{F,j}\right) \int_0^{\infty} \Phi_{S,j}(\rho z) \exp\left(-\chi_{s,j}\ \rho z\right) \mathrm{d}(\rho z)} \tag{7.9}$$

Where $I_{C,i}$ is the X-ray intensity generated in the film by the i-th element while $I_{S,i}$ is the substrate intensity of the j-th element; ε_i and ε_j are the detector efficiencies at the X-ray energies of the i-th and j-th elements respectively; $c_{C,i}$ and $c_{S,i}$ are the atomic fractions of i-th and j-th elements in the film and in the substrate, and the subscripts refer respectively to the layer and the X-ray energy.

EDDIE allows measuring film mass thickness in a fast and accurate way, as demonstrated by the comparison of the method results with benchmark techniques,

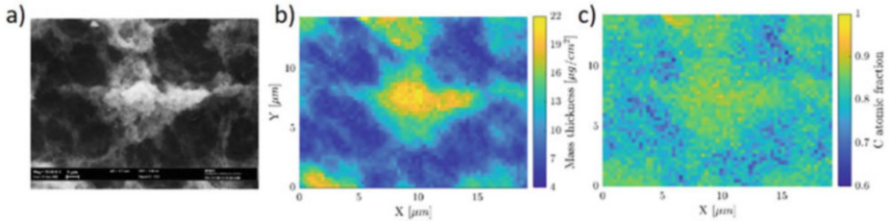

Fig. 7.9 (**a**) SEM image of a Carbon nanofoam with Oxygen contamination produced by Pulsed-Laser Deposition. Mass thickness (**a**) and Carbon fraction (**b**) maps of the same sample, obtained by the EDDIE method. Adapted with permission from reference [46] copyright (2019) (Elsevier)

and opens new characterization capabilities. Since reference sample and multiple acquisitions at different accelerating voltages are not needed, the EDS capability to obtain X-ray 2D maps can be used to retrieve maps of both mass thickness and atomic concentrations, as shown in Fig. 7.9. This is a particularly interesting feature for the nanofoam characterization, because not only the mean density can be accurately measured, but also 2D maps of mass thickness can be realized, useful to quantify the film porosity and non-homogeneity.

7.5 Carbon Nanofoam on Flexible Substrates for Laser-Driven Acceleration

An interesting application of ultra-low denisty nanofoam grown by PLD is represented by the development of innovative targets for laser-driven ion acceleration experiments. Compact ion accelerators based on superintense laser-matter interaction represents a promising alternative to conventional accelerators thanks to their potential for an increased energy tunability and reduced size, radioprotection issues and overall cost [47].

Laser-driven acceleration exploits the interaction of an ultra-intense ultra-short laser pulse ($I > 10^{18}$ W cm^{-2}) with a target, which rapidly ionizes turning into a plasma. The laser-plasma coupling induces a strong charge separation and, consequently, the intense longitudinal electric fields responsible for the ion acceleration process. In the so-called target normal sheath acceleration (TNSA) scheme, the laser irradiates a μm-thick solid target where part of the laser energy is absorbed by the electron population, which expands at relativistic energies towards the target back side and generates an intense sheath electric field (few MV μm^{-1}) [47–49]. This field drives the acceleration of bunches of the light ions (e.g. hydrogen from water vapor contamination) located on the rear surface of the target, resulting in an exponential energy spectrum and a well-defined cut-off energy in the multi-MeV range.

One of the most promising strategy for enhancing both the number and the energy of the accelerated ions focuses on the development of advanced engineered targets that could optimize the laser-plasma coupling and allow for a more efficient laser absorption.

In this frame, a large body of research confirms that the laser-plasma coupling is dramatically improved in the near-critical regime [50], i.e. whenever the plasma electron density n_e is close to a critical value n_c: $n_e \sim n_c = \varepsilon_0 m_e \omega_l^2 / e^2$ where ω_l is the laser frequency, ε_0 the vacuum permittivity, and e and m_e are the charge and the electron mass respectively.

Exploiting this interaction regime in laser-driven ion acceleration schemes is appealing. However, it poses a significant challenge from the point of view of material science and technology.

Indeed, if we consider that the number of nuclei in a fully ionized critical plasma is n_c/Z and that the nuclear mass can be approximated by $A\ m_p$ (being Z the atomic number, A the atomic mass and m_p the proton mass), we can express the mass density of a near-critical material in terms of the laser wavelength λ:

$$\rho_c = n_c \frac{A}{Z} m_p = \pi m_p \frac{A}{Z} \frac{1}{R_c} \frac{1}{\lambda^2} \approx \frac{A}{Z} \frac{1.865}{(\lambda\,[\mu\mathrm{m}])^2}\ \mathrm{mg/cm^3} \tag{7.10}$$

Where the last equality is obtained by substituting the numerical values of the classical electron radius R_c and the proton mass m_p. Since the typical wavelength of high intensity laser systems is around 0.8–1 μm and the A/Z ratio is around 2 for most elements, the near-critical requirement corresponds to a mass density of few mg cm^{-3}, a few times the density of air at standard conditions.

Given that the TNSA process requires a solid target with a flat back surface, very few options are available. One of the most studied involves the design of Double Layer Targets (DLTs) made of a thin solid foil coated by a near-critical layer [23, 51]. The specific nature of the thin solid foil, which act as a *substrate* for the deposition of the near-critical layer, depends on the experimental needs; typically it varies from 50-100 nm thick polymeric films to 5-10 μm thick metallic foils, although sub 10 nm solutions have been tested [52]. The optimal thickness of the near-critical layer depends on the laser parameters, and typically varies from few up to tens of micrometers [50]. Moreover, in order to accommodate tens or hundreds of laser shots on the same target, the surface of DLTs could encompass an area of some cm^2.

From a material scientist perspective, the specifications related to the DLT optimization translates into the following requirements on the low-density layer:

1. deposition technique compatible with thin, flexible and delicate substrates
2. mass density in the range 5-25 mg/cm^3
3. thickness from 4 to 20 μm
4. spatial uniformity over an area of some cm^2

Therefore, in the light of these aspects, PLD represents a natural choice for the production of the near critical layer in DLT in the form of an ultra-low density nanofoam deposited onto a flexible thin substrate.

For what concerns the first point, we have already highlighted what makes PLD an ideal technique for the deposition of nanofoam on flexible and delicate substrate: the reason lies in the fact that aggregation occurs in flight, and aggregates land on substrate with a relatively low energy. This is not a general feature of PLD though, as it is possible to achieve conditions in which the ablated species arrive on the substrate as highly energetic atoms or ions [Toftmann2013]. Rather, it is a hallmark of the peculiar PLD regime characterized by moderate pulse energy and high background pressure that determines the snowfall-like growth mechanism, as described in details in reference [11].

Coming to requirement on the nanofoam mass density is important to recognize that what matters within the framework of the laser-plasma interaction is actually the density averaged over a volume given by the laser spot size times the foam thickness. If we consider a situation in which the spot size (typically few times the laser wavelength, i.e. 5 to 10 microns) is larger than the aggregate size, we the averaged mass density ρ_f is related to fractal scaling law (see Eq. 7.1) by the following equation:

$$\rho_f = K\ \rho_{np}\left(\frac{R_{np}}{2R_g}\right)^{3-D_f} \tag{7.11}$$

Where we have already defined the pre-factor K, the average fractal dimension D_f, the average aggregate gyration radius R_g, and the nanoparticle radius R_{np}, while ρ_{np} is the average nanoparticle density.

Figure 7.10 shows the morphology and the EDXS density map for a PLD carbon nanofoam. It is possible to observe that local non-homogeneity due to the

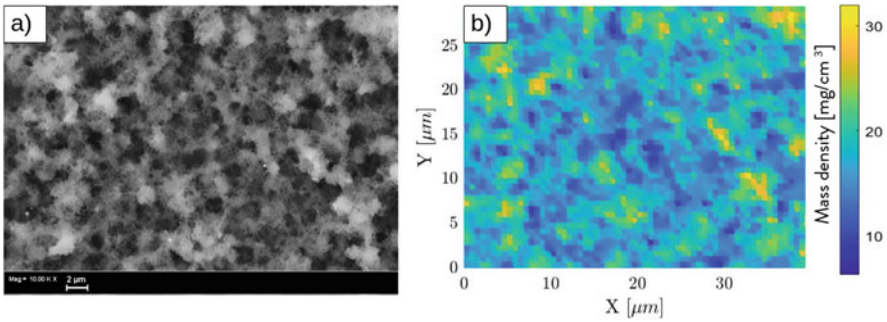

Fig. 7.10 (**a**) SEM images and (**b**) EDXS density maps of a carbon nanofoams deposited with 7000 shots, background pressure of 1000 Pa Ar, laser fluence 2.1 J/cm^2,target-to-substrate distance 4.5 cm, laser repetition rate 10 Hz. The average thickness is 8 μm. Adapted with permission from reference [11] (Copyright 2019) (American Physical Society)

foam structure washes out over a length scale of ~10 μm and the average density $\rho_f \approx 18.7$ mg/cm^3, as requested for typical DLT applications.

PLD also offers a straightforward way to control the nanofoam thickness, since the latter grows linearly with the deposition time. There is however a lower limit on the foam thickness given by the average gyration radius: since the nanofoam grows by packing of aggregates with a defined size, it is not possible to deposit nanofoams having a thickness lower than the average aggregate diameter. Nevertheless, since the typical aggregate diameter is of the order of 1 μm (see figure) and the near-critical layer thickness in DLT rarely falls below 4 μm, this aspects does not represent a criticality with respect to DLT fabrication.

The achievement of a uniform deposit is usually a more challenging issue. In the high-pressure deposition regime the plume is confined, and its length is generally shorter than the target-to-substrate distance [11]. Most of the ablated material tends to deposit in a circular shape region concentric to the axis of the plume. The spatial profile of the deposited mass for each shot depends on multiple factors, such as laser fluence, background gas pressure and target-to-substrate distance. Generally speaking, it not guaranteed that such spatial profile would result in the desired uniformity of the sample. One way to address this issue involves a suitable movement routine for the substrate holder, so that the final profile is the result of moving average over the deposition profile of each subsequent shot. In Fig. 7.11 we show the SEM cross-sectional image of a nanofoam (above) together with the thickness profile with respect to the lateral dimension. A good lateral uniformity is obtained over a distance of ~3 cm.

Two examples representative of the rich assortment of DLT configurations involving carbon nanofoams are shown in Fig. 7.12. Figure 7.12a is a millimetric DLT composed by a 100 nm thick polyethylene film as a substrate and a 10 μm thick nanofoam with ultra-low density (~ 12 mg/cm^3) nanofoam acting as near-critical layer. The glass frame that holds the polymeric film was directly placed in the PLD chamber for the foam deposition. In spite of its delicate nature, the substrate was not damage because of the foam deposition. Much larger DLTs made of 4 cm x 4 cm aluminum foils (thickness 1.5 μm) are shown in Fig. 7.12b. The near-critical layers are made of ~18 mg/cm^3, ~12 μm thick nanofoam. The holder on the left host a DLT as it appears after the nanofoam deposition, while the one on the right shows clear signs of the irradiation with superintense laser pulses.

We conclude by remarking that DLTs for laser-driven acceleration represent an interesting and multidisciplinary example of how PLD can be exploited to deposit nanostructured carbon foams on a wide variety of flexible substrates, but is far from being the only one. Many other applications can benefit form the peculiarities of the PLD deposition technique, ranging from electronics and supercapacitors to wearable devices and biological scaffolds for tissue growth. The picture shown in Fig. 7.12 is another example illustrative of the potential and versatility of nanofoam pulsed laser deposition on flexible substrates.

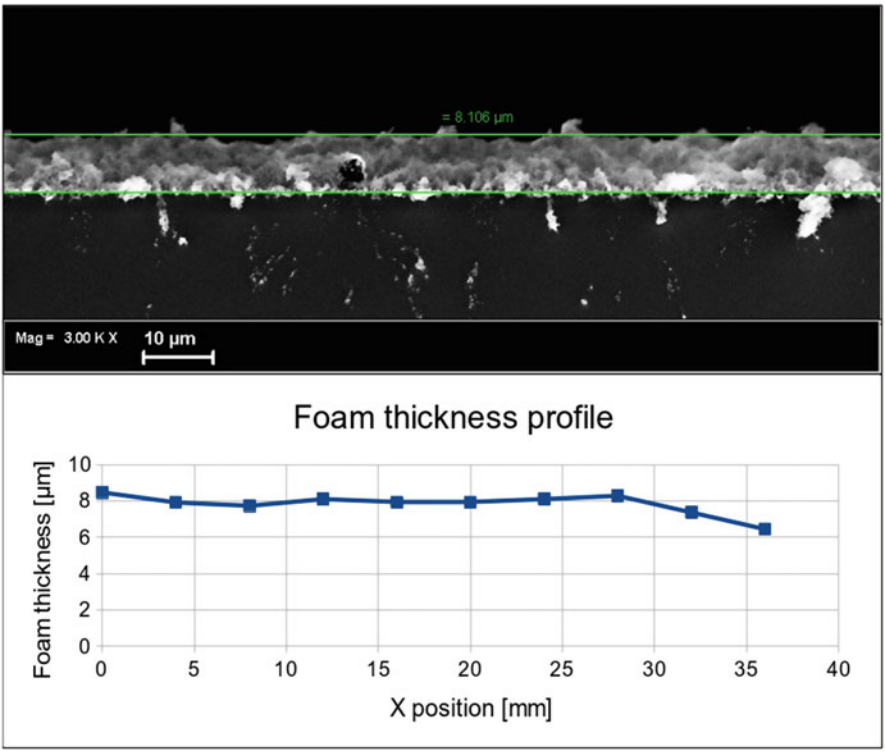

Fig. 7.11 Above: SEM cross-section of a nanofoam deposited with a background pressure of 1000 Pa Ar, laser fluence 2.1 J/cm^2, target-to-substrate distance 4.5 cm, laser repetition rate 10 Hz. Below: Thickness profile as a function of the lateral dimension

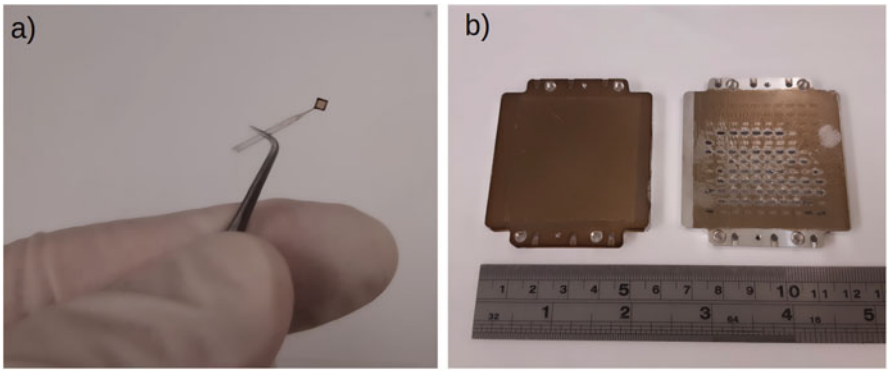

Fig. 7.12 Examples of DLTs for laser-driven acceleration experiments. (**a**) a glass frame holds a 100 nm thick polyethylene film (1 mm x 1 mm size) coated by a 10 μm *thick* carbon nanofoam with average density ~ 12 mg/cm^3. Substrate and substrate holder are courtesy form the Institute for Laser Engineering, Osaka, Japan. (**b**) Large area DLTs (~16 cm^2) before (left) and after (right) the irradiation with the super-intense laser DRACO (The Helmholtz-Zentrum Dresden-Rossendorf, Dresden, Germany). The substrate is a 1.5 μm thick aluminum foil coated with a ~ 18 mg/cm^3, ~12 μm thick nanofoam (Fig 7.13)

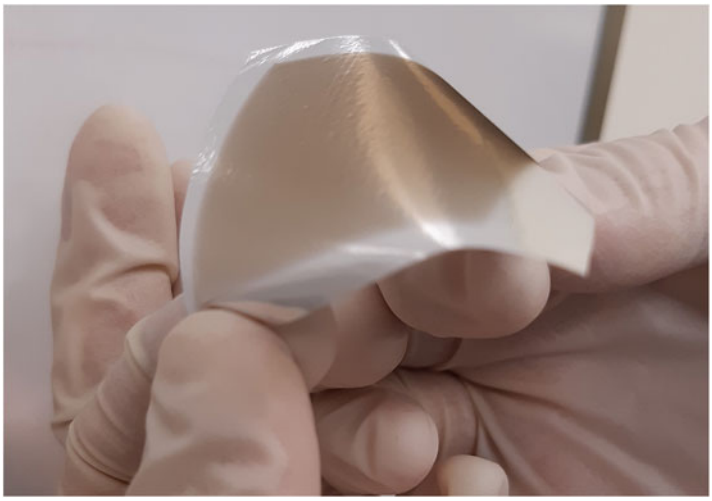

Fig. 7.13 An ultra-low density, ~1*0* μm thick carbon nanofoam layer deposited on a large titanium foil with micrometric thickness

Acknowledgments The authors wish to thank Professor C.E. Bottani. The research line related to the deposition and study of carbon nanostructures at Politecnico di Milano started under his guidance. This project has received funding from the European Research Council (ERC) under the European Union's Horizon 2020 research and innovation program (ENSURE grant agreement No 647554).

Bibliography

1. Shanov, V., Cho, W., Malik, R., Alvarez, N., Haase, M., Ruff, B., Kienzle, N., Ochmann, T., Mast, D., Schulz, M.: Surf. Coat. Technol. **230**, 77–86 (2013)
2. Vetter, J.: Surf. Coat. Technol. **257**, 214–240 (2014)
3. Coşkun, Ö.D., Zerrin, T.: Diam. Relat. Mater. **56**, 29–35 (2015)
4. Pappas, D.L., Saenger, K.L., Bruley, J., Krakow, W., Cuomo, J.J., Gu, T., et al.: Pulsed laser deposition of diamond like carbon films. J. Appl. Phys. **71**, 5675–5684 (1992)
5. Voevodin, A.A., Donley, M.S.: Surf. Coat. Technol. **82**, 199–213 (1996)
6. Siegal, M.P., Tallant, D.R., Martinez-Miranda, L.J., Barbour, J.C., Simpson, R.L., Overmyer, D.L.: Phys. Rev. B. **61**(15), 10451–10462 (2000)
7. Bonelli, M., Ferrari, A.C., Fioravanti, A., Li Bassi, A., Miotello, A.: Ossi PM. Eur. Phys. J. B. **25**, 269–280 (2002)
8. Rode, A.V., Gamaly, E.G., Luther-Davies, B.: Formation of cluster assembled carbon nanofoam by high-repetition-rate laser ablation. Appl. Phys. A Mater. Sci. Process. **70**, 135–144 (2000)
9. Siegal, M.P., Overmyer, D.L., Kottenstette, R.J., Tallant, D.R., Yelton, W.G.: Nanoporous-carbon films for microsensor preconcentrators. Appl. Phys. Lett. **80**(21), 3940–3942 (2002)
10. Zani, A., Dellasega, D., Russo, V., Passoni, M.: Carbon. **56**, 358 (2013)
11. Maffini, A., Pazzaglia, A., Dellasega, D., Russo, V., Passoni, M.: Phys. Rev. Mater. **3**, 083404 (2019)
12. Gilbert, D.A., Burks, E.C., Ushakov, S.V., Abellan, P., Arslan, I., Felter, T.E., Navrotsky, A., Liu, K.: Chem. Mater. **29**, 9814 (2017)
13. Guoxin, G., Bin, W.H., Shujiang, D., Li-Min, L., Wen, L.X.: Small. **11**, 804 (2014)
14. Fu, S., Song, J., Zhu, C., Xu, G.-L., Amine, K., Sun, C., Li, X., Engelhard, M.H., Du, D., Lin, Y.: Nano Energy. **44**, 319 (2018)
15. Zhong, L.S., Hu, J.S., Liang, H.P., Cao, A.M., Song, W.G., Wan, L.J.: Adv. Mater. **18**, 2426 (2006)
16. Xiaoming, L., Lu, W., Yubo, F., Qingling, F., Fu-Zhai, C., Fumio, W.: J. Biomed. Mater. Res. Part A. **101A**, 2424 (2013)
17. Rode, A.V., Gamaly, E.G., Christy, A.G., Fitz Gerald, J.G., Hyde, S.T., Elliman, R.G., Luther-Davies, B., Veinger, A.I., Androulakis, J., Giapintzakis, J.: Phys. Rev. B. **70**, 054407 (2004)
18. Shvedov, V.G., Rode, A.V., Izdebskaya, Y.V., Desyatnikov, A.S., Krolikowski, W., Kivshar, Y.S.: Phys. Rev. Lett. **105**, 118103 (2010)
19. Blinc, R., Cevc, P., Arˇcon, D., Zalar, B., Zorko, A., Apih, T., Milia, F., Madsen, N.R., Christy, A.G., Rode, A.V.: Phys. Status Solidi B. **243**, 3069 (2006)
20. Rode, A., Hyde, S., Gamaly, E., Elliman, R., McKenzie, D., Bulcock, S.: Appl. Phys. A Mater. Sci. Process. **69**, S755 (1999)
21. Gamaly, E.G., Madsen, N.R., Golberg, D., Rode, A.V.: Phys. Rev. B. **80**, 184113 (2009)
22. Henley, S.J., Carey, J.D., Silva, S.R.P., Fuge, G.M., Ashfold, M.N.R., Anglos, D.: Phys. Rev. B. **72**, 205413 (2005)
23. Prencipe, I., Sgattoni, A., Dellasega, D., Fedeli, L., Cialfi, L., Choi, I.W., Kim, I.J., Janulewicz, K.A., Kakolee, K.F., Lee, H.W., Sung, J.H., Lee, S.K., Nam, C.H., Passoni, M.: Plasma Phys. Control Fusion. **58**, 034019 (2016)

24. Passoni, M., Arioli, F.M., Cialfi, L., Dellasega, D., Fedeli, L., Formenti, A., Giovannelli, A.C., Maffini, A., Mirani, F., Pazzaglia, A., Tentori, A.: Plasma Phys Control Fusion. **62**(1), 014022 (2019 Dec 6)
25. Gamaly, E.G., Rode, A.V., Luther-Davies, B.: Laser Part Beams. **18**, 245–254 (2000)
26. Ferrari, A.C., Robertson, J.: Phys. Rev. B. **61**, 14095 (2000)
27. Brett, M.J.: J. Vac. Sci. Technol. A: Vac Surf. Films. **6**(3), 1749–1751 (1988)
28. Maffini, A., Uccello, A., Dellasega, D., Russo, V., Perissinotto, S., Passoni, M.: J. Nucl. Mater. **463**, 944 (2015)
29. Karatzas, I., Shreve, S.E.: "Brownian Motion." Brownian Motion and Stochastic Calculus, pp. 47–127. Springer, New York, NY (1998)
30. Witten Jr., T.A., Sander, L.M.: Phys. Rev. Lett. **47**(19), 1400 (1981)
31. Filippov, A.V., Zurita, M., Rosner, D.E.: J Colloid Interface Sci. **229**(1), 261–273 (2000)
32. Sander, L.M., Cheng, Z.M., Richter, R.: Phys. Rev. B. **28**(11), 6394 (1983)
33. Witten, T.A., Sander, L.M.: Phys. Rev. B. **27**(9), 5686 (1983)
34. Celardo, G.L.: et al. Mater. Res. Express. **4**(1), 015013 (2017)
35. Botet, R., Jullien, R.: Phys. Rev. Lett. **55**(19), 1943 (1985)
36. Jullien, R., Kolb, M.: J. Phys. A Math. Gen. **17**(12), L639 (1984)
37. Asnaghi, D., et al.: Phys. Rev. A. **45**(2), 1018 (1992)
38. Cavaliere, E., Benetti, G., Celardo, G.L., Archetti, D., Pingue, P., Ferrini, G., Gavioli, L.: J. Nanopart. Res. **19**, 311 (2017)
39. Nishikawa, K., Takano, K., Miyahara, H., Kawamura, T., Okino, A., Hotta, E., Nayuki, T., Oishi, Y., Fujii, T., Wang, X., Nemoto, K.: Appl. Phys. Lett. **89**, 243112 (2006)
40. Meakin, P.: Phys. Scr. **46**, 295 (1992)
41. Tamas, V.: Fractal Growth Phenomena, 2nd edn. World Scientific, Singapore (1992)
42. Lin, M.Y., Lindsay, H.M., Weitz, D.A., Klein, R., Ball, R.C., Meakin, P.: J. Phys. Condens. Matter. **2**, 3093 (1990)
43. Merlet, C.: *Microchim. Acta*. **114**(1), 363–376 (1994)
44. Prencipe, I., Dellasega, D., Zani, A., Rizzo, D., Passoni, M.: Sci. Technol. Adv. Mater. **16**(2), 025007 (2015)
45. Llovet, X., Salvat, F.: Microsc. Microanal. **23**(3), 634 (2017)
46. Pazzaglia, A., Maffini, A., Dellasega, D., Lamperti, A., Passoni, M.: Mater. Charact. **153**, 92–102 (2019)
47. Macchi, A., Borghesi, M., Passoni, M.: Rev. Mod. Phys. **85**, 751 (2013)
48. Passoni, M., Lontano Phys, M.: Rev. Lett. **101**, 115001 (2008)
49. Formenti, A., Maffini, A., Passoni, M.: New J. Phys. **22**, 053020 (2020)
50. Pazzaglia, A., Fedeli, L., Formenti, A., Maffini, A., Passoni, M.: Commun. Phys. **3**, 133 (2020)
51. Passoni, M., Sgattoni, A., Prencipe, I., Fedeli, L., Dellasega, D., Cialfi, L., Choi, I.W., Kim, I.J., Janulewicz, K.A., Lee, H.W., Sung, J.H., Lee, S.K., Nam, C.H.: Phys. Rev. Accel. Beams. **19**, 061301 (2016)
52. Jiao, Z., et al.: Preparation of ultra-thin DLC target for laser ion acceleration. High Power Laser and Part. Beams. **25**(7), 1723–1726

Chapter 8
Porosity of Nanostructured Carbon Thin Films

Alessandra Del Giudice, Giulio Benetti, Claudio Piazzoni, and Francesca Borghi

Abstract The multiscale (from nano to macro) characterization of porous materials, in particular of thin films integrated in sensors, as in electrochemical, catalytic and biomedical devices, asks for non-invasive methods. Since the mechanical and morphological properties of the substrate may affect the resulting structural organization and the network of the porous film structure, the porosity of the thin film has to be characterized in situ, without removing it from the integrating substrate, by recognizing the different contributions.

This chapter deals with standard methods used to characterize porosity, the theoretical framework used to describe the evolution of porosity with film thickness, the development of combined approaches which provide the possibility to describe many features of pores in thin films on different length scales. As a case study we present an in-depth analysis of the porosity and structure of carbon cluster-assembled thin films used as electrodes in energy devices.

Keywords Porosity · Surface area · Thin films · Gas adsorption · Small-angle X-ray scattering

A. Del Giudice
Dipartimento di Chimica, Università degli Studi di Roma "La Sapienza", Rome, Italy

G. Benetti
Department of Pathology and Diagnostics, Medical Physics Unit, Azienda Ospedaliera Universitaria Integrata, Verona, Italy

C. Piazzoni · F. Borghi (✉)
CIMaINa and Dipartimento di Fisica "Aldo Pontremoli", Università degli Studi di Milano, Milan, Italy
e-mail: francesca.borghi@unimi.it

F. Borghi et al. (eds.), *Nanoporous Carbons for Soft and Flexible Energy Devices*,
Carbon Materials: Chemistry and Physics 11,
https://doi.org/10.1007/978-3-030-81827-2_8

8.1 Introduction to the Porosity Characterization of Materials

Porous materials are ideal templates for the study of the non-linear phenomena associated to surface confinement conditions occurring inside pores [1–3], as also for the investigation of the enhanced interfacial interactions between the solid walls and the fluid, promoted by the high surface area available in the porous matrix. More interestingly, the functional properties of porous materials and granular thin films (coatings, electrodes, sensors and catalytic interfaces, etc . . .) depend on their porosity. The control on the morphological properties of highly porous films is strategic since the film porosity controls mass transfer rates in catalytic devices [4], electron diffusion pathway in dye-sensitize solar cells [5], double-layer organization of the electrolyte in electrochemical devices [6] and performance of gas sensor films [7].

Methodologies used to measure the overall porosity (defined as the void to the total sample volume fraction), the pores size and shape distributions, and the specific surface area of materials can be classified into "direct methods", based on volume determination of at least two among the bulk volume of the sample, its pore volume, and the volume of its solid matrix, and "indirect methods", that exploit the measurement of other quantities to calculate porosity, such as properties of the fluid interacting inside the void space with the confining walls [8]. The most important methods are listed in Fig. 8.1, according to the range of pores diameter investigated; in fact, a single method can barely provide all the information desired and cover all the pore dimension spectra.

The measurement of the effective connected porosity, as also the possibility to characterize both the open and closed porous structures for a large library

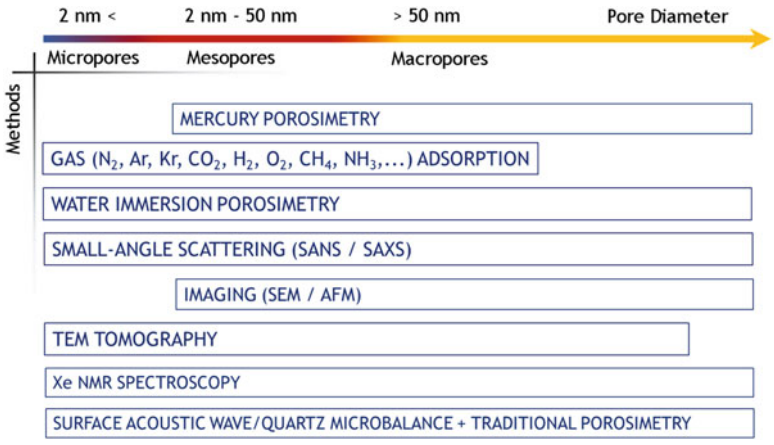

Fig. 8.1 Graphical list of the principal methods used to determine porosity according to the pores size

of materials, are important features which define the pertinence of a particular methodology for a specific investigation task among all the possibilities. For example, Mercury Intrusion Porosimetry (MIP) detects open porosity with high precision but it is not able to penetrate closed porosity; Helium Pycnometry (HP) measures the density of porous materials referring to the void volume due to the open porosity connected to the surface, but it cannot provide information on pore size distribution; Imaging Analysis methods (IA) measure both open and closed porosity [9, 10], but they fail to distinguish between the two and their results are statistically poor since Atomic Force Microscopy (AFM) – Scanning Electron Microscopy (SEM) – Trasmission Electron Microscopy (TEM) can analyze only a very small portion of the sample. The study of the spin relaxation time of trapped water and the more promising hyperpolarized Xenon in confined geometry are suitable for measuring only open pore diameters up to the micrometer scale [11]. Differently, Small Angle Neutron Scattering (SANS), employing contrast matching, can provide considerable information concerning the porosity of materials [12]. SANS with contrast matching (SANS-CM) [13, 14] is sensitive to both closed and open accessible pores, and provides an almost complete description of porosity, while small angle X-ray scattering (SAXS) provides scattering data from both the open and closed porosity but they cannot be decoupled.

Even if the combination of small-angle and wide-angle scattering techniques can cover a very wide range of pore dimension scales, this is inherently smaller than the real range of porosity in materials and they characterize only average properties of the samples analyzed. It is therefore valuable to combine porosity measurements and information concerning pores size and shape from different complementary techniques.

Interesting works, in the framework of porosity in mineralogy, make use of a combined approach based on mercury intrusion porosimetry (MIP), SEM and neutron scattering [15, 16]: MIP provides information on effective and accessible pore size distribution, SEM shows with great accuracy the local morphological details, whereas SANS reveals statistically significant information about pore size, porosity, pore volume, surface area and fractal behavior.

In order to visualize complex morphologies, complementary advanced methods of electron microscopy for 3D imaging can be required; as an example, TEM tomography, slice-and-view focused ion beam (FIB) and serial block face (SBF) combined with SEM are used in a combined approach for the characterization of synthetic polymeric systems in Ref. [10]. The samples are pre-sliced in an ultramicrotome and analyzed by TEM; TEM resolution for details is very high, even smaller than 1 nm, but the imaged volume is relatively small, about few μm^3. The advantage of 3D image reconstruction combined with slice-and-view FIB/SEM [17, 18] and SBF/SEM [18] is a more complete overview of the porous structure, since these methods have a resolution between those of TEM and X-ray tomography; these methods demonstrated to fully characterize the morphology of polymeric membranes, obtaining information on their asymmetric porosity, as well as to reveal details of hierarchical porous isotropic films [19, 20].

Thermally sprayed coatings have been studied [21] by IA, implemented with the microstructural information obtained using advanced characterization techniques, such as SANS and computer micro-tomography (CMT). While quantitative information regarding the constituent component porosity, the mean open pores dimension and anisotropy are obtained from SANS, CMT allows the visualization of the pore size distribution and spatial position within the coating. The results obtained from these techniques can be correlated to IA methods, thus giving confidence in their mutual utility, reliability and robustness.

A common approach to study composite and porous materials, is to consider them as homogeneous ensembles with effective parameters. This approach, usually labelled as effective medium approximation (EMA), can predict many different physical properties, such the optical and mechanical constants, as a function of the porosity. Reversing the issue, if one can measure the effective physical properties, EMA allows to retrieve the average film porosity. Often, this is the case of spectroscopic ellipsometry [22] and of pump-probe experiments on ultrathin metallic films [23].

The combined use of different techniques is necessary for the characterization of open and closed porosity of powders, polymeric structures and hybrid materials according to the scale dimension of the features of interest, but they are more and more necessary in the study of thin films structure which exhibit a heterogeneity of pores shape and size and an evolution of their morphologies with thickness.

8.2 Theoretical Description of Porosity Evolution in Thin Film

The morphological properties of a porous material depend on many different features, in particular on the synthesis and deposition strategies [24, 25]. The deposition of nanoparticles with kinetic energy low enough to prevent fragmentation upon impact on the substrate, as in aerosol processes and cluster beam depositions [26], results in thin films having a nanostructure provided by the assembling of nanoscale units that maintain their individuality after deposition.

The growth of such thin films usually proceeds through nucleation and interfacial phenomena, such as adsorption, surface diffusion, chemical binding and other atomic processes at the interfaces [27]. The morphological properties, as bulk porosity and surface roughness, of a granular deposit can be tailored by properly adjusting the kinetic energy of the particles approaching the deposit [28], as well as the dimension of the precursor particles [29].

Generally, the porosity of a thin film evolves from a denser region close to the substrate, to a more porous area at the upper interface. In particular, the three regions which characterize the film at different heights are: the denser near-wall (NW), the central portion of the film which is uniform and the active-growth (AG) region close to the upper interface [28, 30, 31]. Different deposition conditions

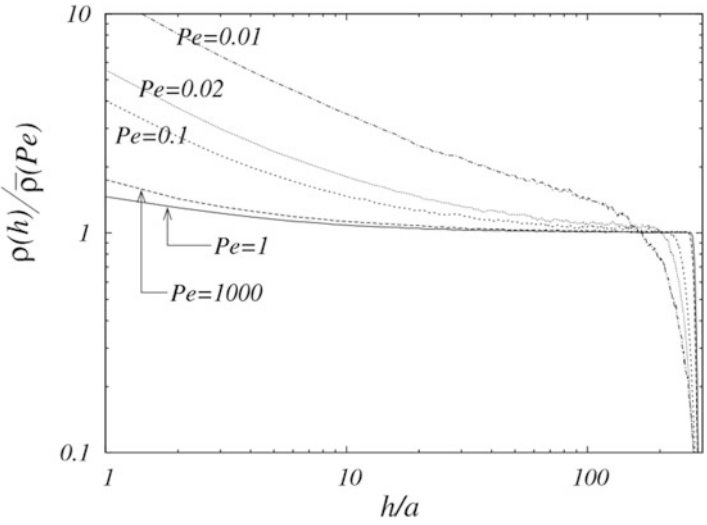

Fig. 8.2 Log-log density profiles, normalized to the uniform region density, versus the deposit height according to the Pe value. Adapted with permission from Ref. [30]

affect the properties of these three portions of the thin film [28, 30]. The two main models which describe the particles motions towards the surface are the diffusion-limited deposition (DLD) model [32] and the ballistic deposition (BD) model [33]: the former describes particles moving in a stochastic manner due to thermal fluctuations, while the latter refers to particles moving in a deterministic way. Péclet number $\mathrm{Pe} = \mathrm{V}a/\mathrm{D}$, where V is the mean velocity, D the diffusion coefficient and a stands for the particle diameter [30], identifies the deposition regime: it tends to 0 for the DLD model [25], while it tends to ∞ in BD limit [25].

In Fig. 8.2, the normalized densities of thin films as a function of thickness are reported, according to different deposition regime described by the Pe number.

The density is always higher in the near-wall region and becomes lower close to the topmost layer of the film, while the degree of packaging of these regions depends on the specific Pe number.

As mentioned before, many different techniques consider the overall porosity and treat the porous materials as homogeneous ensembles characterized by effective parameters. This "averaged" approach can be a good practical strategy to investigate film porosity, but the complex organization of granular and porous material has to be carefully considered in the discussion of the resulting data.

8.3 Experimental Strategies to Study the Porosity of Nanostructured Materials

The investigation of the inner complex structure of a thin film, which depends on the deposition method, the substrate it is deposited on and integrated into, and that evolves with thickness according to the theoretical models explained before, is a challenge: the very low amount of mass often cannot be measured directly due to the limited resolution of the instruments and the thin film has to be usually destroyed and reduced in powders in order its porosity to be measured. Although the advances of standard techniques can shift their intrinsic limit and allow better performances, innovative strategies have been explored to describe thin film porosity in a non-invasive manner.

Two common techniques used to measure small changes in mass are quartz crystal microbalances (QCMs) and surface acoustic wave (SAW) devices, whose sensitivity of the latter increases order of magnitude compared to the former. In Ref. [34], the surface area and porosity of thin films have been characterized by a SAW device combined with traditional porosimetry; for each partial pressure of nitrogen, the shift in the frequency of the surface acoustic wave propagating through the film due to the quantity of nitrogen adsorbed, is recorded and analyzed.

Exploiting the optical properties of a porous material, in the framework provided by EMA, spectroscopic ellipsometry can be used to obtain the average porosity of a material. To create a more complex and realistic model, more layers with different average porosity can be considered, even though, in this case, the risk of overfitting due to the high number of free parameters might pose a serious challenge to the analysis. In addition to the porosity, these EMA models allow to quantify other materials or impurities inside a matrix or a thin film, like in the case of a porous Ag-Ti film where small Ag particles are embedded on a matrix of amorphous Ti [22].

Similarly, the time-resolved analysis of the film breathing modes using the EMA, opens for the quantification of the amounts of voids and infiltrated fluid inside nanogranular ultrathin silver coatings with thickness in the 10–40 nm range [35]. The scheme, visible in Fig. 8.3, relies on the impulsive photoacoustic excitation of hypersonic mechanical breathing modes, and in the acousto-optical read-out of the breathing modes frequency shift upon liquid infiltration, a technique usually known as pump-probe.

Also Xe NMR has become a popular technique for the characterization of porous solids [36]. However, application of thermally polarised ^{129}Xe NMR to materials is often hampered by a relatively weak signal due to low concentration of the adsorbed xenon and long relaxation. An increase in sensitivity of several orders of magnitude (~10^4) can be achieved by using optical pumping techniques to produce hyperporalised (HP) Xenon, which have made it very attractive for materials applications and should allow very small quantities of matter to be probed. In Ref. [11] they report the first direct probing of thin supported films of mesoporous silica by the application of a continuous flow of HP ^{129}Xe NMR to the porous films.

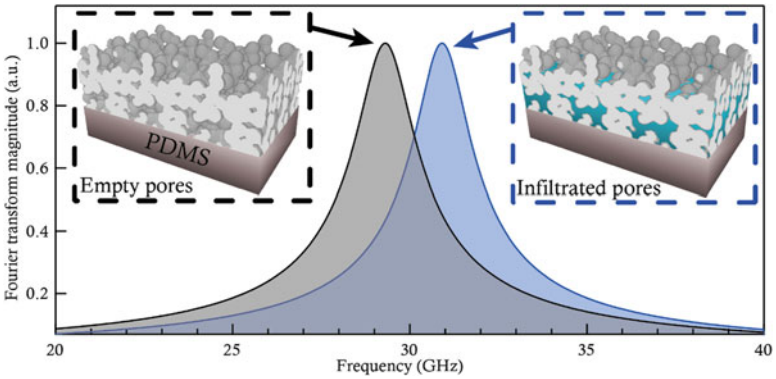

Fig. 8.3 Frequency shift of the nano-granular thin film breathing eigenmode due to water infiltration. Adapted with permission from Ref. [35]; further permissions related to the material excerpted should be directed to the ACS

Techniques such as TEM, X-ray powder diffraction (XRD) and gas adsorption isotherms are very useful to gain a maximum of relevant and accurate data about the porous network, its accessibility and its connectivity. In mesoporous thin films the porosity can be estimated by nitrogen adsorption isotherms; however this technique usually requires either to scratch off a few tens of samples from their substrates or to perform the analysis within a home-made cell that can accommodate a large set of thin films. An interesting strategy has been suggested in Ref. [37], measuring by gas adsorption technique the specific surface area and porosity of few hundreds nm thin film deposited on long and thin substrates which can be directly inserted inside the sample holder [37, 38]. Pore size distribution, the overall porosity and specific surface area can indeed be measured in a non-invasive manner, without destroying the thin film structure.

Interestingly, the thermally driven time evolution of nanoporous gold's 3D structure has been studied by A. Falqui and coworkers (A. Falqui et al., private communication) combining in a smart way *in situ* heating SEM and Serial Block Face (SBF)-SEM, the latter basically consisting in ultramicrotomy performed inside a low-pressure SEM. Indeed, the in situ heating SEM imaging allowed determining how the surface of a gold porous specimen evolved over time upon thermal stimulus. Once such an evolution reached a steady state, the sample was brought back at room temperature and then cut over its whole volume by SBF-SEM in order to investigate how the porosity changed as a function of the specimen thickness.

8.4 The Role of the Porosity of Carbon Thin Films in Energy Devices

The integration of low-cost micrometric energy sources into flexible devices, characterized by higher energy and power, as also with longer cycle life, are necessary features to be developed for their implementation into portable electronic devices and micro-electro-mechanical systems (MEMS). In particular, lithium-ion batteries and electrochemical capacitors (ECs) are among the most promising micro energy storage devices which meet these demands. Figure 8.4 shows the plot of specific power against specific energy density, also called Ragone plot, of the most important energy storage systems. Li-ion batteries, although costly, are the best in terms of performance, with energy densities that can reach 200 watt hours per kilogram. Nevertheless Li-ion batteries provide a slow power delivery and uptake. ECs currently fill the gap between batteries and conventional solid state and electrolytic capacitors, as faster and higher-power energy storage systems. In fact, ECs are power devices that can be charged or discharged in few seconds. Their energy density is lower than in batteries, approximately 5 Wh/kg, but a much higher power delivery and uptake can be achieved for shorter times. Electrochemical capacitors can store hundreds or thousands of times more charge because of a much larger

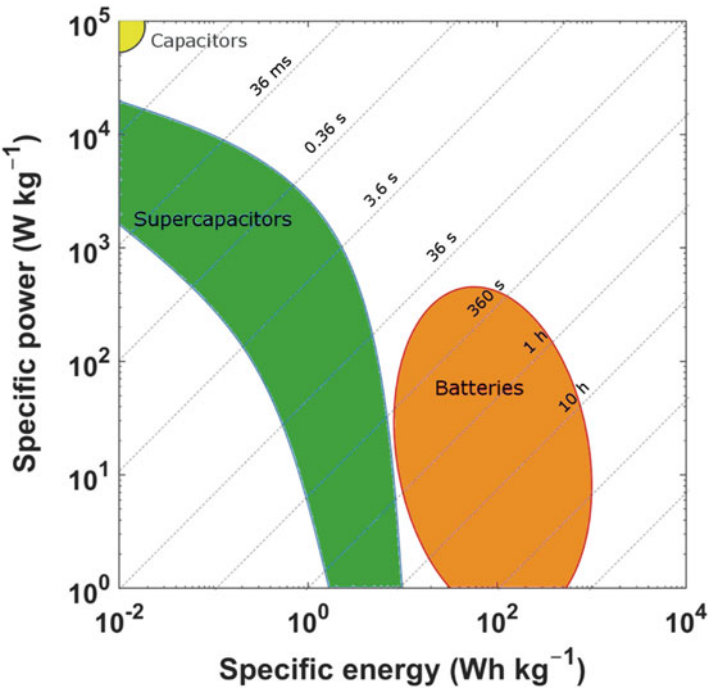

Fig. 8.4 Ragone plot comparing various electrochemical energy storage devices

surface area (1000–2000 m^2/g) available for charge storage in Electrochemical Double Layer Capacitor (EDLC) devices.

The high interfacial area of nanostructured electrodes available for double layer structuring of the electrolyte and fast reversible Faradaic reactions is one of the main advantages of their use into energy storage systems as EDLCs, together with their good electrical conductivity, chemical and mechanical stability [39, 40]. These advantages include also the reduction of electronic and ionic transport resistance at smaller diffusion length scales and the ability to incorporate high-energy materials into an outer nanostructured framework capable of sustaining high powers [6, 41].

Carbonaceous materials characterized by an high surface area (>1000 m^2/g), have been used as nanostructured electrodes for supercapacitors and electrochemical devices, in order to increase the overall gravimetric and volumetric capacities [40, 42, 43]. Despite nanostructured porous carbon offers limited energy storage capacity (typically below 400 F g^{-1}), while pseudo-capacitive materials or redox-supercapacitors based on metal oxides materials or electrically conducting polymers show higher capacitive responses [44], they are extensively used as electrodes in energy devices because of their good electrical conductivity, relatively low cost and easy integration into devices. A detailed comparison between the capacitive performance of various carbon-based electrodes and the most commonly studied pseudo-capacitive materials in the literature is well provided in Ref. [43].

Among carbonaceous materials, activated carbon composites and fibers [45, 46] with surface areas up to 2000 m^2/g, as well as carbon nanotubes [47, 48] and graphene [44] have been employed in the fabrication of ECDLs [49]. Activated carbons are especially attractive as electrodes for devices from the economical point of view, and due to their large surface area and easy processability. In fact, a very high surface area, with a distribution of pores well controlled during the activation process, can be reached: typically, longer activation time and higher temperature lead to larger mean pore size. Theoretically, the higher the specific surface area of an activated carbon, the higher the specific capacitance should be expected.

Practically, the situation is more complicated, since some activated carbons with smaller surface area give a larger specific capacitance than those with a larger surface area. In Fig. 8.5 specific capacitance of activated carbon studied in Refs. [50, 51] are reported.

In carbon supercapacitors, the specific capacitance is related to carbon capability to adsorb ions from the electrolyte and to adjust its structure according to a double-layer distribution of ions. This explains why the specific capacitance is not strictly linearly dependent on the specific surface area in Fig. 8.5. Since the electrolyte pore accessibility has to be taken into account, the characterization of the specific surface area of the activated carbons is not sufficient to predict their ionic adsorption efficiency. Pore size distribution and the contribution of the different pores to the overall pores volume have to be considered in order to correctly interpret the data.

Controversial debate is being held regarding the role of micropores (pores with diameter lower than 2 nm), where opposing positions are supported by experimental and computational data too. The first idea is the classical one, which states that the

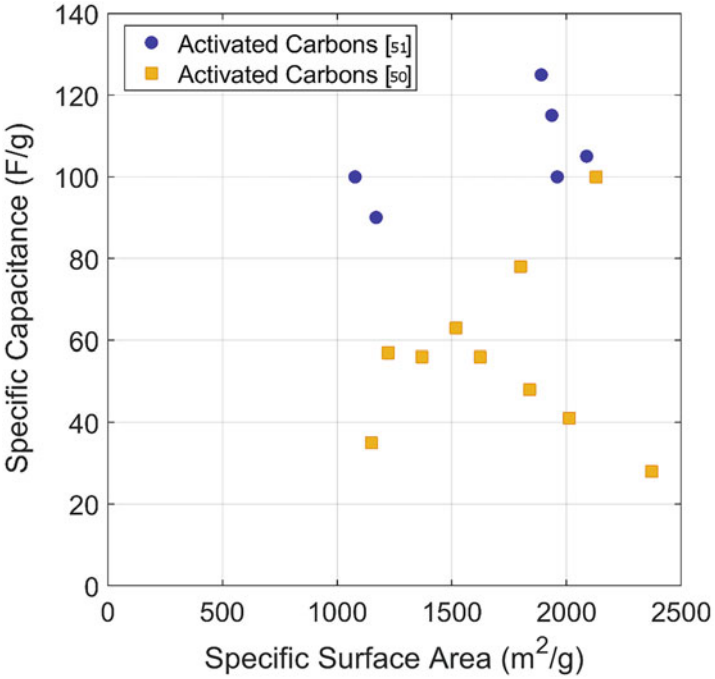

Fig. 8.5 Specific capacitance as a function of specific surface area of activated carbon used as electrode in Refs. [50, 51]. Adapted with permission from Refs. [50, 51]

increase of the microporous volume leads to an increase of the specific surface area but that the whole part of this microporous volume (in particular the one related to pores smaller than 0.5–1 nm) is not accessible to the hydrated/solvated ions, since their size limits their adsorption to the largest pores [48, 51–54]. The data shown in Fig. 8.5 are interpreted in this sense, by attributing the deviation from a linear trend of the specific capacitance with increasing surface area to a different effective accessible surface area of the electrolyte ions due to the reduced dimension of micropores. These results are consistent with the work reported in Ref. [55] showing that ions carry a dynamic sheath of solvent molecules that requires some hundreds of kilojoules per mole to be removed in the case of water molecules. For this reason, a pore size distribution in the range 2–5 nm can be then identified to improve the energy density and the power capability. Interestingly, Salitra et al. [56] suggested that a partial desolvation of ions could occur in activated carbon cloth, allowing access to small pores (diameter < 2 nm). High capacitance was observed for mesoporous carbons formed by micropores [52, 57, 58], suggesting that partial ion desolvation could lead to an improved capacitance. Due to these experimental evidences, a second hypothesis has been therefore taken into consideration, suggesting the increase of specific capacitance in carbon electrodes characterized by pores smaller than the solvated ion size, as also

shown by experiments using carbide-derived carbons (CDCs) [59–61] as the active material. The normalized capacitance ($\mu F/cm^2$) described in Ref. [61] decreases with decreasing pore size until a critical value close to 1 nm was reached, and then sharply increases when the pore size approaches the ion size. This work [62] suggests that the removal of the solvation shell, which is required for ions to enter the micropores, has been executed.

For all these evidences, the role of pore dimensions has been stressed as important as the specific surface area of porous carbon in order to evaluate their successful integration and adaptability to specific task into energy devices.

8.5 The Case of Cluster-Assembled Carbon Thin Film Integrated into Flexible Substrates

Nanostructured carbon thin films (ns-C) produced by supersonic cluster beam deposition (SCBD) [26, 63] have been employed as electrodes for the development of planar supercapacitors on rigid substrate [49], on polymer [64] and on paper [65], as also as gate electrodes for flexible transistors [64, 66] based on organic polymer. The very high specific surface area and porosity of ns-C thin films [37] allow the penetration of the electrolyte (in these cases ionic liquids – ILs) into the porous carbon matrix, and its structuring at the interface into an electrostatic double layer according to the voltage applied to the carbon electrodes.

The porosity of ns-C thin films deposited by SCBD forms from the structuring of nanometer clusters [67–69] into a rough and disordered surface, organized at the nano and mesoscale, according to a ballistic deposition model [37]. In particular, the morphological properties, as the root-mean-square roughness Rq, scale according to power laws [70, 71], while the porosity of ns-C thin films is 60%–80%, calculated from nitrogen adsorption characterization of the carbon interfaces described in Ref [37]. In Fig. 8.6a AFM topographical map stresses the rough and porous structure of ns-C thin films.

The ionic liquid passes through the open-air rough interface [70–72] and permeates the porous carbon matrix; in this condition spatial confinement, where the interactions of the IL with the constraining surfaces are relevant with respect to the mutual interactions of IL ions, may occur [3]. The formation of solid-like structures of ionic liquid at the upper interfaces of confining porous oxidized silica and carbon nanostructured thin film have been demonstrated in literature [73, 74]. Anyway, there are not evidences of the formation of such solid-like terraces inside the porous carbon matrix yet.

The comprehension of the evolution of the porosity of nanostructured carbon thin film with its thickness is of paramount importance for the study and the theoretical description of the effects of ionic liquid surface confinement through the height of the film. In fact, the contribution of the upper surface area to the total surface area

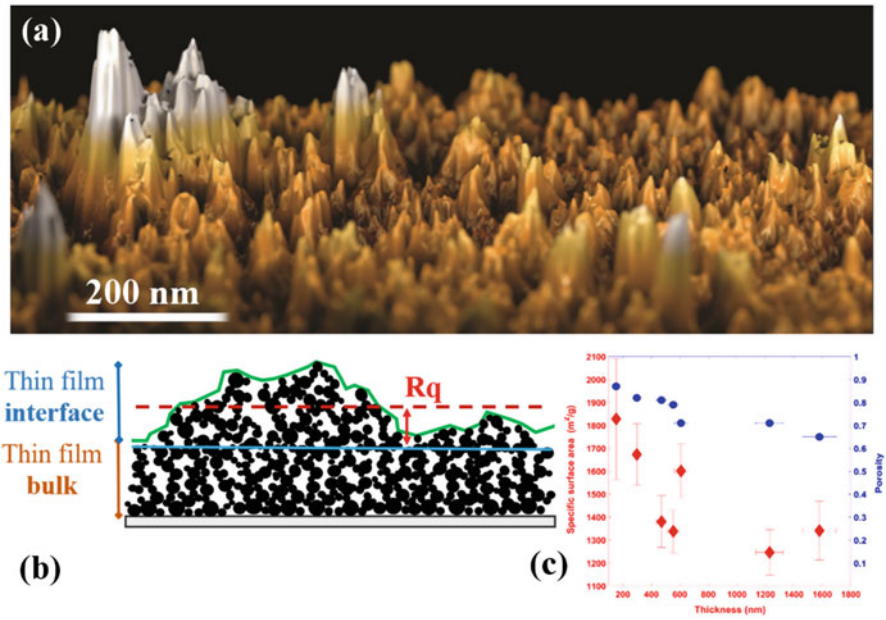

Fig. 8.6 AFM (**a**) image shows the granular and rough morphology of the porous bulk and upper surface of ns-C film; adapted with permission from Ref. [75]. Schematic representation of the thin film (**b**); specific surface area and porosity depending on the ns-C film thickness (**c**); adapted with permission from Ref. [37]

of carbon film (schematically shown in Fig. 8.6b), its porosity (Fig. 8.6c) and pore size distribution evolve with film thickness [37].

The ns-C film density measured experimentally (d 0.5 g/cm^3) does not vary appreciably with the film thickness, and it differs slightly by the value obtained with numerical simulations (d 0.7–0.8 g/cm^3) [76]. Anyway, it is important to stress that the almost constant experimental porosity of ns-C thin films with respect to film thickness represents the overall porosity of the thin film (Fig. 8.6c); furthermore the mean value p 80% is consistent with the predictions of the ballistic deposition model [28, 77]. By BET measurement, we expect that the "bulk" portion of the thin film is characterized by a higher density of 0.7–0.8 g/cm^3, while the upper interface with open larger pores decreases the value of the overall porosity up to 0.5 g/cm^3.

This hypothesis is confirmed by X-ray reflectivity analysis on the ns-C films deposited on Si substrates with different thicknesses (Fig. 8.7). In the case of the thickest film (thickness about 800 nm, as characterized by AFM measurements) the reflectivity profile clearly shows two minima at incident angles (α_i) of 0.1° and 0.13°, well below the critical angle for total external reflection of the substrate (α_{i_Si} 0.22°). These minima are related to the carbon film and reflect the existence of two layered structure with different densities (as pictured in Fig. 8.6b). By comparing the experimental to simulated reflectivity curves, the two values of

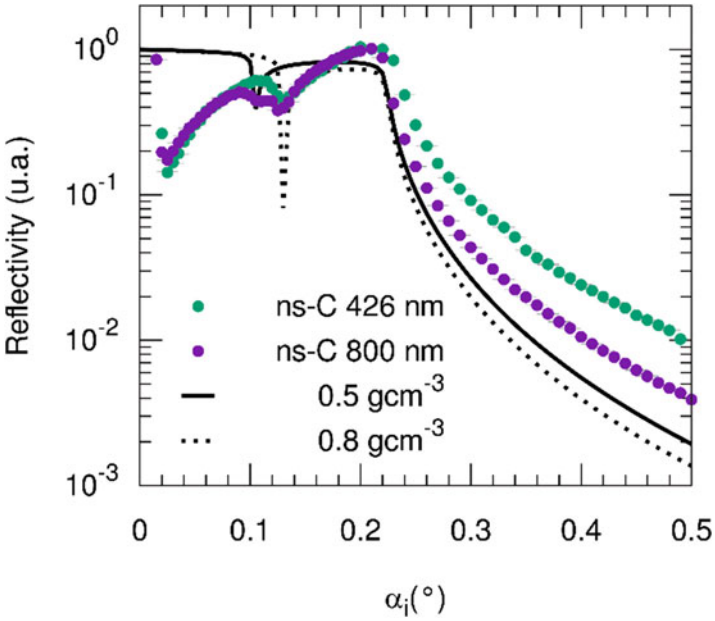

Fig. 8.7 Experimental X-ray reflectivity curves measured for ns-C films deposited on Si (thickness from AFM is 426 nm – green dots – and 800 nm – purple dots). Simulated profiles [78] are reported for 800 nm carbon films with 50 nm roughness deposited on smooth Si and density of 0.5 g cm^{-3} (solid black line) and 0.8 g cm^{-3} (dotted black line). The experimental profiles are normalized for the intensity counts/s of the first data point

critical angle can be ascribed to carbon layers with densities of 0.5 and 0.8 g·cm^{-3}, respectively. The reflectivity profile of the thinnest carbon film shows only one minimum, at incident angles $\alpha_i \sim 0.13°$, which corresponds to a carbon layer with density of 0.8 g·cm^{-3}. The density value of 0.8 g·cm^{-3} corresponds to the bulk of the thin film, which evolves into a lower density of 0.5 g·cm^{-3} for the upper interfacial region of the film, which is more pronounced in the thickest carbon film.

X-ray reflectivity analysis confirms the existence of carbon layers of different densities on ns-C film deposited by SCBD, whose values are in good agreement with BET measurements [37] and simulation [76], and which are predicted by the porosity model provided in paragraph 2 of this chapter, concerning the evolution of thin film morphology, from higher lo lower density region by moving far away from the substrate surface.

The specific surface area (A_{BET}) of carbon cluster-assembled thin films does not change significantly with the film thickness and its mean value is $A_{BET} = 1500 \pm 200$ m^2/g [37], as it is shown in Fig. 8.6.c. Its high constant value with thickness is due to the very small dimension of the clusters, which do not coalesce during the growth of the thin film and to the good accessibility of the pores. The high specific surface area value is in excellent agreement with the

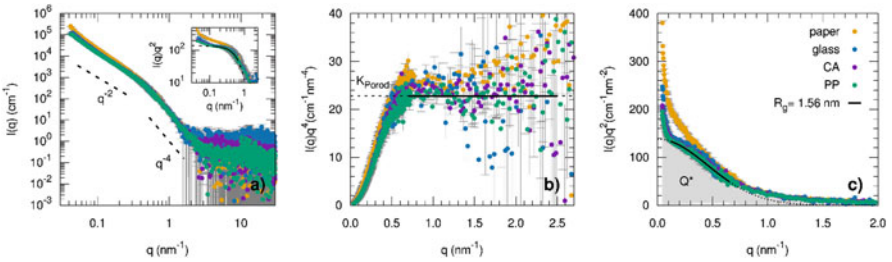

Fig. 8.8 Transmission SAXS characterization of ns-C films (thickness 426 nm) on different substrates: polypropylene film ("PP", green dots), cellulose acetate film ("CA", purple dots), thin glass (blue dots), paper (orange dots). a) Background subtracted intensities in absolute units (macroscopic scattering cross section, I(q), obtained by dividing for the film thickness in cm) on log-log scale, in which characteristic power laws followed at low and large q are shown (dashed lines). The scattering vector magnitude is defined as $q = 4\pi \sin\theta/\lambda$, with λ =0.15419 nm and 2θ being the scattering angle. In the inset, the q region in which the change of slope is observed (the "knee") is highlighted by plotting the data multiplied by q^2 to eliminate the initial q^{-2} dependence, and by comparing with a Guinier-law approximation (black line). b) Porod plots ($I(q)\cdot q^{-4}$ vs. q) which allowed determination of the horizontal intercept (the Porod constant K_{Porod}) used in the calculation of the surface area and porosity. c) Kratky plot ($I(q)\cdot q^{-2}$ vs. q) visualization of the SAXS data highlighting how the invariant $Q^* = \int_0^\infty I(q)q^2dq$ is represented by the subtended area, global parameter used in the estimate of the surface area. The result of the fit of the data from the ns-C film on PP in the q range 0.12–0.65 nm^{-1}, according to the Guinier approximation for planar geometry, is shown as a black line, as in the inset of panel a)

one calculated by numerical simulations of nanoporous carbon thin films (specific surface area 1500 m^2/g) deposited by cluster-assembling at low kinetic energy (deposition energy $E_d = 0.1$ eV/atom) [76].

In order to verify the identical growth mechanism of carbon thin film integrated onto different substrates, we have performed transmission SAXS on 426 nm thick ns-C film deposited on four different substrates: polypropylene film (PP), cellulose acetate film (CA), thin glass slides (glass) and paper (in Fig. 8.8 SAXS results are reported).

After subtraction of the scattering contribution from the respective bare substrates, the resulting SAXS profiles of the ns-C films largely overlap (Fig. 8.8a), indicating the high reproducibility of the film structure obtained by SCBD; only data acquired from the carbon thin film deposited on paper show small deviations from general trend, which is probably due to the proper porosity of the paper which partially influences the thin film growth.

In general, the SAXS signal of porous ns-C films derives from the electron density contrast between the carbon skeleton and the voids, i.e. the pores. If the two-phase system has inhomogeneities within the length scales probed in the available range of reciprocal space vector q (in the experiments shown, from approximately 70 nm to 0.2 nm, from lowest to highest q values), these will contribute to the scattering, and information about the total amount of interface and the characteristic sizes and shape of the inhomogeneities can be derived from the scattering profiles.

In the experimental profiles of the ns-C thin films three regions can be recognized, which contain structural information at different length scales: i) at $q < 0.3\ nm^{-1}$ (length scales larger than 10 nm, as estimated by $>\pi/q$) a characteristic power law close to q^{-2} is followed; ii) a change of slope is observed in the q range 0.3–0.7 nm^{-1} giving rise to a "knee" feature, whose position and slope can be related to the characteristic sizes of the inhomogeneities which compose the porous solid (micropores and nanocarbon structural units); iii) for $q > 0.7\ nm^{-1}$ the signal goes to noise level following the q^{-4} power law expected for smooth interfaces, according to the Porod law [79]. At these length scales (approximately $q > 1\ nm^{-1}$, sizes smaller than 1 nm) the scattering signal is given by the carbon-voids interfaces, irrespectively of their morphology at larger scale. At even larger q values, in the wide-angle X-ray scattering regime, peaks related to the interatomic distances of the internal structure of the carbon skeleton can contribute, but in our case, which is the one of a very thin film and not a bulk powder sample of porous carbon, such a signal is too low to be clearly detected and only a weak intensity excess can be appreciated at q around 15 nm^{-1}, which can be related to the stacking distances between sp^2 carbon planes of the order of $2\pi/q = 0.4$ nm.

Irrespective of a morphological interpretation of the pore structure, the SAXS analysis provides a global estimate of the specific surface area, calculated from the measure of the total amount of carbon-voids interface which contributes to the scattering. According to the Porod law [79], in the large q limit the scattering intensity $I(q)$ [cm^{-1}] of a system with a sharp interface between regions of different scattering length density with contrast $\Delta\rho$ [cm^{-2}] follows a q^{-4} power law in which the coefficient is related to the total surface (per unit volume) S/V:

$$I(q) \rightarrow \frac{2\pi}{q^4}(\Delta\rho)^2\frac{S}{V} \tag{8.1}$$

Therefore the S/V could be extracted by the plateau value (the "Porod constant", $K_{Porod} = 2\pi(\Delta\rho)^2 S/V$) reached in the large q limit by a plot of $I(q) \bullet q^4$ vs. q (the Porod plot, Fig. 8.8b). Deviations from these behavior (not seen in our case) can be given by a residual constant background, which could be accounted for by fitting also a non-zero slope in the line extrapolation of the Porod plot, or by fluctuations in the carbon layers which would contribute with an additional q^{-2} term that can be subtracted [80].

In practice, to avoid the estimate to be relying on the correctness of the absolute intensity scaling, the S/V is better calculated by using the so-called invariant Q^*, obtained by integrating the data in the $I(q) \bullet q^2$ vs. q form ("Kratky plot"), for normalization:

$$Q^* = \int_0^\infty I(q)q^2 dq = 2\pi^2(\Delta\rho)^2\Phi\,(1-\Phi) \tag{8.2}$$

where Φ is the volume fraction of the dense phase (the carbon skeleton) in the probed volume.

Table 8.1 Parameters obtained by the SAXS analysis of ns-C films (thickness 426 nm) on different substrates

Sample	paper	glass	CA	PP
K_{Porod} ($cm^{-1}\cdot nm^{-4}$)[a]	24.2 ± 0.5	24.7 ± 0.3	23.9 ± 0.2	22.8 ± 0.2
Q^* ($cm^{-1}\cdot nm^{-3}$)[b]	114.0 ± 0.2	95.2 ± 1.0	91.7 ± 0.3	88.2 ± 0.2
$S/V = \pi K_{Porod}/Q^*$ ($m^2\cdot cm^{-3}$)	667 ± 14	817 ± 14	817 ± 6	812 ± 7
Assumed film density ($g\cdot cm^{-3}$)	0.5	0.5	0.5	0.5
Specific surface area ($m^2\cdot g^{-1}$)	1335 ± 28	1633 ± 29	1634 ± 12	1623 ± 13
Assumed $\Delta\rho$ (10^{10} cm^{-2})	16.95	16.95	16.95	16.95
$\Phi(1-\Phi)$ from Q^* (Eq. 8.2)	0.201 ± 0.001	0.168 ± 0.002	0.162 ± 0.001	0.155 ± 0.001
$1-\Phi$ (porosity)	0.722 ± 0.002	0.787 ± 0.005	0.797 ± 0.002	0.808 ± 0.002

[a]From extrapolation of the limiting value of $I(q)\cdot q^4$ using data in the q range 0.7–2.5 nm^{-1} (Fig. 8.8b)
[b]From integration of the $I(q)\cdot q^2$ vs. q plot (Fig. 8.8c), obtained using the SasView software (https://www.sasview.org/)

In this way the *S*/*V* can be obtained by:

$$\frac{S}{V} = \pi \frac{K_{Porod}}{Q^*} \tag{8.3}$$

and it can be converted to specific surface area in m^2/g by dividing for the density value of the porous films. The results from the SAXS experimental data on the ns-C films reported in Table 8.1 show values of the specific surface area of approximately 1600 cm^2/g, with a smaller value around 1300 cm^2/g for the film deposited on paper, in good agreement with the BET results [37].

The relationship of Eq.8.2 can be also used to calculate the porosity (defined as $1-\Phi$), by considering a certain value of the scattering length density contrast $\Delta\rho$. Using the value calculated by assuming a carbon skeleton density of 2 g/cm^3 and assuming the electron density of the voids to be negligible, a porosity of 80% is obtained, with a smaller value of 72% for the film deposited on paper; also porosity obtained by SAXS analysis is in good agreement with the one obtained by nitrogen adsorption measurements [37], by confirming a very high surface area of ns-carbon thin films.

Regarding the possibility to extract information on the shape and size of the porous structure [81], in the limit of a low pore concentration, the intensity scattered would be simply the sum of the intensity scattered by all individual pores, and the features of the scattering profile in the relevant length scale could be related to the average size and shape of single pores, treated as globular particles. However, in a highly porous solid the presence of pore-pore correlations within length scales of the

Table 8.2 Parameters obtained by the SAXS analysis of ns-C films (thickness 426 nm) on different substrates

Sample	paper	glass	CA	PP
[a]*Two power law fit (q range 0.04–2.5 nm^{-1})* $I(q) = \begin{cases} scale \bullet q^{-m1} & q \le q_c \\ scale\left(q_c{}^{m2}/q_c{}^{m1}\right) \bullet q^{-m2} & q > q_c \end{cases}$				
Scale	0.272 ± 0.002	0.284 ± 0.004	0.364 ± 0.003	0.403 ± 0.003
Crossover q point q_c (nm^{-1})	0.473 ± 0.001	0.509 ± 0.003	0.500 ± 0.001	0.480 ± 0.002
$1/q_c$ (nm)	2.116 ± 0.006	1.965 ± 0.011	2.000 ± 0.006	2.085 ± 0.007
$m1$	2.457 ± 0.002	2.378 ± 0.003	2.309 ± 0.002	2.278 ± 0.002
$m2$ (fixed)	4	4	4	4
[a]*Generalized Guinier-Porod model* [82] *(q range 0.1–2.5 nm^{-1})*				
Scale factor	0.67 ± 0.02	0.98 ± 0.04	1.06 ± 0.02	1.06 ± 0.03
R_g (nm)	1.18 ± 0.01	1.31 ± 0.02	1.34 ± 0.01	1.38 ± 0.01
D exponent for initial q^{-D} power law	2.256 ± 0.006	2.091 ± 0.012	2.066 ± 0.006	2.063 ± 0.006
Porod exponent (fixed)	4	4	4	4
Guinier fit for planar geometry $I(q)\cdot q^2{}_{q<1/R_g} \approx \left[I(q)\cdot q^2\right]_{q=0} \exp\left(-R_g^2 q^2\right)$				
q range (nm^{-1})	0.30–0.54	0.13–0.64	0.12–0.68	0.12–0.65
R_g (nm)	1.68 ± 0.04	1.51 ± 0.02	1.47 ± 0.01	1.56 ± 0.02
Thickness (nm)	5.8 ± 0.14	5.2 ± 0.07	5.1 ± 0.03	5.4 ± 0.07
$[I(q) \bullet q^2]_{q=0}$ (cm^{-1} nm^{-2})	177 ± 1	143 ± 1	137 ± 1	138 ± 1

[a]Fitting performed with the SasView software (https://www.sasview.org/)

same magnitude as the pore sizes cannot be neglected and rather gives an important contribution to the scattering, especially at q values immediately lower than those corresponding to the characteristic pore sizes. In particular, the observation of a characteristic power law q^{-D} at low angle would be an indication of "aggregates" of pores, i.e. of interconnected voids volumes, with fractal dimension D. The slope close to q^{-2} observed for q values between 0.1–0.3 nm^{-1} in the SAXS of the ns-C films (Table 8.2), suggests that the porous solid at a length scale above 10 nm is composed of inhomogeneities with planar geometry ("slit" shaped porosity), with only one dimension below this size limit (i.e. the "thickness").

Such characteristic size could be roughly estimated from the q position of the Guinier-like "knee" (as 1/q = 1/0.5 nm^{-1}, around 2 nm) or by performing a Guinier fit for planar objects according to $I(q)\cdot q^2{}_{q<1/R_g} \approx \left[I(q)\cdot q^2\right]_{q=0} \exp\left(-R_g^2 q^2\right)$, where R_g is the radius of gyration of the thickness for the planar inhomogeneities. Values of R_g around 1.5 nm could be obtained (Table 8.2), which would correspond to estimated thicknesses of $\sqrt{12}\cdot R_g \approx 5$ nm. Alternatively, a unified Guinier-Porod model function [82] assuming a variable low q exponent, a generalized Guinier behavior and a final Porod slope at high q, was used to fit the data (Table 8.2). The results are consistent with the previous estimates, confirming the q^{-2} initial power

law and providing best-fit values for the R_g of 1.3 nm, corresponding to a thickness of 4.5 nm.

From the inset of Fig. 8.8a it could be noted that a power law with a more negative q^{-D} exponent ($D > 2$) is observed for $q < 0.1$ nm^{-1} and also for the entire low q range in the case of the ns-C on paper substrate. This indicates that the approximation of a planar shape for the porosity is valid up to a length scale of the order of 30 nm, but topologies with larger fractal dimensions up to macroscopic surfaces would represent the system at larger length scales not accessible in the SAXS experiments.

In view of the specific film formation method based on the deposition of carbon clusters, the carbon skeleton should also be composed by structural units of nm size. Therefore, the SAXS signal in the intermediate range where the "knee" is observed could originate from both the micropores and carbonaceous structural units, within a similar size range, according to the "Babinet" principle for the scattering of two-phase systems. According to this alternative view in which the nm-sized correlations are rather related to the carbon nanoclusers than the voids, the power law decay of intensity observed at low q with characteristic exponent D would be related to the fractal dimension of the aggregate structure formed by carbon nanoclusters and which constitutes the porous material skeleton.

8.6 Conclusions

In this chapter we have critically described the standard methods used to characterize porosity in thin films, with particular attention to in situ approaches. The combination of different and complementary approaches provides the possibility to deeply characterize many structural features of pores in thin films on different length scales, and to compare the results with the theoretical model describing the evolution of thin film porosity with thickness. As a case study we have thoroughly discussed the analysis of the porosity and structuring of nanostructured carbon thin films used as electrodes in energy devices.

The organization into porous structure of nanostructured carbon materials is of paramount importance for the performance of carbon-based energy devices. The amount of specific surface area of the carbon electrode accessible to the electrolyte, as well as the dimension of pores are strategic features which have to be considered in the development of the ideal electrode architecture for a specific task. The combination of different experimental porosity characterization techniques is crucial for a detailed description of such morphological properties.

In the specific case of nanostructured cluster-assembled carbon thin film deposited by SCBD, results of nitrogen adsorption measurements are confirmed by small angle X-ray scattering analysis performed directly on carbon thin film deposited on different substrates, which highlight a very high surface area of approximately 1550 m^2/g and an overall porosity of 80%. X-ray reflectivity investigation succeeded in describing the evolving density of carbon thin film with thickness. In particular, carbon thin film develops as a layered structure

characterized by different densities according to the region considered: a denser film characterizes the region in contact with the substrate, while a lighter zone characterizes the upper open-pores interface, according to the theoretical model.

References

1. Evans, R.: J. Phys. Condens. Matter. **2**, 8989 (1990)
2. Tarazona, P., Marconi, U.M.B., Evans, R.: Mol. Phys. **60**, 573 (1987)
3. Borghi, F., Podestà, A.: Adv Phys: X. **5**, 1736949 (2020)
4. Thybo, S., Jensen, S., Johansen, J., Johannessen, T., Hansen, O., Quaade, U.J.: J. Catal. **223**, 271 (2004)
5. Grätzel, M.: Nature. **414**, 338 (2001)
6. Simon, P., Gogotsi, Y.: Nat. Mater. **7**, 845 (2008)
7. Dimitrov, D.T., Luchinin, V.V., Moshnikov, V.A., Panov, M.V.: Tech. Phys. **44**, 468 (1999)
8. Anovitz, L.M., Cole, D.R.: Rev. Mineral. Geochem. **80**, 61 (2015)
9. Monticeli, F.M., Ornaghi, H.L., Cornelis Voorwald, H.J., Cioffi, M.O.H.: Compos. A: Appl. Sci. Manuf. **125**, 105555 (2019)
10. Alvarez, J., Saudino, G., Musteata, V., Madhavan, P., Genovese, A., Behzad, A.R., Sougrat, R., Boi, C., Peinemann, K.-V., Nunes, S.P.: Sci. Rep. **9** (2019)
11. Nossov, A., Haddad, E., Guenneau, F., Mignon, C., Gédéon, A., Grosso, D., Babonneau, F., Bonhomme, C., Sanchez, C.: Chem. Commun. **2476** (2002)
12. Calo, J., Hall, P., Antxustegi, M.: Colloids Surf. A Physicochem. Eng. Asp. **187–188**, 219 (2001)
13. Hall, P.J., Machado, W.R., Galan, D.G., Barria, E.B., Sherrington, D.C.: J. Chem. Soc. Faraday Trans. **92**, 2607 (1996)
14. Stuhrmann, H.B., Miller, A.: J. Appl. Crystallogr. **11**, 325 (1978)
15. Clarkson, C.R.R., Wood, J.M.M., Burgis, S.E.E., Aquino, S.D.D., Freeman, M.: SPE Reserv. Eval. Eng. **15**, 648 (2012)
16. Swift, A.M., Anovitz, L.M., Sheets, J.M., Cole, D.R., Welch, S.A., Rother, G.: Environ. Geosci. **21**, 39 (2014)
17. Nunes, S.P., Sougrat, R., Hooghan, B., Anjum, D.H., Behzad, A.R., Zhao, L., Pradeep, N., Pinnau, I., Vainio, U., Peinemann, K.-V.: Macromolecules. **43**, 8079 (2010)
18. Sundaramoorthi, G., Hadwiger, M., Ben-Romdhane, M., Behzad, A.R., Madhavan, P., Nunes, S.P.: Ind. Eng. Chem. Res. **55**, 3689 (2016)
19. Chisca, S., Musteata, V.-E., Sougrat, R., Behzad, A.R., Nunes, S.P.: Sci. Adv. **4**, eaat 0713 (2018)
20. Musteata, V.-E., Chisca, S., Meneau, F., Smilgies, D.-M., Nunes, S.P.: Faraday Discuss. **209**, 303 (2018)
21. Deshpande, S., Kulkarni, A., Sampath, S., Herman, H.: Surf. Coat. Technol. **187**, 6 (2004)
22. Cavaliere, E., Benetti, G., Van Bael, M., Winckelmans, N., Bals, S., Gavioli, L.: Nano. **7**, 442 (2017)
23. Peli, S., Cavaliere, E., Benetti, G., Gandolfi, M., Chiodi, M., Cancellieri, C., Giannetti, C., Ferrini, G., Gavioli, L., Banfi, F.: J. Phys. Chem. C. **120**, 4673 (2016)
24. Perez, A., Melinon, P., Dupuis, V., Jensen, P., Prevel, B., Tuaillon, J., Bardotti, L., Martet, C., Treilleux, M., Broyer, M., Pellarin, M., Vaille, J.L., Palpant, B., Lerme, J.: J. Phys. D. Appl. Phys. **30**, 709 (1997)
25. Jensen, P., Barabási, A.-L., Larralde, H., Havlin, S., Stanley, H.E.: Phys. Rev. B. **50**, 15316 (1994)
26. Wegner, K., Piseri, P., Tafreshi, H.V., Milani, P.: J. Phys. D. Appl. Phys. **39**, R439 (2006)
27. Venables, J.A., Spiller, G.D.T., Hanbucken, M.: Rep. Prog. Phys. **47**, 399 (1984)

28. Castillo, J.L., Martin, S., Rodriguez-Perez, D., Perea, A., Garcia-Ybarra, P.L.: KONA Powder Part. J. **31**, 214 (2014)
29. Bréchignac, C., Cahuzac, P., Carlier, F., Colliex, C., de Frutos, M., Kébaïli, N., Le Roux, J., Masson, A., Yoon, B.: Eur Phys J D. **16**, 265 (2001)
30. Rodríguez-Pérez, D., Castillo, J.L., Antoranz, J.C.: Phys. Rev. E. **76**, 011407 (2007)
31. Banerjee, K., Shamanna, J., Ray, S.: Phys. Rev. E. **90**, 022111 (2014)
32. Witten, T.A., Sander, L.M.: Phys. Rev. Lett. **47**, 1400 (1981)
33. Meakin, P., Ramanlal, P., Sander, L.M., Ball, R.C.: Phys. Rev. A. **34**, 5091 (1986)
34. Taylor, D., Fleig, P., Hietala, S.: Thin Solid Films. **332**, 257 (1998)
35. Benetti, G., Gandolfi, M., Van Bael, M.J., Gavioli, L., Giannetti, C., Caddeo, C., Banfi, F.: ACS Appl. Mater. Interfaces. **10**, 27947 (2018)
36. Ito, T., Fraissard, J.: J. Chem. Phys. **76**, 5225 (1982)
37. Borghi, F., Milani, M., Bettini, L.G., Podestà, A., Milani, P.: Appl. Surf. Sci. **479**, 395 (2019)
38. Subramanian, A., George, B., Bobbara, S.R., Valitova, I., Ruggeri, I., Borghi, F., Podestà, A., Milani, P., Soavi, F., Santato, C., Cicoira, F.: AIP Adv. **10**, 065314 (2020)
39. Parsons, R.: Chem. Rev. **90**, 813 (1990)
40. Pandolfo, A.G., Hollenkamp, A.F.: J. Power Sources. **157**, 11 (2006)
41. Aricò, A.S., Bruce, P., Scrosati, B., Tarascon, J.-M., van Schalkwijk, W.: Nat. Mater. **4**, 366 (2005)
42. Zhang, L.L., Zhao, X.S.: Chem. Soc. Rev. **38**, 2520 (2009)
43. Zhai, Y., Dou, Y., Zhao, D., Fulvio, P.F., Mayes, R.T., Dai, S.: Adv. Mater. **23**, 4828 (2011)
44. Zhang, L.L., Zhou, R., Zhao, X.S.: J. Mater. Chem. **20**, 5983 (2010)
45. Subramanian, V., Luo, C., Stephan, A.M., Nahm, K.S., Thomas, S., Wei, B.: J. Phys. Chem. C. **111**, 7527 (2007)
46. Kim, C., Choi, Y.-O., Lee, W.-J., Yang, K.-S.: Electrochim. Acta. **50**, 883 (2004)
47. Futaba, D.N., Hata, K., Yamada, T., Hiraoka, T., Hayamizu, Y., Kakudate, Y., Tanaike, O., Hatori, H., Yumura, M., Iijima, S.: Nat. Mater. **5**, 987 (2006)
48. Frackowiak, E., Béguin, F.: Carbon. **40**, 1775 (2002)
49. Bettini, L.G., Galluzzi, M., Podestà, A., Milani, P., Piseri, P.: Carbon. **59**, 212 (2013)
50. Frackowiak, E., Béguin, F.: Carbon. **39**, 937 (2001)
51. Gamby, J., Taberna, P., Simon, P., Fauvarque, J., Chesneau, M.: J. Power Sources. **101**, 109 (2001)
52. Vix-Guterl, C., Frackowiak, E., Jurewicz, K., Friebe, M., Parmentier, J., Béguin, F.: Carbon. **43**, 1293 (2005)
53. Shi, H.: Electrochim. Acta. **41**, 1633 (1996)
54. Qu, D., Shi, H.: J. Power Sources. **74**, 99 (1998)
55. Reichardt, C.: Angew. Chem. **99**, 826 (1987)
56. Salitra, G., Soffer, A., Eliad, L., Cohen, Y., Aurbach, D.: J. Electrochem. Soc. **147**, 2486 (2000)
57. Eliad, L., Salitra, G., Soffer, A., Aurbach, D.: Langmuir. **21**, 3198 (2005)
58. Eliad, L., Pollak, E., Levy, N., Salitra, G., Soffer, A., Aurbach, D.: Appl. Phys. A. **82**, 607 (2006)
59. Jänes, A., Lust, E.: J. Electrochem. Soc. **153**, A113 (2006)
60. Shanina, B.D., Konchits, A.A., Kolesnik, S.P., Veynger, A.I., Danishevskii, A.M., Popov, V.V., Gordeev, S.K., Grechinskaya, A.V.: Carbon. **41**, 3027 (2003)
61. Chmiola, J., Yushin, G., Dash, R., Gogotsi, Y.: J. Power Sources. **158**, 765 (2006)
62. Chmiola, J.: Science. **313**, 1760 (2006)
63. Barborini, E., Piseri, P., Milani, P.: J. Phys. D. Appl. Phys. **32**, L105 (1999)
64. Soavi, F., Bettini, L.G., Piseri, P., Milani, P., Santoro, C., Atanassov, P., Arbizzani, C.: J. Power Sources. **326**, 717 (2016)
65. Bettini, L.G., Bellacicca, A., Piseri, P., Milani, P.: Flex. Print. Electron. **2**, 025002 (2017)
66. Yi, Z., Bettini, L.G., Tomasello, G., Kumar, P., Piseri, P., Valitova, I., Milani, P., Soavi, F., Cicoira, F.: J. Polym. Sci. B Polym. Phys. **55**, 96 (2017)
67. Borghi, F., Podestà, A., Di Vece, M., Piazzoni, C., Milani, P.: In: Klaus, W. (ed.) Encyclopedia of Interfacial Chemistry: Surface Science and Electrochemistry, pp. 417–427. Elsevier (2018)

68. Bettini, L.G., Galluzzi, M., Podestà, A., Piseri, P., Milani, P.: In: Rocca, M., Rahman, T.S., Vattuone, L. (eds.) Springer Handbook of Surface Science, pp. 1217–1228. Springer International Publishing, Cham (2020)
69. Mirigliano, M., Borghi, F., Podestà, A., Antidormi, A., Colombo, L., Milani, P.: Nanoscale Adv. **1**, 3119 (2019)
70. Podestà, A., Borghi, F., Indrieri, M., Bovio, S., Piazzoni, C., Milani, P.: J. Appl. Phys. **118**, 234309 (2015)
71. Borghi, F., Podestà, A., Piazzoni, C., Milani, P.: Phys. Rev. Appl. **9**, 044016 (2018)
72. Borghi, F., Sogne, E., Lenardi, C., Podestà, A., Merlini, M., Ducati, C., Milani, P.: J. Appl. Phys. **120**, 055302 (2016)
73. Borghi, F., Milani, P., Podestà, A.: Langmuir. **35**, 11881 (2019)
74. Borghi, F., Piazzoni, C., Ghidelli, M., Milani, P., Podestà, A.: J. Phys. Chem. C. (2021)
75. Borghi, F., Chighizola, M., Maffori, L.., https://Science.Sciencemag.Org/Content/355/6327 (2017)
76. Donadio, D., Colombo, L., Milani, P., Benedek, G.: Phys. Rev. Lett. **83**, 776 (1999)
77. Mädler, L., Lall, A.A., Friedlander, S.K.: Nanotechnology. **17**, 4783 (2006)
78. Henke, B.L., Gullikson, E.M., Davis, J.C.: At. Data Nucl. Data Tables. **54**, 181 (1993)
79. Glatter, O., Kratky, O. (eds.): Small Angle X-Ray Scattering. Academic, London/New York (1982)
80. Härk, E., Ballauff, M.: C. **6**, 82 (2020)
81. Saurel, D., Segalini, J., Jauregui, M., Pendashteh, A., Daffos, B., Simon, P., Casas-Cabanas, M.: Energy Storage Mater. **21**, 162 (2019)
82. Hammouda, B.: J. Appl. Crystallogr. **43**, 716 (2010)

Index

F. Borghi et al. (eds.), *Nanoporous Carbons for Soft and Flexible Energy Devices*,
Carbon Materials: Chemistry and Physics 11,
https://doi.org/10.1007/978-3-030-81827-2